

**UCLA**

**UCLA Electronic Theses and Dissertations**

**Title**

Kinetic Plasma Simulation: Meeting the Demands of Increased Complexity

**Permalink**

<https://escholarship.org/uc/item/98q8g2m6>

**Author**

Tableman, Adam Ryan

**Publication Date**

2019

Peer reviewed|Thesis/dissertation

UNIVERSITY OF CALIFORNIA  
Los Angeles

Kinetic Plasma Simulation: Meeting the Demands of Increased Complexity

A dissertation submitted in partial satisfaction  
of the requirements for the degree  
Doctor of Philosophy in Physics

by

Adam Ryan Tableman

2019

© Copyright by  
Adam Ryan Tableman  
2019

# ABSTRACT OF THE DISSERTATION

Kinetic Plasma Simulation: Meeting the Demands of Increased Complexity

by

Adam Ryan Tableman

Doctor of Philosophy in Physics

University of California, Los Angeles, 2019

Professor Warren B. Mori, Chair

This dissertation concerns the development and use of numerical simulation techniques for studying nonlinear plasma systems in which accurate representations of the electron distribution function are required. The kinetic description of the electrons is accomplished via two different simulation modalities: the code OSHUN, which directly solves the Vlasov-Fokker-Planck (VFP) partial differential equation, and the code OSIRIS, which uses the particle-in-cell (PIC) method including an option for a separate Monte Carlo collision model.

The dissertation consists of ten chapters that are based on reprints of refereed publications that describe the development and use of OSHUN and OSIRIS. The increasing complexity of today's computers necessitates an increase in the complexity of software to take full advantage of the available computing resources. This requires that software be engineered properly to ensure correct functioning and to enable more developers to contribute. The dissertation includes examples of the creation — that is, combining new and novel algorithms with software engineering techniques — and novel usage of simulation software packages capable of exploiting the power of today's computers to enable new capability and discovery.

OSHUN includes relativistic corrections to the Vlasov equation but uses a non-relativistic description for the collision operator. The fields can be advanced in time using the full set of Maxwell's equations explicitly, just the electrostatic fields, or an implicit set of equations

that includes Ampere’s law without the displacement current. An arbitrary number of spherical harmonics can be included permitting efficient studies of physics when the distribution function is nearly in or far from equilibrium. This can drastically reduce the computational cost when only a few spherical harmonics are required. OSHUN was tested against a variety of problems spanning collisional and collisionless systems including Landau Damping, the two stream instability, Spitzer-Harm, and Epperlein-Haines heat flow coefficients in warm magnetized and unmagnetized plasmas. It was also used to explore how the heat flow in the laser entrance hole could modify Stimulated Raman Backscatter in Inertial Confinement Fusion relevant plasmas.

New numerical/algorithmic techniques were implemented in the PIC code OSIRIS. In particular, new software engineering techniques facilitated the addition of an algorithm which uses PIC in the r-z coordinates system with a gridless description in the azimuthal angle  $\phi$ . The fields, equations, and current are decomposed into an azimuthal mode,  $m$ , expansion. This Quasi-3D description permits 3D simulations at a drastically lower computational cost (approaching the cost of 2D simulations) in systems that exhibit nearly azimuthal (cylindrical) symmetry. This capability was used to examine laser wakefield acceleration (LWFA). It was used to verify scaling laws for LWFA in a nonlinear, self-guide regime. The Quasi-3D algorithm was coupled to an independently developed module in OSIRIS that allows simulation of LWFA in a Lorentz-boosted frame. Doing the calculations in this frame yields a computational savings that scales as  $\gamma^2$  (where  $\gamma$  is the Lorentz boost factor) which typically ranges from 100 to 100,000 in the systems under consideration. These modules required the development of novel field solvers and current deposition algorithms to eliminate a numerical instability called the Numerical Cerenkov Instability (NCI). These were added to OSIRIS using the new software engineering techniques now possible with Fortran 2003.

OSIRIS was updated to utilize the Graphics Processing Units (GPUs) present in exascale systems like the Summit supercomputer recently built at the Oak Ridge National Laboratory. A GPU version of OSIRIS was used to examine the interactions of Laser Speckles from Stimulated Raman Scattering (SRS). It was found that speckles can mutually interact via

scattering light, plasma waves, or non-thermal electrons transporting from speckles above threshold from SRS. This can trigger SRS in speckles that were below threshold.

Efforts towards the ultimate (and ongoing) goal of fully integrating the Quasi-3D, Lorentz-boosted frame, and GPU modules is described. When combined, these modules have the potential speed up 3D laser-plasma simulations by immense factors of  $\approx 1e^6$  or more.

The dissertation of Adam Ryan Tableman is approved.

Troy A. Carter

Viktor K. Decyk

Chandra J. Joshi

George J. Morales

Warren B. Mori, Committee Chair

University of California, Los Angeles

2019

*To Mike Meyers: You were Alwaysz into Somethin'. Smart. Resilient. Determined. Funny. Memelord. We would have done so much Physics and caused so much trouble and probably would have been run out of the building by the maintenance people long ago. You are missed.*

*To Maha Ashour-Abdalla: You did more than take teaching seriously.. you took the student's learning seriously. I loved teaching with you. I loved our tête-à-têtes even more. You were a trailblazing scientist and a classy grande dame. UCLA was diminished by your passing.*



# TABLE OF CONTENTS

Acknowledgments . . . . .	ix
Curriculum Vitae . . . . .	xvi
1 Introduction . . . . .	1
2 A multi-dimensional Vlasov-Fokker-Planck code for arbitrarily anisotropic high-energy-density plasmas. . . . .	7
3 Resonance between heat-carrying electrons and Langmuir waves in inertial confinement fusion plasmas . . . . .	18
4 Validation of OSHUN against collisionless and collisional plasma physics. . . . .	29
5 Implementation of a hybrid particle code with a PIC description in r-z and a gridless description in phi into osiris . . . . .	38
6 An Examination of the Scaling Laws for LWFA in the Self-Guided Non-linear Blowout Regime . . . . .	53
7 Mitigation of numerical Cerenkov radiation and instability using a hybrid finite difference-FFT Maxwell solver and a local charge conserving current deposit . . . . .	58
8 Enabling Lorentz boosted frame particle-in-cell simulations of laser wake-field acceleration in quasi-3D geometry . . . . .	67
9 Modeling of Laser Wakefield Acceleration In Lorentz Boosted Frame Using a Quasi-3D OSIRIS Algorithm . . . . .	80

10 Controlling the numerical Cerenkov instability in PIC simulations using a customized finite difference Maxwell solver and a local FFT based current correction. . . . .	85
11 Interactions of Laser Speckles Due to Kinetic Stimulated Raman Scattering . . . . .	97
12 Conclusion . . . . .	102
Bibliography . . . . .	103

## ACKNOWLEDGMENTS

This dissertation is the chit which closes the accounts and certifies a level of knowledge about the subject at hand but it would be incomplete without me acknowledging - as I reflect on my time at UCLA - the most important personal lesson I learned... no.. learned is the wrong word... it's more that I had forgotten and had to relearn... but God willing, as I type this, I pray that I will never forget again. To an older version of me who happens to read this: remember to "Remember Lot's wife."

There is not enough space in this dissertation for a roll call of the things I learned and for which I would thank Viktor Decyk. Viktor does everything with a characteristic unassuming equanimity. You see it in the clear boundaries/goals which delineate his projects. You see it in the way he treats people - like how he will always stop what he is doing and help anyone who comes to his door or when he patiently explains - for what must be the 50th time - to a new student why GOTO statements are not always abominations. You even see it in the striking, self-documenting directness of his code which reads like Hemingway and which, in comparison, makes my code look like Proust. Working with Viktor was an honor that helped me be a better, more unaffected scientist and thinker.

I am indebted to Karoly Holczer for his help, advice, caring, and for occasionally reminding me there is more to graduate school/life/physics than sitting behind a computer... and for many refreshing/memorable conversations and coffees.

I thank fellow student Michail Tzoufras for his invaluable advice, collaboration, and significant contributions to my research and learning. Michail was among the most competent and earnest people I have ever worked with in my professional life. His departure from academia was a loss (and a missed opportunity) for the Plasma Physics community.

I thank fellow student Peicheng Yu. Not only is he outrageously smart and capable.. but also patient and caring. I learned lots of Physics and lots about China from him... getting to know him was a highlight of my time in graduate school. His departure from academia

was a loss (and a missed opportunity) for the Plasma Physics community.

I thank my fellow students Asher Davidson, Josh May, and Thamine Dalichaouch for their camaraderie.

## **Personal**

I thank my mother, Beth Tableman.. the fiercest of protectors who taught me to literally fear no man. And my father, Kent Tableman, who in many ways could have been mimeographed from any given page of *Portnoy's Complaint*... but in a crisis can hose himself off, show up, and have your back.

I thank longtime family friend, Albert "Lib" Liberatore, from whom - as a child - I learned the word 'physics' as he taught my brother and I how to play pool. He always cared and always gave - uncannily appearing with the right thing at the right time. He gave me my first computer - an "APF MP 1000" - and figuring out how it worked became the center of my 7 year-old life giving me a focus through some difficult years. As I grew up he expanded my horizons introducing ideas/books ranging from the Gospels to Kierkegaard to Castaneda each given at a time when I was able to be receptive. Lib, again, thank you.

I thank my Aunt Kara who first introduced me to post-structuralist/postmodern theory helping me to appreciate the likes of Derrida and Foucault. I didn't/don't agree with all these ideas but - without a doubt, especially introduced in my formative years - they made me a practiced reader and instilled in me the necessity (maybe wish?) to challenge the more pedantic + literal + circumscribed thought patterns that reductive science tends to engender in its practitioners... there is always context.

I thank one of the finest men that I know, my older brother Nathan. He taught me to read at an early age (he would have me sound out the word, and punch me if I got it wrong or cried. I learned fast.). He taught me Cartesian coordinates (I drew a picture of a pumpkin on graph paper but I didn't know how to get the x,y values of the pixels for the PLOT command from my drawing.. he helped by pointing to a pixel and telling me to guess

the numbers.. punching me if I was wrong. I learned fast.) He taught me how to solder, program, electronics.. it goes on and on. I took my first physics class because he loved it and I wanted to beat him at it. It wasn't all punches and rivalry - as we got older he taught me to appreciate music, good food, staying at nice hotels sometimes.. took me to my first dance club (the legendary Limelight in NYC right before it closed)... so much more.. in short, how to add a flourish to life.

I don't know how to thank my sister, Katie. I don't have the ability to adequately describe how she made my life better. She was there and on my side in a 1000 different ways.. there and present and insightful.

I thank my companions Locky, Whaley, Dino, Lobby, Snakey, Snakette, Quetzalcotyl, Darnell, and Muffin... especially Muffin. This PhD may be (literally) as much his as it is mine. And those who didn't make it, like my my beloved lost Penguin.

## **Collaborators**

Chapter 2 contains a reprint of the article "M. Tzoufras, A. Tableman, F. S. Tsung, W. B. Mori, and A. R. Bell, "A multi-dimensional Vlasov-Fokker-Planck code for arbitrarily anisotropic high-energy-density plasmas," *Phys. Plasmas*, vol. 20, no. 5, p. 056303, 2013". I wish to acknowledge the contributions of my coauthors: M.Tzoufras for being the primary author and creator of OSHUN (the code considered in the article). F. S. Tsung for general guidance/advice on matters of physics and computational methods. W. B. Mori and A. R. Bell for being co-PIs.

Chapter 3 contains a reprint of the article "W. Rozmus, T. Chapman, A. Brantov, B. J. Winjum, R. L. Berger, S. Brunner, V. Y. Bychenkov, A. Tableman, M. Tzoufras, and S. Glenzer, "Resonance between heat-carrying electrons and Langmuir waves in inertial confinement fusion plasmas," *Phys. Plasmas*, vol. 23, no. 1, p. 012707, 2016". I wish to acknowledge the contributions of my coauthors: W. Rozmus for being primary author. T. Chapman, and A. Brantov for close collaboration on all aspects of the article. B. J. Winjum for providing direct advice/insight/help performing the OSHUN simulation used in the article. R. L. Berger for

his general physics insight/advice. S. Brunner for his insight/advice especially drawing on his extensive experience with VFP simulations methods. M. Tzoufras for his role as original creator of OSHUN. S. Glenzer for his general physics insight/advice.

Chapter 4 contains a reprint of the article "A. S. Joglekar, B. J. Winjum, A. Tableman, H. Wen, M. Tzoufras, and W. B. Mori, "Validation of OSHUN against collisionless and collisional plasma physics," *Plasma Phys. Controlled Fusion*, vol. 60, no. 6, p. 064010, 2018". I wish to acknowledge the contributions of my coauthors: A. S. Joglekar for being the primary author and proponent of the research considered. B. J. Winjum for providing advice and expertise in using OSHUN. H. Wen for providing general guidance/advice of the physics being examined. M. Tzoufras for being the original creator of OSHUN. W. B. Mori for being PI.

Chapter 5 contains a reprint of the article "A. Davidson, A. Tableman, W. An, F. S. Tsung, W. Lu, J. Vieira, R. A. Fonseca, L. O. Silva, and W. B. Mori, "Implementation of a hybrid particle code with a PIC description in r-z and a gridless description in phi into osiris," *J. Computational Phys.*, vol. 281, pp. 1063–1077, 2015". I wish to acknowledge the contributions of my coauthors: A. Davidson for being primary author. F. S. Tsung and W. An for guidance/advice on matters of physics and computational methods. Ricardo A. Fonseca for advice and insight as primary author of OSIRIS. L. O. Silva and W. B. Mori for being co-PIs.

Chapter 6 contains a reprint of the article "A. Davidson, A. Tableman, P. C. Yu, W. M. An, F. Tsung, W. Lu, R. A. Fonseca, and W. B. Mori, "An Examination of the Scaling Laws for LWFA in the Self-Guided Nonlinear Blowout regime," *Adv. Accelerator Concepts*, vol. 1812, pp. UNSP 040014–1, 2017". I wish to acknowledge the contributions of my coauthors: A. Davidson for being primary author. Peicheng Yu for general advice/guidance as well as expertise in LWFA simulation. Weiming An and Frank S. Tsung for guidance/advice on matters of physics and computational methods. Wei Lu for advice/insight drawing from his seminal work in developing LWFA scaling laws. Ricardo A. Fonseca for advice and as primary author of OSIRIS. Warren B. Mori for being PI.

Chapter 7 contains a reprint of the article "P. C. Yu, X. L. Xu, A. Tableman, V. K. Decyk, F. S. Tsung, F. Fiuza, A. Davidson, J. Vieira, R. A. Fonseca, W. Lu, L. O. Silva, and W. B. Mori, "Mitigation of numerical Cerenkov radiation and instability using a hybrid finite difference-FFT Maxwell solver and a local charge conserving current deposit," *Computer Phys. Comm.*, vol. 197, pp. 144–152, 2015". I wish to acknowledge the contributions of my coauthors: Peicheng Yu for being primary author and creator of the method described in the article. Xinlu Xu for his close collaboration and expertise in aiding development of the Lorentz boosted frame method. Viktor K. Decyk for insight, experience, and advice pertaining to the numerical methods used. Frank S. Tsung and Jorge Vieira for guidance/advice on matters of physics and computational methods. A. Davidson for aiding in adapting the methods for use in OSIRIS. Ricardo A. Fonseca for advice and insight as primary author of OSIRIS. Wei Lu, L. O. Silva and W. B. Mori for being co-PIs.

Chapter 8 contains a reprint of the article "P. C. Yu, X. L. Xu, A. Davidson, A. Tableman, T. Dalichaouch, F. Li, M. D. Meyers, W. M. An, F. S. Tsung, V. K. Decyk, F. Fiuza, J. Vieira, R. A. Fonseca, W. Lu, L. O. Silva, and W. B. Mori, "Enabling Lorentz boosted frame particle-in-cell simulations of laser wakefield acceleration in quasi-3D geometry," *J. Computational Phys.*, vol. 316, pp. 747–759, 2016". I wish to acknowledge the contributions of my coauthors: Peicheng Yu for being primary author and creator of the method described in the article. Xinlu Xu for his close collaboration and expertise in aiding development of the Lorentz boosted frame method. A. Davidson for his work implementing the quasi-3D cylindrical modes module in OSIRIS and help in integrating it with the Lorentz boosted frame method. Thamine Dalichaouch for his work developing data processing/visualization tools for analyzing the results of quasi-3D cylindrical modes simulations. Fei Li for collaboration in improving and testing the Lorentz boosted frame method. Michael D. Meyers for executing several of the example simulations used in the article. Frank S. Tsung and Jorge Vieira for guidance/advice on matters of physics and computational methods. Viktor K. Decyk for insight, experience, and advice pertaining to the numerical methods used. Frederico Fiuza for his general advice and insight on the physics applications of the Lorentz boosted frame

method. Ricardo A. Fonseca for advice and insight as primary author of OSIRIS. Wei Lu, L. O. Silva and W. B. Mori for being co-PIs

Chapter 9 contains a reprint of the article "P. Yu, A. Davidson, X. Xu, A. Tableman, V. K. Decyk, F. S. Tsung, J. Vieira, R. A. Fonseca, W. Lu, L. O. Silva, and W. B. Mori, "Modeling of Laser Wakefield Acceleration In Lorentz Boosted Frame Using a Quasi-3D OSIRIS algorithm," *Adv. Accelerator Concepts, (aac 2014)*, vol. 1777, p. UNSP 040020, 2016". I wish to acknowledge the contributions of my coauthors: Peicheng Yu for being primary author and creator of the method described in the article. A. Davidson for his work implementing the quasi-3D cylindrical modes module in OSIRIS and help in integrating it with the Lorentz boosted frame method. X. Xu for his close coloration and expertise in aiding development of the Lorentz boosted frame method. Viktor K. Decyk for insight, experience, and advice pertaining to the numerical methods used. F. S. Tsung and J. Vieira for guidance/advice on matters of physics and computational methods. Ricardo A. Fonseca for advice and insight as primary author of OSIRIS. Wei Lu, L. O. Silva and W. B. Mori for being co-PIs.

Chapter 10 contains a reprint of the article "F. Li, P. C. Yu, X. L. Xu, F. Fiuza, V. K. Decyk, T. Dalichaouch, A. Davidson, A. Tableman, W. M. An, F. S. Tsung, R. A. Fonseca, W. Lu, and W. B. Mori, "Controlling the numerical Cerenkov instability in PIC simulations using a customized finite difference Maxwell solver and a local FFT based current correction," *Computer Phys. Comm.*, vol. 214, pp. 6–17, 2017". I wish to acknowledge the contributions of my coauthors: Fei Li for being primary author and creator of the finite difference method being described. Peicheng Yu and Xinlu Xu who were close collaborators with Fei Li and aided in the development of the method described. Frederico Fiuza for providing motivation, advice, and insight around the relativistic plasma drift examples simulated in the article. Viktor K. Decyk for insight, experience, and advice pertaining to the numerical methods used. Thamine Dalichaouch for setting up, executing, and processing the data from the example simulations used within the article. Asher Davidson for his implementation of the quasi-3D cylindrical modes module in OSIRIS. Weiming An and Frank S. Tsung for



guidance/advice on matters of physics and computational methods. Ricardo A. Fonseca for advice and as primary author of OSIRIS. Wei Lu and Warren B. Mori for being co-PIs.

Chapter 11 is a version of "B. J. Winjum, A. Tableman, F. S. Tsung, and W. B. Mori. Interactions of Laser Speckles Due to Kinetic Stimulated Raman Scattering. Manuscript in preparation, 2018." I wish to acknowledge the contributions of my coauthors: B. J. Winjum for being the primary author. Frank S. Tsung for guidance/advice on matters of physics and computational methods. W. B. Mori for being PI.

## CURRICULUM VITAE

- 1993 – 1997            BS in Physics with University High Honors/Phi Beta Kappa,  
Carnegie Mellon University, Pittsburgh, PA
- 2007 – Present        Ph.D. student in Physics, University of California, Los Angeles  
(UCLA).

## PUBLICATIONS

A. S. Joglekar, B. J. Winjum, A. Tableman, H. Wen, M. Tzoufras, and W. B. Mori. Validation of OSHUN against collisionless and collisional plasma physics. *Plasma Phys. Controlled Fusion*, 60(6):064010, 2018

F. Li, P. C. Yu, X. L. Xu, F. Fiuza, V. K. Decyk, T. Dalichaouch, A. Davidson, A. Tableman, W. M. An, F. S. Tsung, R. A. Fonseca, W. Lu, and W. B. Mori. Controlling the numerical Cerenkov instability in PIC simulations using a customized finite difference Maxwell solver and a local FFT based current correction. *Computer Phys. Comm.*, 214:6–17, 2017

A. Davidson, A. Tableman, P. C. Yu, W. M. An, F. Tsung, W. Lu, R. A. Fonseca, and W. B. Mori. An Examination of the Scaling Laws for LWFA in the Self-Guided Nonlinear Blowout regime. *Adv. Accelerator Concepts*, 1812:UNSP 040014–1, 2017

P. C. Yu, X. L. Xu, A. Davidson, A. Tableman, T. Dalichaouch, F. Li, M. D. Meyers, W. M. An, F. S. Tsung, V. K. Decyk, F. Fiuza, J. Vieira, R. A. Fonseca, W. Lu, L. O. Silva, and W. B. Mori. Enabling Lorentz boosted frame particle-in-cell simulations of laser wakefield acceleration in quasi-3D geometry. *J. Computational Phys.*, 316:747–759, 2016

P. Yu, A. Davidson, X. Xu, A. Tableman, V. K. Decyk, F. S. Tsung, J. Vieira, R. A. Fonseca, W. Lu, L. O. Silva, and W. B. Mori. Modeling of Laser Wakefield Acceleration In Lorentz Boosted Frame Using a Quasi-3D OSIRIS algorithm. *Adv. Accelerator Concepts*, (aac 2014), 1777:UNSP 040020, 2016

W. Rozmus, T. Chapman, A. Brantov, B. J. Winjum, R. L. Berger, S. Brunner, V. Y. Bychenkov, A. Tableman, M. Tzoufras, and S. Glenzer. Resonance between heat-carrying electrons and Langmuir waves in inertial confinement fusion plasmas. *Phys. Plasmas*, 23(1):012707, 2016

P. C. Yu, X. L. Xu, A. Tableman, V. K. Decyk, F. S. Tsung, F. Fiuza, A. Davidson, J. Vieira, R. A. Fonseca, W. Lu, L. O. Silva, and W. B. Mori. Mitigation of numerical Cerenkov radiation and instability using a hybrid finite difference-FFT Maxwell solver and a local charge conserving current deposit. *Computer Phys. Comm.*, 197:144–152, 2015

A. Davidson, A. Tableman, W. An, F. S. Tsung, W. Lu, J. Vieira, R. A. Fonseca, L. O. Silva, and W. B. Mori. Implementation of a hybrid particle code with a PIC description in r-z and a gridless description in phi into osiris. *J. Computational Phys.*, 281:1063–1077, 2015

M. Tzoufras, A. Tableman, F. S. Tsung, W. B. Mori, and A. R. Bell. A multi-dimensional Vlasov-Fokker-Planck code for arbitrarily anisotropic high-energy-density plasmas. *Phys. Plasmas*, 20(5):056303, 2013

A. A. Sahai, F. S. Tsung, A. R. Tableman, W. B. Mori, and T. C. Katsouleas. Relativistically induced transparency acceleration of light ions by an ultrashort laser pulse interacting with a heavy-ion-plasma density gradient. *Phys. Rev. E*, 88(4):043105, 2013

# CHAPTER 1

## Introduction

This dissertation is an anthology of published papers that directly use the work I conducted as part of my doctorate research. They can be roughly divided into two categories. The first 3 papers concern work done involving the Vlasov-Fokker-Planck (VFP) code OSHUN. The last 7 papers concern work done involving the particle-in-cell code OSIRIS.

### OSHUN

The first version of OSHUN was written by my collaborator Michail Tzoufras in the language C++ during his time as a postdoc at Oxford under the tutelage of A. R. Bell. I began working with Michail when he later came to UCLA as a postdoc. The paper reprinted in Chapter 2 of this thesis [5] show some of the work I did with Michail. In particular, I helped him write the prose of the article, setup and run some of the physics simulations used as examples, and did the work on obtaining a Courant–Friedrichs–Lewy (CFL) condition for OSHUN (which in practice means finding the CFL for the isotropic part of the collision operator... the CFL gives a region of allowed parameters where stable, valid results can be expected). After this paper, I spearheaded a rewrite of the C++ code - Version 2.0. The old code base used the C++ Standard Template Library (STL) for all it's data access which is the 'recommended', 'correct', and 'generalized/abstracted' way to write C++ code. Previous experience had taught me to not trust STL — especially with numerical code. Replacing STL, among other architectural changes, netted a factor 10,000 speed up of the code - making much larger runs and simulating more far reaching physics possible. I also added was a GPU version of the collision operator, yielding even more speed increase.

During this time, I constructed a 1D pure python version of OSHUN that was intended to have all the physics of OSHUN but be much simpler to use off-the-shelf for new users and much simpler (then the optimized c++ code) to understand and add/test new physics modules. I used this code to develop/test a new collision module that allows for a moving ion species. This version has been used by various researchers as an introduction to OSHUN and for smaller scale simulations. It has also been used by students to explore basic plasma physics.

Also, during this time, I tackled the key - and often overlooked, unfortunately - issue of validating the code against real physics benchmarks. To this end, I created a suite of test cases which simulated various foundational plasma physics problems whose results which could be compared against theory in order to validate OSHUN's calculations. This suite was such that it was easy to run so that the code could be continuously checked for physics mistakes and programming errors. While setting up these physics test cases, I decided that we needed to include one of the most classic (and uniquely) plasma plasma physics problems: Landau Damping. This necessitated adding electrostatic field solver, wave driver, and Poisson solver modules into OSHUN. The results for Landau Damping were especially gratifying and where used as the basis for the work reprinted in Chapter 4[7].

Michail and I always had in mind that OSHUN should be usable in the wider scientific community by other researchers. Lab-mate Ben Winjim became the first person outside Michail and I to use OSHUN — our first 'client' as it were. I worked with Ben extensively to teach him how to use OSHUN, how to setup the simulations of the physics he was interested in, and as a test subject to see what pitfalls new users would face using OSHUN (Ben was extremely patient and helped me finds lots of pitfalls which I would semi-embarrassingly and dutifully fix). Ben began using OSHUN in his research, one result of which is seen in the work he and I did in designing, setting up, and running the OSHUN simulations seen in the reprint which makes up Chapter 3 of this dissertation[6]

Archis Joglekar came to UCLA as a postdoc and began to work with OSHUN. Ben and I worked with him extensively getting him trained on the usage and codebase of OSHUN.

The reprint seen in Chapter 4[7] of this dissertation is the result of Archis's very good work which extends the OSHUN Version 2.0 code-base (including GPU support) and the initial work I had done applying OSHUN to the Landau Damping problem.

## OSIRIS

Describing in detail all of the work I did in the OSIRIS code-base would take us outside the bounds of this introduction. Much of it – in fact – is not described within the anthology of reprints that makes up this dissertation. Rather, it is codified in the living, working code-base of OSIRIS. I will concern myself here with describing the portion needed to give a context/central thread to the work described in this dissertation.

One highlight of my work during graduate school was the version of Osiris I wrote in 2013 which makes use of Graphics Processing Units (GPUs) — my GPU code gave OSIRIS an approximate factor of 100 speed increase. As I wrote the GPU code, I wanted to ensure that it wasn't just a toy code or shallow bragging point about the speed of OSIRIS that could only run selected, simple benchmark cases. Ben Winjim (once again.. thanks Ben!) was my 'test case'.. for his work, he wanted to examine the interactions of Laser Speckles from Stimulated Raman Scattering (SRS). This problem provided a perfect large, real world physics application and I used it as my base test case/benchmark. The results of this work are detailed in the reprint which makes up Chapter 11 of this dissertation.

Programming GPUs can be quite challenging on its own, but equally as challenging were the issues of integrating such a complicated feature into the OSIRIS code-base. OSIRIS was already a complicated piece of software... adding the GPU - or any sufficiently complex - module to OSIRIS was more than the infrastructure could bare, resulting in convoluted, mistake-prone, and unmaintainable code. In short, OSIRIS had outgrown itself.

This need to update OSIRIS was made manifest as I began work with lab-mate Asher Davidson. As part of his graduate work, Asher began implementing the quasi-3D module. This module implements an r-z coordinate system with a gridless description in the azimuthal angle  $\phi$ . Working off my experience adding GPU support, I worked with Asher extensively in

the design and implementation of the structure of his code so it could fit within OSIRIS while remaining as clear and maintainable as possible. I also helped with one of the most tricky parts of adding new numerical simulation physics to any code — validation. By validation I mean, in particular, choosing the best, most useful tests to make sure the code is doing what it should (this is a process that requires experience and taste and it's easy to get lost here. One of the more straightforward examples of this trickiness: working around the vicissitudes of finite precision floating point arithmetic especially when comparing results). The results of this work are detailed in the reprint which makes up Chapter 5 [8].

As I worked with Asher, I took note of his difficulties (as an example of a student physicist and using his experience as an example of the difficulties other grad students might face when adding to OSIRIS) and adding his experience to mine, began designing a new structure for OSIRIS. In late 2015, formal work began with Ricardo Fonseca (OSIRIS's principle author) and I co-designing the updated structure of this new OSIRIS - version 4.0. By mid to late 2016, principle coding on version 4.0 was complete and the codebase was mature enough (i.e. we were confident it made proper physics and met it's design goals) that we 'opened the doors to the public' — ending official future development of 3.0 and officially encouraging users to switch to the new version. OSIRIS 4.0 represents a synthesis of lots and lots and lots (from the important big picture to the small details) of the knowledge I learned in graduate school and it is gratifying to see it out in the world being used.

Asher's Quasi-3D module was the exemplar case Ricardo and I used while hacking out OSIRIS 4.0's design. After 4.0 was prêt-à-porter, I worked with Asher to port his Quasi-3D code from OSIRIS 3.0 to OSIRIS 4.0. Part of this process was re-validating the physics and ensuring correctness. This is part of the work that is behind the reprint that makes up Chapter 6[9] of this dissertation.

During this time (beginning in 2015), I also began working with lab-mate Peicheng Yu as he worked to add a module to OSIRIS which enables simulations — particularly Laser Wakefield Acceleration (LWFA) — in a Lorentz-boosted frame where the plasma moves towards the laser. I worked with Peicheng to integrate his module in OSIRIS 3.0 (and later

into 4.0). I also worked with him on a number of issues relating to his project. I added the Fast Fourier Transform that his work requires into OSIRIS taking special care to abstract out (i.e. make easier to use) the various niggling details that the-care-and-feeding-of-FFTs requires. This FFT work was especially challenging since Peicheng's code primarily uses 1D FFTs which are notoriously difficult to use in parallel computing systems (like the one we use: MPI) in such a way to get good performance. What follows is not a scientific statement but here it goes: some of the physics from Peicheng's module felt a touch 'off'.. real numerics can get messy and floating point always muddies things a bit.. but things felt more muddy than I would expect. This led me to tracking down a pervasive (and startlingly easy to make) mistake that we had in our Fortran code when dealing with complex numbers (luckily complex numbers were not heavily used in most of OSIRIS so this issue was not seen too often) that would cause a halving of precision. I also worked with Peicheng on issues related to diagnostics ('diagnostics' is the term borrowed from experiment given to the actual data that we write out for the user to look at). Peicheng's method calculates in a Lorentz frame.. but usually (most times) we want to see results in the lab frame, which requires a boost back to the lab frame. The challenge comes from the structure of the Lorentz transform (i.e. the mixing of space and time) which requires that data from multiple times steps be used to reconstruct the a single time-step of lab frame data. OSIRIS, in general, did not support keeping multiple time step's worth of data in memory (and writing such data to disk is very expensive so is not an option). I also worked with Peicheng on some details of his scheme - in particular optimization of the windowing function he uses in Fourier space and the strange (unresolved at this point) behavior that if his filtering technique is applied to OSIRIS's current density (the current density is then directly used to solve for the E/B fields) things work well.. but if the same method is applied to the fields DIRECTLY, the whole simulation becomes garbage (the fields become unstable) within a small number of time-steps. This work is part of what makes up the reprint that is Chapter 7[10] of this dissertation. Peicheng's method was later extended by lab-mate Fei Li. Fei constructed a finite-difference (versus FFT) version of Peicheng's method. The help I gave Fei in integrating his work into OSIRIS is part of what makes up Chapter 10[13] of this dissertation.



## Synthesis is Future

Peicheng had a dream. A crazy dream at the time (2015). He called it H<sub>3</sub>O (I had wanted to call it *in nomine Patris et Filii et Spiritus Sancti* — his name is better ).

His dream — to combine GPU, Quasi-3D, and Lorentz Boosted frame — became my dream. This could yield a factor 1e6 or more speed up for LWFA runs (roughly, GPU gives a factor of 100, Quasi-3D a factor 100, and boosted frame a factor  $\gamma^2$  — where  $\gamma$  is the Lorentz boost factor — typically ranging from 100 to 100,000). This would be amazing... allowing, for example, unprecedented parameter scans to optimize LFWA runs.

I worked with Peicheng on his boosted frame code with H<sub>3</sub>O in mind (and indeed H<sub>3</sub>O was part of what drove my work to create OSIRIS 4... since only a new software infrastructure would be able to support the unification of these modules). I continued working with him as he united two of the three modules, Quasi-3D + and Lorentz boosted frames. This work is part of what went into the reprints which make up Chapter 8[11] and Chapter 9[12] of this dissertation.

I leave my PhD with H<sub>3</sub>O not yet completed. The final addition of the GPU code remains undone. But this is a great avenue for future work.

## A multi-dimensional Vlasov-Fokker-Planck code for arbitrarily anisotropic high-energy-density plasmas<sup>a)</sup>

M. Tzoufras,<sup>1,b)</sup> A. Tableman,<sup>1</sup> F. S. Tsung,<sup>1</sup> W. B. Mori,<sup>1</sup> and A. R. Bell<sup>2</sup>

<sup>1</sup>*Department of Physics and Astronomy, University of California, Los Angeles, California 90095, USA*

<sup>2</sup>*Clarendon Laboratory, University of Oxford, Parks Road, Oxford OX1 3PU, United Kingdom and Central Laser Facility, STFC Rutherford-Appleton Laboratory, Chilton, Didcot, Oxfordshire OX11 0QX, United Kingdom*

(Received 30 November 2012; accepted 5 February 2013; published online 16 April 2013)

To study the kinetic physics of High-Energy-Density Laboratory Plasmas, we have developed the parallel relativistic 2D3P Vlasov-Fokker-Planck code OSHUN. The numerical scheme uses a Cartesian mesh in configuration-space and incorporates a spherical harmonic expansion of the electron distribution function in momentum-space. The expansion is truncated such that the necessary angular resolution of the distribution function is retained for a given problem. Finite collisionality causes rapid decay of the high-order harmonics, thereby providing a natural truncation mechanism for the expansion. The code has both fully explicit and implicit field-solvers and employs a linearized Fokker-Planck collision operator. OSHUN has been benchmarked against well-known problems, in the highly kinetic limit to model collisionless relativistic instabilities, and in the hydrodynamic limit to recover transport coefficients. The performance of the code, its applicability, and its limitations are discussed in the context of simple problems with relevance to inertial fusion energy. © 2013 AIP Publishing LLC. [<http://dx.doi.org/10.1063/1.4801750>]

### I. INTRODUCTION

#### A. Ubiquity of kinetic effects in laser-ablated plasmas

The transport of electrons through ionized matter is a basic science and engineering problem, with applications ranging from fusion plasmas, to astrophysics, to semiconductor technology. In each case, one needs to employ a model that incorporates the essential physics of the background material and the laws that govern its interaction with the flow of electrons. The main challenge in developing an accurate simulation capability is finding a simple enough set of rules that retains the pertinent features of the interaction, because a full description of the microscopic physics of individual electron trajectories for large spatial and temporal scales is not currently feasible even on the world's largest computers. Furthermore, even if such calculations become possible they will not be the most efficient way to study the microphysics for many scenarios.

Laser-ablated plasmas typically involve materials with maximum density in excess of solid, that is,  $10^{23} \text{ cm}^{-3}$ , ionized by sub- $\mu\text{m}$ , pico-second to nano-second pulses. Laser energy is absorbed in the under-dense corona up to the critical density,  $n_c \simeq 9.0663 \times 10^{21} \text{ cm}^{-3} \times (0.351 \mu\text{m}/\lambda_0)^2$ , where  $\lambda_0$  is the laser wavelength, and then conducted deeper in the target by electrons. To a first approximation, the plasma can be described as a fluid and heat conduction can be considered a local diffusion process that obeys Fourier's law,  $Q_e = \kappa_{SH} \nabla T_e$ , where  $Q_e$  is the heat flux and  $\kappa_{SH}$  the effective heat conduction coefficient calculated by Spitzer and Härm for a fully ionized plasma.<sup>27</sup> This is a straightforward and

attractive approach, but it assumes that the electron distribution function remains Maxwellian everywhere and that the scale-length of the electron temperature is long compared to the collisional mean free path.

Non-Maxwellian distributions are, however, prevalent in HEDLP. For example, even for moderate intensities, laser absorption due to inverse bremsstrahlung is associated with the Dum<sup>11,12</sup>-Langdon<sup>19</sup>-Matte<sup>23</sup> distributions. For higher intensities, the absorption is dominated by parametric instabilities which produce distributions with high-energy tails. If the intensity increases further more exotic mechanisms can occur, that cause extreme distortions to the electron distribution. Meanwhile, even in a fully Maxwellian plasma, the presence of a steep temperature gradient generates non-Maxwellian features as energetic particles outrun the slower ones. Moreover, these kinetic phenomena do not appear in isolation; the distribution function generated from the absorption of an intense laser pulse determines the characteristics of the electron transport and vice-versa.

#### B. Vlasov-Fokker-Planck modeling for non-Maxwellian plasmas

##### 1. The Vlasov-Fokker-Planck equation

When the correlations between the fluctuating fields are small, the evolution of a distribution of charged particles  $f(\mathbf{r}, \mathbf{p}, t)$  can be described by the Boltzmann equation

$$\frac{\partial f}{\partial t} + \mathbf{v} \cdot \frac{\partial f}{\partial \mathbf{r}} + q \left( \mathbf{E} + \frac{\mathbf{v}}{c} \times \mathbf{B} \right) \cdot \frac{\partial f}{\partial \mathbf{p}} = \left( \frac{\delta f}{\delta t} \right)_c, \quad (1)$$

where  $\mathbf{E}$  and  $\mathbf{B}$  represent the ensemble-averaged fields and  $\left( \frac{\delta f}{\delta t} \right)_c$  the change in the distribution function due to collisions. For a collisionless plasma, one can set  $\left( \frac{\delta f}{\delta t} \right)_c = 0$  to

<sup>a)</sup>Paper YI2 3, Bull. Am. Phys. Soc. 57, 369 (2012).

<sup>b)</sup>Invited speaker. Electronic mail: mtzoufras@physics.ucla.edu.

obtain the entropy-conserving Vlasov equation. In a plasma with large number of particles in a Debye sphere  $N_D = (4/3)n\lambda_D^3 = (4/3)n(k_B T_e / 4\pi n q)^{3/2} \gg 1$ , but not so large as to render the plasma collisionless, the cumulative effect of many distant interactions dominates the collision operator which may be written as a conservation equation

$$\left(\frac{\delta f}{\delta t}\right)_{FP} = -\frac{\partial}{\partial \mathbf{v}} \cdot [f \langle \Delta \mathbf{v} \rangle] + \frac{1}{2} \frac{\partial}{\partial \mathbf{v}} \frac{\partial}{\partial \mathbf{v}} : [f \langle \Delta \mathbf{v} \Delta \mathbf{v} \rangle], \quad (2)$$

where  $\Delta \mathbf{v}$  is the velocity increment per unit time. This is the Fokker-Planck collision operator. A compact expression for this collision operator that is amenable to numerical solution was derived by Rosenbluth *et al.*<sup>26</sup> under the assumption that changes in velocity are due to binary Coulomb interactions. Substitution of the Fokker-Planck equation into Boltzmann's equation yields the Vlasov-Fokker-Planck equation

$$\frac{\partial f}{\partial t} + \mathbf{v} \cdot \frac{\partial f}{\partial \mathbf{r}} + q \left( \mathbf{E} + \frac{\mathbf{v}}{c} \times \mathbf{B} \right) \cdot \frac{\partial f}{\partial \mathbf{p}} = \left(\frac{\delta f}{\delta t}\right)_{FP}. \quad (3)$$

This equation encompasses much of the kinetic physics of interest to HEDLP, because it describes the evolution of an arbitrary distribution function in the presence of both electromagnetic fields and small-angle binary collisions.

## 2. Exploitation of spherical geometry from VFP codes

Vlasov-Fokker-Planck codes solve Eq. (3) to simulate the evolution of the electron distribution function, which is a four- to six-dimensional quantity for a one- to three-dimensional configuration-space, respectively. VFP simulations, therefore, demand large amounts of computer memory which, in practice, limits the number of time-steps that can be taken. To get around this, some property of the system is usually exploited, either to shrink the volume of the required information or to solve a reduced set of equations and take large time-steps (or both).

The ‘‘diffusive approximation’’ relies on angular scattering to maintain near-isotropy in momentum-space, while relaxation to a Maxwellian is not assumed. The distribution function may then be expressed as a sum of the isotropic distribution  $f_0(p)$ , where  $p \equiv |\mathbf{p}|$ , and a perturbation  $f_1(p)$  multiplied by the direction cosines

$$f(\mathbf{p}) \simeq f_0(p) + \frac{\mathbf{p}}{p} \cdot \mathbf{f}_1(p). \quad (4)$$

Thus, the entire 3D momentum-space can be represented with four 1D arrays, containing  $f_0$  and  $\mathbf{f}_1$ . However, only weakly anisotropic phenomena can be captured by this scheme; any anisotropic physics must occur in time-scales that are much longer than the characteristic time for momentum isotropization due to electron-ion collisions,  $\tau_{ei} = \tau_e / Z = \frac{3\sqrt{m_e}(k_B T_e)^{3/2}}{4\sqrt{2}\pi n_e e^4 \ln \Lambda}$ . This stringent restriction on the shape of the distribution notwithstanding, diffusive VFP simulations in 1D<sup>4,8,22,28</sup> and 2D<sup>15–18,29</sup> have been successful in revealing many features of non-local electron transport.

The expansion to spherical harmonics, of which the diffusive approximation is the first-order truncation, allows for

a complete representation of the electron distribution function

$$f(\mathbf{r}, \mathbf{p}, t) = \sum_{\ell=0}^{\infty} \sum_{m=-\ell}^{\ell} f_{\ell}^m(\mathbf{r}, p, t) P_{\ell}^{m|}(\cos \theta) e^{im\phi}, \quad (5)$$

where  $f_{\ell}^{-m} = (f_{\ell}^m)^*$ ,  $P_{\ell}^{m|}(x)$  are the associated Legendre polynomials, and we follow the same conventions as in Tzoufras *et al.*,<sup>32</sup> that is  $(p_x, p_y, p_z) = (p \cos \theta, p \sin \theta \cos \phi, p \sin \theta \sin \phi)$ . This expansion must be terminated for some  $(\ell_0, m_0)$  such that the remainder of the series for  $(\ell > \ell_0, \text{ or } m > m_0)$  is negligible.

Small-angle angular scattering yields a rate of decay  $\gamma_d \propto \ell(\ell+1)/v^3$  for the amplitudes of the spherical harmonics  $f_{\ell}^m$ . Hence, convergence can be ensured for a given momentum value as long as sufficient harmonics are included. This property offers the key justification for using the expansion (5). The more collisional the plasma, and the lower the momenta of interest, the fewer terms are required. However, the truncated expansion becomes increasingly brittle for large momenta, because for any specific spherical harmonic the decay rate vanishes as  $v^{-3}$ . To determine  $(\ell_0, m_0)$  one must first decide what part of the momentum-space is important, and then perform a convergence study in this region. Hence, systems involving energetic particles require a large number of terms in the expansion, even if the bulk of the plasma is accurately described by the diffusive approximation. This will be discussed extensively in Sec. III.

## 3. Synergies between VFP codes and other kinetic approaches

An accurate method for incorporating non-local electron transport in a hydrodynamic framework is crucial to modeling laser-irradiated plasmas. Yet, after more than three decades of research, a universally accepted model remains elusive. In fluid codes, a flux limiter  $f < 1$  is often introduced to prevent the heat flux  $Q_e$  due to a sharp temperature gradient from exceeding the ‘‘free-streaming heat flux’’  $Q_f = n_e T_e v_t$ , i.e., the flux that would result if all of the electrons were to free stream at their thermal velocity  $v_t = \sqrt{k_B T_e / m_e}$ . The heat conduction equation may then be written as  $Q_e = f \kappa_{SH} \nabla T_e$ . This heuristic approach artificially bottles up the hot-electron energy that would otherwise be carried by non-local electrons far from the hot region. Improved models rely on the convolution of the local heat flux with a non-local kernel that may be derived analytically or inferred from VFP simulations.<sup>13</sup> This convolution approach, formulated by Bell<sup>2</sup> and first incarnated by Luciani *et al.*,<sup>20</sup> can capture features of both the flux inhibition and the preheat associated with hot electrons. However, it is only strictly valid for small temperature variations and for time-independent problems, which excludes virtually all laser-irradiated plasmas. Application of such a non-local transport model must therefore be properly justified, especially because different methods can exhibit markedly different behavior outside the sanctioned regime.

The development of Vlasov-Fokker-Planck codes has largely been driven by the imperative of providing an

accurate description for non-local heat conduction in Inertial Confinement Fusion (ICF) plasmas (see Thomas *et al.*<sup>30</sup> and references therein). VFP codes can be used to benchmark the non-local electron transport models, or to replace them altogether, by adding a VFP species to a hydro code. The latter may be an overkill, because it saddles the hydro code with a powerful but computationally intensive kinetic code “merely” to get the heat conduction right. The reverse is more common, fluid ions can be incorporated into a VFP code<sup>3</sup> to facilitate kinetic simulations over timescales for which ion motion can play a role.

Another way of incorporating kinetic effects into fluid codes is using the Particle-In-Cell approach. Instead of describing the plasma in terms of ensemble-averaged fields it models a single ensemble of finite-size particles. A modified collision operator exists for the interaction between finite-size particles, such that a Boltzmann equation can be derived following the standard methods for point particles, and thermal fluctuations can also be calculated. Thus, PIC simulations allow instabilities to grow from “noise.” Nevertheless, when the Vlasov-Fokker-Planck Eq. (3) is the appropriate representation of the plasma, VFP codes are an attractive way of solving it, particularly in situations where the noise source is not critical. Whereas VFP and PIC are complementary approaches, coupling the two is also possible. For example, a PIC species of super-hot particles can be added to a background of weakly non-Maxwellian plasma that is described by the VFP equation.

Until recently, the ability to develop and apply VFP codes had been limited due to the lack of computational resources. The advent of parallel computer clusters in the last decade, and especially the last few years, opens the way for dispensing with assumptions on the shape of the distribution function and performing multi-dimensional VFP simulations with highly structured momentum-space.

#### 4. Status of VFP codes

The most common VFP codes are those that employ the spherical harmonic expansion—or the formally equivalent approach of the Cartesian tensor expansion—in momentum-space. For the diffusive approximation, both the formalism and numerical techniques are robust and well-tested and a number of such codes are currently being used to study the modification of electron transport due to non-local effects.<sup>4,8,15–18,22,28,29</sup>

A more detailed representation of the distribution function requires the KALOS<sup>5</sup> formalism which describes the effect of advection and electromagnetic fields on each spherical harmonic. The implementation of these equations is considerably more involved than those in the diffusive approximation, even in a fully explicit scheme. A code based on this scheme was described in Tzoufras *et al.*<sup>32</sup> and will be further discussed here in the context of HEDLP. The KALOS approach is also being applied to the study of cosmic ray acceleration<sup>6</sup> and a new multi-dimensional hybrid MHD-VFP code, where the VFP species is used for the cosmic rays, has been recently developed by Reville and Bell.<sup>25</sup>

In contrast, fully Cartesian codes facilitate use of fast algorithms, but because they do not attempt to utilize any *a priori* knowledge of the underlying physics they demand excessive computing power. Such a Cartesian Maxwell-Fokker-Planck-Landau code has been developed by Ducloux *et al.*<sup>10</sup> and is mostly used for validation purposes.

#### C. Outline

In this article, we discuss the VFP code OSHUN<sup>32</sup> In Secs. II A–II C, we briefly review the algorithms we presented in Tzoufras *et al.*<sup>32</sup> Subsequently, in Sec. II D, we present the new implicit method for the electric field, and in Secs. II E–II F the heat-source implementations. Good practices for setting up and diagnosing the simulations are discussed in Secs. III A–III C, and the applicability of the code is demonstrated with two examples in Sec. IV. Finally, in Sec. V, we enumerate the main conclusions from this work.

### II. FORMULATION OF THE NUMERICAL SCHEME

The KALOS formalism<sup>5</sup> was developed to allow VFP codes to model arbitrary momentum distribution functions. In OSHUN we have implemented the full KALOS formalism in 2D3P along with a rigorous collision operator.

#### A. The KALOS formalism of the Vlasov equation

The KALOS formalism exploits the orthogonality of the spherical harmonics to derive a hierarchy of equations

$$\frac{\partial f_\ell^m}{\partial t} - \sum_{i=x,y,z} (A_{\ell,i}^m + B_{\ell,i}^m + E_{\ell,i}^m) = C_\ell^m + S_\ell^m, \quad (6)$$

where  $A_{\ell,i}^m$ ,  $B_{\ell,i}^m$ , and  $E_{\ell,i}^m$  are expressions for the effects of spatial advection, magnetic fields, and electric fields respectively on the evolution of each amplitude  $f_\ell^m$ . These expressions were presented by Bell *et al.*<sup>5</sup> (Additional terms can be added on the left hand side to accommodate a mixed coordinate frame.<sup>25</sup>) In formulating a fully explicit algorithm for Eq. (6) we derived a set of operators that describe how each  $f_\ell^m$  affects the other amplitudes.<sup>32</sup> The algorithm in OSHUN scans the space of spherical harmonics and applies these operators to each  $f_\ell^m$ . The computational cost is split between the advection and electric-field operators, with the magnetic field being almost an order of magnitude cheaper. The time-step associated with this fully explicit scheme is limited by the need to resolve plasma waves. In Sec. II D, we present an implicit algorithm for the electric field that removes this constraint by dropping the displacement current.

The first term on the right hand side of Eq. (6) incorporates the effect of collisions. OSHUN utilizes a semi-anisotropic collision operator that has been implemented using a semi-implicit scheme.<sup>32</sup> The presence of collisions facilitates the convergence of the spherical harmonic expansion by damping the high-order terms.

A laser pulse can be simulated directly by adding external fields to the left hand side of Eq. (6). This requires that both the laser period and wavelength be resolved. For a laser with wavelength  $\lambda_0 = 0.351 \mu\text{m}$  one needs  $\Delta x \sim \lambda_0/30 \sim 12 \text{ nm}$  and  $\Delta t \sim \lambda_0/(30c) \sim 1.2 \text{ fsec}/30 \sim 0.04 \text{ fsec}$ . These

parameters are several orders of magnitude smaller than any other scale of interest in a typical laser-solid interaction. Instead, we can incorporate the macroscopic effect of laser heating by adding external source terms, i.e.  $S_\ell^m$ , to the right hand side of Eq. (6). In this article, we present two such terms, a phenomenological heat source in Sec. II E and an inverse bremsstrahlung source in Sec. II F.

## B. Maxwell's equations

In the explicit scheme, we update the electromagnetic fields from Maxwell's equations

$$\frac{\partial \mathbf{B}}{\partial t} = -\nabla \times \mathbf{E}, \quad (7)$$

$$\frac{\partial \mathbf{E}}{\partial t} = \nabla \times \mathbf{B} - \mathbf{J}, \quad (8)$$

where we have adopted the same normalizations as in Tzoufras *et al.*,<sup>32</sup> namely,  $t \rightarrow \omega_p t$ ,  $\mathbf{r} \rightarrow k_p \mathbf{r}$ ,  $q \rightarrow q/e$ ,  $m \rightarrow m/m_e$ ,  $v \rightarrow v/c$ ,  $n \rightarrow n/n_p$ ,  $\{\mathbf{E}, \mathbf{B}\} \rightarrow e\{\mathbf{E}, \mathbf{B}\}/(m_e c \omega_p)$  where  $n_p$  is the plasma density,  $\omega_p = \sqrt{4\pi e^2 n_p/m_e}$  the plasma frequency and  $k_p^{-1} = c/\omega_p$  the skin depth.

## C. The semi-anisotropic Fokker-Planck collision operator

The Fokker-Planck collision operator for a distribution  $f$  of particles with mass  $m$  and charge  $q = ze$  scattering off a distribution  $F$  of particles with mass  $M = \mu m$  and charge  $Q = Ze$  can be written as

$$\frac{1}{\Gamma_{zZ}} \left( \frac{\delta f}{\delta t} \right) = \frac{4\pi}{\mu} F f + \left( \frac{\mu-1}{\mu+1} \right) \bar{\nabla} \mathbb{H}(F) \cdot \bar{\nabla} f + \frac{\bar{\nabla} \bar{\nabla} \mathbb{G}(F) : \bar{\nabla} \bar{\nabla} f}{2}, \quad (9)$$

where  $\bar{\nabla}$  is the gradient in velocity space,  $\Gamma_{zZ} = 4\pi(zZe^2)^2 \ln \Lambda / m^2$  and  $\mathbb{H}, \mathbb{G}$  the Rosenbluth potentials<sup>26</sup> are integral operators for  $F$ . This collision operator is fully nonlinear and couples the amplitude of each harmonic to all of the other harmonics.

In Tzoufras *et al.*,<sup>32</sup> we linearized Eq. (9) assuming that the distribution functions are weakly anisotropic. Writing the distribution functions  $F, f$  as a sum of an isotropic part  $F_0^0, f_0^0$  and an anisotropic perturbation  $\tilde{F}_a, \tilde{f}_a$ ,  $F = F_0^0 + \tilde{F}_a$ ,  $f = f_0^0 + \tilde{f}_a$ , Eq. (9) yields

$$\frac{1}{\Gamma_{zZ}} \left( \frac{\delta f_0^0}{\delta t} \right) = \frac{4\pi}{\mu} F_0^0 f_0^0 + \left( \frac{\mu-1}{\mu+1} \right) \bar{\nabla} \mathbb{H}(F_0^0) \cdot \bar{\nabla} f_0^0 + \frac{\bar{\nabla} \bar{\nabla} \mathbb{G}(F_0^0) : \bar{\nabla} \bar{\nabla} f_0^0}{2}, \quad (10a)$$

$$\frac{1}{\Gamma_{zZ}} \left( \frac{\delta \tilde{f}_a}{\delta t} \right) = \frac{4\pi}{\mu} [F_0^0 \tilde{f}_a + f_0^0 \tilde{F}_a] + \left( \frac{\mu-1}{\mu+1} \right) [\bar{\nabla} \mathbb{H}(F_0^0) \cdot \bar{\nabla} \tilde{f}_a + \bar{\nabla} f_0^0 \cdot \bar{\nabla} \mathbb{H}(\tilde{F}_a)] + \frac{\bar{\nabla} \bar{\nabla} \mathbb{G}(F_0^0) : \bar{\nabla} \bar{\nabla} \tilde{f}_a}{2} + \frac{\bar{\nabla} \bar{\nabla} f_0^0 : \bar{\nabla} \bar{\nabla} \mathbb{G}(\tilde{F}_a)}{2}. \quad (10b)$$

Equation (10a) is nonlinear for the zeroth order amplitudes. On the other hand, Eq. (10b) is linear for the high-order amplitudes. These expressions are valid for any set of species, not just electrons and ions, and enable the development of a multi-species VFP code. OSHUN currently assumes immobile ions,  $\mu \rightarrow \infty$ , with a density profile determined by Gauss' law. For immobile ions, there are no self-collisions and the electron-ion collision operator reduces to an expression for angular scattering

$$\left( \frac{\delta f_\ell^m}{\delta t} \right)_{e,i,\mu \rightarrow \infty} = -\frac{\ell(\ell+1)}{2} \times \frac{n_i \Gamma_{ei}}{v^3} f_\ell^m. \quad (11)$$

Below we discuss self-collisions, i.e.,  $F \equiv f$ .

### 1. Isotropic self-collisions

A formulation of the isotropic part of the collision operator that can be discretized in way that conserves the non-relativistic energy and number density integrals was derived by Bobylev and Chuyanov<sup>7</sup>

$$\left( \frac{\delta f_0^0(v)}{\delta t} \right)_{ee} = \frac{4\pi \Gamma_{ee}}{3} \frac{1}{v^2} \frac{\partial}{\partial v} \left[ \frac{1}{v} \frac{\partial W(f_0^0(v), v)}{\partial v} \right], \quad (12a)$$

$$W(f_0^0, v) = f_0^0 \int_0^v f_0^0 u^4 du + v^3 f_0^0 \int_v^\infty f_0^0 u du - 3 \int_v^\infty f_0^0 u du \int_0^v f_0^0 u^2 du, \quad (12b)$$

where  $(4\pi/3)\Gamma_{ee} \equiv (4\pi/3)4\pi e^4 \ln \Lambda_{ee}/m_e^2$ . In Tzoufras *et al.*,<sup>32</sup> we normalized time to  $\omega_p^{-1}$ , velocity to the speed of light  $c$ , and the distribution function  $f$  to  $n_e/c^3$ , in order to maintain the same dimensionless units as the Vlasov part of the code. However, this normalization is awkward for a non-relativistic collision operator, and yields an expression no more enlightening than Eq. (12) itself. Here, we use the dimensionless units  $t = t/\tau_e = \left( \frac{3\sqrt{m}(kT_e)^{3/2}}{4\sqrt{2\pi}n_e e^4 \ln \Lambda} \right)^{-1} t$ ,  $v = v/v_t$ , and  $f_0^0 = [n_e/(\sqrt{2\pi}v_t)^3]^{-1} f_0^0$ . In these units, a Maxwellian distribution with thermal velocity  $v_t$ , becomes  $f_M(v) = e^{-v^2/2}$ . Noting that  $[\tau_e n_e/(\sqrt{2\pi}v_t)^3]^{-1} = (4\pi/3)\Gamma_{ee}$  Eq. (12) becomes

$$\left( \frac{\delta f_0^0(v)}{\delta t} \right)_{ee} = \frac{1}{v^2} \frac{\partial}{\partial v} \left[ \frac{1}{v} \frac{\partial W(f_0^0(v), v)}{\partial v} \right]. \quad (13)$$

This expression can be discretized directly and shown to conserve  $\mathbb{E} = \sum_{n=1}^N (f_0^0)_n v_n^4 \Delta_n$  and  $\mathbb{N} = \sum_{n=1}^N (f_0^0)_n v_n^2 \Delta_n$ , where  $\Delta_n = (v_{n+1} - v_{n-1})/2$ .

The cell-size in velocity-space is determined by the need to resolve the coldest distribution in the system. In laser-ablated plasmas, the lowest temperature is usually found in the high-density region of the plasma, where the heat capacity is large and the distribution function nearly Maxwellian. Under these conditions the cell-size is usually chosen  $\Delta v \lesssim 0.1 v_{t,\text{cold}} \Rightarrow \Delta v \lesssim 0.1$ . If this  $\Delta v$  is sufficient in the beginning of the simulation,  $f(v)$  should remain well-resolved thereafter, as the laser raises the temperature of the

plasma. A CFL condition for Eq. (12) can be written as  $\Delta t_{\text{CFL}} \propto (\Delta v)^2$ . Using a 4th order Runge-Kutta scheme we performed an extensive parameter scan and derived the approximate CFL condition<sup>34</sup>

$$\Delta t_{\text{iso-FP}} \lesssim 0.3(\Delta v)^2 \iff \Delta t_{\text{iso-FP}} \lesssim 0.3 \left( \frac{\Delta v}{v_t} \right)^2 \tau_e. \quad (14)$$

Although this numerical scheme conserves the non-relativistic integrals  $\mathbb{E}$  and  $\mathbb{N}$ , it does not conserve the fully relativistic energy and number density integrals. When this operator is used in conjunction with a fully relativistic scheme for the Vlasov description, as is done in OSHUN, energy and—to a lesser degree—density may not be conserved exactly. In laser-ablated plasmas, this can affect the under-dense corona which has low heat capacity and its temperature can be raised by laser irradiation to values above 5 keV.

## 2. Anisotropic self-collisions

The anisotropic part of the collision operator (10b) yields an expression for each of the amplitudes of the spherical harmonics.<sup>32</sup> Including angular scattering and anisotropic self-collisions the expression for  $f_\ell^m$  becomes  $\delta f_\ell^m / \delta t = [\mathbf{M}_\ell(f_\ell^0) - \frac{\ell(\ell+1)}{2} \times \frac{n_e \Gamma_{e\alpha}}{v^3} \mathbf{I}] f_\ell^m$ , where the matrices  $\mathbf{M}_\ell(f_\ell^0)$  are linear functions of  $f_\ell^0$  that depend on  $\ell$ , and  $\mathbf{I}$  is the unit matrix. Whereas the isotropic self-collisions are advanced separately by solving equation (10a) we can calculate for each  $\ell$  the matrix  $\mathbf{M}_\ell(f_\ell^{0,[n+1]})$  to develop the implicit scheme

$$f_\ell^{m,[n+1]} = \left[ \left( 1 + \frac{\ell(\ell+1)}{2} \frac{n_e \Gamma_{e\alpha} \Delta t}{v^3} \right) \mathbf{I} - \Delta t \mathbf{M}_\ell^{[n+1]} \right]^{-1} f_\ell^{m,[n]}, \quad (15)$$

where  $\mathbf{M}_\ell^{[n+1]}$  denotes  $\mathbf{M}_\ell(f_\ell^{0,[n+1]})$ . Because  $\mathbf{M}_\ell^{[n+1]}$  does not depend on the  $m$  index, only  $\ell$  matrices need to be inverted. Finally we note that if the determinant of  $(1 + \frac{\ell(\ell+1)}{2} \frac{n_e \Gamma_{e\alpha} \Delta t}{v^3}) \mathbf{I} - \Delta t \mathbf{M}_\ell^{[n+1]}$  vanishes this indicates that  $\Delta t$  is too large to yield realistic results.  $\Delta t \lesssim \tau_{e\alpha}$  is necessary to ensure accurate modeling of electron transport.

## D. Implicit solver for the electric field

Collisions in dense plasmas tend to damp high-frequency waves. It is therefore common to drop the displacement current from Ampère's law, i.e.,  $\mathbf{J} \simeq \nabla \times \mathbf{B}$ , to avoid having to resolve inconsequential high-frequency phenomena including electromagnetic and plasma waves. Moreover, in such plasmas, the conservation of charge guarantees quasi-neutrality  $\nabla \cdot \mathbf{J} = 0 \iff \partial_t \rho = 0$ . For the numerical scheme, this means that Ampère's law becomes an expression for updating the current, as opposed to the electric field

$$\left( \frac{\partial \mathbf{B}}{\partial t} = -\nabla \times \mathbf{E}^{[n]} \right) \rightarrow \mathbf{B}^{[n+1]}, \quad (16a)$$

$$\mathbf{J}^{[n+1]} = \nabla \times \mathbf{B}^{[n+1]}. \quad (16b)$$

A separate expression is then required to update the electric field. The fact that Eq. (16a) must be satisfied by the distribution function can be used to predict the electric field  $\mathbf{E}^{[n+1]}$

$$\varepsilon_{ijk} \nabla_j \mathbf{B}_k^{[n+1]} = J_i^{[n+1]} = J_i^{[n+1]}(0) + \frac{\delta J_i(\delta E_j)}{\delta E_j} \cdot E_j^{[n+1]}, \quad (17)$$

where  $J_i^{[n+1]}(0)$  is the current in the absence of an electric field,  $\frac{\delta J_i}{\delta E_j}$  a “conductivity” tensor which shows the effect of electric field perturbations  $\delta E_j$  on the current  $\delta J_i$ , and  $E_j^{[n+1]}$  to be determined.<sup>35</sup> Before discussing how Eq. (17) is to be treated we remind that the current is directly connected to the first order spherical harmonics

$$J_x = -\frac{4\pi}{3} \int_0^\infty dp \frac{p^3}{\gamma} f_1^0, \quad (18a)$$

$$J_y + iJ_z = -\frac{8\pi}{3} \int_0^\infty dp \frac{p^3}{\gamma} \{ \Re[f_1^1] - i\Im[f_1^1] \}. \quad (18b)$$

To calculate  $J_i^{[n+1]}(0)$  we first complete the explicit part of the calculation with  $\mathbf{E} = 0$ . This includes the effect of the magnetic field and spatial advection on  $f$ , the collisions for the isotropic part of  $f$ , and the heat source (if any). We denote the resulting value of  $f$  as  $f^{[n+1],\text{expl}}$ , where the “\*” symbol indicates that the effect of the electric field on  $f$  has been omitted. We then apply the anisotropic part of the collision operator to  $f_1^0$  and  $f_1^1$  to obtain  $(f_1^0)^{[n+1]}(0)$ ,  $(f_1^1)^{[n+1]}(0)$ , and therefore  $\mathbf{J}^{[n+1]}(0)$  from Eqs. (18).

For the conductivity tensor, we start from  $f^{[n+1],\text{expl}}$  and find the plasma response to three perturbations  $\delta E_\nu \hat{e}_\nu$ ,  $\nu = x, y, z$ . The electric field operators (expressions (A1)–(A8) in Tzoufras *et al.*<sup>32</sup>) do not need to be applied to all of the harmonics, just those that affect the values of  $(f_1^0)^{[n+1]}$  and  $(f_1^1)^{[n+1]}$ . For a second order method, e.g., RK2, these calculations will involve harmonics with  $\ell \leq 3$  for the first sub-step and  $\ell \leq 2$  for the second. A map of the operator applications for a second order scheme is presented in Fig. 1. For  $\delta E_x \hat{e}_x$  we need to perform the operations on the top row and then use the anisotropic part of the collision operator on  $f_1^0$  and  $f_1^1$  to obtain  $\mathbf{J}^{[n+1]}(\delta E_x \hat{e}_x)$ . The process is repeated for  $\delta E_\nu \hat{e}_\nu$ ,  $\nu = y, z$  to obtain  $\mathbf{J}^{[n+1]}(\delta E_y \hat{e}_y)$  and  $\mathbf{J}^{[n+1]}(\delta E_z \hat{e}_z)$ . Substitution of the resulting tensor  $\delta J_i / \delta E_j$  into Eq. (17) yields

$$\varepsilon_{ijk} \nabla_j \mathbf{B}_k^{[n+1]} = J_i^{[n+1]}(0) + \frac{J_i^{[n+1]}(\delta E_j) - J_i^{[n+1]}(0)}{\delta E_j} E_j^{[n+1]}. \quad (19)$$

This is a  $3 \times 3$  system of equations for  $\mathbf{E}^{[n+1]}$ . The final steps are to use this electric field to update the entire distribution function and then apply the anisotropic part of the collision operator.

This algorithm imposes negligible computational cost, and because it drops high-frequency waves it allows for large time-steps to be taken. We typically choose the time-step on the order of the collision time. In OSHUN the user can decide between this scheme and the algorithm described in Secs. II A-II C in the input file.

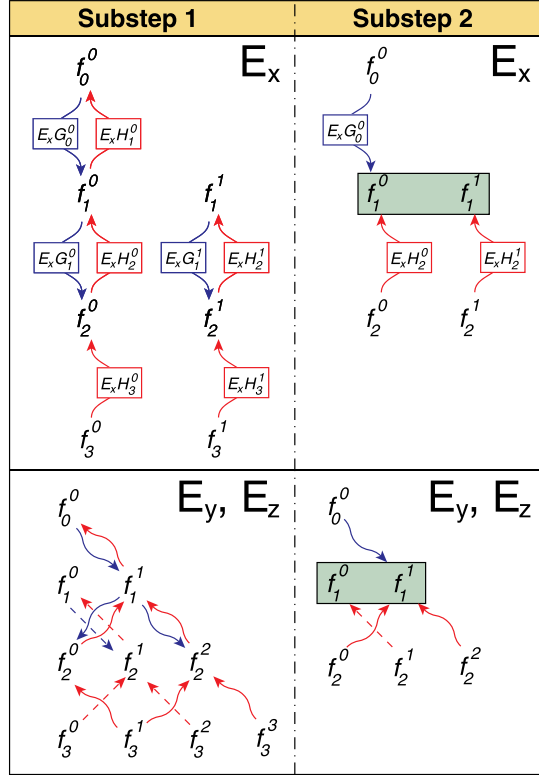


FIG. 1. A map of the operations necessary to calculate the effect of  $\delta E_i \hat{e}_i$ ,  $i = x, y, z$  on the current in a second order scheme. The top row shows the algorithm for  $\delta E_x \hat{e}_x$ , which requires a total of 11 operations. The bottom row is for  $\delta E_y \hat{e}_y$ , or  $\delta E_z \hat{e}_z$  and it requires a total of 17 operations.

### E. Phenomenological laser source

To incorporate a phenomenological laser source we assume that a portion  $0 \leq \alpha < 1$  of the distribution function  $f(t)$  is converted to a new “hot” distribution in a time interval  $\Delta t$ , i.e.,  $f(t + \Delta t) = \alpha f_{hot}(t) + (1 - \alpha)f(t)$ , where the distribution  $f_{hot}(t)$  can be specified by the user. The temperature rise is then expressed as  $\Delta T = T(t + \Delta t) - T(t) = \alpha [T_{hot}(t) - T(t)]$ . For a specified heat-source profile, the deposition of energy  $\Delta E_i$  in each cell “ $i$ ” causes a temperature rise equal to  $\Delta T_i = \Delta E_i / (n_i V_i)$ , where  $n_i$  is the local density and  $V_i$  the cell volume. This yields the local value for  $\alpha_i = \Delta E_i / [n_i V_i (T_{hot,i}(t) - T_i(t))]$ . We usually assume that  $f_{hot}(t)$  is a Maxwellian with temperature determined from the local laser intensity.

### F. Inverse bremsstrahlung operator

The inverse bremsstrahlung source associated with a dipole electric field  $E(t) = E_0 \cos(\omega_0 t)$  can be written as<sup>19</sup>

$$\frac{\partial f_0^0(v)}{\partial t} = \frac{A}{3} \left( \frac{v_{os}}{v} \right)^2 \frac{\partial}{\partial v} \left( \frac{g(v)}{v} \frac{\partial f_0^0(v)}{\partial v} \right), \quad (20)$$

where  $g(v) = [1 + (v_{os}/v)^6]^{-1}$ ,  $A = 2\pi n_i Z^2 \frac{e^4}{m_e^2} \log \Lambda_{ei}$ ,  $v_{os} = eE_0 / (m_e \omega_0)$ , and the coefficient  $v_{os}$  is determined from the

expression  $v_{ei}(v_{os}) = A/v_{os}^3 = \omega_0/2$ . To simplify Eq. (20), we assume a quasi-neutral plasma  $n_e \simeq Z n_i$  and  $\log \Lambda_{ei} \simeq \log \Lambda_{ee}$ . Using dimensionless velocity  $v = v/v_t$  (and  $v_{os} = v_{os}/v_t$ ) and time  $t = t/\tau_e$ , and substituting  $A = 3v_t^3 (\sqrt{\pi}/8) (Z/\tau_e)$  into Eq. (20) we obtain

$$\frac{\partial f_0^0(v)}{\partial t} \simeq \sqrt{\frac{\pi}{8}} Z v_{os}^2 \frac{1}{v^2} \frac{\partial}{\partial v} \left( \frac{g(v)}{v} \frac{\partial f_0^0(v)}{\partial v} \right). \quad (21)$$

Equation (20) may be discretized in the same way as expression (13) for the self-collision operator, and we have incorporated such an explicit inverse bremsstrahlung source into OSHUN.

In Fig. 2, we show the benchmark of the inverse bremsstrahlung operator against an external dipole electric field; to our knowledge this is the first such comparison. We initialize a Maxwellian plasma with thermal velocity  $v_t = 0.04421c$ , that is  $T_e \simeq 1$  keV, density  $n_e = 1.5 \times 10^{21} \text{ cm}^{-3}$  and  $Z = 12$ . The distribution function at initialization is shown with a solid black line. A laser with intensity  $I = 6.95 \times 10^{15} \text{ W/cm}^2$  and wavelength  $\lambda_0 = 0.351 \mu\text{m}$  is assumed, such that  $v_{os} \simeq 0.025c \simeq 0.57v_t$ . For these parameters, we performed a simulation with an external electric field  $E = E_0 \cos(\omega_0 t) \hat{e}_y$ , where  $(\ell_0, m_0) = (3, 2)$  and  $\Delta t = 0.0123\omega_0^{-1}$ , and the resulting electron distribution function after 2.666 ps is shown in Fig. 2 with the dotted red line. We repeated the simulation using the inverse bremsstrahlung operator instead of the external dipole field and the new distribution after 2.666 ps is shown with the broken blue line. Both of these approaches recover the flat-top shape near the origin and the sharp fall-off at large velocities predicted by Langdon<sup>19</sup> and they are in excellent agreement with each other.

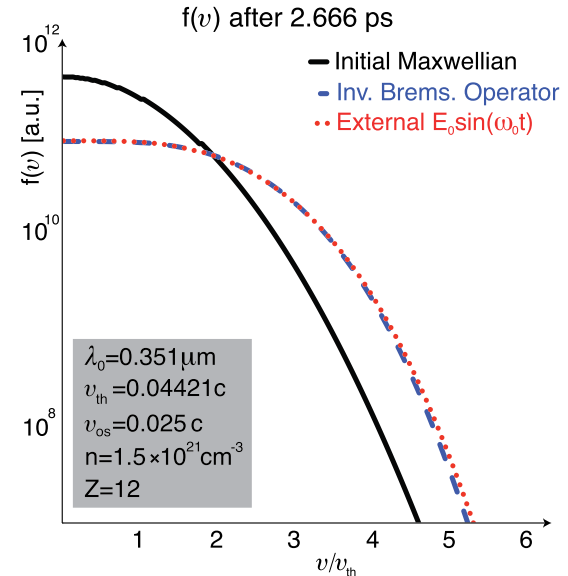


FIG. 2. An initial Maxwellian plasma (solid black line) heated by the inverse bremsstrahlung operator (broken blue line) or a dipole electric field (dotted red line). The inverse bremsstrahlung operator recovers the shape of the DLM<sup>11,12,19,23</sup> distribution function calculated using a dipole electric field.

### III. DIAGNOSING NUMERICAL ARTIFACTS AND EXTRACTING PHYSICS FROM VFP SIMULATIONS

#### A. 1D2P simulations

The most glaring failures of a numerical scheme for simulating HEDLP are those accompanied by unphysical moments of the distribution function, for example, when the plasma density or the temperature become negative. Unfortunately, numerical artifacts originating from an inconsiderate truncation of the spherical harmonic expansion do not always manifest themselves so blatantly, because most quantities of interest are associated with the isotropic zeroth-order harmonic that is only indirectly affected by the truncation. Furthermore, to establish the validity of a kinetic code, we must examine kinetic information, namely, distribution functions or particle trajectories; integrals over the particle distribution can obscure underlying unphysical structures. Here, we present such a convergence study for a 1D2P non-local transport problem under conditions similar to those found in ICF *Hohlraums*.

We consider a 1D system,  $0 \leq x[\text{cm}] \leq 1$ , with initial temperature 1 keV,  $Z = 4$ , and constant density  $5 \times 10^{20} \text{ cm}^{-3}$ . The plasma is heated by an inverse bremsstrahlung source corresponding to a laser with intensity profile  $I = 10^{16} e^{-0.5[x/(1.21\text{mm})]^2} \text{ W/cm}^2$  and wavelength  $\lambda_0 = 0.33 \mu\text{m}$ , such that  $Z \times v_{os}^2 \simeq 1.0$ . The heating profile is constant in time, the boundaries are reflecting, and the implicit algorithm is used for the electric field. This allows us to choose a timestep  $\Delta t = 30\omega_p^{-1} \simeq \tau_{ei}/32 \simeq 24\text{fs}$ . The simulation is terminated after 200 ps at which time the maximum temperature in the simulation domain is about 5 keV. The maximum magnitude of momentum in the p-mesh is set to  $p_{max} = 0.6m_e c$ , such that a plasma with temperature 5 keV and thermal velocity  $v_{r,5\text{keV}} \simeq 0.1c$  can be accommodated. The total number of mesh-points in p-space is 432 to ensure that the coldest distribution, the initial Maxwellian with  $v_{r,1\text{keV}} = 0.4421$ , is finely resolved with  $30\Delta v < v_{r,1\text{keV}}$ .

In Fig. 3, we show the projection of the distribution function onto Cartesian phase-space after 200 ps, i.e.  $f(p_x, x, 200\text{ps}) = \int_{-\infty}^{\infty} \int_{-\infty}^{\infty} f(\mathbf{p}, x, 200\text{ps}) dp_y dp_z$ , from four simulations using: the diffusive approximation, 4 harmonics, 8 harmonics, and 32 harmonics. The color bars show the amplitude of  $f(p_x, x, 200\text{ps})$  in logarithmic scales. For

positive/negative values of  $f(p_x, x, 200\text{ps})$  we use the orange/blue color-scale. The maximum value for the blue color-scale is reduced from panel to panel to allow us to discern negative values for  $f(p_x, x, 200\text{ps})$  as the number of harmonics increases. In principle  $f(p_x, x, 200\text{ps})$  should be positive definite, negative values are numerical artifacts. We note that these negative values are merely projections of the distribution produced by data post-processing, they are not used in the code which only cares for spherical harmonics.

During the simulation, the plasma is heated on the left side of the box and multi-keV particles start streaming across the simulation domain generating non-Maxwellian tails for  $p_x > 0$ . The plasma self-consistently generates a return-current to maintain charge neutrality. In the first panel on the left in Fig. 3 we plot the distribution function from a simulation using the diffusive approximation. Negative values are prevalent throughout the simulation for  $p_x \lesssim -0.2m_e c$ . For momenta  $|p_x| < 0.2m_e c$  the diffusive approximation seems sufficient. For  $|p_x| > 0.2m_e c$  angular scattering is not strong enough to damp the high-order harmonics and the electron distribution exhibits negative values. (For positive momenta, the presence of the non-local electrons masks any artifacts of the background population.) When we increase the number of harmonics to 4, see second panel from the left, we notice that the negative values show up for  $p_x \lesssim -0.27m_e c$  and they are two orders of magnitude smaller. Increasing the number of terms in the expansion to 8, and then to 32, we observe that the negative values continue to shift farther out in the tail of the distribution and their absolute values become vanishingly small. In the last panel, for  $\ell_0 = 31$ , the errors due to the truncation are negligible, compared, for example, with the errors due to the usage of a non-relativistic collision operator, and we can safely argue that the expansion has converged.

Another way of tracking the accuracy of the diffusive approximation, is to monitor the ratio of  $f_1^0(p)/f_0^0(p)$  and report instances of  $f_1^0(p)/f_0^0(p) \sim 1$ . However, unless there is a mitigation strategy, or at least a way of finding out how the lack of convergence at  $p \gg p_i$  affects the physics at lower momenta, the usefulness of this approach is going to be limited. Full convergence studies are advisable unless  $f_1^0(p)/f_0^0(p) \ll 1, \forall p$ .

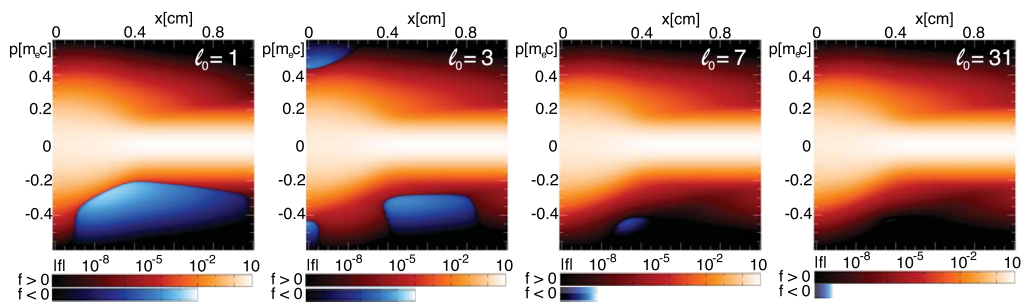


FIG. 3. Four non-local transport simulations using different numbers of spherical harmonics and projected onto a Cartesian mesh. A plasma with density  $5 \times 10^{20} \text{ cm}^{-3}$ ,  $Z = 4$ , and initial temperature 1 keV is heated from the left with an inverse bremsstrahlung source with profile  $I = 10^{16} e^{-0.5[x/(1.21\text{mm})]^2} \text{ W/cm}^2$  and  $\lambda_0 = 0.33 \mu\text{m}$ . This set of simulations shows that convergence can be achieved when sufficient number of spherical harmonics is used.



## B. 2D3P simulations

To describe the three-dimensional  $p$ -space two indices ( $\ell \leq \ell_0, m \leq m_0 \leq \ell_0$ ) are needed, as opposed to just one ( $\ell \leq \ell_0$ ) for 1D2P simulations. In Tzoufras *et al.*,<sup>32</sup> we argued that  $m_0 < \ell_0$  may often be used with no apparent difference in the physics. (In particular we showed that the structure of the current filaments in the early non-linear stage of the electromagnetic instability were virtually identical for simulations with  $\ell_0 = 48$  and  $3 \leq m_0 \leq 48$ .) We have observed that using  $m_0 < \ell_0$  also works well for many laser-irradiated plasmas. However, if either  $\ell_0$  or  $m_0$  is set to values much lower than those required for convergence the code can produce strikingly artificial structures. Paradoxically the diffusive approximation, with  $m_0 = \ell_0 = 1$ , is the least prone to such artifacts and diffusive simulations tend to run rapidly and stably generating seemingly plausible results. This insidious feature of the diffusive approximation is likely due to the fact that  $m_0 = \ell_0 = 1$  precludes anisotropic pressure and temperature from building up and driving numerical instabilities, such that would expose the need for a more careful treatment.

## C. The current-filamentation instability as a numerical artifact

The growth of the current-filamentation instability<sup>33</sup> from numerical noise is one of the biggest challenges for multi-dimensional simulations with OSHUN. This instability grows whenever there is anisotropy in the particle distribution function and it is associated with a feedback mechanism between magnetic fields and current filaments.<sup>14</sup> Its manifestation can vary depending on the degree of anisotropy in the distribution function<sup>9</sup> and the level of collisionality.<sup>24</sup> For modes with long wavelength the growth rate reduces—but remains non-zero—with the wavenumber of the perturbation,  $\gamma \sim O(k)$ . The maximum growth rate of the instability occurs at much shorter wavelengths.<sup>9,24,31</sup>

In VFP codes, there is no natural noise for instabilities to grow from. To study instabilities, one must provide suitable well-resolved perturbations, otherwise, they may grow from the only source of noise in the system, that is, the numerical mesh. In multi-dimensional VFP simulations, we typically choose cell-sizes several orders of magnitude larger than the natural wavelength for the current-filamentation instability, i.e.,  $\Delta x \gg O(c/\omega_p)$ . As a result, the fastest-growing mode supported by the mesh has filaments with width equal to the cell-size. The presence of the instability is then correctly predicted by the code, but neither its growth rate nor its wavelength is physical.

In Sec. IV B, we consider the interaction of a moderate-intensity ( $\sim 10^{16}$  W/cm<sup>2</sup>) laser with an inhomogeneous plasma with density ranging from underdense to solid. PIC simulations show that the absorption is dominated by parametric instabilities and there is no evidence of the current-filamentation instability even though the resulting electron distribution in the underdense region is anisotropic. In order to model non-local heat conduction for realistic temporal and spatial scales, we ignore the microphysics of the parametric instabilities and use OSHUN with an external heat source that describes the macroscopic effect of laser heating.

However, an unintended consequence of dropping these competing phenomena, is that the current-filamentation instability can grow from numerical noise in the underdense plasma. In this scenario, we may need to look for ways of suppressing this instability.

The most straightforward solution is to perform electrostatic simulations. This may be sufficient in problems where no significant magnetic fields arise. Alternatively, the diffusive approximation allows us to use magnetic fields and suppresses the instability by prohibiting temperature/pressure anisotropy. Another option, one that facilitates both magnetic fields and a detailed description of the particle distribution, is to use very coarse resolution in configuration-space to reduce the growth of the instability enough that it remains effectively suppressed for the entire simulation. This approach was used in Sec. IV B.

## IV. EXAMPLES

### A. A physical picture for flux-limited heat conduction

For a time-independent sinusoidal temperature perturbation  $T(x) = T_0 + T_1 \sin(kx)$ , with  $T_1 \ll T_0$ , the corresponding heat flux is<sup>1</sup>  $Q(x) = Q_1 \sin(kx + \pi/2)$ . A general temperature profile  $T(x) = T_0 + T_1(x)$  may then be decomposed into harmonic functions with amplitude  $\hat{T}(k)$  which result in a heat flux with magnitude  $\hat{Q}(k)$ . An effective heat conduction coefficient  $\hat{\kappa}(k)$  can be defined such that  $\hat{Q}(k) = -ik\hat{\kappa}(k)\hat{T}(k)$ . The inverse Fourier transform of this expression yields a convolution integral for heat conduction  $Q(x) = -\int_{-\infty}^{\infty} ik\hat{\kappa}(k)\hat{T}(k)e^{ikx}dk = -\int_{-\infty}^{\infty} G(x-x')\nabla\hat{T}_1(x')dx'$ , where  $G(x) = \int_{-\infty}^{\infty} \hat{\kappa}(k)e^{ikx}dk$ . The challenge is finding an expression for the kernel  $G(x)$  or equivalently for the effective heat conduction coefficient  $\hat{\kappa}(k)$ . Epperlein and Short<sup>13</sup> performed a series of VFP simulations for high-Z materials with 1D sinusoidal perturbations  $\hat{T}_1(x) = T_1 \sin(k_i x)$  to obtain the values for  $\hat{\kappa}(k_i)$ . Here, we repeat these tests using OSHUN with the explicit electric-field solver for  $Z = 1$ . A more detailed discussion including higher  $Z$  was recently presented by A. Marrocchino *et al.*<sup>21</sup>

We initialize a homogeneous plasma with density  $10^{23}$  cm<sup>-3</sup> and a sinusoidal temperature profile  $T[\text{eV}] = 307 \text{ eV} + 12.5 \text{ eV} \times \sin(k_i x)$  in a 1D periodic box with size  $L_i = 2\pi/k_i$ . The maximum box size for this parameter scan is  $L_1 = 1000\lambda_e$ , where the mean free path is  $\lambda_e = v_i\tau_e$ . The simulation time is  $\tau_S = 40\tau_e$  to allow particles at the tail of the distribution with velocity  $v \sim 3v_i$  to undergo 90° scattering. The  $p$ -space was resolved with 108 cells and  $p_{max} = 0.15m_e c \simeq 6m_e v_i$ . Sufficient spherical harmonics are kept in the expansion to accurately capture the angular profile of the distribution function.

Quoting a single number for the effective heat conduction coefficient from each simulation suggests the existence of a steady state. For a smooth temperature profile,  $L_i \gg \lambda_e$ , the ratio  $Q(x)/\nabla T_e(x)$  reaches steady state after about  $20\tau_e$  and is nearly constant throughout the simulation box. The effective heat conduction coefficient may then be measured unambiguously. For the highly non-local cases (i.e., those with short perturbation wavelength) a steady state is established more quickly, as hot electrons decouple from the background and travel many times around the box sharing

their energy with the entire plasma and causing rapid dissolution of the temperature perturbation. In all cases, the ratio  $Q(x)/\nabla T_e(x)$  is measured at steady state, when its value becomes constant across the simulation box. The parameter scan has been repeated for different types of perturbations, and the results are identical once a steady state is established. This confirms that the effective heat conduction coefficient only depends on the wavelength of the perturbation normalized to the mean free path.

The ratio of the effective heat conduction coefficient  $\hat{\kappa}(k_i)$  from VFP simulations to the Spitzer and Härm value  $\kappa_{SH} = 3.20$  is shown with red squares in Figure 4. This ratio can be viewed as a “flux limiter”  $f(k_i) = \hat{\kappa}(k_i)/\kappa_{SH}$ . The longitudinal axis is the temperature wavenumber normalized to the mean free path  $\lambda_e \langle T_e \rangle$ . For long wavelengths most of the electrons transfer their energy locally, and  $f \sim 1$ . As the wavenumber increases, the hot electrons decouple from the system and belong collectively to the entire simulation box, rather than any one location. Fewer electrons are then available to transfer energy locally, and those that do have less energy to carry. This causes an apparent reduction in the local heat flux which is captured by the drop in the ratio  $\hat{\kappa}(k_i)/\kappa_{SH}$ .

To derive an analytical estimate based on this physical picture we consider an electron moving with velocity  $v_c = \alpha v_t$ . The time it takes for this electron to undergo  $90^\circ$  scattering is  $\tau_c = \alpha^3 \tau_e$  and the distance it travels is  $v_c \tau_c = \alpha^4 \lambda_e$ . If the mean free path  $v_c \tau_c$  exceeds the “de-coupling” length the contribution of this electron to the heat flux can be ignored. This de-coupling length is the distance that must be traveled to ensure that  $\nabla T$  switches sign. For a sinusoidal temperature profile, this distance is equal to half the wavelength of the perturbation, i.e.,  $\pi/k = \alpha^4 \lambda_e \Rightarrow v_c = (k \lambda_e / \pi)^{-1/4} v_t$ . Electrons with initial velocities  $|v_x| > v_c$  form a “superfluid” that belongs collectively to the entire system and does not contribute to the local heat flux.

In a Maxwellian plasma, the heat flux of the electrons with velocity  $|v_x| > v_c$  is  $\langle v^2 |v_x| \rangle_{|v_x| > v_c} = \frac{4\sqrt{2}}{\sqrt{\pi}} v_t^3 \left( \frac{v_c^2}{4v_t^2} + 1 \right) e^{-v_c^2/(2v_t^2)}$ . The ratio of the effective heat conduction

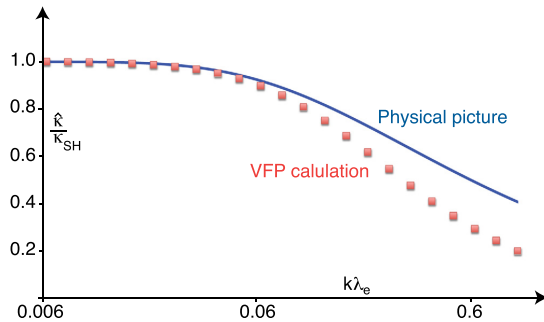


FIG. 4. The ratio of the effective heat conduction coefficient from VFP simulations to the Spitzer and Härm value,  $f = \hat{\kappa}(k_i)/\kappa_{SH}$ , is shown with red squares as a function of the wavenumber of the temperature perturbation. We have also overlaid a blue solid line that corresponds to expression (22) in the text. Good agreement between the VFP results and expression (22) is observed for  $k\lambda_e \ll 1$ .

coefficient to  $\kappa_{SH}$  becomes  $f = 1 - \frac{\langle v^2 |v_x| \rangle_{|v_x| > v_c}}{\langle v^2 |v_x| \rangle_{|v_x| > 0}}$ . From the discussion above, we can substitute the velocity  $v_c$  in the expression for the heat flux to obtain

$$\frac{\hat{\kappa}(k)}{\kappa_{SH}} \sim 1 - \left( 1 + \frac{1}{4} \sqrt{\frac{\pi}{k\lambda_e}} \right) e^{-\frac{1}{2} \sqrt{\frac{\pi}{k\lambda_e}}}. \quad (22)$$

The ratio  $\hat{\kappa}/\kappa_{SH}$  from Eq. (22) is shown in Figure 4 and agrees well with the detailed VFP calculations for  $k\lambda_e \ll 1$ .

## B. Asymmetric heating of a solid-density target

One of the main motivations for developing OSHUN is to model multi-dimensional non-local transport in laser-irradiated plasmas. Here, we present an example of such a simulation, part of a study we have undertaken to understand how asymmetry in the irradiation pattern affects the pressure profile in dense targets. At present ion motion has not been incorporated into the code and simulation times must be relatively limited.

We consider a planar target with constant temperature 500 eV,  $Z = 4$ , and a sharp density gradient rising from  $10^{21} \text{ cm}^{-3}$  to  $10^{23} \text{ cm}^{-3}$  within about  $30 \mu\text{m}$ . The exact density profile is replicated on top of each of the plots in Figure 5. A phenomenological heat source is introduced with intensity

profile  $I = 10^{16} e^{-\frac{y^2}{2 \times (250 \mu\text{m})^2}} \times \left[ 1 - \left( 1 - \frac{t}{10 \text{ ps}} \right) \text{H} \left( 1 - \frac{t}{10 \text{ ps}} \right) \right] \frac{\text{W}}{\text{cm}^2}$ , where  $\text{H}(x) = \int_{-\infty}^x \delta(t) dt$  is the Heaviside step function. We assume that the laser energy is deposited in the low-density region—as one might expect from laser-plasma instabilities—

with a Gaussian profile  $e^{-\frac{(x-180 \mu\text{m})^2}{(120 \mu\text{m})^2}}$ . The “hot” Maxwellian distribution has temperature  $T_{hot} = T_e + \sqrt{\frac{I}{10^{13} \text{ W/cm}^2 \mu\text{m}}} \frac{\lambda_0}{\text{cm}^2} \text{ keV}$ , where  $I$  is the heat source intensity and  $\lambda_0 = 0.351 \mu\text{m}$ . The simulation employs the implicit solver for the electric field presented in Sec. II D. The system is resolved with  $\Delta x = 7.3 \mu\text{m}$  and  $\Delta y = 31.25 \mu\text{m}$ , where the resolution in  $x$  is set by the need to resolve the density gradient and in  $y$  to resolve the structure of the heat source and its imprint on the plasma. 300 cells are used for the magnitude of momentum with  $p_{max} = 0.6 m_e c$ , and  $(\ell_0, m_0) = (16, 4)$ , that is 75 terms in the harmonic expansion. The implicit time-step was set to  $\Delta t_{impl} \simeq 0.65 \tau_{ei, 0.5 \text{ keV}} \simeq 1.68 \text{ fs}$ .

The pressure and temperature profiles, as well as the longitudinal electric ( $E_x$ ) and transverse magnetic ( $B_z$ ) fields are shown in Figure 5 after 10 ps (top row) and 20 s (bottom row). (The results in the bottom row have been reflected to facilitate comparison with those on the top row.) A detailed discussion of the physics requires further analysis and additional simulations; here we briefly point out the salient features of the interaction.

A heat-front develops in the under-dense corona and starts climbing the sharp density gradient. Pressure builds on the gradient reaching 110 Mbar at the end of the simulation. Meanwhile, non-local electrons travel in the solid-density plasma (up to  $100 \mu\text{m}$ ) and lead to a measurable change in both temperature and pressure. The sharp density gradient generates an electric field  $E_x = -\nabla P/e$ . Transversely

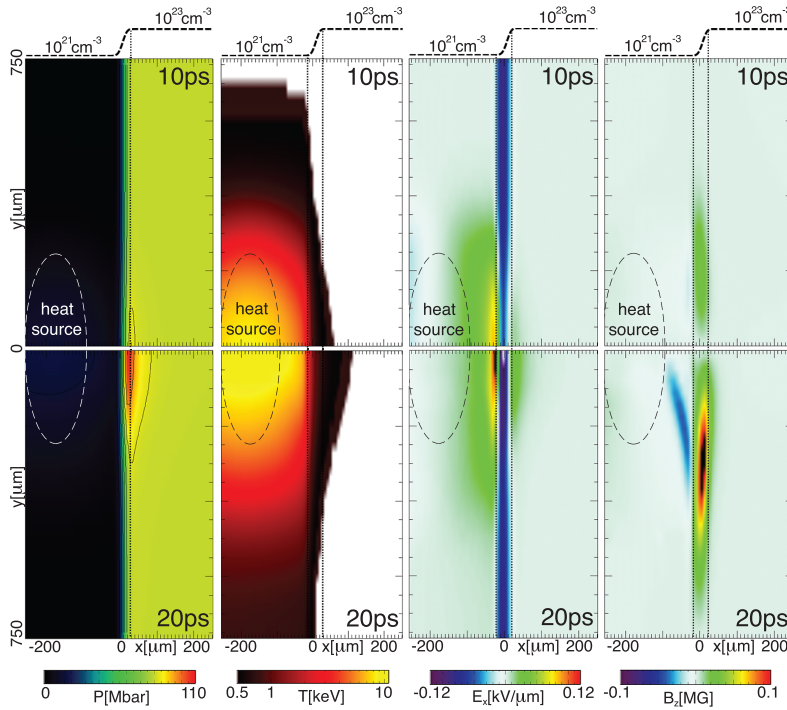


FIG. 5. The corona of a planar solid-density target is heated by a source with intensity

$$I = 10^{16} e^{-\frac{y^2}{2 \times (250 \mu\text{m})^2}} \times [1 - (1 - \frac{t}{10\text{ps}}) \text{H}(1 - \frac{t}{10\text{ps}})] \frac{\text{W}}{\text{cm}^2}.$$

The pressure and temperature profiles, as well as the longitudinal electric ( $E_x$ ) and transverse magnetic ( $B_z$ ) fields are shown after 10 ps and 20 ps.

asymmetric heating on this gradient can be expected to generate an electric field with maximum magnitude on axis, thereby driving a magnetic field (due to the Biermann battery). However, here the situation is more complex. The heat source resides in a region with constant density, and early in time the gradient is heated by non-local electrons which are accompanied by a resistive electric field. This field has the opposite sign from the one due to  $\nabla P$ . From Figure 5, we see that  $|E_x(10\text{ps})|$  is smaller on-axis in the region between the dotted lines, where  $\nabla n \neq 0$ . At the same time, resistive electric fields are visible both to the left and right of the gradient. At 20 ps the heat front has reached the region between the dotted lines and  $|E_x(20\text{ps})|$  is maximum on axis. The resistive electric field in the solid density material at 20 ps is also more prominent. The evolution of the electric field leads to the large changes observed in the  $B_z$  structure from 10 ps to 20 ps. It is conceivable that for systems with higher peak density and longer irradiation time  $B_z$  on the surface of the target is strong enough to magnetize the plasma. The relative importance of the underlying phenomena depends on the density and heat-source profiles.

## V. CONCLUSIONS

We have developed the VFP code OSHUN to study High Energy Density Laboratory Plasmas. OSHUN employs the spherical harmonic expansion in momentum-space to facilitate the description of arbitrarily anisotropic distribution functions in the presence of collisions. It implements the KALOS hierarchy of equations<sup>5</sup> for the effects of spatial advection, electric and magnetic fields, and incorporates a

rigorous semi-anisotropic Fokker-Planck collision operator. The code is currently being used for a number of studies relevant to Inertial Fusion Energy (IFE), which have motivated further advances in the numerical scheme and have allowed us to assess the potential and the limitations of OSHUN

- (1) An implicit algorithm for the electric field has been developed. Its computational cost is nearly the same as that of the explicit algorithm in Tzoufras *et al.*,<sup>32</sup> but it allows us to circumvent the CFL condition(s) due to high-frequency waves, thereby enabling *nsec*-scale electron transport simulations.
- (2) An inverse bremsstrahlung source has been implemented and shown to recover the DLM distribution functions. Benchmarks against simulations with a dipole electric field yield excellent agreement.
- (3) A careful convergence study is always required to justify the truncation of the spherical harmonic expansion. Otherwise it is difficult to identify whether the simulation results are physical or numerical artifacts.
- (4) Non-local transport leads to anisotropic particle distributions which are susceptible to the current-filamentation instability. Although VFP codes are noiseless, the instability can still grow from numerical noise. We can avoid this by carefully choosing the simulation parameters.
- (5) Non-local transport can be simulated for realistic IFE target geometries and time-scales. To perform such simulations we must incorporate mobile ions. This can be done either by modeling the ions as a fluid or adding them as a separate distribution function. Both approaches will be pursued.

## ACKNOWLEDGMENTS

We acknowledge support by the DOE under Fusion Science Center through a University of Rochester Subcontract No. 415025-G and under DE-FG52-09NA29552 and DE-NA0001833. Simulations were performed at the Hoffman2 cluster in UCLA. We also acknowledge useful discussions with Dr. B. Reville.

- <sup>1</sup>A. R. Bell, "Transport in laser-produced plasmas," In *proceedings of the Forty Fifth Scottish Universities Summer School in Physics, St. Andrews* (1995), pp. 138–167.
- <sup>2</sup>A. R. Bell, "Electron energy transport in ion waves and its relevance to laser-produced plasmas," *Phys. Fluids* **26**(1), 279–284 (1983).
- <sup>3</sup>A. R. Bell and M. Tzoufras, "Electron transport and shock ignition," *Plasma Phys. Controlled Fusion* **53**(4), 045010 (2011).
- <sup>4</sup>A. R. Bell, R. G. Evans, and D. J. Nicholas, "Electron energy transport in steep temperature gradients in laser-produced plasmas," *Phys. Rev. Lett.* **46**(4), 243–246 (1981).
- <sup>5</sup>A. R. Bell, A. P. L. Robinson, M. Sherlock, R. J. Kingham, and W. Rozmus, "Fast electron transport in laser-produced plasmas and the Kalos code for solution of the Vlasov–Fokker–Planck equation," *Plasma Phys. Controlled Fusion* **48**(3), R37–R57 (2006).
- <sup>6</sup>A. R. Bell, K. M. Schure, and B. Reville, "Cosmic ray acceleration at oblique shocks," *Mon. Not. R. Astron. Soc.* **418**(2), 1208–1216 (2011).
- <sup>7</sup>A. V. Bobylev and V. A. Chuyanov, "On the numerical solution of Landau's kinetic equation," *USSR Comput. Math. Math. Phys.* **16**(2), 121–130 (1976).
- <sup>8</sup>S. Brunner and E. Valeo, "Simulations of electron transport in laser hot spots," *Phys. Plasmas* **9**(3), 923–936 (2002).
- <sup>9</sup>R. C. Davidson, D. A. Hammer, I. Haber, and C. E. Wagner, "Nonlinear development of electromagnetic instabilities in anisotropic plasmas," *Phys. Fluids* **15**(2), 317–333 (1972).
- <sup>10</sup>R. Ducloux, B. Dubroca, F. Filbet, and V. Tikhonchuk, "High order resolution of the Maxwell-Fokker-Planck-Landau model intended for icf applications," *J. Comput. Phys.* **228**(14), 5072–5100 (2009).
- <sup>11</sup>C. T. Dum, "Anomalous heating by ion sound turbulence," *Phys. Fluids* **21**(6), 945–955 (1978).
- <sup>12</sup>C. T. Dum, "Anomalous electron transport equations for ion sound and related turbulent spectra," *Phys. Fluids* **21**(6), 956–969 (1978).
- <sup>13</sup>E. M. Epperlein and R. W. Short, "A practical nonlocal model for electron heat transport in laser plasmas," *Phys. Fluids B* **3**(11), 3092–3098 (1991).
- <sup>14</sup>B. D. Fried, "Mechanism for instability of transverse plasma waves," *Phys. Fluids* **2**(3), 337 (1959).
- <sup>15</sup>M. J. Keskinen, "Fully kinetic Fokker-Planck model of thermal smoothing in nonuniform laser-target interactions," *Phys. Rev. Lett.* **103**(5), 055001 (2009).
- <sup>16</sup>M. J. Keskinen, "Kinetic model for ion pressure perturbations in inhomogeneous laser-matter interactions," *Phys. Plasmas* **17**(5), 054507–054507–4 (2010).
- <sup>17</sup>R. J. Kingham and A. R. Bell, "An implicit Vlasov-Fokker-Planck code to model non-local electron transport in 2-d with magnetic fields," *J. Comput. Phys.* **194**(1), 1–34 (2004).
- <sup>18</sup>R. J. Kingham and A. R. Bell, "Nonlocal magnetic-field generation in plasmas without density gradients," *Phys. Rev. Lett.* **88**(4), 045004 (2002).
- <sup>19</sup>A. Bruce Langdon, "Nonlinear inverse bremsstrahlung and heated-electron distributions," *Phys. Rev. Lett.* **44**(9), 575–579 (1980).
- <sup>20</sup>J. F. Luciani, P. Mora, and J. Virmont, "Nonlocal heat transport due to steep temperature gradients," *Phys. Rev. Lett.* **51**(18), 1664–1667 (1983).
- <sup>21</sup>A. Marocchino, M. Tzoufras, S. Atzeni, A. Schiavi, Ph. D. Nikolai, J. Mallet, V. Tikhonchuk, and J.-L. Feugeas, "Comparison for non-local hydrodynamic thermal conduction models," *Phys. Plasmas* **20**, 022702 (2013).
- <sup>22</sup>J. P. Matte and J. Virmont, "Electron heat transport down steep temperature gradients," *Phys. Rev. Lett.* **49**(26), 1936–1939 (1982).
- <sup>23</sup>J. P. Matte, M. Lamoureux, C. Moller, R. Y. Yin, J. Delettrez, J. Virmont, and T. W. Johnston, "Non-Maxwellian electron distributions and continuum x-ray emission in inverse bremsstrahlung heated plasmas," *Plasma Phys. Controlled Fusion* **30**(12), 1665 (1988).
- <sup>24</sup>K. Molvig, "Filamentary instability of a relativistic electron beam," *Phys. Rev. Lett.* **35**(22), 1504–1507 (1975).
- <sup>25</sup>B. Reville and A. R. Bell, "Universal behaviour of shocks in the presence of efficient cosmic-ray acceleration," *Mon. Not. R. Astron. Soc.* **430**(4), 2873–2884 (2013).
- <sup>26</sup>M. N. Rosenbluth, W. M. MacDonald, and D. L. Judd, "Fokker-Planck equation for an inverse-square force," *Phys. Rev.* **107**(1), 1–6 (1957).
- <sup>27</sup>L. Spitzer and R. Härm, "Transport phenomena in a completely ionized gas," *Phys. Rev.* **89**(5), 977–981 (1953).
- <sup>28</sup>A. Sunahara, J. A. Delettrez, C. Stoeckl, R. W. Short, and S. Skupsky, "Time-dependent electron thermal flux inhibition in direct-drive laser implosions," *Phys. Rev. Lett.* **91**(9), 095003 (2003).
- <sup>29</sup>A. G. R. Thomas, R. J. Kingham, and C. P. Ridgers, "Rapid self-magnetization of laser speckles in plasmas by nonlinear anisotropic instability," *New J. Phys.* **11**(3), 033001 (2009).
- <sup>30</sup>A. G. R. Thomas, M. Tzoufras, A. P. L. Robinson, R. J. Kingham, C. P. Ridgers, M. Sherlock, and A. R. Bell, "A review of Vlasov–Fokker–Planck numerical modeling of inertial confinement fusion plasma," *J. Comput. Phys.* **231**(3), 1051–1079 (2012).
- <sup>31</sup>M. Tzoufras, C. Ren, F. S. Tsung, J. W. Tonge, W. B. Mori, M. Fiore, R. A. Fonseca, and L. O. Silva, "Stability of arbitrary electron velocity distribution functions to electromagnetic modes," *Phys. Plasmas* **14**(6), 062108 (2007).
- <sup>32</sup>M. Tzoufras, A. R. Bell, P. A. Norreys, and F. S. Tsung, "A Vlasov–Fokker–Planck code for high energy density physics," *J. Comput. Phys.* **230**(17), 6475–6494 (2011).
- <sup>33</sup>E. S. Weibel, "Spontaneously growing transverse waves in a plasma due to an anisotropic velocity distribution," *Phys. Rev. Lett.* **2**(3), 83–84 (1959).
- <sup>34</sup>The algorithm for the isotropic self-collision operator transitions from utilizing the full distribution function to employing its Taylor-expansion as  $p \rightarrow 0$ . The CFL condition slightly varies, depending on the location where this transition occurs.
- <sup>35</sup>Summation over repeated indices is assumed,  $\epsilon_{ijk} = 1$  if  $(i, j, k)$  is an even permutation of  $(x, y, z)$ ,  $\epsilon_{ijk} = -1$  if it is an odd permutation, and 0 if it has repeated indices.

## Resonance between heat-carrying electrons and Langmuir waves in inertial confinement fusion plasmas

W. Rozmus,<sup>1</sup> T. Chapman,<sup>2</sup> A. Brantov,<sup>3</sup> B. J. Winjum,<sup>4</sup> R. L. Berger,<sup>2</sup> S. Brunner,<sup>5</sup>  
 V. Yu. Bychenkov,<sup>3</sup> A. Tableman,<sup>6</sup> M. Tzoufras,<sup>6</sup> and S. Glenzer<sup>7</sup>

<sup>1</sup>Department of Physics, University of Alberta, Edmonton, Alberta T6G 2G7, Canada

<sup>2</sup>Lawrence Livermore National Laboratory, Livermore, California 94551, USA

<sup>3</sup>P.N. Lebedev Physics Institute, Russian Academy of Sciences, Moscow 119991 Russia  
 and Center for Fundamental and Applied Research, VNIIA, ROSATOM, 127055 Moscow, Russia

<sup>4</sup>Department of Electrical Engineering, UCLA, Los Angeles, California 90095, USA

<sup>5</sup>Association EURATOM-Confederation Suisse, EPFL, 1015 Lausanne, Switzerland

<sup>6</sup>Department of Physics and Astronomy, UCLA, Los Angeles, California 90095, USA

<sup>7</sup>LCLS, Stanford, California 94025, USA

(Received 26 October 2015; accepted 22 December 2015; published online 15 January 2016)

In ignition scale hot plasmas, temperature gradients and thermal transport modify electron distributions in a velocity range resonant with Langmuir waves typical of those produced by stimulated Raman scattering. We examine the resultant changes to the Landau damping experienced by these Langmuir waves and the levels of thermal plasma fluctuations. The form factor and Thomson scattering cross-section in such plasmas display unique characteristics of the background conditions. A theoretical model and high-order Vlasov-Fokker-Planck simulations are used in our analysis. An experiment to measure changes in thermal plasma fluctuation levels due to a thermal gradient is proposed. © 2016 AIP Publishing LLC.

<http://dx.doi.org/10.1063/1.4939603>

### I. INTRODUCTION

This paper deals with non-Maxwellian electron distribution functions (EDFs) resulting from thermal transport in plasmas relevant to large-scale inertial confinement fusion (ICF) experiments. We examine the linear plasma response under such conditions, with focus given to the linear plasma wave damping and Thomson scattering (TS) cross-section.

Local thermal transport theories such as the Spitzer-Härm (SH) model<sup>1</sup> or Braginskii's transport relations<sup>2</sup> follow from a perturbative solution of a Boltzmann-Vlasov (kinetic) equation for plasma with local electron temperature  $T_e$ , density  $n_e$ , thermal velocity  $v_{th}$ , and ionic charge state  $Z$ . In such treatments, the leading term in the expansion of the EDF is a local Maxwellian and the expansion is carried out in terms of the smallness parameter  $\delta_T = \lambda_{ei}/L_T \ll 1$ , where  $\lambda_{ei}$  is the electron-ion ( $e$ - $i$ ) mean free path and  $L_T = |\nabla \ln(T_e)|^{-1}$  is the scale length of the profile of  $T_e$ .

More precisely, the parameter that occurs naturally in the expansion of the EDF is  $\delta_T \sqrt{Z}$  (see, e.g., Ref. 3). It has been established<sup>4-8</sup> that  $\delta_T$  must be small, on the order of 0.01, for classical transport theory to be valid. For example, in the theory of nonlocal hydrodynamics of Ref. 9, significant deviations from the SH or Braginskii thermal transport coefficients have been observed for  $\delta_T \geq 0.065/\sqrt{Z}$ . In the following, we will discuss several examples of inhomogeneous plasmas where  $\delta_T$  is within or near the theoretically predicted limit of validity of classical hydrodynamics. However, the corresponding EDFs display significant deviations from the equilibrium state, leading to changes in the linear plasma response based on these EDFs.

An important example of a plasma where our findings are of relevance is the indirect drive ICF target, where laser

light must heat and propagate through plasma within a hohlraum. Near the laser entrance hole (LEH) of the hohlraum, many laser beams overlap, heating a plasma of volume  $\sim 1 \text{ mm}^3$  primarily via inverse Bremsstrahlung radiation. This localized heating establishes a negative temperature gradient from the LEH along the trajectories of beams within the plasma. In ICF experiments, such as those carried out at the National Ignition Facility (NIF), stimulated Raman scattering (SRS) produces deleterious plasma reflectivities of up to  $\sim 30\%$  along beam trajectories that pass close to the target capsule (along  $23^\circ$  and  $30^\circ$  cone paths at the NIF). During SRS, light scatters from and drives Langmuir waves. The SRS process, and accordingly interpretations of experimental SRS spectra, is sensitive to the Landau damping of these Langmuir waves. Furthermore, Landau damping of Langmuir waves is a source of hot electrons that prematurely heats the ICF target, impeding efficient target compression.

Studies have indicated that SRS may occur both deep into the hohlraum<sup>10</sup> and near the LEH via a collective (many-beam) process.<sup>11</sup> We find under ICF-relevant conditions that heat flow along the direction of beam propagation (opposite to the thermal gradient) results in an increase in Landau damping relative to that of a thermal (Maxwellian) plasma across a broad range of parameters. This occurs via a resonance between heat-carrying electrons and SRS-produced Langmuir waves. Conversely, Landau damping is reduced in the opposite direction (the direction relevant to the rescattering of light that is produced by back-scattering via SRS).

The ICF plasmas we consider are of a length on the order of several millimeters or a thousand  $\lambda_{ei}$ . It is sufficient in order to demonstrate the physics that we wish to discuss to consider a problem with one spatial dimension (1D).

Furthermore, such a simplification permits close comparison between theory (both existing and new) and numerical simulations. Accordingly, we specify the EDF as  $\tilde{f} = \tilde{f}(x, \vec{v}, t)$ , where  $x$ ,  $\vec{v}$ , and  $t$  are position, velocity, and time, respectively, and  $x$  is parallel to the direction of heat flow. The kinetic description of the EDF evolution is given by the Vlasov-Fokker-Planck (VFP) equation

$$\frac{\partial \tilde{f}}{\partial t} + \vec{v} \cdot \nabla \tilde{f} - \frac{e}{m} \vec{E} \cdot \frac{\partial \tilde{f}}{\partial \vec{v}} = -C_{ee}[\tilde{f}, \tilde{f}] - C_{ei}[\tilde{f}], \quad (1)$$

where  $C_{ee}$  is the Landau electron-electron collisional operator,  $C_{ei}$  is the Lorentz electron-ion collision operator, and here  $\nabla = (\partial/\partial x, 0, 0)$ .

The standard approach to finding the solution for  $\tilde{f}(x, \vec{v}, t)$  involves expansion in the Legendre polynomials  $P_l$

$$\tilde{f}(x, \vec{v}, t) = \sum_{l=0}^{\infty} \tilde{f}_l(x, v, t) P_l(\mu), \quad (2)$$

where  $v = |\vec{v}|$ ,  $\mu = \cos \theta$ , and  $\theta$  is the polar angle of  $\vec{v}$  relative to the  $x$ -axis. In the most basic approximation, two terms (harmonics) in the sum of Eq. (2) are kept:  $\tilde{f} = \tilde{f}_0 + \mu \tilde{f}_1$ . In high- $Z$  plasmas, the  $e$ - $e$  collision operator in the equation for the first harmonic,  $\tilde{f}_1$ , is often neglected. The electric field  $E$  may be calculated in 1D from a zero-current condition. The two-term truncation of the sum in Eq. (2) constitutes the so-called diffusive approximation.<sup>3</sup> In this limit, the SH result is obtained when the isotropic part (zeroth-order harmonic) of the EDF,  $\tilde{f}_0$ , is taken to be the local Maxwellian,  $\tilde{f}_M = \tilde{f}_M[v, T_e(x)]$ , giving (see, e.g., Ref. 12),

$$\tilde{f}_1(x, v) = \sqrt{\frac{2}{9\pi}} \left(\frac{v}{v_{th}}\right)^4 \left(4 - \frac{v^2}{2v_{th}^2}\right) \tilde{f}_M \delta_T. \quad (3)$$

For both the diffusive approximation and the SH model to be valid,  $\tilde{f}_1$  must be smaller than  $\tilde{f}_0$  and  $\tilde{f}_M$ , respectively. However, it is clear from Eq. (3) that the ratio  $|\tilde{f}_1|/\tilde{f}_M$  will *always* reach values larger than 1 at sufficiently high electron velocities for given  $\delta_T$ . One is required therefore to consider values of  $\delta_T$  small enough such that the validity of these transport models extends over an adequately wide range of velocities. In particular, one should ensure that  $|\tilde{f}_1|/\tilde{f}_M < 1$  for  $v/v_{th} \sim 3.7$ , where from Eq. (3) contributions of  $\tilde{f}_1$  to the heat flux are at a maximum. The same limitation applies to other theories based on similar approximations, such as the  $M_1$  model of Ref. 13.

Modeling of ICF experiments requires treating heat transport. Experimental scales make fully kinetic simulations that solve the VFP equation, using, e.g., continuum or particle-in-cell representations of the EDF, computationally impossible for three and sometimes even two spatial dimensions. Approximate treatments are therefore required, such as the hydrodynamics codes Hydra and Lasnex. Recently, the high flux model<sup>14</sup> (HFM) has been widely-used in such ICF simulations. In the HFM, the electron heat flux,  $q_e$ , is taken to be equal to the smaller out of the values given by either the SH expression  $q^{SH} = -\kappa^{SH} \nabla T_e$  or the reduced free streaming expression  $q^{FS} = f_q n_e v_{th} T_e$ , where  $\kappa^{SH} \propto \delta_T$  is

defined in full in Ref. 1 and  $f_q$  is a so-called flux limiter typically equal to 0.15. The condition  $|\tilde{f}_1|/\tilde{f}_M < 1$  for velocities  $v \lesssim 4v_{th}$  corresponds to the flux limiter  $f_q \approx 0.1$  (cf. e.g., Sec. 7.2 of Ref. 12).

Central to the motivation of this work is the observation that electrons responsible for the heat flow are resonant with SRS-produced Langmuir waves. At the NIF, the majority of SRS light is thought to originate in regions where  $n_e/n_c \sim 0.1$  and  $T_e = 2.5$  keV, where  $n_c$  is the critical density of 351 nm light.<sup>10,15</sup> Electrons satisfying  $3 \approx \vec{v} \cdot \vec{k}_L / (v_{th} k_L) \lesssim 4$  will modify the Landau damping of SRS-produced Langmuir waves, where  $\vec{k}_L$  is the wave vector of the Langmuir wave. From Eq. (3), it is evident that electrons responsible for heat flow have velocities within this range. Contributions to the modification of Landau damping are made by both the isotropic and anisotropic parts of the EDF. A sufficiently large modification of the distribution function due to heat flow may in principle result in Langmuir waves becoming unstable.<sup>16</sup> However, in the cases we have studied, we do not observe instability in our simulations when enough terms (harmonics) in Eq. (2) are kept such that the result is numerically converged; this is discussed further in the following.

The paper is organized as follows: Section II introduces the VFP code OSHUN. ICF-relevant temperature profiles generated using OSHUN by the relaxation of a hot spot and the resulting EDFs are discussed. Landau damping rates in EDFs generated in the diffusive approximation and using many (15) harmonics are compared to those of a Maxwellian EDF. In Sec. III, a new theory using 3 harmonics is proposed and applied to an ICF-relevant profile. This theory is demonstrated to perform significantly better than the SH model in ICF-relevant temperature profiles generated using OSHUN. From this theory, an analytic expression for the Landau damping of Langmuir waves that depends on the first and second spatial derivatives of the temperature profile is obtained. Section IV describes a Thomson scattering experiment that could provide an experimental measurement of the non-Maxwellian EDFs present during heat flow. Section V discusses the implications of this work.

## II. SIMULATIONS AND LINEAR PLASMA RESPONSE

The principal part of our work involves numerical simulations using the VFP code OSHUN.<sup>17–19</sup> OSHUN uses a Cartesian mesh (here 1D) in configuration space and applies a spherical harmonic expansion of the EDF in momentum space to solve the VFP equation. The  $e$ - $e$  collision term in Eq. (1) is the Landau operator that acts on all terms in the harmonic decomposition of the EDF; there is no validity constraint on  $Z$ . The number of harmonics (including the zeroth-order harmonic),  $N_h$ , necessary to obtain a converged solution can vary depending on the nature of the problem and it is large ( $N_h = 15$ ) for the presented profiles when we investigate the high velocity tail of the EDF. In order to make direct comparisons with simulations where  $N_h = 2$ , results from the SH model are shown *without* the use of a flux limiter.

### A. Hot spot relaxation

We have applied OSHUN to the hot spot relaxation problem<sup>18,20</sup> in which a localized temperature perturbation relaxes due to thermal conduction. As in previous studies, an initial hot spot is used to produce a temperature gradient and related EDF on a spatial scale of relevance to experimental conditions. In the cases we consider here, the relaxed state (which is analyzed) has a temperature profile characteristic of hydrodynamic simulations of ICF plasmas, sampled from the 3D volume along a 1D trajectory that corresponds to an inner (23° or 30° cone at the NIF) laser beam. Laser light following this path sees a temperature that is highest near the LEH and falls deeper into the hohlraum. We are interested in changes to the linear plasma response along such a 1D trajectory. Related studies<sup>3,20</sup> have examined non-Maxwellian EDFs and thermal transport under similar conditions in the direction perpendicular to the laser propagation direction.

In our simulations, the initial electron temperature profile is prescribed according to  $T_e(x, t=0) = T_0 + T_1 \exp(-x^2/2l_0^2)$ , where  $l_0$ ,  $T_0$ , and  $T_1$  are constants, and the density is homogeneous ( $n_e$  does not evolve in our simulations due to the 1D geometry and zero-current condition). The region  $x > 0$  is displayed and analyzed after relaxation for varying choices of initial conditions. In Fig. 1, the initial temperature profile using  $T_0 = 1$  keV,  $T_1 = 5$  keV, and  $l_0 = 0.043L = 0.25$  mm is shown for a plasma with  $Z=2$  (He) and  $n_e = 10^{21} \text{ cm}^{-3} \approx 0.1n_c$ . Also shown is  $T_e$  at  $t = 66.5/\nu_{ei}$  generated using (i) OSHUN ( $N_h=15$ , black solid line), (ii) oshun ( $N_h=2$ , blue solid line), and (iii) the SH model (blue dashed line). The  $e$ - $i$  collision rate  $\nu_{ei}$  is given here by  $\nu_{ei} = Z\nu_{ee} = 4(2\pi)^{1/2}Zn_e e^4 \Lambda / (3m_e^{1/2} T_0^{3/2})$ , evaluated by using  $\Lambda = 7$  for the Coulomb logarithm and  $T_e = T_0$ . The system length  $L = 5.7$  mm is large enough to ensure system boundaries do not affect our analysis and  $L \gg \lambda_{ei} = v_{th}/\nu_{ei} = 10.7$   $\mu\text{m}$  where  $\lambda_{ei}$  has also been evaluated using  $T_0$ .

The plotted SH heat transport model result is given by solving

$$\frac{3}{2} n_e \frac{\partial \bar{T}_e}{\partial t} = \kappa \frac{\partial}{\partial x} \left[ \bar{T}_e^{5/2} \frac{\partial \bar{T}_e}{\partial x} \right], \quad (4)$$

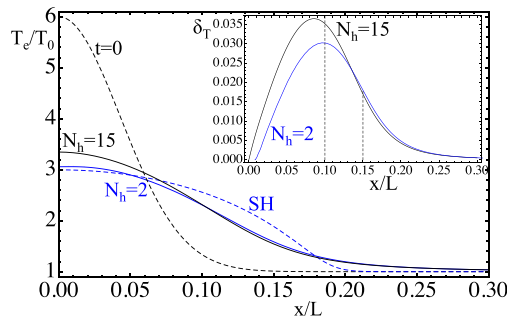


FIG. 1. Relaxation of an initial hot spot ( $t=0$ , black dashed line) where  $Z=2$  to three different states at  $t = 66.5/\nu_{ei}$ , using (i) oshun ( $N_h=15$ , black solid line), (ii) oshun ( $N_h=2$ , blue solid line), and (iii) the SH model [blue dashed line; see Eq. (4)]. Inset,  $\delta_T$  calculated using  $T_e(x, t = 66.5/\nu_{ei})$  from the oshun calculations is shown.

$$\kappa = \frac{128 (Z + 0.24)}{3\pi (Z + 4.2)} \frac{n_e T_0}{m_e \nu_{ei}(T_0)}, \quad (5)$$

where  $\bar{T}_e \equiv T_e/T_0$ . In Fig. 1, the SH model result differs from the VFP (OSHUN) results for  $N_h=2$  as well as  $N_h=15$ . The three temperature profiles shown at  $t = 66.5/\nu_{ei}$  in Fig. 1 agree to within 20% for  $x \lesssim 0.2$ . For  $x \gtrsim 0.2$ , fast weakly collisional electrons in the VFP simulations form a hot tail in the spatial profile of  $T_e$  that is not captured by the SH model; relative to the VFP calculation,  $T_e$  in the SH model reaches a steeper gradient, and plasma preheat is reduced. Shown next, the EDF and its resultant impact on the linear plasma response differs significantly between the three cases even for  $x \lesssim 0.2$ . Displayed in the inset in Fig. 1 and discussed later,  $\delta_T$  is calculated using  $T_e(x, t = 66.5/\nu_{ei})$ .

### B. Electron distribution functions

In Fig. 2, the EDFs from VFP simulations integrated over velocities perpendicular to the thermal gradient,  $v_\perp$  (with azimuthal angle  $\varphi$ ), are shown, where  $f(x, u, t) = \int_{\Gamma} v_\perp \tilde{f}(x, \vec{v}, t) dv_\perp d\varphi$  and  $u = \mu v$ . EDFs are sampled at  $x = 0.1L = 0.57$  mm ( $\delta_T = 0.035$  for  $N_h=15$  and  $\delta_T = 0.03$  for  $N_h=2$ ) and  $x = 0.15L = 0.86$  mm ( $\delta_T = 0.017$  for  $N_h=15$  and  $\delta_T = 0.018$  for  $N_h=2$ ). All EDFs are unitless, normalized to the local value of  $n_e/v_{th}$ . The upper pair of plots, (a) and (c), shows the anisotropic part of the EDF,  $f - f_0$ , while the lower pair, (b) and (d), shows the deviation of the isotropic component of the EDF from Maxwellian,  $f_0 - f_M$ , where  $f_M = (1/\sqrt{2\pi}) \exp[-u^2/(2v_{th}^2)]$ . Solid lines indicate results from VFP simulations using, as before,  $N_h=15$  (black solid line) and  $N_h=2$  (blue solid line), while the black dashed line refers to an analytic calculation given in Sec. III.

The normalized anisotropic EDF component differs little between the two VFP cases, exhibiting the usual form of a flux of fast heat carrying electrons and a slow return current. The isotropic deviation from Maxwellian  $f_0 - f_M$  shows a substantial difference between the cases  $N_h=15$  and  $N_h=2$  at  $x = 0.1L$ , although  $f_0$  in both cases differs from  $f_M$  by an amount on the order of the anisotropic component. The SH model assumes  $f_0 = f_M$  and therefore fails to describe a key feature of the VFP simulations.

In Fig. 3, the ratio of the anisotropic part of the EDF to the isotropic part  $(f - f_0)/f_0$  at  $x = 0.1L$  is shown. It is evident that the SH model (evaluated at  $\delta_T = 0.03$ ) violates the assumption required for justifying a truncation of an expansion of the EDF at  $N_h=2$ , namely, that  $|f_1|$  is small compared to  $f_0$ , for  $u \gtrsim 3v_{th}$ . Under such conditions, calculations of derived quantities in this region of the EDF (and perhaps outside this region) such as Landau damping (or indeed a spontaneous growth rate due to an inversion of the distribution) using the diffusive approximation may not be physically meaningful; this point is demonstrated in the following.

In Fig. 3, a clear trend of convergence with increasing terms in the expansion of the EDF is apparent: From the SH model (black dashed line) where  $f = f_M + f_1$ , to the diffusive approximation ( $N_h=2$ , solid blue line) VFP calculation where  $f = f_0 + f_1$ , and to the converged VFP result ( $N_h=15$ ,

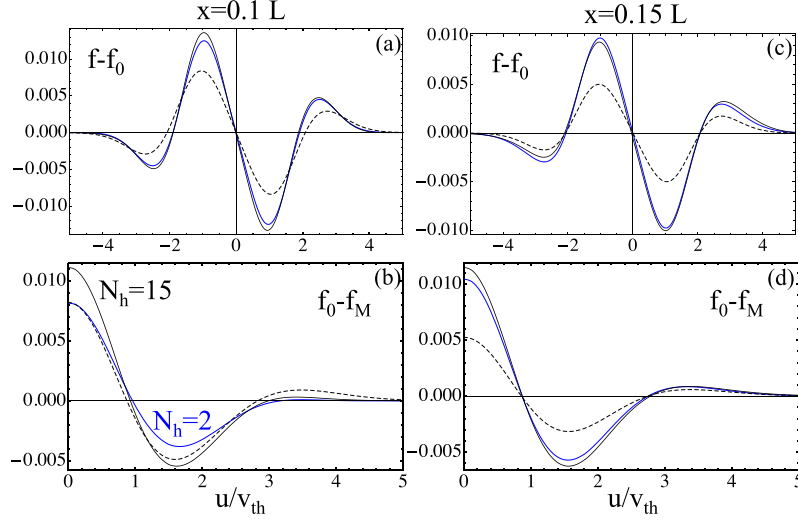


FIG. 2. Electron distribution functions projected on the opposite direction to the temperature gradient, where  $-\nabla T_e \cdot \vec{v} = |\nabla T_e|u$ , at the two locations from Fig. 1. Thermal velocities,  $v_{th}$ , are calculated locally, at  $x = 0.1L$  [panels (a) and (b)] and  $x = 0.15L$  [panels (c) and (d)]. Upper panels, (a) and (c), show anisotropic EDFs that are compared with dashed lines corresponding to theoretical calculations of Sec. III. Lower panels, (b) and (d), show deviations of the isotropic solution,  $f_0$ , from the Maxwellian distribution function,  $f_M$ . The two solutions from oshun,  $N_h = 15$  (black) and  $N_h = 2$  (blue), are marked on panel (b). On all other panels, they are almost indistinguishable in spite of producing quite different damping coefficients in Fig. 4 below.

solid black line). Note that using a large number of harmonics in the expansion of the EDF leads to a cancellation of contributions to higher velocity tails in the projected distribution functions. As a result, one expects  $\lim_{u \rightarrow \pm\infty} (f - f_0)/f_0 = -1$ ; the  $N_h = 15$  VFP simulation in Fig. 3 observes this limit.

### C. Linear plasma response

The linear plasma response, and in particular, the linear Landau damping of Langmuir waves, is of interest in many applications. In typical calculations, the EDF is assumed Maxwellian, and the impact of heat-carrying electrons resonant with the Langmuir waves is not considered. For a linear Langmuir wave (with arbitrary EDF), the Landau damping rate is proportional to the resonant approximation to  $\partial f / \partial u|_{u=v_{ph}}$ , while for a Maxwellian EDF, it is given approximately by  $\gamma_L \approx -[\pi\omega_L^3 / (2k^2)] \partial f / \partial u|_{u=v_{ph}}$ , where  $v_{ph} \equiv \omega_L / k_L$  is the phase velocity,  $\omega_L \approx (\omega_{pe}^2 + 3k^2 v_{th}^2)^{1/2}$  is the frequency, and  $\omega_{pe}$  is the electron plasma frequency.<sup>21,22</sup>

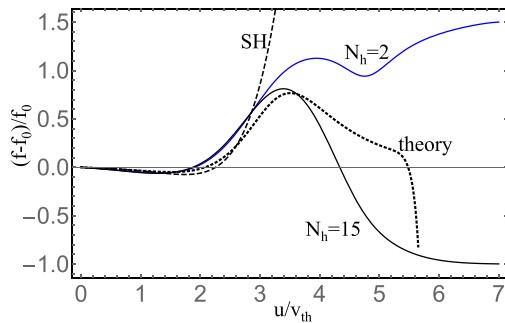


FIG. 3. Ratio of the total anisotropic harmonics to the zeroth order harmonic, projected on the direction of the temperature gradient, as a function of normalized velocity. Physical parameters are the same as in Fig. 1 and the oshun results are at  $x = 0.1L$  for both  $N_h = 2$  and  $N_h = 15$ . The SH results are evaluated for  $\delta_T = 0.03$  and theory curve is based on the results of Sec. III.

Using EDFs from VFP simulations, the ratio of the damping rate to that of a Maxwellian EDF,  $\gamma_L / \gamma_M$ , is evaluated as a function of  $v_{ph}$  (the grey box corresponds to  $0.3 \leq k\lambda_D \leq 0.4$ ) and plotted in Fig. 4 for Langmuir waves propagating both antiparallel ( $\vec{k}_L \parallel -\nabla T_e$ , the linear SRS scattering geometry in ICF hohlraums) and parallel ( $\vec{k}_L \parallel \nabla T_e$ , the rescatter geometry in ICF hohlraums) to the thermal gradient. As in Fig. 2, the EDFs are sampled at  $x = 0.1L$  and  $x = 0.15L$ .

In Fig. 4, but true generally of our simulations, we observe that Langmuir waves propagating parallel to the thermal gradient experience a *reduction* in Landau damping, while Langmuir waves propagating antiparallel experience an *increase* relative to a Maxwellian EDF; the effect we observe is maximized for these two geometries. In the resonant approximation,  $\gamma_L$  is proportional to  $\partial f / \partial u$  and therefore very sensitive to details of the EDF that at higher velocities are not properly modeled in the diffusive approximation ( $N_h = 2$ ). The breakdown of this approximation is illustrated by the negative damping rates in Fig. 4 for  $N_h = 2$ : It is a consequence of the large ratios of  $|f_1|/f_0$  and the invalid truncation of the expansion of the EDF. We observe that VFP results using  $N_h = 15$  exhibit a dramatic reduction of  $\gamma_L$  relative to  $\gamma_M$  for  $\vec{k} \parallel \nabla T_e$ , but never a change of sign.

### III. THEORETICAL MODEL

In the preceding numerical simulations, we have considered temperature profiles characterized by  $\delta_T(x)$  and their corresponding EDFs of relevance to experimental conditions in hot ICF plasmas. It is not computationally feasible to perform a VFP simulation of an entire hohlraum using a code such as oshun in three spatial dimensions and with the requisite number of harmonics to achieve convergence. A need is present therefore for an improvement to modeling heat flow and the EDF for applications in which the linear plasma response is important. In this section, we give a perturbative expansion of the 1D VFP equation, similar to that of Spitzer-



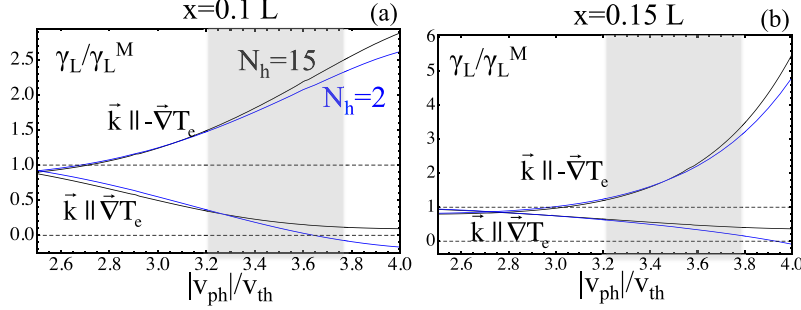


FIG. 4. The local linear electron Landau damping coefficient,  $\gamma_L$ , calculated using EDFs from Fig. 2, divided by the damping rate for a Maxwellian EDF,  $\gamma_L^M$ . EDFs are taken at (a)  $x = 0.1L$  and (b)  $x = 0.15L$ . Damping rates are given for Langmuir waves propagating both parallel and antiparallel to the temperature gradient. The failure of the 2-harmonic approximation is demonstrated by negative values of  $\gamma_L$ . The shaded areas correspond to  $0.3 \leq k\lambda_D \leq 0.4$ .

Härm<sup>1</sup> where solutions to the VFP equation are sought by finding the EDF corresponding to a quasi-stationary  $T_e$  profile. However, there are two key differences to our approach: (i) We work to higher order in  $\delta_T$ , retaining the first 3 terms in the expansion of the EDF rather than 2, and (ii) We permit the evolution of the isotropic (typically non-Maxwellian) component of the EDF. The importance of the latter difference is well-known; see, e.g., Ref. 8.

We begin by defining  $f_e = F_0 + \delta f$ , where the perturbation  $\delta f = \delta f(x, v, \mu)$  is computed up to second order in  $\delta_T$ , and  $F_0$  is a zero-order isotropic term that fully defines the electron density and temperature  $T_e(x)$ . As before, we have  $u = \mu v$  and  $\mu = \cos \theta$ . Consistent with the initialization of the VFP simulations,  $F_0$  will be a local Maxwellian.  $\delta f$  is expanded into a series of Legendre polynomials,  $P_l$ , according to  $\delta f = \sum_{l \geq 0} f_l P_l(\mu)$  and  $\hat{f} = f_e$  is substituted into the VFP equation given by Eq. (1). Truncating the series beyond  $l=2$  ( $N_h=3$ ), linearizing  $e-e$  collisions, and retaining terms up to order  $(\delta_T)^2$ , one finds

$$\frac{\partial f_0}{\partial t} + \frac{v}{3} \frac{\partial f_1}{\partial x} - \frac{eE}{3m_e v^2} \frac{\partial v^2 f_1}{\partial v} = C_{ee}[f_0, F_0], \quad (6)$$

$$\frac{\partial f_1}{\partial t} + v \frac{\partial F_0}{\partial x} - \frac{eE}{m_e} \frac{\partial F_0}{\partial v} = -\nu_{ei} f_1 + C_{ee}[f_1, F_0], \quad (7)$$

$$\frac{\partial f_2}{\partial t} + \frac{2v}{3} \frac{\partial f_1}{\partial x} - \frac{2eEv}{3m_e} \frac{\partial}{\partial v} \left( \frac{f_1}{v} \right) = -3\nu_{ei} f_2 + C_{ee}[f_2, F_0]. \quad (8)$$

Note that Eq. (7) contains terms only up to order  $(\delta_T)$ ; the (neglected) next order terms such as  $(eE/m_e) \partial f_0 / \partial v$  are of order  $(\delta_T)^3$ .

Our approach to solving Eqs. (6)–(8), and in particular, to the treatment of  $e-e$  collisions, borrows from past work on nonlocal transport in Refs. 9 and 23. The key difference in our work lies in the initial conditions, which are replaced here by the prescribed temperature gradient that drives particle transport and non-Maxwellian EDFs. Since we retain terms only up to  $N_h=3$ , we will not obtain solutions used in the derivation of nonlocal transport relations.<sup>9,23,24</sup>

We solve Eqs. (6)–(8) in a quasi-stationary approximation, keeping terms up to second order in the temperature gradient. The lowest order anisotropic harmonic of the EDF,  $f_1$ , is found to be

$$f_1 = \sqrt{\frac{2}{9\pi}} \lambda_{ei} \psi_1 \left( \frac{v}{v_{th}} \right) \frac{d \ln T_e}{dx} F_0, \quad (9)$$

where the basis function  $\psi_1$  satisfies the equation

$$\psi_1 - \frac{v^3 \lambda_{ei}}{v_{th}^4 F_0} C_{ee}[\psi_1, F_0] = S_1, \quad (10)$$

$$S_1 = \frac{v^4}{v_{th}^4} \left( A + \frac{3}{2} - \frac{v^2}{2v_{th}^2} \right). \quad (11)$$

The coefficient  $A$  is defined from the zero-current condition after substitution of  $eE/T_e = -A[d \ln(T_e)/dx]$ .

In the strongly collisional limit for high- $Z$  plasma, one can neglect  $e-e$  collisions. Under this approximation, one has  $\psi_1 = S_1$  and  $A = 5/2$ , and finds an expression for  $f_1$

$$f_1(x, v) = \sqrt{\frac{2}{9\pi}} \left( \frac{v}{v_{th}} \right)^4 \left( 4 - \frac{v^2}{2v_{th}^2} \right) F_0 \frac{\lambda_{ei}}{T_e} \frac{dT_e}{dx}, \quad (12)$$

that follows the SH form [cf. Eq. (3)]. By substituting the expression for  $f_1$  given by Eq. (9) into Eqs. (6) and (8), one can define corrections to the isotropic part of the EDF,  $f_0$ , as well as the second harmonic of the EDF,  $f_2$ . The two perturbations,  $f_a$  ( $a=0, 2$ ), are of the same order and display a similar dependence on the temperature gradient

$$f_a(x, v) = \lambda_{ei}^2 \frac{2}{9\pi} \left[ \psi_a^1 \frac{d^2 \ln T_e}{dx^2} + \psi_a^2 \left( \frac{d \ln T_e}{dx} \right)^2 \right] F_0. \quad (13)$$

The basis functions  $\psi_a^A$  ( $a=0, 2; A=1, 2$ ) satisfy

$$\frac{1}{\nu_{ei}(v_{th})F_0} C_{ee}[\psi_a^A, F_0] - \frac{3v_{th}^3}{v^3} \psi_a^A \delta_{a2} = S_a^A, \quad (14)$$

with different source terms:  $S_0^1 = v\psi_1/(3v_{th})$ ;  $S_2^1 = 2S_0^1$ ;  $S_0^2 = \psi_1 [v^3/(2v_{th}^3) + v/(2v_{th}) + A(2v_{th}/v - v/v_{th})]/3 + v_{th} (d\psi_1/dv)[A - v^2/(2v_{th}^2)]/3$ ; and  $S_2^2 = 2S_0^2 - \psi_1 A(6v_{th}/v)$ .  $\delta_{ij}$  is the Kronecker delta function. The solutions to Eqs. (10) and (14) can be found by expanding basis functions  $\psi_1$  and  $\psi_a^A$  in generalized Laguerre polynomials,  $L_n^{(1/2)}$

$$\psi_a^A(v) = \sum_{m=0}^{\infty} \psi_{a,m}^A L_m^{(1/2)} [v^2/(2v_{th}^2)]. \quad (15)$$

The first two coefficients,  $\psi_{0,0}^A$  and  $\psi_{0,1}^A$ , define perturbations of  $n_e$  and  $T_e$ , respectively. However,  $n_e$  and  $T_e$  are

fully specified by the initial condition and are assumed invariant in our theory. Therefore, one has  $\psi_{0,0}^A = \psi_{0,1}^A = 0$  and the expansion for  $\psi_0^A$  in Eq. (15) starts with  $m=2$  term.

The theoretical EDF is a function of two parameters,  $\delta_T$  and  $\beta_T = \lambda_{ei}^2 d^2 \ln T_e / dx^2$ , which depend on the temperature profile. By comparing collisional terms in Eqs. (6) and (8), one can estimate that the second harmonic  $f_2$  is  $Z$  times smaller than  $f_0$ . Results of theoretical calculations, shown by dotted curves, are compared with oshun VFP simulation results in Fig. 2. Our theory improves upon the SH result for  $f_1$  [cf. Eq. (12)] because it accounts for  $e-e$  collisions and the modification of the isotropic part of the EDF. Figure 2 shows that the theory works very well at  $x = 0.1L$  where corrections to the isotropic part of the EDF,  $f_0$ , are in close agreement with the OSHUN  $N_h=2$  result. The agreement between theory and simulations is poorer at  $x = 0.15L$  since this location is further from the initial hot spot region and consequently the EDF is affected by a higher fraction of fast electrons that produce a larger local deviation from the equilibrium EDF.

For high- $Z$  plasmas, where one can neglect the effect of  $e-e$  collisions, we can estimate the correction to  $f_0$  using Eq. (12) for the first harmonic. Taking the first non-vanishing term in the polynomial expansion given by Eq. (15) results in the following expression for  $f_0$ :

$$f_0(v) = Z(g_1\beta_T + g_2\delta_T^2) \left( 15 - 10\frac{v^2}{v_{th}^2} + \frac{v^4}{v_{th}^4} \right) F_0, \quad (16)$$

where  $g_1 = 80\sqrt{2}/(9\pi)$  and  $g_2 = 40\sqrt{2}/\pi$ .

The expressions for  $f_0$  and  $f_1$  given by Eqs. (16) and (12) permit a quick and effective estimate of the EDF resulting from the specified temperature gradient. From this theoretical EDF, further estimates of kinetic effects may be made, such as the local linear Landau damping,  $\gamma_L$ , of Langmuir waves

$$\gamma_L = \sqrt{\frac{\pi}{8}} \tilde{v}_{ph} k v_{th} \exp\left(-\frac{\tilde{v}_{ph}^2}{2}\right) \times \left[ 1 + Z(g_1\beta_T + g_2\delta_T^2) (\tilde{v}_{ph}^4 - 10\tilde{v}_{ph}^2 + 15) - \cos \zeta \left\{ \frac{\tilde{v}_{ph}^6 - 9\tilde{v}_{ph}^4 + 3\tilde{v}_{ph}^2 + 9}{3\sqrt{2\pi}} + \frac{3e^{\tilde{v}_{ph}^2/2}}{2\tilde{v}_{ph}} \operatorname{erfc}\left(\frac{\tilde{v}_{ph}}{\sqrt{2}}\right) \right\} \delta_T \right], \quad (17)$$

where  $\zeta$  is the angle between the wave vector  $\vec{k}$  and the direction of the temperature gradient and  $\tilde{v}_{ph} = v_{ph}/v_{th}$  is the normalized phase velocity of a Langmuir wave. The above expression is valid for  $\delta_T < 3\sqrt{2\pi}/|\tilde{v}_{ph}^6 - 9\tilde{v}_{ph}^4|$ . This restricts, for example, the value of  $\delta_T$  to  $\delta_T < 0.015$  for  $\tilde{v}_{ph} = 3.5$ , and  $\delta_T < 0.004$  for  $\tilde{v}_{ph} = 4$ .

We compare the Landau damping rate computed using Eq. (17) with that given by direct calculation using the EDF from oshun simulations. We adopt the profile of Fig. 1 ( $T_0 = 1$  keV,  $n_e = 10^{21}$  cm $^{-3}$ ) but increase the ion charge to  $Z=10$  such that the collisionality is consistent with the assumptions in the theory above. The initial temperature profile is the same as in Fig. 1 and the  $e-i$  collisional mean free path is  $\lambda_{ei}(T_0) = 2.14$   $\mu\text{m}$ .

The temperature profiles and parameters  $\delta_T$  and  $\beta_T$  are shown in Fig. 5 at time  $66.5/\nu_{ei}$ . The temperature profile in Fig. 5 is very similar to the results from Fig. 1, but the shorter  $e-i$  mean-free-path reduces  $\delta_T$ , placing these results well within the parameter validity range of local transport theory. Taking the EDF from OSHUN simulations ( $N_h=15$ ) at  $x = 0.1L$ , we calculate the linear Landau damping rate (solid colored lines) and compare it in Fig. 6 with Eq. (17) (dashed colored lines) and the damping rate corresponding to a Maxwellian plasma (solid black line),  $\gamma_L^M$ . Calculations are performed for plasma waves propagating against the temperature gradient ( $\vec{k} \parallel -\vec{\nabla}T_e$ , blue lines) and parallel to the temperature gradient ( $\vec{k} \parallel \vec{\nabla}T_e$ , red lines). As in Fig. 4, the grey region in Fig. 6 corresponds to  $0.3 \leq k\lambda_D \leq 0.4$ . Theory and

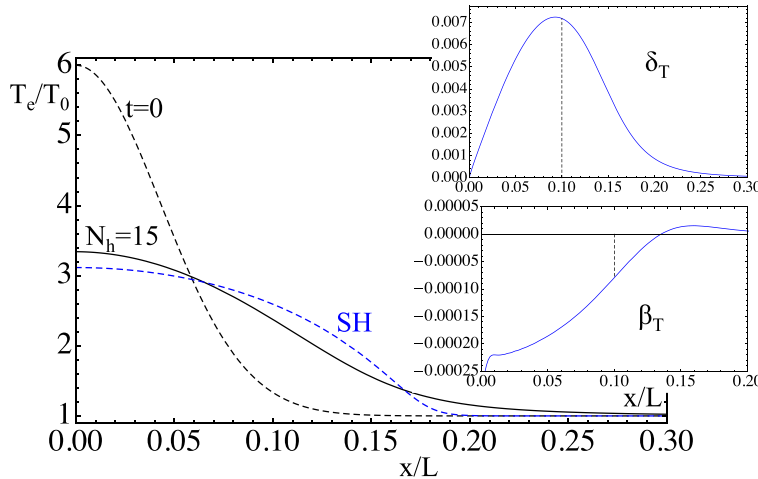


FIG. 5. Temperature profiles for an initial condition identical to Fig. 1 but for  $Z=10$ . Relaxed profiles are again shown at  $t = 66.5/\nu_{ei}$ . The increased plasma collisionality in this case is better suited for comparison with theoretical calculations. The two parameters required in the theory,  $\delta_T$  and  $\beta_T$ , are calculated from the relaxed oshun profile and shown in inset.

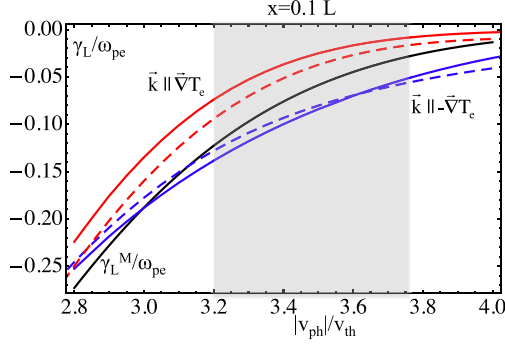


FIG. 6. Comparisons of the Landau damping coefficient  $\gamma_L$  calculated from theory given by Eq. (17) (dashed lines) and oshun simulations (solid red and blue lines) using  $N_h = 15$ , using EDFs from the case shown in Fig. 5 sampled at  $x = 0.1L$ . Landau damping for a Maxwellian EDF is also shown (solid black line).

simulations are in reasonable agreement: the curves corresponding to Eq. (17) illustrate well the main feature of the distribution functions, namely, that the Landau damping is reduced or increased for wave propagating according to  $\vec{k} \parallel -\vec{\nabla}T_e$  or  $\vec{k} \parallel \vec{\nabla}T_e$ , respectively. This property of the theoretical results is also seen for the example shown in Fig. 4 (a comparatively low-collisionality case that violates the assumptions of the derivation above); the Landau damping in this case is plotted in Fig. 7. Note that the failure of the  $N_h = 2$  approximation that leads to  $\gamma_L > 0$  in the OSHUN results shown in Fig. 4 is *not* present in the theoretical results.

#### IV. NONTHERMAL FLUCTUATIONS AND THOMSON SCATTERING

Electrostatic fluctuations in plasmas out of thermodynamic equilibrium are always of interest. These fluctuations define initial levels of ion acoustic and Langmuir modes for the growth of parametric instabilities (such as SRS) and can modify particle collisionality. Furthermore, the correlation function of electron density fluctuations can be measured in scattering experiments, thereby providing a means of experimental characterization of such nonequilibrium systems. In this section, we describe an experimental measurement that offers the opportunity to test the basic premise of this work, namely, the anisotropic modification of the linear plasma response due to heat flow. Calculations in the following

suggest that the proposed measurement is sufficiently sensitive so as to demonstrate the inability of the Spitzer-Härm approximation to describe the linear plasma response under ICF-relevant conditions.

The following TS experiment is well-suited to obtain quantitative measurements of thermal transport and features of the EDFs discussed in this work (cf. also Ref. 25). Consider a plasma that is heated by a heater beam to establish an inhomogeneous temperature profile that is similar to one of the temperature profiles shown in Figs. 1 or 5. A probe laser (e.g., of wavelength  $\lambda_0 = 0.351 \mu\text{m}$ ) that is scattered in the collective regime from ion acoustic and Langmuir wave fluctuations is then applied to the heated volume. Non-Maxwellian EDFs due to thermal transport and the return current will lead to significant changes in the scattered light spectrum as compared to predictions based on a Maxwellian distribution. In hot ICF related plasmas, the wavelength of plasma fluctuations that can be probed by scattering of the pump at the  $\lambda_0$  wavelength is much shorter than the characteristic collisional mean free path, and therefore, the standard collisionless dynamical form factor<sup>26</sup>  $S(\vec{k}, \omega)$  can be employed in the calculations of the TS cross-section. The collisionless  $S(\vec{k}, \omega)$  reads

$$S(\vec{k}, \omega) = \frac{2\pi}{k} \frac{[\bar{f}_e |1 + \chi_i|^2 + Z\bar{f}_i |\chi_e|^2]}{|1 + \chi_e + \chi_i|^2}, \quad (18)$$

where  $\bar{f}_\alpha = \bar{f}_\alpha(\omega/k)$  is the distribution function projected onto  $\vec{k}$  and  $\chi_\alpha = \chi_\alpha(\omega, \vec{k})$  is the susceptibility for species  $\alpha = e, i$ . In this proposed TS experiment, the  $\vec{k}$ -vector is defined by the geometry of the scattering process,  $\vec{k} = \vec{k}_s - \vec{k}_0$  (satisfying  $\omega = \omega_s - \omega_0$ ), where  $k_{0,s} = 2\pi/\lambda_{0,s}$  and  $\omega_{0,s}$  are the wave number and frequency of the pump (0) and scattered (s) light waves. In experiments, the angle  $\phi$  between  $\vec{k}_0$  and  $\vec{k}_s$  is typically fixed, but the magnitude of  $k_s$  is changed as different frequencies (wavelengths  $\lambda_s$ ) are examined in the scattered light spectrum. It is customary to plot  $S(\vec{k}, \omega)$  as a function of  $\lambda_s$ , and this will be done in the following.

Figure 8 illustrates the geometry of the proposed TS experiment. The scattered wave vector  $\vec{k}_s$  is shown in two cases, labeled 1 and 2: (1)  $\vec{k} = \vec{k}_1$  is approximately antiparallel to  $\vec{\nabla}T_e$ , such that  $\vec{k}_1 = \vec{k}_0 - \vec{k}_{s1}$  and the scattered light is red-shifted (red arrow), and (2)  $\vec{k} = \vec{k}_2$  is approximately parallel to  $\vec{\nabla}T_e$ , such that  $\vec{k}_2 = \vec{k}_{s2} - \vec{k}_0$  and the scattered light is blue-shifted (blue arrow). For scattering from ion acoustic fluctuations, one has  $k_s \simeq k_0$ , while for

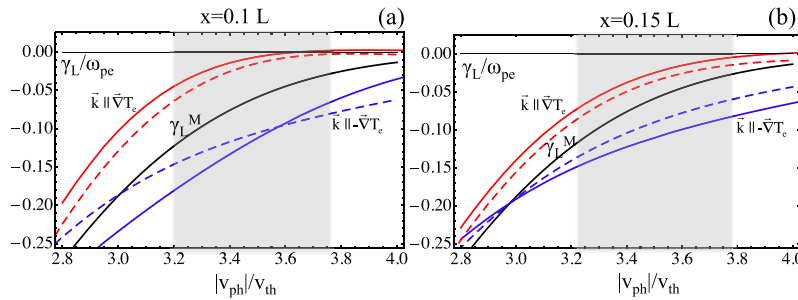


FIG. 7. Comparisons of the Landau damping coefficient  $\gamma_L$  calculated from theory given by Eq. (17) (dashed lines) and oshun simulations (solid red and blue lines) using  $N_h = 15$ , using EDFs from the case shown in Fig. 1 sampled at (a)  $x = 0.1L$  and (b)  $x = 0.15L$ . Landau damping for a Maxwellian EDF is also shown (solid black line).

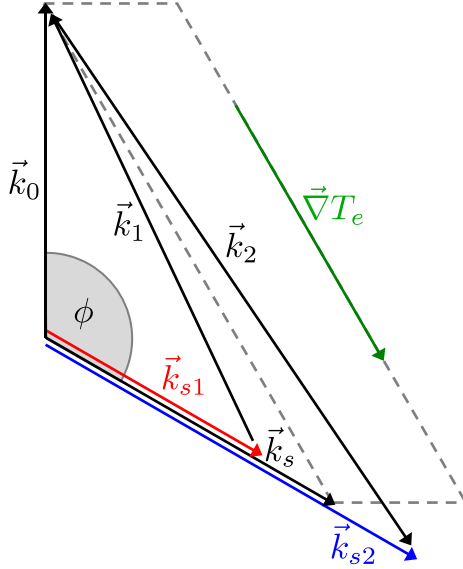


FIG. 8. Geometry of the proposed Thomson scattering measurement. By varying the scattered light wavenumber  $k_s$  for fixed angle  $\phi$  relative to the pump vector  $\vec{k}_0$ , different orientations of plasma waves (wavevector  $\vec{k}$ ) relative to the thermal gradient are probed. Both the redshift case  $\vec{k} = \vec{k}_1 = \vec{k}_0 - \vec{k}_{s1}$  and blueshift case  $\vec{k} = \vec{k}_2 = \vec{k}_2 - \vec{k}_0$  are shown.

scattering from electron plasma waves, this relation does not hold. In the following analysis, we assume for simplicity that  $\vec{k}$  is always either parallel or anti-parallel to  $\nabla T_e$ . While this assumption may be removed, the impact of this assumption is typically small and may be below the experimental resolution.

Consider first the temperature profile from Fig. 5 and respective EDF at  $x = 0.1L$ . This example is characterized by a weak temperature gradient corresponding to  $\delta_T = 0.007$ . Using the EDF obtained from OSHUN ( $N_h = 15$  approximation) in Eq. (18), we obtain  $S(\vec{k}, \omega)$  and compare to form factors obtained using both a Maxwellian EDF and the SH distribution function. The results are shown in Fig. 9 in the low-frequency range of ion acoustic fluctuations and in Fig. 10 for higher-frequency Langmuir wave fluctuations.

In Figs. 9 and 10,  $\omega_p S$  is plotted as a function of the wavelength shift between the scattered light and the pump,  $\lambda_s - \lambda_0$ . The frequency  $\omega$  in Eq. (18) is defined by the frequency difference between  $\omega_0 = ck_0 = 2\pi c/\lambda_0$  and  $\omega_s = ck_s = 2\pi c/\lambda_s$ . In Fig. 9, the angle between  $\vec{k}_s$  and  $\vec{k}_0$  is  $120^\circ$  and  $k\lambda_D = 0.34$  (more precisely,  $k\lambda_D = 0.34$  is achieved only for  $k_s = k_0$ , but varies little over the range of  $\lambda_s - \lambda_0$  in Fig. 9). For Langmuir wave fluctuations (Fig. 10),  $k\lambda_D$  varies between 0.44 at  $\lambda_s - \lambda_0 = -1200 \text{ \AA}$  and 0.27 at  $\lambda_s - \lambda_0 = 2250 \text{ \AA}$ .

The asymmetry between the red- and blue-shifted ion acoustic peaks [Figs. 9(a) and 9(b), respectively] is a well-known effect of the return current of slow electrons. In Fig. 9(a), the  $\vec{k}$ -vector of fluctuations points along the background temperature gradient,  $\vec{k} \parallel \nabla T_e$ , while in Fig. 9(b),  $\vec{k} \perp \nabla T_e$ . In addition to the heat flow and the temperature gradient, the important parameter here is the ion Landau damping given

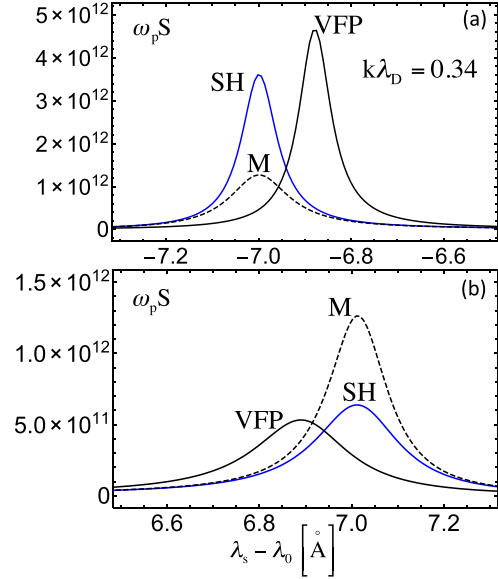


FIG. 9. Dynamical form factor calculated using Eq. (18) at ion acoustic wavelengths. The plasma parameters are those of Fig. 5, sampled at  $x = 0.1L$ . The dashed lines correspond to a Maxwellian (M) EDF. The SH curves (solid blue lines) are calculated using SH distribution function  $f = f_M + f_i$  [cf. Eq. (3)] using  $\delta_T = 0.007$ . VFP curves (solid black line) are calculated using EDFs from oshun simulations where  $N_h = 15$ . The panel (a) shows blue-shifted spectra in the TS spectrum for  $\vec{k} \parallel \nabla T_e$  and the panel (b) shows red-shifted spectra for  $\vec{k} \perp \nabla T_e$ .

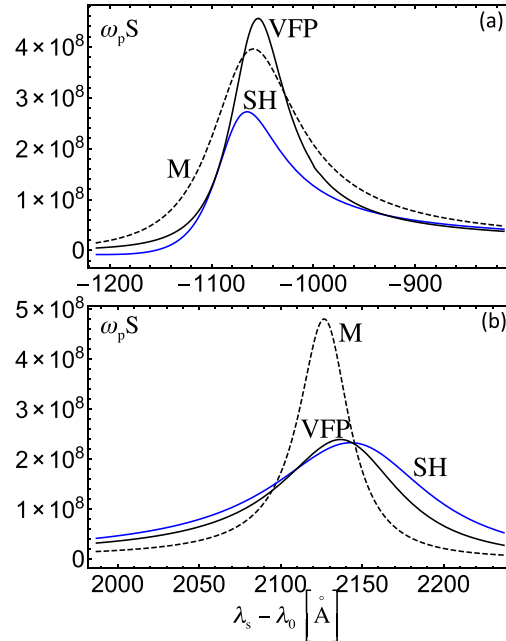


FIG. 10. As in Fig. 9, but for Langmuir waves.

by a Maxwellian ion distribution function and the ion temperature (here,  $T_i = 1500$  eV,  $T_e = 2375$  eV, and  $Z = 10$ ). For  $ZT_e/T_i \gg 1$ , the temperature gradient can drive an ion acoustic instability<sup>27,28</sup> resulting in the growth of ion acoustic waves propagating along the temperature gradient [red-shifted peaks in Fig. 9(a)]. Note that the form factors in Fig. 9 that are calculated using Maxwellian distribution functions (M, black dashed line) are symmetric for both directions of  $\vec{k}$ .

The asymmetry of the SH results (solid blue line) is consistent with the electron damping (or growth) rate of ion acoustic waves calculated using the anisotropic distribution given by Eq. (3). From, e.g., Eq. (12) of Ref. 28, one has

$$\gamma_e^{SH}(k) = \frac{\gamma_0 k \lambda_D}{(1 + k^2 \lambda_D^2)^2} \left[ -1 \pm \frac{3}{2} \left( \frac{k v_{th}}{\omega_{IAW}} \right) \delta_T \right], \quad (19)$$

where  $\gamma_0 = \sqrt{\pi/8} (\omega_{pi}^2 / \omega_{pe})$ ,  $\omega_{IAW}$  is the ion acoustic wave frequency, “+” corresponds to  $k \parallel \nabla T_e$ , and “−” corresponds to  $k \parallel -\nabla T_e$ .

In Fig. 9(a), the narrowing and increased peak height corresponds to a *reduction* in ion acoustic wave damping relative to a Maxwellian distribution, while in Fig. 9(b), the broadening and reduced peak height corresponds to an *increase* in ion acoustic wave damping. Note that in addition to the changes in peak heights, results of OSHUN simulations (VFP, solid black line) show frequency shifts that result in slightly different locations of the two resonances. While the height differences between the M, SH, and VFP curves could be easily measurable in experiments, these frequency shifts are unlikely to be resolved.

These potential resolution problems are less significant for the Langmuir wave spectra shown in Fig. 10 for the same set of parameters and the temperature profile of Fig. 5. One may gain insight into the Maxwellian and OSHUN results for the form factors by comparing them with Landau damping coefficient of Fig. 6. Note that we need to account for the range of wave numbers defined by the geometry of the TS measurement that are probed in Fig. 10(a), i.e.,  $0.4 \leq k \lambda_D \leq 0.44$ , that corresponds to  $2.85 \leq |v_{ph}|/v_{th} \leq 3.05$  (for  $k \parallel \nabla T_e$ ) and in Fig. 10(b),  $0.27 \leq k \lambda_D \leq 0.28$ , that corresponds to  $3.96 \leq |v_{ph}|/v_{th} \leq 4.02$  (for  $k \parallel -\nabla T_e$ ).

The red-shifted VFP peak in Fig. 9(a) is enhanced above the Maxwellian peak, consistent with Fig. 6. The SH result deviates significantly from the VFP curve, illustrating the high sensitivity of our results to details of the EDF, particularly in the regime of relatively small velocities of resonant electrons. Similar to the low frequency spectra in Fig. 9(a), the red-shifted peak VFP with  $k \parallel \nabla T_e$  is enhanced in Fig. 10(a). There is much better agreement between SH and VFP results at higher phase velocities in Fig. 10(b) for the spectra corresponding to the enhanced damping and  $k \parallel -\nabla T_e$ .

For the simulation case corresponding to Fig. 1 (and EDFs shown in Fig. 2),  $S(\vec{k}, \omega)$  is shown in Fig. 11 in the low-frequency range of ion acoustic fluctuations and in Fig. 12 for Langmuir wave fluctuations. The geometry of the TS experiment is unchanged from Figs. 9 and 10. Here,  $T_i = 1000$  eV,  $T_e = 2315$  eV, and  $Z = 2$ . Due to the small value of  $ZT_e/T_i = 4.6$ , the ion Landau damping of ion

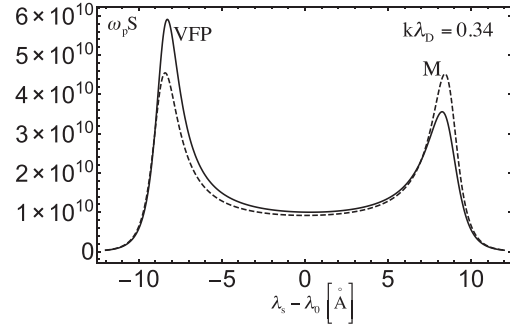


FIG. 11. As in Fig. 9, but using parameters taken from the case shown in Fig. 1 ( $Z = 2$ ,  $N_h = 15$ ,  $x = 0.1L$ ,  $\delta_T = 0.035$ ).

acoustic waves is large and prevents the return current instability from developing. As a result, differences in peak heights are small in Fig. 11 despite the relatively large value of  $\delta_T = 0.035$ . Results for the SH approximation are not shown since this value of  $\delta_T$  lies far outside the range of validity of the SH approximation (and the  $N_h = 2$  oshun simulations), resulting in a change of sign of the Langmuir wave Landau damping coefficient. Again, results for  $S(\vec{k}, \omega)$  in the Langmuir wave regime (Fig. 12) are consistent with Fig. 7(a).

TS has been used previously to investigate thermal transport in laser produced plasmas, either by spatially resolved measurements of the thermal front propagation<sup>29</sup> or by interpreting ion acoustic scattering spectra by means of non-Maxwellian EDFs due to the thermal transport.<sup>30</sup> The novelty of our proposed TS experiment follows from

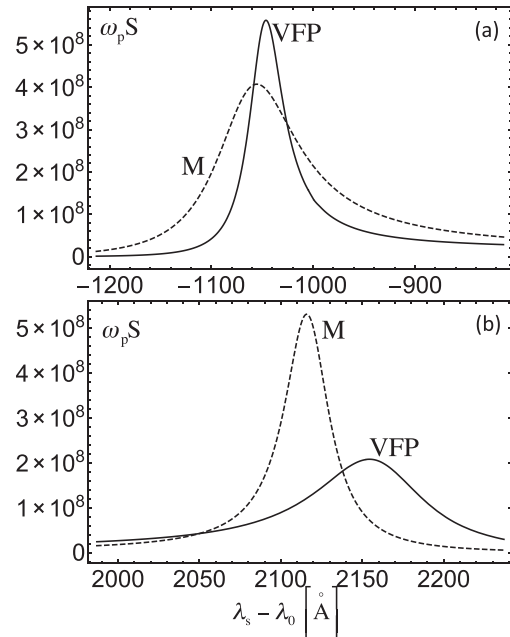


FIG. 12. As in Fig. 10, but using parameters taken from the case shown in Fig. 1 ( $Z = 2$ ,  $N_h = 15$ ,  $x = 0.1L$ ,  $\delta_T = 0.035$ ).

exploiting the asymmetry between Langmuir wave peaks present in Figs. 10 and 12 that arises due to resonance between heat-carrying electrons and Langmuir waves. This feature of the TS cross section is particularly significant in hot ICF-relevant plasmas.

## V. SUMMARY AND CONCLUSIONS

Non-Maxwellian EDFs are ubiquitous in experimental plasmas that are heated non-uniformly and maintain inhomogeneous temperature profiles. For a given temperature gradient, classical transport theories<sup>1,2</sup> describe modifications of the EDF up to the first order in the parameter  $\delta_T = \lambda_{ei}/L_T$ . In these models, the perturbed EDFs describe deviations from a local Maxwellian due to the heat carrying electrons with velocities in the range  $3 \lesssim v/v_{th} \lesssim 4$ .  $\delta_T$  must therefore be small, on the order of  $10^{-2}$  or smaller, for these perturbative solutions of the VFP equation to be valid.<sup>1,2</sup> For sufficiently high  $v$ , any truncation in the expansion of the EDF will cease to be valid, but when this truncation occurs after only the first anisotropic component of the EDF, the assumption that  $|f_1|/f_0$  is small is frequently incorrect for  $v/v_{th} \gtrsim 3$  in ICF-relevant plasmas and a calculation of the linear plasma response under this framework will not be physically meaningful.

In our simulations, typical of ICF plasmas where  $T_e = 2 - 4$  keV and  $n_e = 10^{21} \text{ cm}^{-3}$ , the linear response of the plasma to Langmuir waves driven by stimulated Raman scattering is significantly modified by heat-carrying electrons resonant with the Langmuir waves: damping is reduced for waves propagating parallel to the thermal gradient and enhanced for waves propagating antiparallel to the gradient. In VFP simulations, a high number of harmonics (15) in the expansion of the EDF were typically required to reach a converged solution.

In addition to the loss of laser energy due to SRS, two-plasmon decay (TPD) of laser light (relevant to both direct and indirect-drive ICF experiments) may also lead to the absorption of laser energy at densities lower than intended and generate very fast electrons.<sup>31</sup> It has been shown that TPD can be mitigated by the damping of Langmuir and ion acoustic waves,<sup>32</sup> and we expect therefore that the evolution of TPD will be sensitive to modifications of the EDF by heat flow. Observations of SRS spectra<sup>33–35</sup> from plasmas with peak density above  $n_c/4$  often presented a “gap” in SRS reflectivity corresponding to densities between some minimum value  $n_{min}$  and  $n_c/4$ . The effect of a background temperature gradient and increased damping on Langmuir waves could be a factor contributing to these observations. Similarly, in the novel method to ignite thermonuclear fuel by shock ignition,<sup>36</sup> control of SRS and its timing is critical for the scheme to work.<sup>37</sup>

Another important result of our paper is a new approximate expression for Landau damping in plasmas with a temperature gradient, derived from a theoretical model of the EDF, given by Eq. (17). These theoretical EDFs have been derived to second order in  $\delta_T$  (and to first order in  $\beta_T$ ). This theory allows for an evolution of the isotropic part of the EDF away from Maxwellian.

Our results suggest the need for including kinetic effects in mainline ICF simulations of laser-plasma interaction and in the post-processing of these results via modified calculations of the threshold conditions and gain coefficients of scattering instabilities.


## ACKNOWLEDGMENTS

We would like to acknowledge useful discussions with Laurent Divol, Pierre Michel, and Ed Williams. This work was partly supported the Natural Sciences and Engineering Research Council of Canada and by the Russian Foundation for Basic Research. This work was partly performed under the auspices of the U.S. Department of Energy (DOE) by Lawrence Livermore National Laboratory under Contract No. DE-AC52-07NA27344, by the DOE Office of Science, Fusion Energy Science under FWP 100182, and funded by the Laboratory Research and Development Program at LLNL under project tracking code 15-ERD-038. Support was also provided in part from DOE under Grant Nos. DE-NA0001833 and DE-FC02-04ER54789.

- <sup>1</sup>L. Spitzer, Jr. and R. Härm, *Phys. Rev.* **89**, 977 (1953).
- <sup>2</sup>S. I. Braginskii, in *Review of Plasma Physics*, edited by M. A. Leontovich (Consultants Bureau, New York, 1965), Vol. 1, p. 205.
- <sup>3</sup>S. Brunner and E. Valeo, *Phys. Plasmas* **9**, 923 (2002).
- <sup>4</sup>A. R. Bell, R. G. Evans, and P. J. Nicholas, *Phys. Rev. Lett.* **46**, 243 (1981).
- <sup>5</sup>J.-P. Matte and J. Virmont, *Phys. Rev. Lett.* **49**, 1936 (1982).
- <sup>6</sup>A. R. Bell, *Phys. Fluids* **26**, 279 (1983).
- <sup>7</sup>J. F. Luciani, P. Mora, and J. Virmont, *Phys. Rev. Lett.* **51**, 1664 (1983).
- <sup>8</sup>J. R. Albritton, E. A. Williams, I. B. Bernstein, and K. P. Swartz, *Phys. Rev. Lett.* **57**, 1887 (1986).
- <sup>9</sup>V. Yu. Bychenkov, W. Rozmus, V. T. Tikhonchuk, and A. V. Brantov, *Phys. Rev. Lett.* **75**, 4405 (1995).
- <sup>10</sup>D. E. Hinkel, M. D. Rosen, E. A. Williams, A. B. Langdon, C. H. Still, D. A. Callahan, J. D. Moody, P. A. Michel, R. P. J. Town, R. A. London, and S. H. Langer, *Phys. Plasmas* **18**, 056312 (2011).
- <sup>11</sup>P. Michel, L. Divol, E. L. Dewald, J. L. Milovich, M. Hohenberger, O. S. Jones, L. Berzak Hopkins, R. L. Berger, W. L. Krueer, and J. D. Moody, *Phys. Rev. Lett.* **115**, 055003 (2015).
- <sup>12</sup>S. Atzeni and J. Meyer-Ter-Vehn, *The Physics of Inertial Fusion* (Oxford University Press, Oxford, 2004).
- <sup>13</sup>B. Dubroca, J.-L. Feugeas, and M. Frank, *Eur. Phys. J. D* **60**, 301 (2010).
- <sup>14</sup>M. D. Rosen, H. A. Scott, D. E. Hinkel, E. A. Williams, D. A. Callahan, R. P. J. Town, L. Divol, P. A. Michel, W. L. Krueer, L. J. Suter, R. A. London, J. A. Harte, and G. B. Zimmerman, *High Energy Density Phys.* **7**, 180 (2011).
- <sup>15</sup>J. D. Moody, D. J. Strozzi, L. Divol, P. Michel, H. F. Robey, S. LePape, J. Ralph, J. S. Ross, S. H. Glenzer, R. K. Kirkwood, O. L. Landen, B. J. MacGowan, A. Nikroo, and E. A. Williams, *Phys. Rev. Lett.* **111**, 025001 (2013).
- <sup>16</sup>D. Del Sorbo, J.-L. Feugeas, Ph. Nicolaï, M. Olazabal-Loumé, B. Dubroca, S. Guisset, M. Touati, and V. Tikhonchuk, *Phys. Plasmas* **22**, 082706 (2015).
- <sup>17</sup>M. Tzoufras, A. R. Bell, P. A. Norreys, and F. S. Tsung, *J. Comput. Phys.* **230**, 6475 (2011).
- <sup>18</sup>A. Marocchino, M. Tzoufras, S. Atzeni, A. Schiavi, Ph. D. Nikolai, J. Mallet, V. T. Tikhonchuk, and J.-L. Feugeas, *Phys. Plasmas* **20**, 022702 (2013).
- <sup>19</sup>M. Tzoufras, A. Tableman, F. S. Tsung, and A. R. Bell, *Phys. Plasmas* **20**, 056303 (2013).
- <sup>20</sup>O. V. Batishchev, V. Yu. Bychenkov, F. Detering, W. Rozmus, R. Sydora, C. E. Capjack, and V. N. Novikov, *Phys. Plasmas* **9**, 2302 (2002).
- <sup>21</sup>A. F. Aleksandrov, L. S. Bogdankevich, and A. A. Rukhadze, *Principles of Plasma Electrodynamics* (Springer, Berlin, 1984).
- <sup>22</sup>S. Ichimaru, *Statistical Plasma Physics, Vol. 1: Basic Principles* (Addison-Wesley, Reading, 1992).
- <sup>23</sup>A. V. Brantov, V. Yu. Bychenkov, V. T. Tikhonchuk, and W. Rozmus, *JETP* **83**, 716 (1996).

- <sup>24</sup>A. V. Brantov, V. Yu. Bychenkov, V. T. Tikhonchuk, and W. Rozmus, *Phys. Plasmas* **5**, 2742 (1998).
- <sup>25</sup>R. J. Hennen, S. X. Hu, J. Katz, D. H. Froula, and W. Rozmus, *Bull. Am. Phys. Soc.* **60**, 166 (2015).
- <sup>26</sup>D. H. Froula, S. H. Glenzer, N. C. Luhmann, Jr., and J. Sheffield, *Plasma Scattering of Electromagnetic Radiation: Theory and Measurement Techniques* (Elsevier, Amsterdam, 2011).
- <sup>27</sup>V. T. Tikhonchuk, W. Rozmus, V. Yu. Bychenkov, C. E. Capjack, and E. Epperlein, *Phys. Plasmas* **2**, 4169 (1995).
- <sup>28</sup>A. V. Brantov, V. Yu. Bychenkov, and W. Rozmus, *Phys. Plasmas* **8**, 3558 (2001).
- <sup>29</sup>G. Gregori, S. H. Glenzer, J. Knight, C. Niemann, D. Price, D. H. Froula, M. J. Edwards, R. P. J. Town, A. Brantov, W. Rozmus, and V. Yu. Bychenkov, *Phys. Rev. Lett.* **92**, 205006 (2004).
- <sup>30</sup>J. Hawreliak, D. M. Chambers, S. H. Glenzer, A. Gouveia, R. J. Kingham, R. S. Marjoribanks, P. A. Pinto, O. Renner, P. Soundhauss, S. Topping, E. Wolfrum, P. E. Young, and J. S. Wark, *J. Phys. B* **37**, 1541 (2004).
- <sup>31</sup>W. Seka, D. H. Edgell, J. F. Myatt, A. V. Maximov, R. W. Short, V. N. Goncharov, and H. A. Baldis, *Phys. Plasmas* **16**, 052701 (2009).
- <sup>32</sup>J. F. Myatt, H. X. Vu, D. F. DuBois, D. A. Russell, J. Zhang, R. W. Short, and A. V. Maximov, *Phys. Plasmas* **20**, 052705 (2013).
- <sup>33</sup>H. Figueroa, C. Joshi, and C. E. Clayton, *Phys. Fluids* **30**, 586 (1987).
- <sup>34</sup>R. E. Turner, *Phys. Fluids* **26**, 579 (1983).
- <sup>35</sup>D. W. Phillion, *Phys. Fluids* **25**, 1434 (1982).
- <sup>36</sup>R. Betti, C. D. Zhou, K. S. Anderson, L. J. Perkins, W. Theobald, and A. A. Solodov, *Phys. Rev. Lett.* **98**, 155001 (2007).
- <sup>37</sup>O. Klimo and V. T. Tikhonchuk, *Plasma Phys. Controlled Fusion* **55**, 095002 (2013).

# Validation of OSHUN against collisionless and collisional plasma physics

Archis S Joglekar<sup>1,2</sup> , Benjamin J Winjum<sup>1,2</sup>, Adam Tableman<sup>1,2</sup>, Han Wen<sup>1,2</sup>, Michail Tzoufras<sup>3</sup> and Warren B Mori<sup>1,2</sup>

<sup>1</sup> Department of Physics and Astronomy, University of California—Los Angeles, Los Angeles, CA, United States of America

<sup>2</sup> Electrical Engineering Department, University of California—Los Angeles, Los Angeles, CA, United States of America

<sup>3</sup> Spin Transfer Technologies, Inc., Fremont, CA, United States of America

E-mail: [archis@ucla.edu](mailto:archis@ucla.edu)

Received 31 January 2018, revised 22 March 2018

Accepted for publication 26 March 2018

Published 4 May 2018



CrossMark

## Abstract

OSHUN, a Vlasov–Fokker–Planck–Maxwell code, is successfully validated against a few collisionless and collisional plasma physics test problems. In OSHUN, the distribution function is expanded in velocity (or momentum) space into an arbitrary number of spherical harmonics. OSHUN is shown to accurately recover Landau damping by including a relatively small number of spherical harmonics for an initial value problem as well as a driven plasma wave. The Fokker–Planck operator (both electron–electron and electron–ion) is shown to be able to reproduce the Epperlein–Haines heat-flow coefficient in warm, un-magnetized and magnetized plasmas with varying degrees of ionization. These collisionless and collisional problems are of disparate time- and length- scales ranging from femtoseconds to nanoseconds, and from microns to millimeters. OSHUN’s ability to handle these test problems successfully illustrates the power of the spherical-harmonic expansion when studying both weakly-collisional and collisional plasmas relevant to high-energy-density physics. The implementation and use of new features such as a ponderomotive wave driver and an implicit collision operator is also discussed.

Keywords: Vlasov–Fokker–Planck, kinetic modeling, spherical harmonic, cartesian tensor

(Some figures may appear in colour only in the online journal)

Plasma physics phenomenon can occur over disparate time- and length-scales as well as plasma densities and temperatures. However, plasmas with the same number of particles per Debye sphere,  $N_D = (4/3)\pi n\lambda_D^3$ , behave similarly in terms of normalized parameters. In particular, the ratio of the electron-ion collision frequency to the plasma frequency is proportional to  $N_D^{-1} \log N_D$ . For many plasmas,  $N_D$  is so large that collisions are unimportant. However, in high-energy-density plasmas (HEDP),  $N_D$  can range from  $10^2$  to  $10^4$  so that both collisionless and collisional phenomenon occur simultaneously over time-scales of interest.

In the presence of sufficient collisions, the electron distribution function in a plasma is nearly spherically symmetric in velocity space. In weakly collisional plasmas, the effect of Coulomb collisions is to attempt to limit the perturbation of the

distribution away from a spherical distribution function and to bring the isotropic part close to a Maxwellian. This naturally motivates the use of a spherical harmonic decomposition for the electron distribution function. Historically, a Cartesian tensor expansion, which has been shown to be equivalent to a spherical harmonic decomposition [1–3], has been employed for this purpose. The Cartesian tensor expansion of the electron distribution function,  $f(\mathbf{x}, \mathbf{v})$ , is given by

$$f(\mathbf{x}, \mathbf{v}) = f_0(\mathbf{x}, v) + \frac{\mathbf{v}}{v} \cdot \mathbf{f}_1(\mathbf{x}, v) + \frac{\mathbf{v}\mathbf{v}}{v^2} : \mathbf{f}_2(\mathbf{x}, v) + \dots \quad (1)$$

The expansion-based technique was first used to study kinetic effects from nearly-Maxwellian plasmas. In the presence of steep temperature gradients, non-local heat transport arises, and the description of heat flow requires a kinetic



treatment. Various authors [4–7] showed that the relevant kinetic information is contained in the first two terms of the expanded distribution function given by equation (1), and used this approach to perform self-consistent calculations of non-local heat flow.

To improve upon the work of Braginskii [8], Epperlein and Haines also used the expansion technique, up to the first order, to compute the electron transport coefficients for various ionization states and magnetizations [9]. Epperlein [10, 11] provided details of the numerical implementation of the equations in multiple spatial dimensions, provided an improvement for the Fokker–Planck operator [12] and used the code to study non-local effects in filamentation [13], high-intensity irradiation [14], and ion-acoustic waves [15]. A modification to the collision operator that applies to the zeroth order term enabled the modeling of inverse-bremsstrahlung heating while retaining effects such as the development of a super-Maxwellian electron distribution function [16, 17].

With an increased availability of high-performance computing, the technique has since been specialized for certain applications. Fully implicit algorithms that solve for the first three terms in equation (1) have been developed [18, 19]. These excel at calculating transport problems in nearly-Maxwellian, magnetized plasmas over long time-scales [20, 21].

As noted above, complementary to the Cartesian tensor expansion is an expansion in spherical harmonics. Such an expansion is more appropriate for distribution functions which are further away from a Maxwellian such as arises for weakly collisional plasmas and in laser-plasma interactions. In [22–25], a code called KALOS was described which employed the spherical harmonic expansion to describe a cold, collisional background plasma together with the evolution of fast electrons which are collisionless.

Here, we present results using the code, OSHUN, which is a fully general code that follows the same expansion formalism by expanding the velocity distribution function into an arbitrary number of spherical harmonics, that includes the full Maxwell solver or an implicit field solver, and that includes a non-relativistic electron–electron and electron-ion collision operator that is linearized in the self-interaction of the spherical harmonics, but is fully nonlinear in the zeroth harmonic. It is the first software that implemented the spherical harmonic expansion algorithm in parallel. It was developed in C++ with a framework conducive for high performance and runs on personal as well as national leadership class machines. It has shown the ability to be able to model collisionless physics [26] when many terms in the expansion are used in addition to the fully explicit solver. OSHUN has also been shown to be able to study nonlocal heat transport problems when an implicit field solver is used [27], to recover kinetic features of inverse bremsstrahlung heating [16]. Using the new implicit solver enabled the self-consistent calculation of electron distribution functions in the presence of very steep temperature gradients that require more than two terms in the spherical harmonic expansion [28].

In addition, non-local transport models based on including only the first two terms in the spherical harmonic expansion and

an implicit electric field solver have been implemented and benchmarked in radiation hydro-dynamics codes [29–32].

Other implementations of the spherical harmonic expansion technique include the ability to model electrons with the explicit formalism while in the presence of strong hydrodynamic flow by the use of an alternate-rest-frame equation set [33]. Finally, the expansion technique has also been used to model relativistic electron transport within a hybrid framework [34]. More details on the development and use of expansion-based Vlasov–Fokker–Planck–Maxwell (VFPM) codes towards HEDP applications is given by Thomas *et al* [35].

Here, we focus on the validation of both the fully explicit and the implicit field solve algorithms for the advance of the Vlasov equation in OSHUN. We expand upon the work in [27] by comparing collisionless Landau damping from OSHUN to theory. Furthermore, we also emphasize that the electron–electron- and electron-ion- Fokker–Planck collision terms in OSHUN agree with theoretical calculations of transport coefficients. Reproducing the transport coefficients requires evolution over long time-scales. This is accomplished by using the implicit scheme in OSHUN for solving the fields [27]<sup>4</sup>. By presenting results of both collisionless and collisional regimes, we aim to show that OSHUN offers a unique capability to study, in detail, the dynamics between self-organizing forces and velocity-dependent collisions, in plasmas ranging from nearly-collisionless to strongly collisional.

## 1. OSHUN

The expansion technique implemented in OSHUN rests on the assumption that the distribution function,  $f(\mathbf{x}, \mathbf{v})$ , can be represented by a reasonable number of spherical harmonics such that  $f(\mathbf{x}, \mathbf{v})$  is given by

$$f(\mathbf{x}, \mathbf{v}) = \sum_{l=0}^{N_l} \sum_{m=-N_m}^{N_m} f_l^m(\mathbf{x}, v, t) P_l^m(\cos \theta) e^{im\phi}, \quad (2)$$

where  $N_l, N_m$ , are the number of terms in the expansion. In equation (2),  $f_l^m$  is the coefficient (depends on position, magnitude of  $v$ , and time) of each harmonic in the expansion of the distribution function,  $P_l^m(\cos \theta)$  is the associated Legendre polynomial for the  $f_l^m$  term of the expansion. Typically, the angle  $\theta$  is defined with respect to the  $\hat{z}$  axis. However, in OSHUN it is with respect to the  $\hat{x}$  axis. Therefore, in 1D geometry, gradients only exist in the  $\hat{x}$ . We note that OSHUN has the option for using a spherical harmonic expansion for  $f(\mathbf{x}, \mathbf{p})$  coupled with a relativistically correct Vlasov equation. However, the collision operators are still non-relativistic.  $f_0^0$  is the isotropic component of the distribution, while  $f_1^m$  carries the first order vector information. Consequently, the density, temperature, and current are moments of the individual terms in the spherical expansion

<sup>4</sup> To perform these tests, a ponderomotive driver and implicit  $f_0^0$  collision operator was implemented in addition to the previously published algorithms in OSHUN [26, 27]. The new algorithms are discussed in the [appendix](#).

of the distribution function. The density is given by  $n = 4\pi \sum v^2 f_0^0 \Delta v$ , the temperature by  $T = 2\pi \sum v^4 f_0^0 \Delta v$ , and the current (in  $\hat{x}$ ) by  $j_x = (4/3)\pi e \sum v^3 f_1^0 \Delta v$ . The distribution function information is only stored, and computed, for the velocity amplitude (speed),  $v$ .

The equations, algorithms, and normalizations used in OSHUN have been described previously [22, 26, 27]. The equations are normalized to units defined by the speed of light,  $c$ , the electron mass,  $m$ , and charge,  $e$ , an arbitrary time-scale,  $\omega_0^{-1}$  where the density is normalized as  $[\omega_{p0}/\omega_0]^2$  where  $\omega_{p0}$  is the plasma frequency defined at a location where the density is  $n_0$ . An immobile, uniform profile of ions provides a neutralizing background. OSHUN is parallelized by spatial domain decomposition using MPI.

In the collisionless regime, OSHUN can resolve electron plasma wave oscillations that occur on the inertial length scale,  $\bar{\lambda} = c/\omega_p$ . For HED laboratory plasmas, this regime typically represents time and length scales of  $10^{-16}$  s and 10 nm. In the collisional regime, where phenomenon occurring on the plasma period time-scale are typically not of interest, OSHUN can step over multiple plasma periods using an implicit solver for the fields. The collision operator resolves collisional time-scale behavior and the time step needs to be chosen to resolve this as well. In HED plasmas, this is ps time-scale behavior occurring over 10  $\mu\text{m}$  length-scales and the length of the simulation in time and space are ns and mm respectively. These parameters describe the need for multi-scale modeling required in HEDP, or in describing plasma with density satisfying  $100 < N_D < 10000$ , e.g. the solar corona. This paper demonstrates the ability of OSHUN to span these scales. This is done by testing OSHUN against well-known plasma physics problems in the collisionless and collisional regime, where essentially each term in the non-relativistic Vlasov–Fokker–Planck equation is tested.

In this paper, we describe the ability for OSHUN to accurately reproduce the results for the linear dispersion relation for electrostatic (ES) waves in plasma. This includes carefully comparing results from OSHUN against the theoretical calculations on collisionless, i.e., Landau [36], damping of an electron plasma wave (EPW). We also test the collisional module against previous calculations in Epperlein and Haines [9] for the steady-state heat-flow coefficient for various ionization states and magnetizations. This test also verifies the  $\mathbf{v} \times \mathbf{B}$  term in the Vlasov equation. Last, we discuss newly implemented features in OSHUN that broaden its capabilities.

## 2. Testing collisionless physics

The following subsections discuss the retrieval of the real and imaginary parts of the dispersion relation ES waves in an unmagnetized plasma (electron plasma waves, EPW, for fixed ions). Although not presented here we have also investigated EM waves and found agreement with theory (EM waves do not damp due to wave-particle interactions). The dispersion relations are analytically calculated by linearizing the Vlasov equation and combining it with Maxwell's equations.

Therefore, testing against the dispersion relation enables us to test OSHUN's electric and magnetic field advance and spatial advection terms. The time-advance set of equations used here is given by

$$\begin{aligned} \partial_t f &= (\mathbf{E} + \mathbf{v} \times \mathbf{B}) \cdot \partial_v f \\ \partial_t f &= \mathbf{v} \cdot \partial_x f \\ \partial_t \mathbf{E} &= \mu_0 \mathbf{j} + \nabla \times \mathbf{B} \\ \partial_t \mathbf{B} &= \nabla \times \mathbf{E}. \end{aligned} \quad (3)$$

In what follows we only present results for ES waves where in 1D we update the electric field from Ampere's law by setting  $\nabla \times \mathbf{B} = 0$  rather than solving Poisson's equation.

### 2.1. Electron plasma wave dispersion relation

The development of VFP codes, particularly those that use a Cartesian tensor or a spherical harmonic expansion, was driven by the interest in studying behavior in which collisions keep the distribution function nearly symmetric (problems in which only a few terms in the expansions are needed). However, we show here that such a code, OSHUN, can accurately model collisionless, i.e., Landau damping, of EPWs even when only a limited number of harmonics is kept. OSHUN was previously shown to be able to model the two stream instability [26].

### 2.2. Landau damping

To study Landau damping, we excite a wave with a specified wavenumber and then let it evolve (an initial value problem). We then compute the real and imaginary values for the frequency for the chosen wave number based on the kinetic EPW dispersion relation,  $0 = 1 - \frac{1}{2k^2 \lambda_D^2} Z' \left( \frac{\omega}{\sqrt{(2)k v_{th}}} \right)$  where  $Z$  is the plasma dispersion function [37] and  $\lambda_D \equiv v_{th}/\omega_p$  is the Debye length, and  $k$  is the wavenumber of the wave.

We begin by describing a series of simulations for the same wavenumber,  $k\lambda_D$ , but different spatial and velocity space resolution. A sinusoidal single mode plasma wave is generated using an external term in Ampere's law (similar to adding an external force). In these simulations, the plasma density in the simulation is set to 1,  $n(x) = 1$ , such that the normalizing frequency  $\omega_0 = \omega_p$ . The box length is one wavelength long and periodic boundary conditions are used.

The EPW is driven for  $60\omega_0^{-1}$  with  $t_{rise} = t_{fall} = 10\omega_0^{-1}$  and  $I_{flat} = 40\omega_0^{-1}$  and the meaning of these variables are given in the appendix. The drive is given by  $\Delta E_x / \Delta t = a_0(t) \sin(kx - \omega t)$  (recall that the electric field is normalized to  $mc\omega_p/e$ ) where the maximum value of  $a_0 = 10^{-8}$ , and  $k = 7.5$ . Recall that for  $n_0 = 1$ ,  $k$  is normalized to  $\omega_p/c$ . The EPW frequency is given by solving the dispersion relation for  $n(x) = 1$  and  $v_{th}(x) = 0.04c$  which corresponds to  $k\lambda_D = 0.3$ . For  $k\lambda_D = 0.3$  the dispersion relation gives a real frequency of  $\omega = 1.159847$ . We limit the velocity to a maximum value of  $v_{max} = 8v_{th}$  and the box length is  $L = 0.837758c/\omega_p$  which corresponds to one wavelength. Note that  $N_m = 0$  for an EPW,

**Table 1.** Variance in the Landau damping rate percentage error with respect to different numerical discretization parameters. The standard set of parameters used here is  $N_x = 64$ ,  $N_v = 256$ ,  $N_l = 8$ ,  $\Delta t = 0.01$ . The columns distinguish the various parameters. The numerically measured damping rate is always smaller than the theoretical value.

$N_x$	% error	$N_v$	% error	$N_l$	% error	$\Delta t$	% error
16	18.1	64	1.40	4	16.4	0.08	66.3
32	5.13	128	1.49	8	1.54	0.04	1.54
64	1.53	256	1.53	16	1.21	0.02	1.54
128	0.06	512	1.55	32	1.21	0.01	1.54

i.e., for a longitudinal wave there is no coupling between different  $m$  modes.

We vary  $N_x$ ,  $N_v$ ,  $N_l$ , and  $\Delta t$  to quantify the accuracy of the damping rate. Data from these simulations is provided in table 1 and the evolution in time of the amplitude of the wave results is plotted for three of the simulations in figure 1 for which the number of harmonics and time step were kept fixed at  $N_l = 8$  and  $\Delta t = 0.01$  respectively. The damping rate from the simulations is measured as the slope of the amplitude for the first harmonic (red line) in figure 1. The slope corresponding to the damping rate predicted from the dispersion relation is shown as a dashed line. As seen in table 1, the damping rate is found to be most sensitive to the variation of  $N_x$  such that the simulation with  $N_x = 128$ ,  $N_v = 256$ ,  $N_l = 8$ ,  $\Delta t = 0.01$  recovers the Landau damping rate to within 1 percent. However, there are other errors that arise when  $N_v$  or  $N_l$  are decreased. To describe these, we refer to figure 1, where  $k = 0$ ,  $k = 1$ , and  $k = 2$  harmonics are shown for three different simulations.

In figure 1(a), we show data from the spatial-Fourier-transform of the electric field computed in the simulation that shows the best agreement with the Landau damping rate. The magnitude of the  $k = 1$  mode is plotted on the left axis, and the  $k = 0$  and  $k = 2$  modes are plotted on the right axis. The dotted line nearly overlaps the  $k = 1$  mode confirming the accurate reproduction of the Landau damping rate. The  $k = 2$  mode is nearly  $10^{-7}$  smaller than the  $k = 1$  mode suggesting that the signal-to-noise ratio is very small. The  $k = 0$  mode is barely above machine precision levels when the wave driver is on, and collapses to machine precision levels when the driver turns off. Therefore, the need for techniques like divergence cleaning or the removal of  $k = 0$  mode is not necessary in OSHUN.

Data from the test with  $N_x = 16$  is shown in figure 1(b) where the  $k = 1$  mode is underdamped by nearly 15%. Data from the test with  $N_v = 64$  is shown in figure 1(c) where the damping rate shows excellent agreement. However, the simulation shows recurrence effects in  $k = 1$  near  $t = 175\omega_0^{-1}$  that are common to Vlasov methods [38]. For this case with poor resolution in velocity space, the recurrence occurs much earlier for the  $k = 2$  mode.

In figure 2 we show that both the real and imaginary frequencies obtained from OSHUN. For the OSHUN data in this figure, a series of ten simulations  $k\lambda_D$  was varied from 0.1, 0.14, 0.18, 0.22, 0.26, 0.3, 0.34, 0.38, 0.42, 0.46, 0.5. The numerical parameters were chosen to be the ‘standard’ values,  $N_x = 64$ ,  $N_v = 256$ ,  $N_l = 8$ ,  $\Delta t = 0.01$ . The solid curves correspond to the theoretical values. The results show

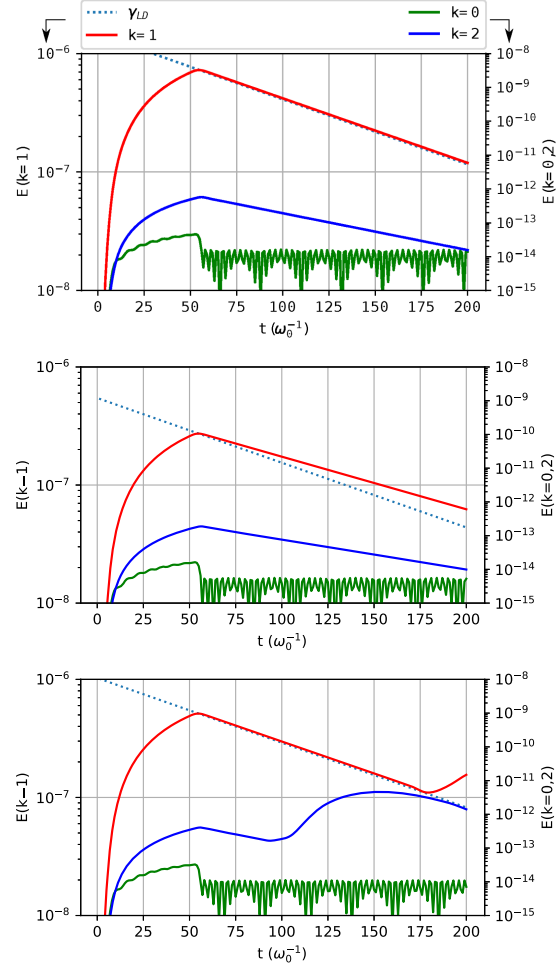


**Figure 1.** An EPW is driven from  $0 - 60\omega_0^{-1}$  after which Landau damping occurs. In the above,  $N_l = 8$  and  $\Delta t = 0.01$ . The  $k = 1$  mode is plotted on the left axis and the  $k = 0$  and 2 modes are plotted on the right. (a) For  $N_x = 128$  and  $N_v = 256$ , we find excellent agreement with the theoretical calculation. For  $N_x = 16$  and  $N_v = 256$  (b), the loss of resolution in  $\hat{x}$  results in a poor calculation, while for  $N_x = 64$  and  $N_v = 64$  (c), the correct damping rate is recovered but recurrence occurs on a very short time-scale.

that OSHUN recovers both the real and imaginary values very accurately when appropriate resolution in real and velocity space is used.

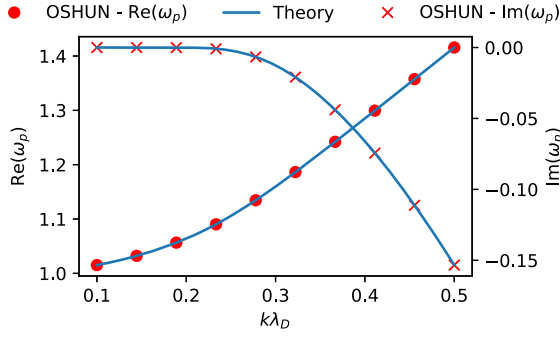


**Figure 2.** The Landau damping rate is reproduced accurately in OSHUN for various  $k\lambda_D$ .

### 3. Testing collisional physics

The Fokker–Planck operator in OSHUN is fully nonlinear for  $f_0^0$  and linearized for  $f_1^m$ . The  $f_1^m$  operator contains the effect of electron-ion collisions. In Epperlein and Haines [9], the authors use the  $f_0^0$ ,  $f_1^0$ , and  $f_1^1$  equations, along with full treatment of electron–electron and electron-ion collisions to calculate the electron transport coefficients for magnetized plasmas for a range of ionization states,  $Z$ . In previous work [27], OSHUN was shown to reproduce the heat flow coefficient for  $Z = 1$  in an unmagnetized plasma with a long temperature gradient-scale-length, and to study non-local heat-flow over shorter gradient-scale-lengths. Here, we further validate the code by reproducing the heat-flow coefficient for heat-flow perpendicular to the magnetic field,  $\kappa_{\perp}$ , for various  $Z$  over a long gradient-scale-length. This offers a robust test of the  $f_0, f_1$  equation set and its Fokker–Planck operator over a collisional time-scale.

#### 3.1. Heat flow coefficient—various $Z$ and $\omega_c\tau$

To calculate the heat flow coefficient,  $\kappa_{\perp}$  for various ionization states,  $Z$ , and magnetic field strengths, a sinusoidal temperature profile is initialized. The simulations use one spatial direction,  $\hat{x}$ , and the magnetic field points in the  $\hat{z}$  direction. The implicit electric field solver [27], and the implicit collision operators described in the appendix, enable time-steps on the order of collision-times. As in the reference calculation [9], only one term in the spherical harmonic expansion is used (and required).  $\kappa_{\perp}(Z)$  is calculated by dividing the gradient of the temperature by the heat flow,  $q = (2/3)\pi\sum v^2 f_1^0 dv$ . For the 1D cases studied here,  $\kappa_{\perp}(Z)$ , is in the  $\hat{x}$  direction which is perpendicular to the applied magnetic field. We examine  $\kappa_x(Z) = \kappa_{\perp}(Z)$  even when there is no magnetic field.

For the following simulations,  $n_0 = 10^{21} \text{ cm}^{-3}$ ,  $v_{th} = 0.07 c$ . A sinusoidal temperature profile is imposed with  $\Delta T/T_0 = 0.01$ . The relevant collisional parameters such as the mean free path and collision frequency are found using the NRL formulary [37]. A uniform profile of immobile ions provides a neutralizing background.

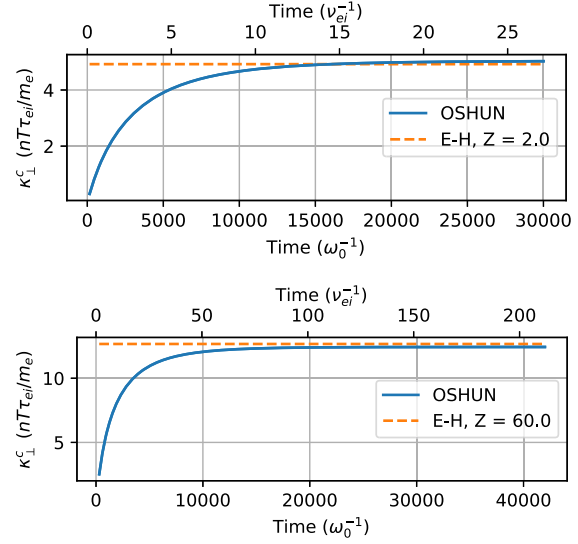


**Figure 3.** The evolution of the heat-flow coefficient in an unmagnetized plasma. It evolves towards the steady-state value computed by Epperlein and Haines [9] for (a)  $Z = 2$ , and (b)  $Z = 60$ . For the low- $Z$  calculation in (a), the off-diagonal components of the  $f_1^m$  electron–electron collision operator are used for greater accuracy. In both cases, we find that the steady-state is reached after  $\mathcal{O}(10)$  collision times.

Large-time-step, and large-spatial-cell calculations are enabled because the collision operators and the electric field solver are implicit. However, some care must be taken when discretizing the grids. When modeling such plasmas in OSHUN using the implicit field solver, one still needs to resolve the collision time, and to some extent, the collisional mean-free-path. In problems such as these, it is typically more intuitive to work in collisional units where the velocity is normalized by the thermal velocity, space normalized by the collisional mean-free-path, and time normalized by the collision time, i.e.  $v_n = v/v_{th}$ ,  $x_n = x/\lambda_{ei}$ ,  $t_n = t/\tau_{ei}$ .

Using this description, the gradient scale length can be quantified by  $T/\nabla T = 1000\lambda_{ei}$ . A shallow temperature gradient ensures heat flow remains local. Since the collisional mean-free-path varies by  $Z$ , the size of the simulation domain is scaled to preserve the specified gradient scale length.

To acquire the data displayed in figures 3 and 4(a) no magnetic field was applied and the simulations had  $\Delta t \sim 1\tau_{ei}$ ,  $\Delta x \sim 10\lambda_{ei}$ . For the low- $Z$  simulations, the timestep can be very large in units of the inverse plasma frequency, e.g., for the conditions listed above, and  $Z = 2$ ,  $\Delta t > 50\omega_p^{-1}$ . Figure 3 shows the heat flow coefficient evolving to the steady state value for  $Z = 2$  and  $Z = 60$ . To reach the steady-state solution [9], the system needs to be run for over  $\mathcal{O}(10)$   $\tau_{ei}$ . The coefficients plotted in figure 4 correspond to the steady state values.

Although not shown here, there is a significantly weaker dependence of the simulation results on the spatial discretization e.g.  $\kappa(\Delta x \sim 100\lambda_{ei}) \approx \kappa(\Delta x \sim 10\lambda_{ei})$ . However, better spatial resolution will be necessary when modeling steeper

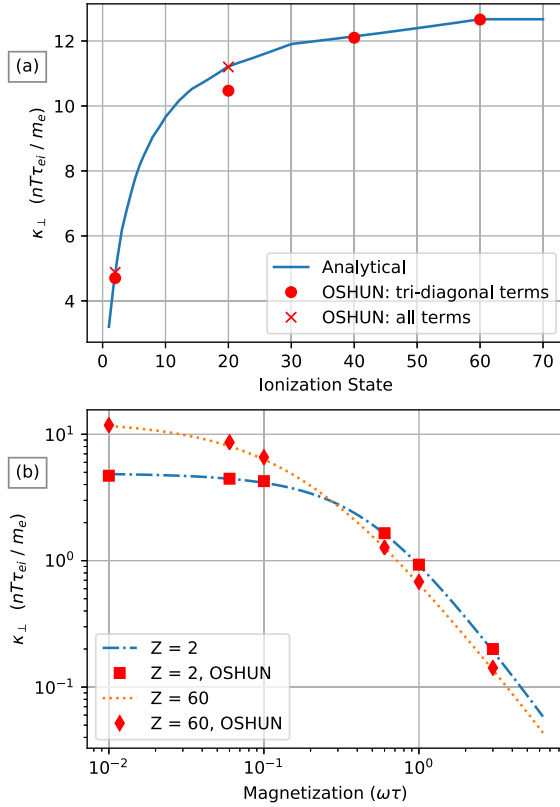


**Figure 4.** The heat flow coefficient after 10 ps in a 1 mm plasma for various (a) ionization states and (b) magnetizations. The solid lines are calculated using formulas from Epperlein and Haines [9]. For (a)  $\Delta t = 1\tau_{ei}$ ,  $\Delta x = 10\lambda_{ei}$  such that for  $Z = 2$ ,  $\Delta t = 330\omega_0^{-1}$ , while for (b), the time-step must be reduced as  $\omega_c\tau$  increases.

plasma gradients where non-local flow effects that depend on accurately resolving the gradient in space of the distribution function become important.

In addition to gradients in temperature and density, OSHUN has the ability to have gradients in the ionization state,  $Z$ . All three should be kept in mind when considering the optimal time-step and grid size for a particular simulation.

Simulations with  $Z \lesssim 20$  require the full electron–electron collision operator given in equation (9) (see appendix) for greater accuracy. When the terms that form a tri-diagonal matrix in the collision operator are used (e.g., when  $Z \gtrsim 20$ ), time-steps on the order of the collision time are possible. To recover the transport coefficient within 5% for  $Z \lesssim 20$ , the terms describing the Rosenbluth potentials of  $f_1^{0,1}$  are necessary. This slows the calculation in two ways. A dense matrix must now be solved using an iterative method rather than the fast, tri-diagonal solver that can be used for  $Z \gtrsim 20$ . To accurately recover the heat-flow, the extra terms require time-steps smaller than the collision time. For example, for  $Z = 2$ , we used a time-step smaller by a factor of 4 to acquire the data in figure 3(a).

Similar simulations are performed in the presence of a constant external magnetic field in the  $\hat{z}$  direction. OSHUN has the ability to impose an external magnetic field in the system. Using this feature, the plasma is held at the desired level of magnetization. Figure 4(b) shows excellent agreement between the results from OSHUN and the calculation in Epperlein and Haines [9] over a range of magnetizations,  $\omega_c\tau_{ei} = 0.01, 0.06, 0.1, 0.6, 1, 3$  for both  $Z = 2$  and  $Z = 60$ . Here,  $\omega_c$  is the gyrofrequency and  $\tau_{ei}$  is the electron-ion collision frequency.

#### 4. Conclusion

We have shown that OSHUN successfully reproduces well-known results for both collisionless and collisional HEDP regimes. We find that Landau damping (the imaginary part of the frequency from the EPW dispersion relation) can be accurately recovered if  $\mathcal{O}(10)$  terms are kept in the spherical harmonic expansion when the collision operator is disabled. Although not shown here (they will appear in a separate publication), we have also found that OSHUN can accurately model nonlinear EPWs if more spherical harmonics are kept,  $\mathcal{O}(10^2)$  and if finer time-, space-, and velocity-resolution is used. We have also shown that the implicit field and collision operator algorithms in OSHUN can model collisional phenomenon with as few as three spherical harmonics and with relatively lax time and space resolution.

These two problems validate OSHUN. The EPW test problems demonstrates that even collisionless physics can be accurately modeled using the spherical harmonic expansion method in the Vlasov equations by itself. The Fokker–Planck operator is tested against the calculation of the heat-flow coefficient carried out by Epperlein and Haines [9]. In these tests we used the implicit field solvers and an implicit collision operator (described in the appendix). Furthermore, we used different approximations to the  $e$ – $e$  collision depending on the  $Z$  of the plasmas. These features in OSHUN enable  $\Delta t \sim \tau_{ei}$  and  $\Delta x \sim 10\lambda_{ei}$  to be used to recover the heat-flow coefficient for a range of ionization states and magnetizations. By recovering the correct coefficients, we validated the implicit field solver and implicit collision operators, in addition to the magnetic field operator.

Currently, OSHUN be used with periodic and reflecting boundaries. Future development will include the implementation of absorbing and open boundary conditions. An absorbing boundary condition for the plasma can be implemented by the use of the collision operator [39] while the absorbing boundary conditions for the fields are well established [40]. Open boundary conditions can be modeled by expanding the domain of the grid efficiently through the use of non-uniformly-spaced grid cells [41].

Laser-plasma experiments often involve weakly-collisional plasmas. The tests described in this paper as well as those presented in [26, 27] show that spherical harmonic expansion-based VFPM codes such as OSHUN can accurately model collisionless and collisional physics. Therefore, such codes are ideal tools to model aspects of these experiments as

well as develop theoretical models for weakly-collisional plasma physics phenomenon. The collisionless physics results are relevant to the study of laser-plasma interactions for inertial fusion, of radiation generation mechanisms, and of astrophysical plasma environments. Being able to model the collisional physics using an *ab initio* tool such as a VFPM code is vital to assessing the performance of magnetohydrodynamics codes that are used to model laser-plasma HEDP and ICF experiments. OSHUN is the latest among such VFP codes, and offers some unique capabilities for studying the weakly-collisional physics in 1X-2V, 1X-3V, 2X-3V dimensionalities. It is available as open source software [42].

## Acknowledgments

AJ would like to thank M Sherlock and CP Ridgers for discussions regarding the implementation of the algorithms employed in OSHUN. AJ would also like to acknowledge discussions with J Brodrick on testing the collisional components of OSHUN. The modeling was performed using computational resources and services provided by the Hoffman2 and Dawson2 Computing Clusters at UCLA. OSHUN is open-source software that is made publicly available by the Particle-In-Cell-and-Kinetic-Simulation Center at UCLA. Partial support was provided by NSF under Grant No. ACI-1339893, DOE under Grant No. DE-NA0002953, and by the UC Office of the President through the UC Laboratory Fees Research Program, Grant ID: LFR-17-449059.

## Appendix. Code modifications and improvements

### A.1. Input decks and code

The code and input decks used to acquire, and the Jupyter notebooks used to process and plot data presented here are available on the PICKSC [42] website. The data is also available in HDF5 format.

### A.2. Implicit $f_0^0$ collision operator

The  $f_0^0$  collision operator originally implented in OSHUN and described in Tzoufras *et al* [26], is fully nonlinear and explicit. It also contains a modification to include inverse-bremsstrahlung heating without resolving the laser frequency [27]. For large laser intensities, the explicit operator requires relatively small time-steps such that the benefit of the implicit  $E$  solver is negated. Here, OSHUN is supplemented with the implicit, improved Chang–Cooper  $f_0^0$  collision algorithm described in [12, 18, 43]. We implemented a version [44] of this in OSHUN and for completeness, we provide the details in what follows. The equation set to be solved is

$$\left( \frac{\delta f_0^0}{\delta t} \right)_{e-e} = \frac{Y_{ee}}{v^2} \frac{\partial F}{\partial p}, \quad (4a)$$

$$F = C(f_0^0)f_0^0 + D(f_0^0)\frac{\partial f_0^0}{\partial v}, \quad (4b)$$

$$C(f_0) = 4\pi \int_0^v f_0^0(\mathbf{x}, v, t)v^2 dv, \quad (4c)$$

$$D(f_0) = \frac{4\pi}{v} \int_0^v dv v^2 \int_v^\infty f_0^0(\mathbf{x}, v', t)dv', \quad (4d)$$

where  $Y_{ee} = (4/3)k_p r_e \ln \Lambda_{ee}$ ,  $k_p = \sqrt{4\pi n_0} r_e$ ,  $r_e = 2.818 \times 10^{-13}$  and  $\ln \Lambda_{ee}$  is calculated from the NRL formulary [37] using the local density and temperature. To solve equation (4) implicitly, a tridiagonal matrix can be formed by appropriately differencing the above equations such that the numerical implementation is given by

$$\alpha_k (f_0^0)_{k+1}^{t+1} + \beta_k (f_0^0)_k^{t+1} + \gamma_k (f_0^0)_{k-1}^{t+1} = (f_0^0)_k^t, \quad (5a)$$

$$\alpha_k = -\frac{Y_{ee} \Delta t}{v_k^2} \left[ C_{k+1/2}^{t*} (1 - \delta_{k+1/2}^{t*}) + \frac{D_{k+1/2}^{t*}}{\Delta v_{k+1/2}} \right], \quad (5b)$$

$$\beta_k = 1 - \frac{Y_{ee} \Delta t}{v_k^2} \left[ C_{k+1/2}^{t*} \delta_{k+1/2}^{t*} - \frac{D_{k+1/2}^{t*}}{\Delta v_{k+1/2}} - C_{k-1/2}^{t*} (1 - \delta_{k-1/2}^{t*}) - \frac{D_{k-1/2}^{t*}}{\Delta v_{k-1/2}} \right], \quad (5c)$$

$$\gamma_k = \frac{Y_{ee} \Delta t}{v_k^2} \left[ C_{k-1/2}^{t*} \delta_{k-1/2}^{t*} - \frac{D_{k-1/2}^{t*}}{\Delta v_{k-1/2}} \right], \quad (5d)$$

where  $\alpha$ ,  $\beta$ ,  $\gamma$  form the subdiagonal, diagonal, and super-diagonal of the tridiagonal matrix.  $C_{k+1/2}^{t*}$  and  $D_{k+1/2}^{t*}$  are lagged nonlinear coefficients given by

$$C_{k+1/2}^{t*} = 4\pi \sum_1^k f_k^{t*} v_k^2 \Delta v_k, \quad (6a)$$

$$D_{k+1/2}^{t*} = \frac{4\pi}{v_{k+1/2}^*} \sum_1^k v_u^2 \left[ \sum_u^{N_u-1} f_{k+1/2}^{t*} v_{k+1/2}^* \Delta v_{k+1/2} \right], \quad (6b)$$

$$v_{k+1/2}^* = \frac{v_{k+1/2} - v_k}{2}. \quad (6c)$$

The boundary conditions are  $C_{1/2}^{t*} = D_{1/2}^{t*} = D_{N_p+1/2}^{t*} = 0$ . The distribution function at  $f_{k+1/2}^{t*}$  is calculated using

$$f_{k+1/2} = (1 - \delta_{k+1/2}) f_{k+1} + \delta_{k+1/2} f_k, \quad (7)$$

where  $\delta_{k+1/2}^*$  is an interpolation weight calculated with

$$W_{k+1/2} = \Delta v_{k+1/2} \frac{C_{k+1/2}}{D_{k+1/2}}, \quad (8a)$$

$$\delta_{k+1/2} = \frac{1}{W_{k+1/2}} - \frac{1}{\exp(W_{k+1/2}) - 1}. \quad (8b)$$

The boundary conditions for this set are  $\delta_{1/2} = \delta_{N_p+1/2} = 0.5$ . An inner iteration is performed to calculate  $D_{k+1/2}$  and  $\delta_{k+1/2}$ . Adding inverse Bremsstrahlung heating into this algorithm via the Langdon heating operator [16] requires modifying  $D_{k+1/2}$  as outlined in Epperlein *et al* [10]. This capability has also been added.

### A.3. $f_l^m$ collision operator

The linearized  $f_l^m$  collision operator is reproduced in

$$\begin{aligned} \frac{1}{Y_{ee}} \left( \frac{\delta f_l^m}{\delta t} \right) = & (8\pi f_0^0) f_l^m + \frac{(I_2 + J_{-1})}{3v} \frac{\partial^2 f_l^m}{\partial v^2} \\ & + \frac{(-I_2 + 2J_{-1} + 3I_0)}{3v^2} \frac{\partial f_l^m}{\partial v} \\ & - \frac{l(l+1)(-I_2 + 2J_{-1} + 3I_0) + Y_{ei}/Y_{ee} f_l^m}{3v^3} \\ & + \left[ A_1 \frac{1}{2v} \frac{\partial^2 f_0^0}{\partial v^2} + B_1 \frac{1}{v^2} \frac{\partial f_0^0}{\partial v} \right] I_{l+2}(f_l^m) \\ & + \left[ A_1 \frac{1}{2v} \frac{\partial^2 f_0^0}{\partial v^2} + B_2 \frac{1}{v^2} \frac{\partial f_0^0}{\partial v} \right] J_{l-1}(f_l^m) \\ & + \left[ A_2 \frac{1}{2v} \frac{\partial^2 f_0^0}{\partial v^2} + B_3 \frac{1}{v^2} \frac{\partial f_0^0}{\partial v} \right] I_l(f_l^m) \\ & + \left[ A_2 \frac{1}{2v} \frac{\partial^2 f_0^0}{\partial v^2} + B_4 \frac{1}{v^2} \frac{\partial f_0^0}{\partial v} \right] J_{l-1}(f_l^m), \end{aligned} \quad (9)$$

where the coefficients  $A_1, A_2, B_1, B_2, B_3, B_4$  are provided in Tzoufras *et al* [26].  $I_2(v), J_{-1}(v)$ , and  $I_0(v)$  are the Rosenbluth potentials of  $f_0(v)$ .

The first four terms of equation (9) are proportional to  $f_l^m$  or its first or second derivatives. This enables the discretization of the first four terms implicitly, forming a tri-diagonal matrix. The last four terms describe the evolution of  $f_l^m$  due to the interaction of its own Rosenbluth potentials with  $f_0$ . Including these terms gives a dense matrix that is more computationally expensive to solve. It is recommended to include these terms as a check for low  $Z$  calculations where the off-diagonal terms describing electron–electron collisions have non-negligible contributions. In practice, we find that the tri-diagonal terms recover most calculations within 5%–10% as long as the discretization is carefully considered.

### A.4. Initializing electron plasma waves

The ability to initialize or drive up and external waves as a function of space and time has been added to OSHUN. The pulse shape and duration of the external drivers can be specified by including rise, fall, and flat times. The shape of the rise and fall is determined by a fifth-order polynomial that smoothly and quickly reaches 0 and 1 on opposite sides. This function is given by

$$A(t') = \begin{cases} 0 & \text{before rise time} \\ 6t'^5 - 15t'^4 + 10t'^3 & \text{during rise time} \\ 1 & \text{during flat time} \\ 1 - 6t'^5 + 15t'^4 - 10t'^3 & \text{during fall time} \\ 0 & \text{after fall time,} \end{cases} \quad (10)$$

where  $t'$  is

$$t'_{\text{rise/fall}} = \frac{t - t_{\text{pulse-center}}}{t_{\text{rise/fall}}}. \quad (11)$$

To drive an electric or magnetic field an external source of the form  $A(x, t)$  is added to Ampere's law or Faraday's law respectively when  $\vec{E}$  or  $\vec{B}$  is being updated. For the plasma wave problems,  $A(x, t) \propto \sin(kx - \omega t)$  where wavenumber,  $k$ , and frequency,  $\omega$ , can be specified as inputs.  $k$  is chosen for the  $k\lambda_D$  of interest and  $\omega$  is chosen close to the real part of the frequency from the dispersion relation.

The values for  $A(x, t)$  and the rise, flat, and fall times are chosen to provide the desired amplitude and proper initial values for the distribution function. This capability is used extensively for the simulations used to generate figures 2 and 4.

### ORCID iDs

Archis S Joglekar  <https://orcid.org/0000-0003-3599-5629>

### References

- [1] Johnston T W 1960 *Phys. Rev.* **120** 1103
- [2] Shkarofsky I P 1963 *Can. J. Phys.* **41** 1753
- [3] Shkarofsky I P, Johnston T W, Bachynski M P and Hirshfield J L 1967 *Am. J. Phys.* **35** 551
- [4] Bell A R, Evans R G and Nicholas D J 1981 *Phys. Rev. Lett.* **46** 243
- [5] Matte J P and Virmont J 1982 *Phys. Rev. Lett.* **49** 1936
- [6] Albritton J R 1983 *Phys. Rev. Lett.* **50** 2078
- [7] Matte J P, Johnston T W, Delettrez J and McCrory R L 1984 *Phys. Rev. Lett.* **53** 1461
- [8] Braginskii S I 1965 *Rev. Plasma Phys.* **1** 205
- [9] Epperlein E M and Haines M G 1986 *Phys. Fluids* **29** 1029
- [10] Epperlein E M, Rickard G J and Bell A R 1988 *Phys. Rev. Lett.* **61** 2453
- [11] Epperlein E M, Rickard G J and Bell A R 1988 *Comput. Phys. Commun.* **52** 7
- [12] Epperlein E 1994 *J. Comput. Phys.* **112** 291
- [13] Epperlein E M and Short R W 1992 *Phys. Fluids B* **4** 2211
- [14] Epperlein E M and Short R W 1994 *Phys. Rev. E* **50** 1697
- [15] Epperlein E M 1994 *Phys. Plasmas* **1** 109
- [16] Langdon A B 1980 *Phys. Rev. Lett.* **44** 575
- [17] Weng S M, Sheng Z M and Zhang J 2009 *Phys. Rev. E* **80** 1
- [18] Kingham R J and Bell A R 2004 *J. Comput. Phys.* **194** 1
- [19] Thomas A G R, Kingham R J and Ridgers C P 2009 *New J. Phys.* **11** 033001
- [20] Ridgers C P, Kingham R J and Thomas A G R 2008 *Phys. Rev. Lett.* **100** 075003
- [21] Joglekar A S, Ridgers C P, Kingham R J and Thomas A G R 2016 *Phys. Rev. E* **93** 043206
- [22] Bell A R, Robinson A P L, Sherlock M, Kingham R J and Rozmus W 2006 *Plasma Phys. Control. Fusion* **48** R37
- [23] Robinson A P L, Bell A R and Kingham R J 2006 *Plasma Phys. Control. Fusion* **48** 1063
- [24] Robinson A P L and Sherlock M 2007 *Phys. Plasmas* **14** 083105
- [25] Bell A R and Tzoufras M 2011 *Plasma Phys. Control. Fusion* **53** 045010
- [26] Tzoufras M, Bell A R, Norreys P A and Tsung F S 2011 *J. Comput. Phys.* **230** 6475
- [27] Tzoufras M, Tableman A, Tsung F S, Mori W B and Bell A R 2013 *Phys. Plasmas* **20** 056303

- [28] Rozmus W, Chapman T, Brantov A, Winjum B J, Berger R L, Brunner S, Bychenkov V Y, Tableman A, Tzoufras M and Glenzer S 2016 *Phys. Plasmas* **23** 012707
- [29] Marocchino A, Tzoufras M, Atzeni S, Schiavi A, Nicolai P D, Mallet J, Tikhonchuk V and Feugeas J-L 2013 *Phys. Plasmas* **20** 022702
- [30] Brodrick J P *et al* 2017 *Phys. Plasmas* **24** 092309
- [31] Sherlock M, Brodrick J P and Ridgers C P 2017 *Phys. Plasmas* **24** 082706
- [32] Brodrick J *et al* 2018 arXiv:1803.05801
- [33] Reville B and Bell A R 2013 *Mon. Not. R. Astron. Soc.* **430** 2873
- [34] Touati M, Feugeas J-L, Nicolai P, Santos J J, Gremillet L and Tikhonchuk V T 2014 *New J. Phys.* **16** 073014
- [35] Thomas A G R, Tzoufras M, Robinson A, Kingham R, Ridgers C, Sherlock M and Bell A 2012 *J. Comput. Phys.* **231** 1051
- [36] Landau L D 1946 *Zh. Eksp. Teor. Fiz.* **10** 25
- [37] Huba J D 2013 *Plasma Physics* (Washington, DC: Naval Research Laboratory) pp 1–71
- [38] Arber T and Vann R 2002 *J. Comput. Phys.* **180** 339
- [39] Strozzi D J, Williams E A, Langdon A B and Bers A 2007 *Phys. Plasmas* **14** 013104
- [40] Berenger J-P 1996 *J. Comput. Phys.* **127** 363
- [41] Joglekar A S, Thomas A G R, Fox W and Bhattacharjee A 2014 *Phys. Rev. Lett.* **112** 105004
- [42] <https://github.com/UCLA-Plasma-Simulation-Group/OSHUN>
- [43] Chang J S and Cooper G 1970 *J. Comput. Phys.* **6** 1
- [44] Ridgers C P and Kingham R J 2009 *Developing a Vlasov–Fokker–Planck Code—K2* private communication Imperial College London





Contents lists available at ScienceDirect

Journal of Computational Physics

www.elsevier.com/locate/jcp



# Implementation of a hybrid particle code with a PIC description in $r$ – $z$ and a gridless description in $\phi$ into OSIRIS



A. Davidson<sup>a,\*</sup>, A. Tableman<sup>a</sup>, W. An<sup>a</sup>, F.S. Tsung<sup>a</sup>, W. Lu<sup>d,e</sup>, J. Vieira<sup>b</sup>,  
R.A. Fonseca<sup>b,c</sup>, L.O. Silva<sup>b</sup>, W.B. Mori<sup>a,d</sup>

<sup>a</sup> Department of Physics and Astronomy, University of California, Los Angeles, CA 90095, USA

<sup>b</sup> GoLP/Instituto de Plasmas e Fusão Nuclear, Instituto Superior Técnico, Universidade de Lisboa, Lisbon, Portugal

<sup>c</sup> Departamento Ciências e Tecnologias da Informação, ISCTE – Instituto Universitário de Lisboa, 1649-026 Lisboa, Portugal

<sup>d</sup> Department of Electrical Engineering, University of California, Los Angeles, CA 90095, USA

<sup>e</sup> Department of Engineering Physics, Tsinghua University, Beijing 100084, China

## ARTICLE INFO

### Article history:

Received 26 March 2014

Received in revised form 23 August 2014

Accepted 28 October 2014

Available online 8 November 2014

### Keywords:

LWFA

PWFA

PIC

OSIRIS

Self-trapping

Hosing

## ABSTRACT

For many plasma physics problems, three-dimensional and kinetic effects are very important. However, such simulations are very computationally intensive. Fortunately, there is a class of problems for which there is nearly azimuthal symmetry and the dominant three-dimensional physics is captured by the inclusion of only a few azimuthal harmonics. Recently, it was proposed [1] to model one such problem, laser wakefield acceleration, by expanding the fields and currents in azimuthal harmonics and truncating the expansion. The complex amplitudes of the fundamental and first harmonic for the fields were solved on an  $r$ – $z$  grid and a procedure for calculating the complex current amplitudes for each particle based on its motion in Cartesian geometry was presented using a Marder's correction to maintain the validity of Gauss's law. In this paper, we describe an implementation of this algorithm into OSIRIS using a rigorous charge conserving current deposition method to maintain the validity of Gauss's law. We show that this algorithm is a hybrid method which uses a particles-in-cell description in  $r$ – $z$  and a gridless description in  $\phi$ . We include the ability to keep an arbitrary number of harmonics and higher order particle shapes. Examples for laser wakefield acceleration, plasma wakefield acceleration, and beam loading are also presented and directions for future work are discussed.

© 2014 Elsevier Inc. All rights reserved.

## 1. Introduction

Particle-in-cell simulations are widely used and well established for simulating plasmas in fields ranging from magnetic fusion, inertial confinement fusion, plasma based acceleration, and space and astrophysics. These simulations are conducted in one, two, and three dimensions. The two dimensional simulations are often conducted in Cartesian “slab” geometry or  $r$ – $z$  “cylindrical” geometry. While the two dimensional simulations can be very useful for carrying out parameter scans and illuminating physics, there are some problems in which three dimensional effects lead to both qualitative or quantitative

\* Corresponding author.

E-mail addresses: davidsoa@physics.ucla.edu (A. Davidson), Tableman@physics.ucla.edu (A. Tableman), anweiming@ucla.edu (W. An), tsung@physics.ucla.edu (F.S. Tsung), luwei@ucla.edu (W. Lu), jorge.vieira@ist.utl.pt (J. Vieira), ricardo.fonseca@iscte.pt (R.A. Fonseca), luis.silva@ist.utl.pt (L.O. Silva), mori@physics.ucla.edu (W.B. Mori).

<http://dx.doi.org/10.1016/j.jcp.2014.10.064>

0021-9991/© 2014 Elsevier Inc. All rights reserved.

differences. For example, in plasma based acceleration the space charge forces of an intense particle beam or the radiation pressure of an intense laser, drive plasma wave wake fields as they propagate through long regions of plasmas. The wakefield structure, the self-trapping of electrons, the beam loading of wakes by trailing beams, and the evolution of the drive particle or laser beams are not properly modeled in 2D slab geometry due to geometrical effects. Therefore  $r$ - $z$  PIC simulations have been used to properly describe the structure of the wakefield. However, the use of an  $r$ - $z$  code precludes hosing and the effect of asymmetric spot sizes of both the drive and trailing particle beams. In addition, a linearly polarized (or circularly polarized) laser is not typically azimuthally symmetric (azimuthally symmetric laser pulses are radially polarized) so a laser driver cannot even be modeled using an  $r$ - $z$  code.

Several methods have been developed for more efficiently modeling plasma-based acceleration in three dimensions (or in lower dimensions). These include the moving window method [2], quasi-static methods [3–5], the ponderomotive guiding center (PGC) method for modeling laser propagation [3,6], and the use of simulating the physics in Lorentz boosted frames [7–10]. In some cases these methods are combined. For example, a combination of quasi-static field equations and the ponderomotive guiding center approximation are used in QuickPIC [5,4] to model laser wakefield acceleration. In addition, each of these methods has advantages and disadvantages when compared to full PIC methods in the rest frame of the plasma. The quasi-static methods cannot accurately model self-injection, and the ponderomotive guiding center model can have difficulty modeling nonlinear laser–plasma interactions over pump-depletion distances (a method to avoid some of these difficulties was discussed in [11]). Despite the recent progress on understanding the numerical Cherenkov instability, there is still research left on the use of Lorentz boosted frames to model nonlinear regimes of laser wakefield acceleration [12–14]. In addition, parameter scans over the plasma length are more straightforward in the lab frame. In a single simulation with a long plasma length, the beam energy, wakefield, and laser, can be plotted as a function of propagation length. In the boosted frame a longer plasma length can be used as well. However, the data needed to plot quantities at a fixed lab frame time correspond to many boosted frame times. Work continues on each of these methods.

Very recently, an algorithm was proposed that would allow modeling laser propagation with similar computational costs to an  $r$ - $z$  code. In this algorithm the fields and currents are expanded into azimuthal harmonics (modes) where the amplitudes of each harmonic are complex and functions of  $r$  and  $z$ . This expansion is substituted into Maxwell's equations to generate a series of equations for the complex amplitudes for each harmonic. In [1] the expansion was truncated at a maximum of  $m = 3$ . Recently, simulations with modes up to  $m = 6$  were presented by Corde et al. [15]. The particles are pushed in 3D Cartesian geometry and are then used to obtain the complex amplitudes for each harmonic of the current. In [1] the current deposition method did not conserve charge so a Marder's method [16] was used to maintain the accuracy of Gauss's law. The Marder's method is an approximation to the Boris correction [17,18] in which a correction,  $\mathbf{E}_c$  is added to an uncorrected field,  $\mathbf{E}'$  such that  $\nabla \cdot (\mathbf{E}' + \mathbf{E}_c) = \rho$ . The correction to the field is defined as  $\mathbf{E}_c = -\nabla\phi_c$  where  $\nabla^2\phi_c = \nabla \cdot (\mathbf{E}') - \rho$ . They also showed results for laser wakefield acceleration and found agreement with a full PIC code.

In this paper, we describe the implementation of such a truncated azimuthal Fourier decomposition (i.e., harmonic expansion) into the OSIRIS simulation framework. OSIRIS is a fully parallelized PIC finite-difference code that has been used in 1D, 2D, 3D geometries [19]. For 2D simulations a Cartesian slab ( $xz$ ) or a cylindrical ( $rz$ ) geometry can be used. We reused as much of the existing 2D  $r$ - $z$  structure as possible. We view this algorithm as a hybrid between a traditional PIC method where quantities are defined on an  $r$ - $z$  grid and a gridless method [20] in  $\phi$  where quantities are expanded in global basis functions (e.g., Fourier modes) defined at all locations and the expansion is truncated. This strategy of combining gridded and gridless algorithms is actually not new. For example, in the early 1980s Godfrey and collaborators developed IPROP [21,22], which was capable of following an arbitrary number of azimuthal modes to study filamentation as well as hosing of high current electron beams propagating in the atmosphere.

In the implementation for OSIRIS an arbitrary number of harmonics can be kept. In addition, OSIRIS uses a rigorous charge conserving current deposition for the PIC part. Therefore, we have used this as a starting point to develop a current deposition scheme which conserves charge for each harmonic particle by particle. OSIRIS can also use higher order particle shapes so we have implemented this into the PIC part of the algorithm. For the gridless part we have used point particle shapes but have described how to extend this to higher order particle shapes. In addition, OSIRIS can model plasma wakefield acceleration and beam loading. We therefore give examples of such simulations using the new algorithm. We also note that this algorithm could be combined with the PGC as well as Lorentz boosted frame ideas for even more dramatic speed-ups over full 3D simulations.

In Section 2 we will discuss the mathematical description of Maxwell's equations using an azimuthal harmonic expansion for the electromagnetic fields and currents. In Section 3 we discuss the specific numerical implementation of these equations, as well as the complications which need to be considered in the cell closest to the cylindrical axis. We also derive the charge conserving current deposition algorithm and discuss its implementation. In Section 4 we give examples from the code of laser wakefield acceleration, plasma wakefield acceleration and beam loading in laser driven wakes including comparison with full 3D simulations. We also test the charge conservation and accuracy of Gauss's law for one test case. Last, in Section 5, conclusions and directions for future work are presented.

## 2. Theory

### 2.1. Electromagnetic fields expressed in azimuthal harmonics

We begin by expanding the electromagnetic fields and the charge ( $\rho$ ) and current densities ( $\mathbf{J}$ ), expressed in cylindrical coordinates, into a Fourier series in  $\phi$ ,

$$\begin{aligned}\mathbf{F}(r, z, \phi) &= \Re \left\{ \sum_{m=0}^{\infty} \mathbf{F}^m(r, z) e^{im\phi} \right\} \\ &= \mathbf{F}^0(r, z) + \Re \{ \mathbf{F}^1 \} \cos(\phi) - \Im \{ \mathbf{F}^1 \} \sin(\phi) \\ &\quad + \Re \{ \mathbf{F}^2 \} \cos(2\phi) - \Im \{ \mathbf{F}^2 \} \sin(2\phi) \\ &\quad + \dots\end{aligned}\quad (1)$$

Note that the amplitudes of each Fourier harmonic (for all fields)  $\mathbf{F}^m$  are complex, whereas the physical fields they are describing,  $\mathbf{F}$ , are real. As shown in [1] a major advantage of this expansion is that it allows modeling a linearly polarized laser with only the first harmonic. Consider a laser with a polarization angle  $\phi_0$  and amplitude  $E_0$ ,

$$\mathbf{E}(r, z, \phi) = E_0 \cos(k_z z - \omega t) \cos(\phi_0) \hat{x} + E_0 \cos(k_z z - \omega t) \sin(\phi_0) \hat{y} \quad (3)$$

$$\mathbf{B}(r, z, \phi) = -E_0 \cos(k_z z - \omega t) \sin(\phi_0) \hat{x} + E_0 \cos(k_z z - \omega t) \cos(\phi_0) \hat{y}, \quad (4)$$

and let  $a(r, z) = E_0 \cos(k_z z - \omega t)$ . Decomposing the Cartesian unit vectors into cylindrical coordinates unit vectors then gives the radial and azimuthal field components which will have  $\sin(\phi)$  and  $\cos(\phi)$  terms. By equating these fields to the expansion in Eq. (1), it can be easily shown that these fields are represented by the  $m = 1$  terms

$$E_r^1 = a(r, z) [\cos(\phi_0) - i \sin(\phi_0)] \quad (5)$$

$$E_\phi^1 = a(r, z) [\sin(\phi_0) + i \cos(\phi_0)] \quad (6)$$

$$B_r^1 = a(r, z) [-\sin(\phi_0) - i \cos(\phi_0)] \quad (7)$$

$$B_\phi^1 = a(r, z) [\cos(\phi_0) - i \sin(\phi_0)]. \quad (8)$$

Circularly and elliptically polarized lasers can be obtained by adding two linearly polarized lasers with equal or non-equal amplitudes and phase and polarization offset by  $\pi/2$ .

The time-evolution of electromagnetic fields is described by Faraday's and Ampere's equations (effectively written in normalized units),

$$\frac{\partial \mathbf{B}}{\partial t} = -\nabla \times \mathbf{E}, \quad (9)$$

$$\frac{\partial \mathbf{E}}{\partial t} = \nabla \times \mathbf{B} - \mathbf{J}. \quad (10)$$

Substituting the expansions for each field into these equations, we obtain the following equations for each mode,  $m$ ,

$$\frac{\partial B_r^m}{\partial t} = -\frac{im}{r} E_z^m + \frac{\partial E_\phi^m}{\partial z} \quad (11)$$

$$\frac{\partial B_\phi^m}{\partial t} = -\frac{\partial E_r^m}{\partial z} + \frac{\partial E_z^m}{\partial r} \quad (12)$$

$$\frac{\partial B_z^m}{\partial t} = -\frac{1}{r} \frac{\partial}{\partial r} (r E_\phi^m) + \frac{im}{r} E_r^m \quad (13)$$

$$\frac{\partial E_r^m}{\partial t} = \frac{im}{r} B_z^m - \frac{\partial B_\phi^m}{\partial z} - J_r^m \quad (14)$$

$$\frac{\partial E_\phi^m}{\partial t} = \frac{\partial B_r^m}{\partial z} - \frac{\partial B_z^m}{\partial r} - J_\phi^m \quad (15)$$

$$\frac{\partial E_z^m}{\partial t} = \frac{1}{r} \frac{\partial}{\partial r} (r B_\phi^m) - \frac{im}{r} B_r^m - J_z^m \quad (16)$$

We use different conventions for the coordinate system than that used in Ref. [1], but the idea is identical. In vacuum, each mode evolves independently of every other mode. In addition, for a linear plasma response there is also no coupling between modes because under this limit each harmonic for the current is only driven by the same harmonic for the fields. However, there is coupling between harmonics due to the macroparticle motion, i.e., nonlinear currents. The finite difference expression of these equations and associated complications near the  $r = 0$  axis will be discussed in Section 3.

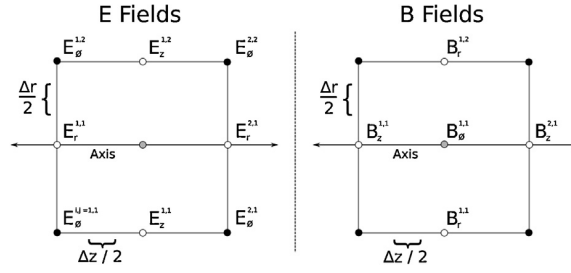


**Fig. 1.** The layout of the grid for the field components in relation to the cylindrical axis. The grid indices associated with the field point are indicated on the superscript. The  $E_r$ ,  $B_z$  and  $B_\phi$  lie on the cylindrical axis for the axial cell.

## 2.2. Symmetry properties of the axis

When implementing the field equations expressed in cylindrical coordinates one inevitably comes across singularities at the axis ( $r = 0$ ). The exact location of the singularities will depend on the layout of the grid values, but you can solve the singularities using symmetry-based arguments. As pointed out in Ref. [1], Constantinescu and Lele [23] discuss in detail how the field values behave at the cylindrical,  $r = 0$ , axis. To summarize, for any scalar and Cartesian fields ( $E_z$ ,  $B_z$ ) only the  $m = 0$  mode is non-vanishing on the  $r = 0$  axis (this was already used in OSIRIS). On the other hand, for cylindrical field components ( $E_r$ ,  $B_r$ ,  $E_\phi$ ,  $B_\phi$ ), only the  $m = 1$  mode is non-vanishing on the  $r = 0$  axis.

## 2.3. Boundary conditions for fields and particles

Currently, we use conducting boundary conditions for the fields, and an absorbing boundary condition for the particle at  $r = r^{\max}$ . We also use a moving window in the  $z$  direction. In the future, more boundary conditions will be added in both  $r$  and  $z$ , including the ability to launch a laser from a wall or a moving antenna.

## 3. Algorithm

The truncated azimuthal mode geometry has been incorporated into the OSIRIS simulation framework. The electromagnetic fields were calculated on  $2m + 1$  2D grids; one grid representing the cylindrically symmetric (and real) 0th order mode, while the rest represented the real and imaginary components of the higher order modes. Each field mode was advanced in accordance to Eqs. (11)–(16), whose implementation will be discussed in more detail in Section 3.1. The macroparticle values ( $x$ ,  $y$ ,  $z$ ,  $p_x$ ,  $p_y$ ,  $p_z$ ) were stored in 3D coordinates. When the fields were interpolated onto the particles, the mode contributions were added together as per Eq. (1), and converted into Cartesian coordinates. The particles were then advanced according to the relativistic equations of motion,

$$\frac{d}{dt}\mathbf{P} = q(\mathbf{E} + (\mathbf{v}/c) \times \mathbf{B}), \quad (17)$$

$$\frac{d}{dt}\mathbf{x} = (1/m\gamma)\mathbf{P}, \quad (18)$$

where  $q$  and  $m$  are the macroparticle charge and mass, respectively. Using the motion of the particles the current can be deposited onto the  $2m + 1$  2D grids using a charge-conserving deposition scheme, particle by particle, as described in detail in Section 3.2.

### 3.1. Field solver

The Maxwell's equations (11)–(16) for each harmonic were discretized over a uniform grid defined on the Yee lattice [24]. Due to staggering, fields of the same index lie in different positions with respect to the axis, as is shown in Fig. 1. Some field values reside exactly on the cylindrical axis, which in this case will cause a singularity when solving Eqs. (13) and (14). It is important to note here that the location of the axis in our simulation is different from that of Lifschitz [1], where the equations for  $B_r$  and  $E_z$  present a singularity. Although the singularities occur for different field components, the logic with which we resolve these issues are effectively the same.

As discussed in Section 2.2, the axial fields are usually zero. The only axial fields we need to solve for are  $B_z^0$ ,  $E_r^1$ , and  $B_\phi^1$ ; the last of which does not pose a singularity. We use the integral form of Faraday's Law to find  $B_z^0$  on the axis by integrating  $\oint \mathbf{E} \cdot d\mathbf{l}$  in a loop around the axis, resulting in

$$B_z^{0,i,1} = B_z^{0,i,1} - 4 \frac{\Delta t}{2} \times \frac{E_\phi^{0,i,2}}{\Delta r}. \quad (19)$$

This is the same method that was used in the 2D cylindrical simulation that was already implemented in OSIRIS. As for the  $m = 1$  mode, we use the fact that

$$\lim_{r \rightarrow 0} \frac{im}{r} B_z^m = im \frac{\partial B_z^m}{\partial r},$$

to define

$$\frac{im}{r} B_z^{m,i,1} = im \left. \frac{\partial B_z}{\partial r} \right|_{r=0} = im \frac{B_z^{m,i,2}}{\Delta r},$$

where the fact that  $B_z^{m,i,1} = 0$  was used. We then obtain a nonsingular expression for  $\frac{\partial E_r^1}{\partial t}$  at the axis,

$$\frac{\partial E_r^{m=1,i,j=1}}{\partial t} = i \frac{1}{\Delta r} B_z^{1,i,2} - \frac{1}{\Delta z} (B_\phi^{1,i,1} - B_\phi^{1,i-1,1}) - J_r^1, \quad (20)$$

where  $j = 1$  is the radial index of the cell that sits on the axis.

### 3.2. Charge conserving current deposition

In OSIRIS Gauss's law is maintained by using a rigorously charge conserving deposit. For example, in 3D Cartesian geometry the particles have a shape

$$S_x(x - x_p(t)) S_y(y - y_p(t)) S_z(z - z_p(t)),$$

and the cell corners (where the charge density is defined) are defined at  $x_g, y_g, z_g$ . The charge density at a time  $t$  at the grid locations is therefore,

$$\rho = S_x(x_g - x_p(t)) S_y(y_g - y_p(t)) S_z(z_g - z_p(t)).$$

The current is defined at different locations (the cell faces) and it is defined such that

$$\frac{\bar{\partial}}{\partial t} \rho + \bar{\nabla} \cdot \mathbf{J} = 0,$$

where  $\bar{\partial}$  indicates a finite difference representation of the derivative, e.g.,

$$\begin{aligned} \left. \frac{\bar{\partial}}{\partial t} \rho \right|^{t+\Delta t/2} &= \frac{1}{\Delta t} [S_x(x_g - x_p(t + \Delta t)) S_y(y_g - y_p(t + \Delta t)) S_z(z_g - z_p(t + \Delta t)) \\ &\quad - S_x(x_g - x_p(t)) S_y(y_g - y_p(t)) S_z(z_g - z_p(t))]. \end{aligned} \quad (21)$$

There is not a unique solution for a  $\mathbf{J}$  such that  $\frac{\bar{\partial}}{\partial t} \rho + \bar{\nabla} \cdot \mathbf{J} = 0$  as one can always add a curl to one solution. To determine  $\mathbf{J}$ , OSIRIS implements the Density Decomposition method described by Esirkepov [25], which is the generalization of the method developed by Villasenor and Buneman [26] for arbitrary particle shapes. In the method of Villasenor and Buneman, linear particle shapes are assumed. If the particle motion stays within a cell and moves from  $x_i, y_i$  to  $x_f, y_f$  in one time step, then this method can be viewed as averaging the current contribution over all paths that are decomposed into segments that include motion orthogonal to a cell face. If the particle motion crosses cell boundaries, then the motion is split into segments lying entirely inside individual cells, and the method in the previous sentence is applied to each individual segment.

Extending the charge conserving current deposit to 2D  $r$ - $z$  is relatively straightforward because the cells are still rectangular. In this case, one needs to recognize that  $S_r(r - r_p(t))$  includes a  $1/r_g$  term. Viewed another way each simulation particle represents a fixed amount of charge so as it moves closer to the  $r = 0$  axis the charge density must increase. The  $J_\phi$  component is simple to define in such a code as it is simply  $\rho v_{\phi,p}$ , where  $v_{\phi,p}$  is the velocity of the particle in the  $\phi$  direction.

On the other hand, it is not straightforward to define  $J_\phi$  in the new algorithm. In particular, for the  $m = 0$  harmonic the standard method works but for the  $m \neq 0$  harmonics more thought is needed. However, as we show next,  $J_\phi^m$  can be determined using the  $J_\perp$  from existing charge conserving deposition scheme for the  $m = 0$  mode. We begin from the definition of the particle shape in cylindrical coordinates,

$$S \equiv S_r(r - r_p(t)) S_\phi(\phi - \phi_p(t)) S_z(z - z_p(t))$$

so the charge density is  $QS$ , where  $Q$  is the charge of a simulation particle. We also note that  $S_r$  has a  $1/r_g$  factor so that

$$\int dr r d\phi dz S = 1.$$

It should be noted here that in the simulation grid the charge is defined on discrete grid points. For b-splines, if the integral over the charge density is unity, then the discrete sum of the charge over the grid points is also unity. The particle positions are known at full integer values of time,  $t + \Delta t n$ , and the particle momentum (and velocity) are known at half integer values of time,  $t + \Delta t(n + \frac{1}{2})$ . In addition, the currents are only defined on the  $r$ - $z$  grid, i.e., there is no grid in  $\phi$ .

Next, we look for solutions for  $\mathbf{J}$  that satisfy the finite difference operator version of the continuity equation

$$\begin{aligned} \frac{\bar{\partial}}{\partial t} \rho \Big|^{n+\frac{1}{2}} &= \sum_p Q_p [S_r(r - r_p^{n+1}) S_\phi(\phi - \phi_p^{n+1}) S_z(z - z_p^{n+1}) \\ &\quad - S_r(r - r_p^n) S_\phi(\phi - \phi_p^n) S_z(z - z_p^n)] \\ &= -\bar{\nabla} \cdot \mathbf{J}^{n+\frac{1}{2}}, \end{aligned} \quad (22)$$

where  $Q_p$  is the charge associated with the particle  $p$ . For simplicity  $Q_p = 1$  for the rest of this derivation. The next step is to expand  $S_\phi$  in global basis functions (azimuthal harmonics),

$$S_\phi(\phi - \phi_p) = \sum_m S_{\phi,m}(\phi_p) e^{im\phi}, \quad (23)$$

where

$$S_{\phi,m} \equiv \int_0^{2\pi} \frac{d\phi'}{2\pi} e^{-im\phi'} S_\phi(\phi' - \phi_p).$$

If  $S_\phi \equiv \delta(\phi - \phi_p)$  then  $S_{\phi,m} = \frac{1}{2\pi} e^{-im\phi_p}$ . In addition,  $\rho$  and  $\mathbf{J}$  defined on the  $r$ - $z$  grid are expanded in azimuthal harmonics

$$\begin{pmatrix} \rho \\ \mathbf{J} \end{pmatrix} = \sum_m \begin{pmatrix} \bar{\rho}_m(r_g, z_g, t) \\ \bar{\mathbf{J}}_m(r_g, z_g, t) \end{pmatrix} e^{im\phi}, \quad (24)$$

where the  $\bar{\phantom{x}}$  refers to a quantity defined only on the grid. The continuity equation can be written as

$$\frac{\bar{\partial}}{\partial t} \rho + \bar{\nabla}_\perp \cdot \mathbf{J}_\perp + \frac{1}{r} \frac{\partial}{\partial \phi} J_\phi = 0, \quad (25)$$

where  $\perp$  refers to the  $r$ - $z$  plane. Substituting Eqs. (23) and (24) into Eq. (25) gives

$$\begin{aligned} \sum_m e^{im\phi} \left\{ \sum_p \frac{1}{\Delta t} [S_r(r_g - r_p^{n+1}) S_{\phi,m}(\phi_p^{n+1}) S_z(z - z_p^{n+1}) \right. \\ \left. - S_r(r_g - r_p^n) S_{\phi,m}(\phi_p^n) S_z(z - z_p^n)] \right. \\ \left. + \bar{\nabla}_\perp \cdot \bar{\mathbf{J}}_{\perp,m}^{n+\frac{1}{2}} + \frac{im}{r} \bar{J}_{\phi,m}^{n+\frac{1}{2}} \right\} = 0 \end{aligned} \quad (26)$$

We next recognize that by definition, for each particle

$$\bar{\rho} = \sum_m \bar{\rho}_m e^{im\phi}, \quad \text{and} \quad \bar{\rho}_m = \bar{\rho}_0 S_{\phi,m}, \quad (27)$$

where  $\bar{\rho}_0$  is the charge for one particle on the  $r$ - $z$  grid for the  $m = 0$  mode (recall  $S_{\phi,0} = 1$  by normalization). Likewise

$$\bar{\mathbf{J}}_\perp = \sum_m \bar{\mathbf{J}}_{\perp,m} e^{im\phi}, \quad \text{and} \quad \bar{\mathbf{J}}_{\perp,m} = \bar{\mathbf{J}}_{\perp,0} S_{\phi,m} \quad (28)$$

in the continuous time limit. We next show that using these definitions and a  $\bar{\mathbf{J}}_{\perp,0}$  defined to conserve charge for the  $m = 0$  mode (what already existing in OSIRIS) leads to an expression for  $\bar{\mathbf{J}}_\perp$ . Substituting these expressions into Eq. (26) gives for each  $m$  and  $p$  in the sum

$$\begin{aligned} \frac{1}{\Delta t} [S_r(r_g - r_p^{n+1}) S_{\phi,m}(\phi_p^{n+1}) S_z(z_g - z_p^{n+1}) - S_r(r_g - r_p^n) S_{\phi,m}(\phi_p^n) S_z(z_g - z_p^n)] \\ + S_{\phi,m}(\phi_p^{n+\frac{1}{2}}) \bar{\nabla}_\perp \cdot \bar{\mathbf{J}}_{\perp,0}^{n+\frac{1}{2}} + \frac{im}{r} \bar{\mathbf{J}}_{\phi,m}^{n+\frac{1}{2}} = 0. \end{aligned} \quad (29)$$

By definition  $\frac{\partial}{\partial t} \bar{\rho}_0 + \bar{\nabla}_\perp \cdot \bar{\mathbf{J}}_{\perp,0} = 0$ , so we are left with

$$\begin{aligned} \bar{J}_{\phi,m}^{n+\frac{1}{2}} = & i \frac{1}{\Delta t} \frac{r}{m} \{ S_r(r_g - r_p^{n+1}) S_z(z_g - z_p^{n+1}) [S_{\phi,m}(\phi_p^{n+1}) - S_{\phi,m}(\phi_p^{n+\frac{1}{2}})] \\ & - S_r(r_g - r_p^n) S_z(z_g - z_p^n) [S_{\phi,m}(\phi_p^n) - S_{\phi,m}(\phi_p^{n+\frac{1}{2}})] \}. \end{aligned} \quad (30)$$

For  $S_\phi = \delta(\phi - \phi_p)$  we have  $S_{\phi,m} = \frac{1}{2\pi} e^{-im\phi_p}$ . We then define  $\bar{\phi}_p \equiv \frac{\phi_p^{n+1} + \phi_p^n}{2}$  and  $\Delta\phi_p \equiv \phi_p^{n+1} - \phi_p^n$ , to obtain the result we use in OSIRIS for each particle,

$$\begin{aligned} \bar{J}_{\phi,m} = & i \frac{r}{m} \frac{1}{\Delta t} \frac{e^{-im\bar{\phi}_p}}{2\pi} [S_r(r_g - r_p^{n+1}) S_z(z_g - z_p^{n+1}) (e^{im\frac{\Delta\phi_p}{2}} - 1) \\ & - S_r(r_g - r_p^n) S_z(z_g - z_p^n) (e^{-im\frac{\Delta\phi_p}{2}} - 1)], \end{aligned} \quad (31)$$

where the particle shapes in  $r$  and  $z$  are still general. Currently, OSIRIS implements linear, and quadratic, interpolation for the new algorithm. The treatment of the current at the boundary is a simple extension of what has already been implemented in the  $r$ - $z$  version of the OSIRIS framework. Due to the finite size of the particles, some current is deposited in the guard cells located across the physical access. Due to the symmetry of the azimuthal modal geometry, we can merely ‘fold’ these current values into the physical cells located above the access, at each time step ( $J^{m,i,j=0,1,1}$  is added to  $J^{0,1,2}$ ,  $J^{0,1,0}$  is added to  $J^{0,1,3}$ , and so on).

### 3.3. Complex exponentials

When evaluating expressions like Eqs. (1) and (31), you need to evaluate the complex exponential  $e^{im\phi}$ . The particle variables are stored in Cartesian coordinates, and nowhere in the simulation is  $\phi$  directly stored or calculated. In addition, evaluating trigonometric functions will be computationally inefficient. Instead, we use double and triple angle formulas to obtain these values up to  $m = 4$ ,

$$e^{i\phi} = (x + iy)/r \quad (32)$$

$$e^{i2\phi} = ((x^2 - y^2) + 2ixy)/r \quad (33)$$

$$e^{i3\phi} = (4x^3/r^3 - 3x/r) - i(y^3/r^3 - 3y/r) \quad (34)$$

$$e^{i4\phi} = ((x^2 - y^2)^2 - 4x^2y^2)/r^4 + 4ixy(x^2 - y^2)/r^4. \quad (35)$$

This same optimization is used by Lifschitz [1]. In order to calculate  $e^{-im\phi}$  one only needs to swap the sign of the imaginary part. One may extend this method to an arbitrary number of modes using the exponential relation  $e^{im\phi} = e^{i\phi} \times e^{i(m-1)\phi}$ , which is what is done in OSIRIS to capture any number of modes specified by the user.

## 4. Results

In this section we present examples from simulations using the new algorithm. We present simulation results for a laser wakefield accelerator (LWFA), a plasma wakefield accelerator (PWFA), and an LWFA case with beam loading (combining the laser and beam propagation capabilities) case respectively. In [1] only an LWFA example was given. We also demonstrate the degree to which Gauss’ law is conserved with the new current deposit algorithm. The new algorithm has many more potential applications than LWFA and we will discuss some in the conclusions and directions for future work section. For the ‘‘hybrid’’  $r$ - $z$  simulations, we typically use 2 particles per cell in the  $r$ - $z$  directions, and 8 or 16 particles distributed evenly over  $0 \leq \phi < 2\pi$  (the particles are distributed along spokes at each  $z$ ). The former can be considered as 16 particles per cell when comparing to the speed-up from the full 3D simulation. The effect of the particle resolution in  $\phi$  will be discussed for some of the examples, but for these simulations 8 particles appeared to be enough to capture the physics. We note that different methods for initiating the particles can be considered and we leave this for future work.

For the LWFA simulations, we model the example given in Lu et al., [27]. In this example a circularly polarized 200 TW, 30 fs, 0.8  $\mu\text{m}$  laser pulse with a spot size of 19.5  $\mu\text{m}$  propagates through a fully ionized plasma of density  $n = 1.5 \times 10^{18} \text{ cm}^{-3}$ . The laser has a normalized vector potential of magnitude  $a_0 = 4$ . In Ref. [27], it was found using full 3D OSIRIS simulations that such a laser could generate an ultrashort (10 fs) self-injected mono-energetic bunch with an energy centered at 1.5 GeV. We have reproduced the 3D simulation for this paper using quadratic splines (linear splines were used in [27]).

### 4.1. Charge conservation tests

We start by checking the degree to which charge, i.e., Gauss’ law is conserved. To test the effectiveness of the deposition scheme in Eq. (31), we need to carefully examine Gauss’ law for the new algorithm. We begin by expanding Gauss’ law as per Eq. (1),

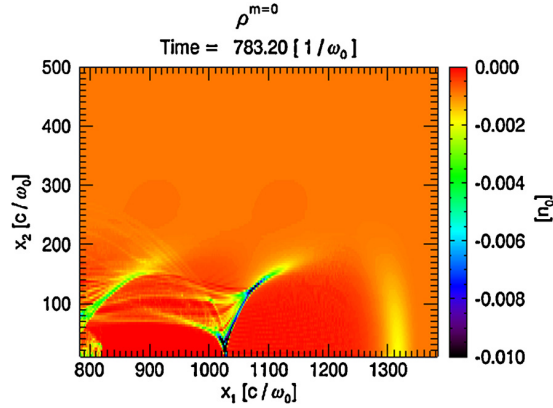


**Fig. 2.** A wake formed by a circularly polarized laser penetrating 0.1 mm into the plasma, presented here in the  $m = 0$  azimuthal mode of the charge density. The charge conservation tests presented in Fig. 4 correspond to this result of this simulation. If you take the divergence of the electric fields in mode 0, it will correspond to this plot exactly.

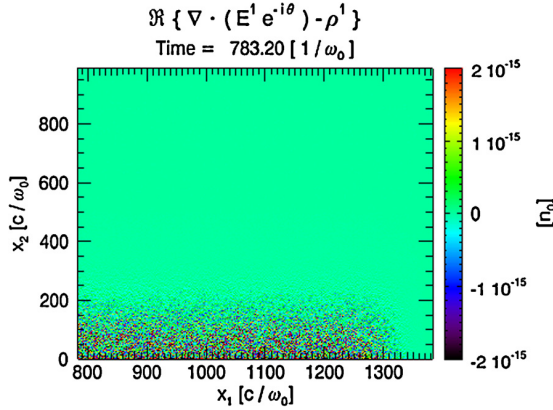


**Fig. 3.** The deviation of the charge conservation (Gauss' law) of the real part of mode  $m = 1$ , for a simulation utilizing quadratic particle interpolation. The deviation in the Gauss' law is maintained to within the accuracy of double precision arithmetic.

$$\nabla \cdot \mathbf{E} - \rho = \Re \left\{ \sum_m \nabla \cdot [\mathbf{E}^m(r, z) e^{im\phi}] - \sum_m \rho^m(r, z) e^{im\phi} \right\} = 0 \quad (36)$$

$$\implies \nabla_{\perp} \cdot \mathbf{E}^m + i \frac{m}{r} E_{\phi} - \rho^m = \frac{1}{r} \frac{\partial}{\partial r} (r E_r) + \frac{\partial E_z}{\partial z} + i \frac{m}{r} E_{\phi} - \rho^m = 0. \quad (37)$$

This means that the charge of each mode must be conserved independently from each other mode, and that the divergence is simultaneously affected by both the real and imaginary parts of the fields. If Eq. (37) is not satisfied, as would be the case in a non-charge-conserving code, we would have to add a correction to the longitudinal part of the electric field (this was done in [1]). We used the LWFA case described above as the test case. For these tests we used a smaller computational window of dimensions  $76.4 \mu\text{m} \times 127 \mu\text{m}$ , and  $3000 \times 256$  grid points. We let the laser pulse propagate (0.1 mm) into the plasma, so that a well defined wake is formed as shown in Fig. 2. We used 2 particles per cell in the  $r$ - $z$  direction and 8 particles in the  $\phi$  direction, giving a total of 16 particles per cell. We ran simulations keeping up to the 2nd harmonic and the charge conservation of each mode was tested rigorously. Both linear and quadratic interpolations were tested (the particle shape in the  $\phi$  direction was a delta function). The output of the charge conservation diagnostic for the real part of mode 1 (for which the numerical noise was the greatest) is shown in Fig. 3. In these simulations we used double precision floating point numbers, which have 15 numerical orders of accuracy in decimal units. When subtracting two nearly identical numbers, a roundoff error  $10^{-15}$  below the working order of magnitude, which in this case is 2.83 will be observed. In Fig. 3 charge is conserved to within the roundoff error of the double precision arithmetic at each grid point of the simulation. The noise is slightly larger as  $r$  approaches zero, since the field values are scaled to  $1/r$  when calculating the divergence.

The lineout along the axis of the charge conservation for each mode is presented in Fig. 4. The numerical noise was slightly higher for the quadratic interpolation than the linear interpolation, but in each case the charge conservation was satisfied to roundoff error for every mode. In addition, the largest residual error is in the  $m = 1$  harmonic which includes the laser field. The error in Gauss's law can accumulate over time since it is an integral over time of the continuity equation.



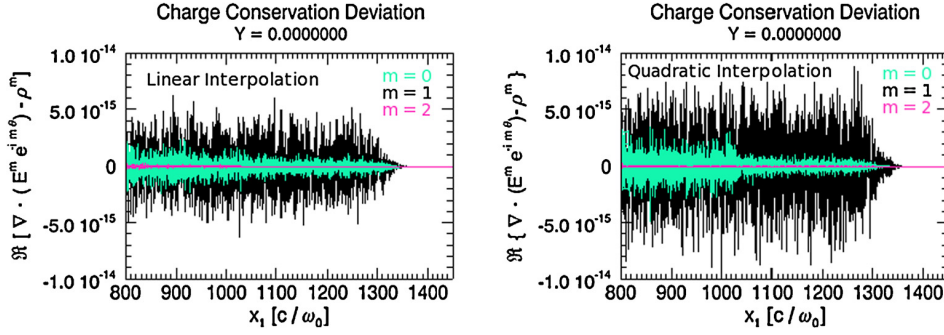


Fig. 4. The deviation of charge conservation (Gauss' law), along  $r=0$ , for modes 0, 1, and 2. Quadratic interpolation (right) shows a slightly larger roundoff error than the linear interpolation result (left). The error in  $m=1$  (the component with the laser) is the largest in both cases.

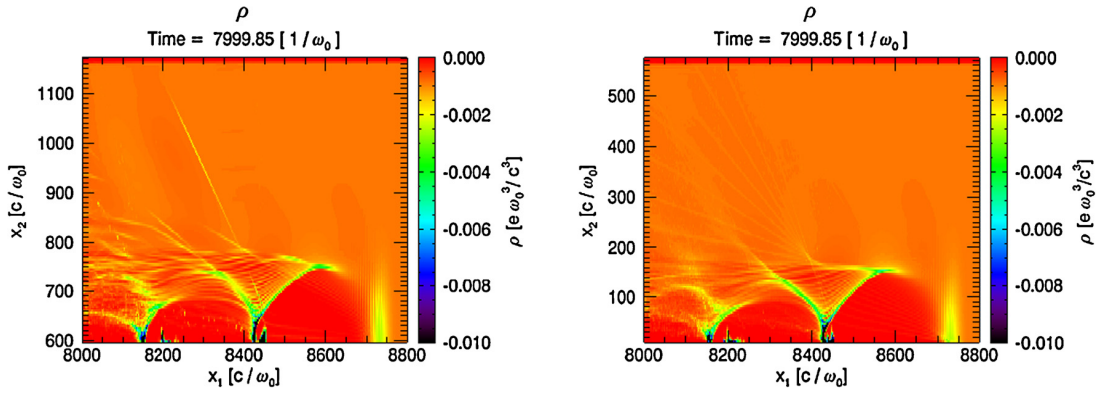


Fig. 5. These are the electron charge density distributions for the full 3D simulation at 0.1 cm (left) and the cylindrical mode simulation at 0.1 cm (right). The cylindrical mode density cross-sections are taken at  $\phi=0$ , which corresponds to the top half of the cross section of the 3D simulation at  $y=0.0$ . Both simulations used quadratic interpolation, and both simulations used the same cell sizes.

However, the signs of the errors are random so the accumulation of the errors will be less than the accumulation of the magnitude of the errors. In the future we may include a Marder's correction to clean up any accumulated errors to the longitudinal part of the electric field if necessary. These tests validate the use of Eq. (31) and the existing current depositing algorithm for the  $m=0$  harmonic in the  $r$ - $z$  grid. We have also tested the charge conservation for many more cases.

#### 4.2. Comparison of LWFA results with 3D simulations

We next present results from the LWFA simulation described earlier keeping only up to the  $m=1$  harmonic. The LWFA simulation discussed at the beginning of this section was run to about 0.1 cm. For the full 3D simulation, a  $4000 \times 300 \times 300$  grid with dimensions  $101.9 \mu\text{m} \times 149.2 \mu\text{m} \times 149.2 \mu\text{m}$  was used with 2 particles per cell. The time step was chosen as close as possible to the Courant limit. The hybrid  $r$ - $z$  simulation used a computational window of dimensions  $101.9 \mu\text{m} \times 74.6 \mu\text{m}$  and  $4000 \times 150$  grid points. The simulation was conducted with 2 particles per cell in the  $r$ - $z$  directions with 16 particles in the  $\phi$  direction. For typical LWFA simulations, the  $m=1$  mode captures enough modal asymmetry to effectively simulate the physics for round laser beams without any tilts. In later publications we will describe the additional physics that can be studied by including more harmonics. Note that the wake excited by a linearly or circularly polarized cylindrically symmetric laser is itself cylindrically symmetric. For the hybrid  $r$ - $z$  simulations we use a time step as close to the stability limit as possible. We note that we empirically found that this limit is close to the 3D Courant limit where we use an "effective" cell size in the  $\phi$  direction roughly given by  $\Delta r \pi / m_{\text{max}}$  where  $m_{\text{max}}$  is the highest harmonic kept. In addition, we found that only 8 particles across  $0 \leq \phi < 2\pi$  were needed to avoid substantial noise in the first bubble. The signal-to-noise ratio scales as  $\sqrt{m_{\text{max}}}$ , so the fewer modes you use the fewer particle resolution you need across the  $\phi$  coordinate [1]. Therefore, the effective speed-up is roughly proportional to the number of simulation particles. In a 3D simulation  $n_p^{3D} = N_x N_y N_z N_{pc}$  particles are used, where  $N_x$ ,  $N_y$ , and  $N_z$  are the number of cells in each Cartesian direction, and  $N_{pc}$  is the number of particles per cell. In the 2D hybrid simulation it is  $n_p^{2D\text{-hybrid}} = N_z \frac{N_x}{2} N_{p,r-z} N_{p,\phi}$ , where  $N_{p,r-z}$  is the number of particles in the  $r$ - $z$  plane and  $N_{p,\phi}$  is the number of particles distributed over  $0 \leq \phi < 2\pi$ .

We show results after the laser was propagated through the plasma over a distance of 0.1 cm. Two-dimensional density plots corresponding to a cut across the data of the 3D simulation or the  $\phi=0$  plane for the hybrid simulation are shown in Fig. 5. The 2D density contours for the wake were identical throughout most of the simulation, aside from a small number

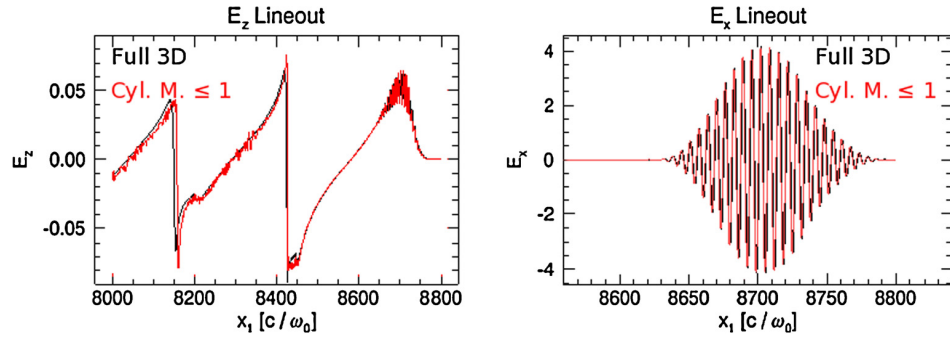


**Fig. 6.** Lineouts along the laser for the  $E_z$  and  $E_x$  fields for the 3D (black) and 2D hybrid (red) simulations. The lineout of  $E_x$  is zoomed in to more easily see the matching of the phase of the laser. (For interpretation of the references to color in this figure legend, the reader is referred to the web version of this article.)

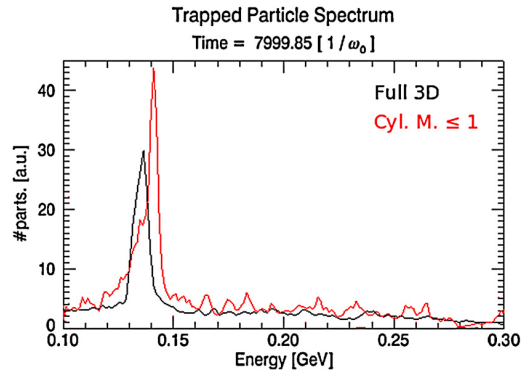


**Fig. 7.** The spectrum of the trapped particles from the 3D (black) and 2D hybrid (red) simulations. The laser has propagated 0.1 cm into the plasma. (For interpretation of the references to color in this figure legend, the reader is referred to the web version of this article.)

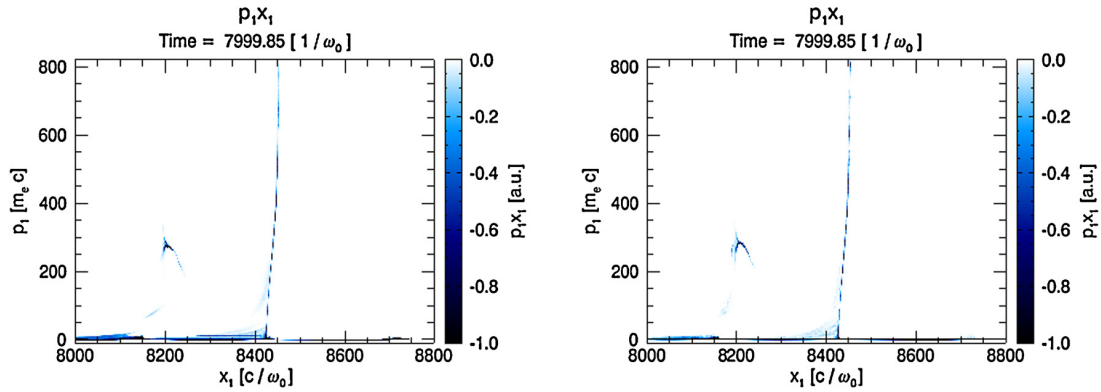


**Fig. 8.** The  $p_1 x_1$  phase-space plot for the 3D (left) and 2D hybrid (right) simulations, after the laser had propagated 0.1 cm into the plasma.

of particles which had been trapped late in the full 3D simulation. However, this did not significantly affect the acceleration process of the mono-energetic bunch. The accelerating electric fields of the 3D and the 2D hybrid modal simulations are shown on the left hand side, and the laser profiles are shown on the right hand side of Fig. 6. The spectrum of the trapped particles in the two cases are shown in Fig. 7 and longitudinal momentum distribution in Fig. 8. There is excellent agreement between the hybrid simulation keeping up to mode 1 and the 3D simulation, both quantitatively and qualitatively.

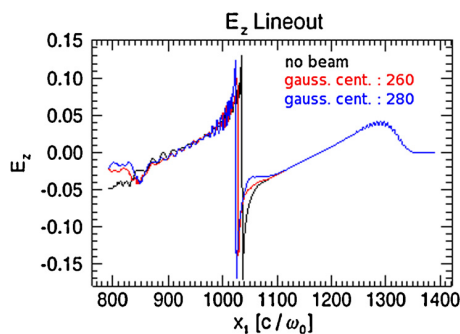


**Fig. 9.** Lineouts of  $E_z$  along the laser for LWFA simulations including beam loading. The black is the wake without beam loading. The red and blue lines show the wake as it is loaded with a Gaussian beam with its center at  $z_0 = 260c/\omega_0$ , and  $z_0 = 280c/\omega_0$ , respectively. The center of the laser is initially at  $503c/\omega_0$ , and the laser has propagated 0.1 mm into the plasma.

#### 4.3. Beam loading in LWFA

Implementing the new algorithm into OSIRIS immediately provides the capability of modeling beam driven plasma based acceleration concepts as well as beam loading of laser produced wakes as well as modeling beam loading over pump depletion distances. Beam loading in particle beam driven wakes has been studied extensively using  $r$ - $z$  PIC simulations as well as 3D quasi-static PIC simulations. On the other hand, beam loading studies for laser driven wakes has had to rely on a limited number of full 3D simulations or ponderomotive guiding center simulations (3D,  $r$ - $z$ , or quasi-static). However, the ponderomotive guiding center has limitations for high laser intensities. Therefore, combining the ability for studying laser propagation in  $r$ - $z$  together with the ability to launch a particle beam will permit rapid parameter scans for LWFA beam loading scenarios. We next show preliminary results where we beam load the wake in the LWFA simulations shown previously. Recently, Tzoufras et al. [28] described how to analyze beam loading in nonlinear wakes, but there has been very little computational studies of beam loading in nonlinear wakes created by lasers due to the inability to routinely study this in three dimensions. Here we show that the hybrid scheme could be a very useful tool for such studies. We loaded a Gaussian beam with  $k_p\sigma_z = 0.5$  and  $k_p\sigma_r = 0.2$ , and a peak density such that  $(n_b/n_p)k_p^2\sigma_r^2 \equiv \Lambda \approx 2$  into the wake. Here  $1/k_p$  is the plasma skin depth, and  $\sigma_z$  and  $\sigma_r$  are the standard deviation of the Gaussian profile in the  $r$  and  $z$  dimensions, respectively.  $n_b$  is the peak density of the beam profile, and  $n_p$  is the density of the plasma. The charge per unit length,  $\Lambda$ , is the critical normalized parameter which describes the degree of nonlinearity in the wakefield driven by the beam [27,29]. For  $n_p = 1.5 \times 10^{18} \text{ cm}^{-3}$ , this corresponds to a bunch with  $\sigma_z = 2.2 \text{ }\mu\text{m}$ ,  $\sigma_r = 0.87 \text{ }\mu\text{m}$ , and  $N \approx 1.9 \times 10^9$  ( $\approx 300 \text{ pC}$ ). The spacing between the laser and the particle beam was varied. The trailing beam was initialized with an energy of 20 GeV, i.e., with a proper velocity of  $\gamma v_z = 40000.0c$ . The beam loading of the wake is presented in Fig. 9. This figure shows how the wake is loaded differently depending on the spacing between the laser and the trailing beam. In the future, the hybrid scheme will enable routine studies of how the qualities of the trailing bunch and the overall efficiency depend on the location, shape, and current profile of the bunch. It will provide detailed parameter scans including the lowest order three dimensional effects and point towards parameters for full 3D simulations.

#### 4.4. Hosing of particle beam driver

In this section we present an example of a particle beam driver, i.e., PWFA. Axisymmetric  $r$ - $z$  simulations have been effectively utilized to study PWFA. However, such simulations cannot investigate asymmetric effects such as hosing and asymmetric spot-size effects. Here we present a sample result for a PWFA simulation including  $m \leq 2$  harmonics. The parameters are  $n_b/n_p = 10.0$ , with  $k_p\sigma_z = 1$ , and  $k_p\sigma_r = 0.2$ ,  $\Lambda = 0.4$ . The simulation box size was  $600c/\omega_p \times 120c/\omega_p$  in the  $z$  and  $r$  directions, respectively. The initial beam proper velocity was  $\gamma v_z = 40000.0c$ . The plasma was simulated with 16 particles across  $\phi$ , while the beam was simulated with 32 particles across  $\phi$ . There were 4 particles per  $r$ - $z$  cell both species. The beam was initialized as an azimuthally symmetric beam.

For this simulation we kept up to the 2nd harmonic. Initially, as expected, the beam produces an azimuthally symmetric wake (and the beam remains symmetric). For short propagation distances the  $m = 1$  and  $m = 2$  modes are not important and the 2D  $r$ - $z$  and hybrid 2D results look the same as seen in Fig. 10. The 2D  $r$ - $z$  plot was generated by mirroring the result from positive  $r$  to “negative”  $r$ . We also note that the 2D  $r$ - $z$  code and full 3D results have been compared for round beams with no tilt and excellent agreement was found [30]. For longer propagation distances hosing occurs. Hosing theory [31,32] is based on coupling the  $m = 1$  modes for the centroid of the beam to that of the wake. In this simulation hosing grows from random noise in the beam density and it can clearly be seen in Fig. 11. The upper plot is from a 2D  $r$ - $z$  simulation where hosing is precluded. The lower plot is from a 2D hybrid simulation. We emphasize that the result from a 2D hybrid and full 3D simulation will not quantitatively agree if physics which grows from a random noise source is important. However, if the dominant source for growth is the beam tilt agreement should exist and the growth rates should agree well. After a longer period of time the spot size begins to deviate due to a higher modal ( $m = 2$ ) effect. This is shown

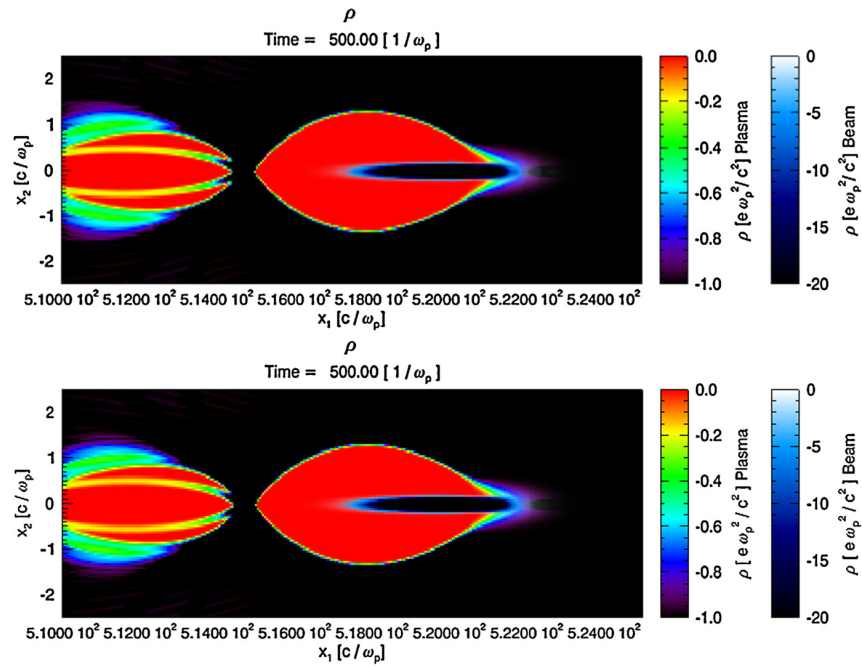


**Fig. 10.** The density from PWFA simulations with a 2D cylindrical geometry simulation (top) and an  $m \leq 2$  hybrid simulation (bottom). The beam has only moved  $500c/\omega_p$  into the plasma. The bottom plot was created by summing the modes at  $\phi = 0$  on the top half of the grid, and at  $\phi = \pi$  on the bottom, which gives us the  $y = 0$  cross-section of the three-dimensional beam. The 2D cylindrical simulation plot simply mirrors the bottom half from the top. For short distances the two simulations agree very well.

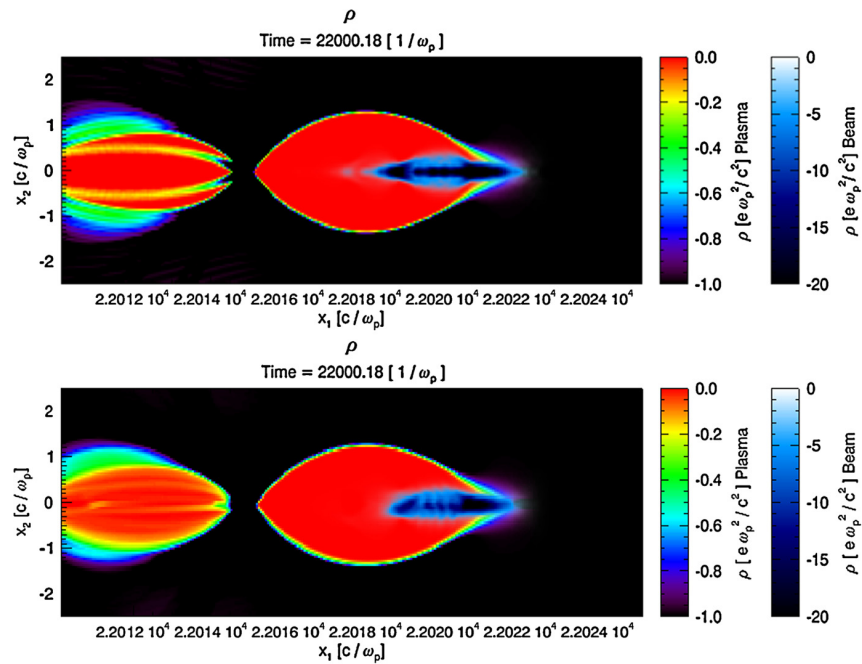


**Fig. 11.** The density plots after the beam has propagated  $22000.18c/\omega_p$  into the plasma. Hosing is observed  $m \leq 2$  hybrid simulation (bottom). A result from an equivalent 2D cylindrical simulation is shown for comparison (top). The bottom plot was created by summing the modes at  $\phi = 0$  on the top half of the grid, and at  $\phi = \pi$  on the bottom, which gives us the  $y = 0$  cross-section of the three-dimensional beam. The 2D cylindrical simulation plot was generated by simply mirroring the bottom half from the top.

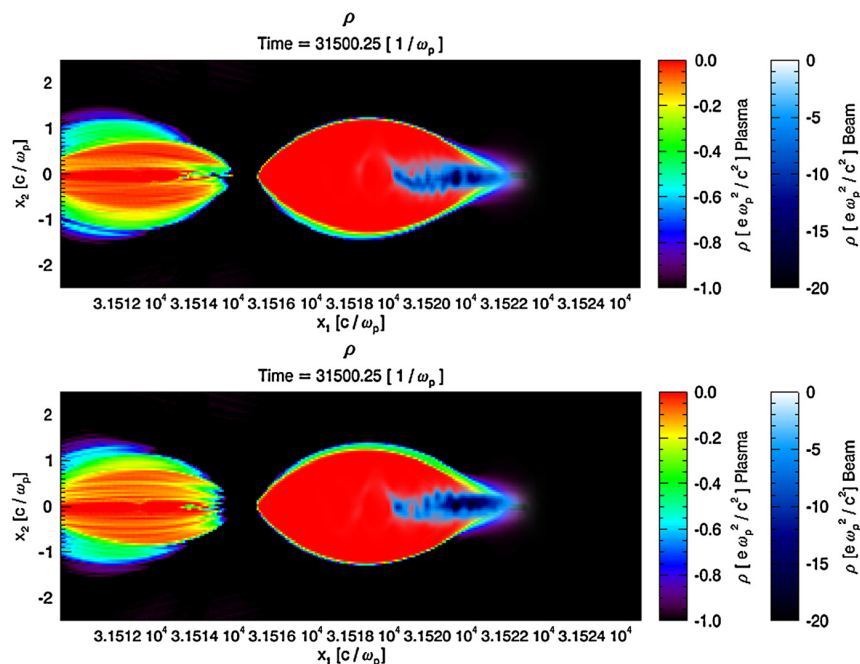


Fig. 12. Cross section of the beam and plasma density for the  $x$ - $z$  (top) and  $y$ - $z$  (bottom) planes.

in Fig. 12. If the  $m = 2$  was not present then hosing would only occur in a single plane. The fact that it is occurring in both planes shows that  $m = 2$  is present. In principle, the more azimuthally asymmetric the problem being simulated, the more modes we would want to retain. For example, if an initial tilt was provided for the beam, the greater the tilt, the greater number of modes we would want to converge with full 3D results. Future work will include modeling beams with tilts and studying how the results change as the harmonic number increases.

## 5. Conclusion

In this paper, we describe how we have implemented into OSIRIS the ability to expand the fields on an  $r$ - $z$  grid into an arbitrary number of Fourier harmonics in  $\phi$ . We used the fact that this is a hybrid PIC and gridless algorithm to develop a rigorous charge conserving current deposit for the hybrid algorithm. We showed that if the current amplitude for each harmonic in the  $r$ - $z$  plane is defined as  $\mathbf{J}_{\perp,m} = \mathbf{J}_{\perp,0} e^{-im\phi_p}$  where  $\mathbf{J}_{\perp,0}$  is the current for the particle in the existing axisymmetric code and  $\phi_p$  is the angle of the particle at the velocity time indicates, then an expression for  $J_\phi$  on the grid can be derived that conserves charge for any particle order. We give examples that show the new scheme conserved charge to round off errors. We also present examples demonstrating the new algorithm's ability to efficiently study key physics in plasma based acceleration including LWFA, PWFA, and beam loading.

The new algorithm reproduces qualitatively and quantitatively results from Lu et al. [27] in the non-linear self-guided blowout regime for LWFA. The 3D Cartesian simulation requires  $2 \times 300 = 600$  more cells ( $2 \times N_z$  where  $N_z$  is the number of cells in the transverse direction, and the factor of 2 comes from only needing half the box in  $r$ ) and  $600/8 = 75$  more particles (the factor of 8 comes from the number of particle empirically needed in  $\phi$ ).

We also showed that keeping a few harmonics allows hosing of a particle beam to be studied and that both beam loading in laser driven wakes and hosing of the trailing beam can be studied by keeping only the  $m = 0$  and  $m = 1$  modes. The new code is currently  $\approx 1/2$  the speed of the  $r$ - $z$  code in a per particle basis when the  $m = 1$  mode is included.

Directions for future work include optimizing the algorithm to reduce the overhead of keeping  $m$  copies of the mesh and interpolating the forces on the particles, including ionization, binary collision, and the PGC approximation, as well as additional field solvers with improved dispersion properties, and boundary conditions such as perfectly matched layers. We are interested in using the new hybrid code to study asymmetric spot size self-modulation and self-focusing and other self-modulation processes [33–35, and references therein] for the laser and also how these couple to related instabilities for the trailing particles. We are also interested in using the new hybrid code to study laser solid interactions involved in fast ignition [36–38] and proton acceleration [39], as well as stimulated Raman scattering [40,41] and the high frequency hybrid instability of a single speckle [42]. We will also pursue using this new scheme in a Lorentz boosted frame to obtain even more dramatic speed-ups.

## Acknowledgements

This work was supported by the U.S. Department of Energy contracts DE-SC0008491, DE-SC0008316, DE-NA0001833, DE-FC02-04ER54789, DE-FG02-92ER40727, U.S. National Science Foundation under grants ACI 1339893, the European Research Council (EU) through the Advanced Grant Accelerates (ERC-AdG2010 no. 267841) and by the European Commission through Laserlab-Europe, EC-GA 284464, and in China under the NSFC Grant 11175102, thousand young talents program.

## References

- [1] A. Lifschitz, X. Davone, E. Lefebvre, J. Faure, C. Rechatin, V. Malka, Particle-in-cell modelling of laser–plasma interaction using Fourier decomposition, *J. Comput. Phys.* 228 (5) (2009) 1803–1814, <http://dx.doi.org/10.1016/j.jcp.2008.11.017>.
- [2] C.D. Decker, W.B. Mori, T. Katsouleas, Particle-in-cell simulations of Raman forward scattering from short-pulse high-intensity lasers, *Phys. Rev. E* 50 (5) (1994) R3338–R3341.
- [3] P. Mora, T. Antonsen, Kinetic modeling of intense, short laser pulses propagating in tenuous plasmas, *Phys. Plasmas* 4 (1) (1997) 217–229, <http://dx.doi.org/10.1063/1.872134>.
- [4] C. Huang, V. Decyk, M. Zhou, W. Lu, W. Mori, QuickPIC: a highly efficient fully parallelized pic code for plasma-based acceleration, *J. Phys. Conf. Ser.* 46 (2006) 190–199, <http://dx.doi.org/10.1088/1742-6596/46/1/026>.
- [5] W. An, V.K. Decyk, W.B. Mori, T.M. Antonsen Jr., An improved iteration loop for the three dimensional quasi-static particle-in-cell algorithm: QuickPIC, *J. Comput. Phys.* 250 (2013) 165–177, <http://dx.doi.org/10.1016/j.jcp.2013.05.020>.
- [6] D. Gordon, W. Mori, T. Antonsen, A ponderomotive guiding center particle-in-cell code for efficient modeling of laser–plasma interactions, *IEEE Trans. Plasma Sci.* 28 (4) (2000) 1224–1232.
- [7] J.L. Vay, Noninvariance of space- and time-scale ranges under a Lorentz transformation and the implications for the study of relativistic interactions, *Phys. Rev. Lett.* 98 (13) (2007), <http://dx.doi.org/10.1103/PhysRevLett.98.130405>.
- [8] J.L. Vay, C.G.R. Geddes, E. Cormier-Michel, D.P. Grote, Effects of hyperbolic rotation in Minkowski space on the modeling of plasma accelerators in a Lorentz boosted frame, *Phys. Plasmas* 18 (3) (2011), <http://dx.doi.org/10.1063/1.3559483>.
- [9] S.F. Martins, R.A. Fonseca, W. Lu, W.B. Mori, L.O. Silva, Exploring laser-wakefield-accelerator regimes for near-term lasers using particle-in-cell simulation in Lorentz-boosted frames, *Nat. Phys.* 6 (4) (2010) 311–316, <http://dx.doi.org/10.1038/NPHYS1538>.
- [10] S.F. Martins, R.A. Fonseca, J. Vieira, L.O. Silva, W. Lu, W.B. Mori, Modeling laser wakefield accelerator experiments with ultrafast particle-in-cell simulations in boosted frames, in: 51st Annual Meeting of the Division-of-Plasma-Physics of the American-Physics-Society, Atlanta, GA, November 02–06, 2009, *Phys. Plasmas* 17 (5) (2010), <http://dx.doi.org/10.1063/1.3358139>.
- [11] C. Benedetti, C. Schroeder, E. Esarey, W. Leemans, Efficient modeling of laser–plasma accelerators using the ponderomotive-based code inf&no, in: *Proceedings of ICAP2012, 2012*.
- [12] X. Xu, P. Yu, S.F. Martins, F.S. Tsung, V.K. Decyk, J. Vieira, R.A. Fonseca, W. Lu, L.O. Silva, W.B. Mori, Numerical instability due to relativistic plasma drift in EM-PIC simulations, *Comput. Phys. Commun.* 184 (11) (2013) 2503–2514, <http://dx.doi.org/10.1016/j.cpc.2013.07.003>.
- [13] P. Yu, X. Xu, V.K. Decyk, W. An, J. Vieira, F.S. Tsung, R.A. Fonseca, W. Lu, L.O. Silva, Modeling of laser wakefield acceleration in Lorentz boosted frame using EM-PIC code with spectral solver, *J. Comput. Phys.* 266 (1) (2014) 124–138, <http://dx.doi.org/10.1016/j.jcp.2014.02.016>.
- [14] B.B. Godfrey, J.-L. Vay, Numerical stability of relativistic beam multidimensional PIC simulations employing the Esirkepov algorithm, *J. Comput. Phys.* 248 (2013) 33–46, <http://dx.doi.org/10.1016/j.jcp.2013.04.006>.
- [15] S. Corde, C. Thauray, A. Lifschitz, G. Lambert, K.T. Phuoc, X. Davoine, R. Lehe, D. Douillet, A. Rousse, V. Malka, Observation of longitudinal and transverse self-injections in laser–plasma accelerators, *Nat. Commun.* 4 (2013), <http://dx.doi.org/10.1038/ncomms2528>.
- [16] B. Marder, A method for incorporating Gauss law into electromagnetic PIC codes, *J. Comput. Phys.* 68 (1) (1987) 48–55, [http://dx.doi.org/10.1016/0021-9991\(87\)90043-X](http://dx.doi.org/10.1016/0021-9991(87)90043-X).
- [17] A.B. Langdon, On enforcing Gauss law in electromagnetic particle-in-cell codes, *Comput. Phys. Commun.* 70 (3) (1992) 447–450.
- [18] C. Birdsall, A. Langdon, *Plasma Physics via Computer Simulation*, Adam Hilger Ser. Plasma Phys., McGraw–Hill, 1985, <http://books.google.com/books?id=7TmBAQAIAAJ>.
- [19] R. Fonseca, L.O. Silva, F. Tsung, V. Decyk, W. Lu, C. Ren, W.B. Mori, S. Deng, S. Lee, T. Katsouleas, OSIRIS: a three-dimensional, fully relativistic particle in cell code for modeling plasma based accelerators, in: *Lect. Notes Comput. Sci.*, vol. 2331, 2002, pp. 342–351.
- [20] J. Dawson, The electrostatic sheet model for a plasma and its modification to finite-size particles, in: B. Alder, S. Fernbach, M. Rotenberg (Eds.), *Methods in Computational Physics. IX. Plasma Physics*, Academic Press, London, UK, 1970, pp. 1–28.
- [21] B. Godfrey, M.R.C.A. NM, The IPROP Three-Dimensional Beam Propagation Code, Defense Technical Information Center, 1985, [http://books.google.com/books?id=hos\\_OAAACAAJ](http://books.google.com/books?id=hos_OAAACAAJ).
- [22] B. Godfrey, M.M. Campbell, M.R.C.A. NM, IVORY: A Three-Dimensional Beam Propagation Code, Defense Technical Information Center, 1982.
- [23] G. Constantinescu, S. Lele, A highly accurate technique for the treatment of flow equations at the polar axis in cylindrical coordinates using series expansions, *Comput. Phys. Commun.* 183 (1) (2002) 165–186, <http://dx.doi.org/10.1006/jcph.2002.7187>.
- [24] K. Yee, Numerical solution of initial boundary value problems involving Maxwell's equations in isotropic media, *IEEE Trans. Antennas Propag.* 14 (3) (1966) 302–307, <http://dx.doi.org/10.1109/TAP.1966.1138693>.
- [25] T. Esirkepov, Exact charge conservation scheme for particle-in-cell simulation with an arbitrary form-factor, *Comput. Phys. Commun.* 135 (2) (2001) 144–153, [http://dx.doi.org/10.1016/S0010-4655\(00\)00228-9](http://dx.doi.org/10.1016/S0010-4655(00)00228-9).
- [26] J. Villaseñor, O. Buneman, Rigorous charge conservation for local electromagnetic field solvers, *Comput. Phys. Commun.* 69 (1992) 306–316, [http://dx.doi.org/10.1016/0010-4655\(92\)90169-Y](http://dx.doi.org/10.1016/0010-4655(92)90169-Y).
- [27] W. Lu, M. Tzoufras, C. Joshi, F. Tsung, W. Mori, J. Vieira, R. Fonseca, L. Silva, Generating multi-GeV electron bunches using single stage laser wakefield acceleration in a 3D nonlinear regime, *Phys. Rev. Spec. Top., Accel. Beams* 10 (2007) 061301, <http://dx.doi.org/10.1103/PhysRevSTAB.10.061301>.
- [28] M. Tzoufras, W. Lu, F. Tsung, C. Huang, W. Mori, T. Katsouleas, J. Vieira, R. Fonseca, L. Silva, Beam loading by electrons in nonlinear plasma wakes, *Phys. Plasmas* 16 (2009) 056705, <http://dx.doi.org/10.1063/1.3118628>.
- [29] W. Lu, C. Huang, M. Zhou, W.B. Mori, T. Katsouleas, Nonlinear theory for relativistic plasma wakefields in the blowout regime, *Phys. Rev. Lett.* 96 (2006) 165002, <http://dx.doi.org/10.1103/PhysRevLett.96.165002>.
- [30] R.G. Hemker, Particle-in-cell modeling of plasma-based accelerators in two and three dimensions, PhD thesis, University of California, Los Angeles, 2000.
- [31] D. Whittum, W. Sharp, S. Yu, M. Lampe, G. Joyce, Electron-hose instability in the ion-focused regime, *Phys. Rev. Lett.* 67 (8) (1991) 991–994, <http://dx.doi.org/10.1103/PhysRevLett.67.991>.
- [32] C. Huang, W. Lu, M. Zhou, C.E. Clayton, C. Joshi, W.B. Mori, P. Muggli, S. Deng, E. Oz, T. Katsouleas, M.J. Hogan, I. Blumenfeld, F.J. Decker, R. Ischebeck, R.H. Iversen, N.A. Kirby, D. Walz, Hosing instability in the blow-out regime for plasma-wakefield acceleration, *Phys. Rev. Lett.* 99 (25) (2007), <http://dx.doi.org/10.1103/PhysRevLett.99.255001>.

- [33] W. Mori, The physics of the nonlinear optics of plasmas at relativistic intensities for short-pulse lasers, *IEEE J. Quantum Electron.* 33 (11) (1997) 1942–1953, <http://dx.doi.org/10.1109/3.641309>.
- [34] B. Duda, W. Mori, Variational principle approach to short-pulse laser–plasma interactions in three dimensions, *Phys. Rev. E* 61 (2) (2000) 1925–1939, <http://dx.doi.org/10.1103/PhysRevE.61.1925>.
- [35] P. Sprangle, J. Krall, E. Esarey, Hose-modulation instability of laser-pulses in plasmas, *Phys. Rev. Lett.* 73 (26) (1994) 3544–3547, <http://dx.doi.org/10.1103/PhysRevLett.73.3544>.
- [36] J. Tonge, J. May, W.B. Mori, F. Fiuza, S.F. Martins, R.A. Fonseca, L.O. Silva, C. Ren, A simulation study of fast ignition with ultrahigh intensity lasers, in: 50th Annual Meeting of the Division of Plasma Physics of the American-Physical-Society, Dallas, TX, February 01, 2008, *Phys. Plasmas* 16 (5) (2009), <http://dx.doi.org/10.1063/1.3124788>.
- [37] F. Fiuza, M. Marti, R.A. Fonseca, L.O. Silva, J. Tonge, J. May, W.B. Mori, Efficient modeling of laser–plasma interactions in high energy density scenarios, *Plasma Phys. Control. Fusion* 53 (7) (2011), <http://dx.doi.org/10.1088/0741-3335/53/7/074004>.
- [38] J. May, J. Tonge, F. Fiuza, R.A. Fonseca, L.O. Silva, C. Ren, W.B. Mori, Mechanism of generating fast electrons by an intense laser at a steep overdense interface, *Phys. Rev. E* 84 (2,2) (2011), <http://dx.doi.org/10.1103/PhysRevE.84.025401>.
- [39] D. Haberberger, S. Tochitsky, F. Fiuza, C. Gong, R.A. Fonseca, L.O. Silva, W.B. Mori, C. Joshi, Collisionless shocks in laser-produced plasma generate monoenergetic high-energy proton beams, *Nat. Phys.* 8 (1) (2012) 95–99.
- [40] L. Yin, B.J. Albright, H.A. Rose, K.J. Bowers, B. Bergen, R.K. Kirkwood, Self-organized bursts of coherent stimulated Raman scattering and hot electron transport in speckled laser plasma media, *Phys. Rev. Lett.* 108 (24) (2012), <http://dx.doi.org/10.1103/PhysRevLett.108.245004>.
- [41] B.J. Winjum, J.E. Fahlen, F.S. Tsung, W.B. Mori, Anomalous hot electrons due to rescatter of stimulated Raman scattering in the kinetic regime, *Phys. Rev. Lett.* 110 (16) (2013), <http://dx.doi.org/10.1103/PhysRevLett.110.165001>.
- [42] B. Afeyan, E. Williams, Unified theory of stimulated Raman-scattering and 2-plasmon decay in inhomogeneous plasmas – high-frequency hybrid instability, *Phys. Rev. Lett.* 75 (23) (1995) 4218–4221, <http://dx.doi.org/10.1103/PhysRevLett.75.4218>.

# An Examination of the Scaling Laws for LWFA in the Self-Guided Nonlinear Blowout Regime

Asher Davidson<sup>1,a),b)</sup>, Adam Tableman<sup>1,c)</sup>, Peicheng Yu<sup>1,d)</sup>, Weiming An<sup>1,e)</sup>, Frank Tsung<sup>1,f)</sup>, Wei Lu<sup>3,g)</sup>, Ricardo A. Fonseca<sup>2,h)</sup> and Warren B. Mori<sup>1,i)</sup>

<sup>1</sup>*University of California, Los Angeles, CA 90095, USA.*

<sup>2</sup>*GoLP/Instituto de Plasmas e Fusão Nuclear, Instituto Superior Técnico, Universidade de Lisboa, Lisbon, Portugal*

<sup>3</sup>*Tsinghua University, Beijing, China*

<sup>a)</sup>Corresponding author: davidsoa@ucla.edu

<sup>b)</sup>URL: picks.idre.ucla.edu

<sup>c)</sup>tableman@physics.ucla.edu

<sup>d)</sup>tpc.1983@gmail.com

<sup>e)</sup>anweiming@ucla.edu

<sup>f)</sup>tsung@physics.ucla.edu

<sup>g)</sup>weilu@mail.tsinghua.edu.cn

<sup>h)</sup>fricardo.fonseca@iscte.pt

<sup>i)</sup>mori@physics.ucla.edu

**Abstract.** A detailed study of the scaling laws for LWFA in the self-guided, nonlinear blowout regime is presented. The study is enabled through the recent implementation of the quasi-3D algorithm into OSIRIS, which permits particle-in-cell simulations of LWFA at lower densities and higher laser energy. We find that the scaling laws continue to work well when we fix the normalized laser amplitude, pulse-length, and spot size, while reducing the plasma density. We examine parameters for which the self-injected electron energies are between 1 and 10 GeV. Over a wide parameter space, the evolution of the electron energy and laser spot size are similar when plotted in normalized units.

## INTRODUCTION

In Ref. [1], a set of phenomenological scaling laws for laser wakefield acceleration in the nonlinear blowout regime is presented and discussed. Full-scale particle-in-cell simulations were presented on how 1–2 GeV electrons could be generated for 100 TW class lasers. Differences and similarities between this regime and what is referred to as the bubble regime [2] were also presented. It was noted that the phenomenon of self-guiding does not “scale” the same as other phenomena, so that further analysis was needed to understand how this regime of LWFA would scale to 10 GeV or higher energies. In particular, as the laser energy is increased, then the ratio of the acceleration distance to the Rayleigh length increases. It was suggested in ref. [1] that to ensure self-guiding would still occur over the “longer” laser propagation distances, the normalized laser amplitude would have to scale as  $a_0 \sim (1/n_p)^{1/5}$ . At that time, simulations were not feasible to examine how self-guiding would perform at lower plasma densities. Due to a recent implementation of the quasi-3D geometry into the OSIRIS framework [3, 4], simulations that include the proper geometrical effects of self-guiding are now feasible over a wide range of plasma and laser parameters. Laser self-focusing is very different in 2D slab (cartesian) and 2D cylindrical geometries. In the quasi-3D simulations, the particle-in-cell method is used on a r-z coordinate mesh, and fields and currents are expanded into azimuthal harmonics. The particles are pushed in full 3D geometry. A laser with an azimuthally symmetric spot can be represented by the first azimuthal harmonic<sup>1</sup>, thereby permitting quasi-3D simulations for nearly round laser beams with the computational cost of a 2D

---

<sup>1</sup>Even if the spot of a laser is symmetric, the electromagnetic fields of the laser are not, in general, azimuthally symmetric.



r-z code. This has permitted us to revisit studying LWFA in the self-guided blowout regime for low plasma densities and long acceleration distances.

The issue of self-guiding, where there is a balance of diffraction with local pump depletion, brings forth two important questions that must be considered when extrapolating the scaling laws of Ref. [1] to higher electron energies. First, we want to know how well the laser remains self-guided for longer dephasing lengths, in units of Rayleigh lengths, if the normalized laser amplitude is kept constant. Second, we are interested to know how well the self-guiding and the scaling laws work, if we scale the laser amplitude as  $(1/n_p)^{1/5}$ . The goal is to achieve higher electron energy. As a result, we present two different sets of simulations: one set, in which  $a_0$  is kept constant as we scale to lower densities and longer dephasing lengths, and another, in which we scale  $a_0 \sim (1/n_p)^{1/5}$  as we explore results for lower densities.

Performing simulations at progressively lower densities, with parameters scaled to longer dephasing lengths and higher beam energies, quickly becomes computationally impractical if one were conducting fully 3D Cartesian simulations. Estimates for the number of particle steps for a sequence of such simulations are presented in Table 1. The required number of CPU hours would be proportional to the number of particle steps, if parallel scalability and load balancing are ideal, so they provide a lower estimate on the necessary CPU hours. The estimates were calculated by assuming a “standard” resolution of  $\Delta z = 0.2k_0^{-1}$ ,  $\Delta r = 0.1k_p^{-1}$ , and a box size of about  $5.2W_0$  in the longitudinal direction (width comparable to the original Lu et al. runs), and a transverse box size equal to the initial spot size times the total number of Rayleigh lengths over the dephasing lengths  $(L_d W_0 / Z_R)^2$ . We also assumed four particles were initialized per cell. When we use a quasi-3D algorithm, however, we can expect a speedup on the order of the number of cells in the transverse dimension (which is a dimension we no longer have to resolve). This can mean more than a hundred times the speedup, and the parameters presented in Table 1 were proven to be feasible using this geometry.

**TABLE 1.** A list of laser and plasma parameters for simulations that could test the scaling laws of [1]. The table also includes estimates of the number of particle steps required for full 3D or quasi-3D OSIRIS simulations.

Est. Particle Steps -3D-	-Quasi-3D-	Power (TW)	$n_p$ ( $cm^{-3}$ )	$W_0$ ( $\mu m$ )	$L_d$ ( $cm$ )	$a_0$	$\Delta E$ (GeV)
$1.9 \times 10^{15}$	$8.5 \times 10^{12}$	200	$1.5e18$	19.5	$1.5^3$	4.0	1.58
$6.0 \times 10^{15}$	$2.1 \times 10^{13}$	324	$1.0e18$	22.0	2.62	4.44	2.52
$4.6 \times 10^{16}$	$1.2 \times 10^{14}$	649	$5.0e17$	31.7	7.37	4.44	5.28
$3.6 \times 10^{17}$	$6.6 \times 10^{14}$	1298	$2.5e17$	44.8	20.8	4.44	10.57
$\vdots$	$\vdots$	$\vdots$	$\vdots$	$\vdots$	$\vdots$	$\vdots$	$\vdots$

For comparison, Table 1 also shows the number of particle steps for equivalent simulations in the quasi-3D geometry, with 16 particles per r-z cell (they were loaded at 8 locations in the azimuthal angle). If it takes 500 ns to advance a particle each timestep, the third and fourth rows in Table 1 correspond to 3 million and 26 million CPU hours for the full 3D Cartesian simulations. Using the quasi-3D framework can give hundreds of times the speedup in comparison to these full 3D simulations, which make these simulations very feasible. We use quadratic splines for the particle shapes.

## SIMULATION RESULTS

Two sets of LWFA simulations were conducted to better understand the scaling to higher energies and the effectiveness of adjusting the laser’s normalized amplitude to scale self-guiding to lower densities. In one set, the normalized amplitude was kept fixed at  $a_0 = 4.44$  and the matched spot size and pulse length were scaled as the density was lowered. The plasma density was varied from  $n_p = 1.0 \times 10^{18} cm^{-3}$ , to  $5.0 \times 10^{17} cm^{-3}$ , and finally to  $2.5 \times 10^{17} cm^{-3}$ . According to [1], the estimated particle energies would scale from 2.52 GeV, 5.28 GeV, and to 10.57 GeV, respectively. In the other set of simulations, the normalized laser amplitude was scaled to  $a_0 = 5.1$  and 5.86 for the

<sup>2</sup>We found that for our simulations we needed large box sizes to accurately simulate laser evolution over many Rayleigh lengths, even with PML boundary conditions (for information on this ‘perfectly matched layer’ method for absorbing boundaries, see Ref. [5]).

<sup>3</sup>Ref. [1] conducted this simulation over 0.75 cm, and not the entire dephasing length,  $L_d$ .

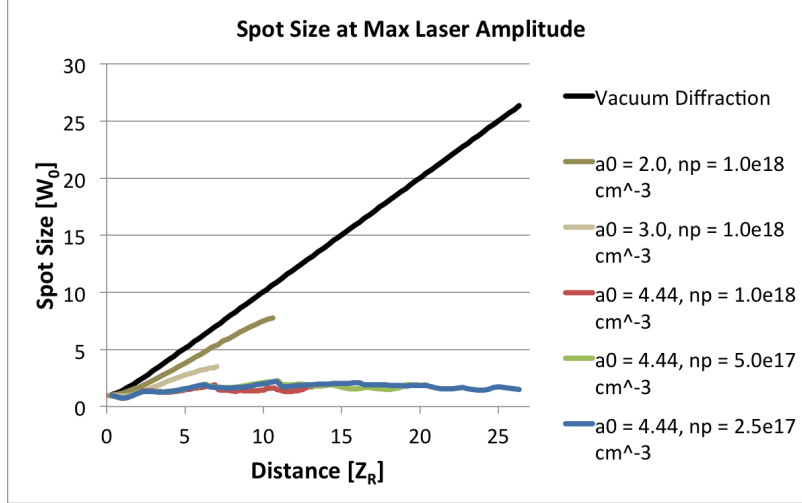


**FIGURE 1.** The evolution of the spot sizes at the location of the maximum laser amplitude is plotted over distance in Rayleigh lengths is presented. Self-guiding over many Rayleigh lengths is clearly demonstrated. The plot for vacuum diffraction is shown for comparison, and two simulations with  $a_0 < 4.0$  are also presented to show that, at low normalized laser amplitudes, self-guiding is not effective.

$n_p = 5.0 \times 10^{17} \text{ cm}^{-3}$  and  $2.5 \times 10^{17} \text{ cm}^{-3}$  cases, as suggested in [1]. The energy estimates for these simulations are 5.8 GeV and 13.9 GeV. Each simulation was conducted with the quasi-3D OSIRIS algorithm with only the azimuthal modes  $m \leq 1$ , with 2 particles initialized in each  $r$ - $z$  cell, and 8 particles initialized along  $\phi$  of  $2\pi$ . The cell sizes are  $\Delta z = 0.2k_0^{-1}$ ,  $\Delta r \approx 0.1k_p^{-1}$ , respectively. The laser's longitudinal pulse was symmetric and defined by a smooth polynomial spacing [1].

It was argued in [1] that self-guiding would not be as effective, as we scale to higher energies (i.e., lower densities), if  $a_0$  is kept constant. For the  $a_0 = 4.44$  cases, according to [1], the acceleration distance corresponds to  $13.8Z_R$  and  $26.4Z_R$  for the  $5.0 \times 10^{17} \text{ cm}^{-3}$  and  $2.5 \times 10^{17} \text{ cm}^{-3}$  densities, respectively, where  $Z_R$  is the Rayleigh length. In Fig. 1, we plot the evolution of the spot size at the axial slice of the maximum laser amplitude in units of the initial spot sizes. As can be seen, self-guiding clearly occurs under the appropriate conditions. For properly matched beams, the evolution of the laser spot size appears to be very stable, even as the acceleration distance is nearly doubled in Rayleigh lengths, indicating that self-guiding works better than might be expected.

In order to illustrate how well the scaling laws describe the phenomena, on the left side of Fig. 2 we plot the plasma density of the wake and self-injected electrons ( $m = 0$  mode) for the three  $a_0 = 4.44$  simulations, in the scaled units, at a laser propagation distance corresponding to half the calculated dephasing distances,  $L_d$ , in each case. In each plot, the transverse and axial units are scaled to the initial spot size,  $W_0$ . In absolute units, the simulation box gets larger as the density is lowered. These plots not only show that the physics behind the scaling laws is correct, but that the physics scales so well that a single simulation with its normalized units can be used to represent family results for different absolute units. We note that this self-similarity is for different reasons than argued in Ref. [6]. The plot shows that, in scaled units, the details of the wake, including the location of the self-injected electrons, look very similar. The scaling is not expected to be perfect, because some aspects of the laser evolution depends on the ratio of the propagation distance to the number of Rayleigh lengths. This ratio increases for lower densities, i.e., the Rayleigh length does not scale the same as the spot size. However, the results indicate that self-focusing “scales” better than might have been anticipated, if the normalized laser amplitude is kept fixed.

On the two lower panels of the right side of Fig. 2, results from simulations in which the normalized laser amplitudes are adjusted are shown. As expected, the results do not scale as well. Part of the differences is due to the larger number of self-trapped particles. The reason for increasing the normalized laser amplitude,  $a_0$ , was to improve self-guiding, and, hence, to ensure that the acceleration length is longer, so that higher electron energies are obtained. On the top right of Fig. 2, we plot the evolution of the laser spot sizes for all of the simulations to show that the laser remains self-guided in each case, and to show that, indeed, increasing  $a_0$  does improve the self-guiding. However, as just discussed, the evolution of the bubble structure is different. The evolution of the electron energy (the maximum

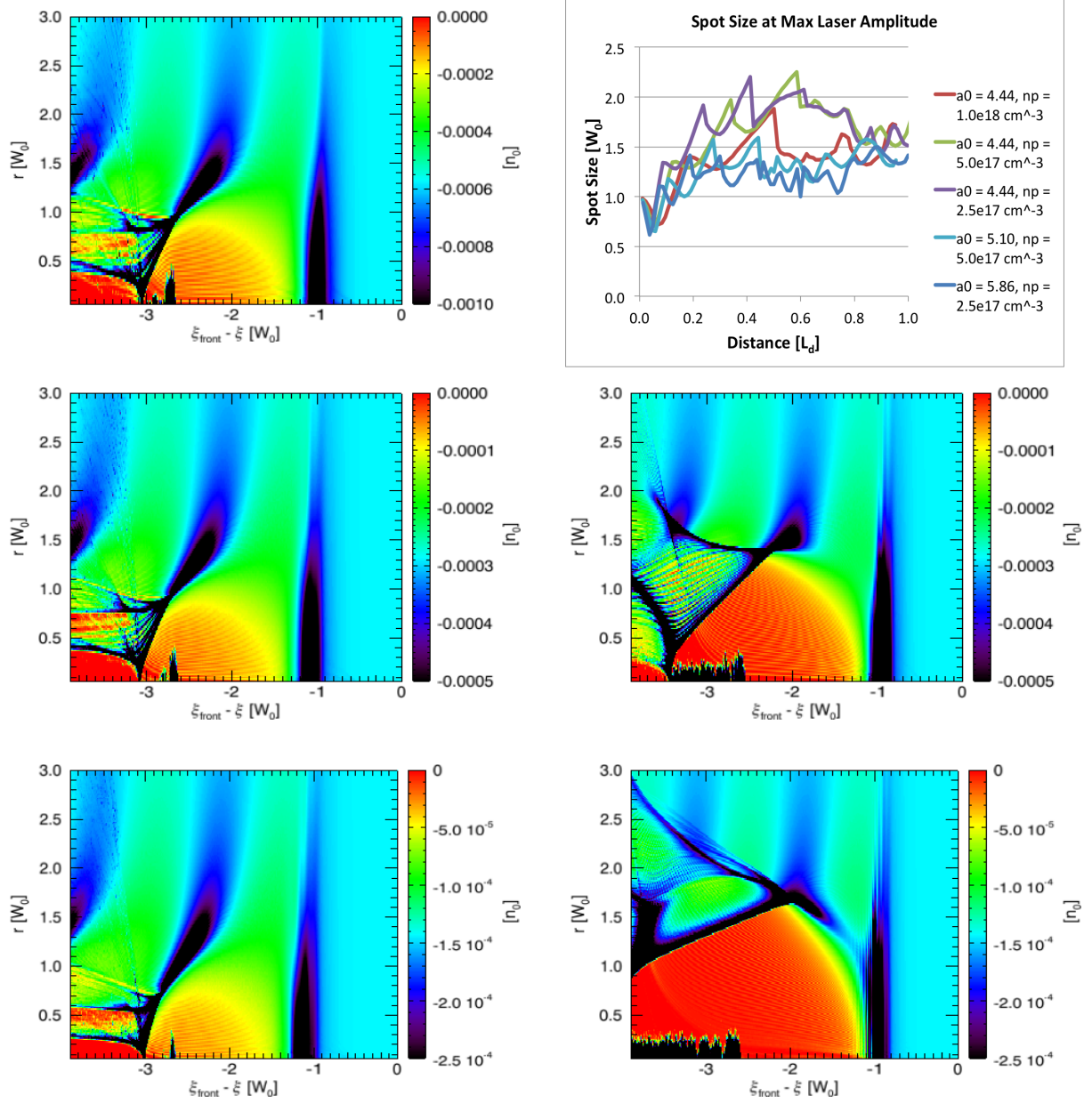


**FIGURE 2.** Evolution of the wake and laser. On the left, the 0-th azimuthal mode of the density of the  $n_p = 1.0 \times 10^{18}$  (top),  $n_p = 5.0 \times 10^{17}$  (middle), and  $n_p = 2.5 \times 10^{17}$  (bottom) for fixed  $a_0 = 4.44$ . On the right,  $a_0 = 5.1$  (middle right), and  $5.86$  (bottom right) for the  $n_p = 5.0 \times 10^{17}$  and  $n_p = 2.5 \times 10^{17}$  cases, respectively. The laser has traversed  $0.5L_d$  into the plasma. The horizontal axis is measured as the distance  $\xi$ , expressed in terms of the initial spot sizes,  $W_0$ , from the front of the initial laser profile,  $\xi_{front}$ . On the top right, we also show a plot of the evolution of the spot size of the laser, illustrating how the laser remains self guided in each of these simulations.

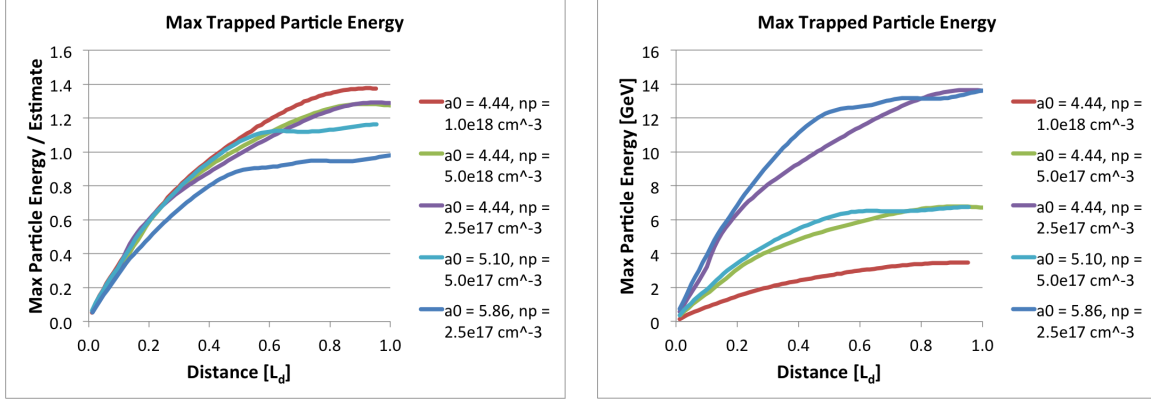


**FIGURE 3.** The evolution of the maximum trapped particle energies in normalized units (left), and in absolute units (right) for each scaled simulation.

energy for a self-injected electron) with propagation distance, in scaled units, is shown on the left side of Fig. 3. This shows that for fixed  $a_0$ , that the shapes of the curves are remarkably similar. The curves for the higher  $a_0$  are also somewhat similar, but they have different shapes than lower  $a_0$  cases. On the right-hand side of Fig. 3 we show the evolution of the maximum energy, in absolute units, against the propagation distance in normalized units. This shows that, although self-focusing works better when  $a_0$  is scaled upward, the final electron energy in absolute units is not higher. This appears to arise because the laser front gets steeper, causing the bubble size to increase, which effectively shortens the dephasing length. More detail will be provided in future publications.

## CONCLUSION

The implementation of the quasi-3D geometry in the OSIRIS simulation framework has enabled a more detailed study of the Lu et al. scaling laws for LWFAs operating in the self-guided, nonlinear blowout regime [1]. When plotted in scaled parameters, the evolution of the self-trapped electron energy and the evolution of the wake scale well for fixed  $a_0$ . Self-guiding continues to occur sufficiently as the density is lowered and the laser parameters are scaled properly. We find that self-guiding does improve, if  $a_0$  is scaled upward as the density is decreased, but that the evolution of the laser, wake, the particle energy evolve differently.

## ACKNOWLEDGMENTS

This work was supported by the US National Science Foundation under NSF Grants No. ACI-1339893 and 1500630, and the US Department of Energy under Grants No. DE-SC0010064 and No. DE-SC0014260. The simulations were performed on the UCLA Hoffman 2 and Dawson 2 Clusters, and the resources of the National Energy Research Scientific Computing Center and the Blue Waters through NSF ACI-1440071.

## REFERENCES

1. W. Lu, M. Tzoufras, C. Joshi, F. S. Tsung, W. B. Mori, J. Vieira, R. A. Fonseca, and L. O. Silva, *Phys. Rev. ST Accel. Beams* **10**, 061301 (2007), 10.1103/PhysRevSTAB.10.061301.
2. A. Pukhov and J. Meyer-ter Vehn, *Appl. Phys. B* **74**, 355–361 (2002).
3. A. F. Lifschitz, X. Davone, E. Lefebvre, J. Faure, C. Rechatin, and V. Malka, *J. Comput. Phys.* **228**, 1803–1814 (2009).
4. A. Davidson, A. Tableman, W. An, F. S. Tsung, W. Lu, J. Vieira, R. A. Fonseca, L. O. Silva, and W. B. Mori, *J. Comput. Phys.* **281**, 1063–1077 (2015).
5. J. Berenger, *J. Comput. Phys.* **114**, 185–200 (1994).
6. S. Gordienko and A. Pukhov, *Phys. Plasmas* **12**, 043109 (2005), 10.1063/1.1884126



Contents lists available at ScienceDirect

## Computer Physics Communications

journal homepage: [www.elsevier.com/locate/cpc](http://www.elsevier.com/locate/cpc)

## Mitigation of numerical Cerenkov radiation and instability using a hybrid finite difference-FFT Maxwell solver and a local charge conserving current deposit



Peicheng Yu<sup>a,\*</sup>, Xinlu Xu<sup>b</sup>, Adam Tableman<sup>c</sup>, Viktor K. Decyk<sup>c</sup>, Frank S. Tsung<sup>c</sup>, Frederico Fiuza<sup>d</sup>, Asher Davidson<sup>c</sup>, Jorge Vieira<sup>e</sup>, Ricardo A. Fonseca<sup>e,f</sup>, Wei Lu<sup>b</sup>, Luis O. Silva<sup>e</sup>, Warren B. Mori<sup>a,c</sup>

<sup>a</sup> Department of Electrical Engineering, University of California Los Angeles, Los Angeles, CA 90095, USA

<sup>b</sup> Department of Engineering Physics, Tsinghua University, Beijing 100084, China

<sup>c</sup> Department of Physics and Astronomy, University of California Los Angeles, Los Angeles, CA 90095, USA

<sup>d</sup> Lawrence Livermore National Laboratory, Livermore, CA, USA

<sup>e</sup> GOLP/Instituto de Plasma e Fusão Nuclear, Instituto Superior Técnico, Universidade de Lisboa, Lisbon, Portugal

<sup>f</sup> ISCTE—Instituto Universitário de Lisboa, 1649–026, Lisbon, Portugal

## ARTICLE INFO

## Article history:

Received 11 February 2015

Received in revised form

25 June 2015

Accepted 21 August 2015

Available online 28 August 2015

## Keywords:

PIC simulation

Hybrid Maxwell solver

Relativistic plasma drift

Numerical Cerenkov instability

Quasi-3D algorithm

## ABSTRACT

A hybrid Maxwell solver for fully relativistic and electromagnetic (EM) particle-in-cell (PIC) codes is described. In this solver, the EM fields are solved in  $k$  space by performing an FFT in one direction, while using finite difference operators in the other direction(s). This solver eliminates the numerical Cerenkov radiation for particles moving in the preferred direction. Moreover, the numerical Cerenkov instability (NCI) induced by the relativistically drifting plasma and beam can be eliminated using this hybrid solver by applying strategies that are similar to those recently developed for pure FFT solvers. A current correction is applied for the charge conserving current deposit to ensure that Gauss's Law is satisfied. A theoretical analysis of the dispersion properties in vacuum and in a drifting plasma for the hybrid solver is presented, and compared with PIC simulations with good agreement obtained. This hybrid solver is applied to both 2D and 3D Cartesian and quasi-3D (in which the fields and current are decomposed into azimuthal harmonics) geometries. Illustrative results for laser wakefield accelerator simulation in a Lorentz boosted frame using the hybrid solver in the 2D Cartesian geometry are presented, and compared against results from 2D UPIC-EMMA simulation which uses a pure spectral Maxwell solver, and from OSIRIS 2D lab frame simulation using the standard Yee solver. Very good agreement is obtained which demonstrates the feasibility of using the hybrid solver for high fidelity simulation of relativistically drifting plasma with no evidence of the numerical Cerenkov instability.

© 2015 Elsevier B.V. All rights reserved.

### 1. Introduction

Fully relativistic, electromagnetic particle-in-cell (PIC) codes are widely used to study a variety of plasma physics problems. In many cases the solver for Maxwell's equations in PIC codes use the finite-difference-time-domain (FDTD) approach where the corresponding differential operators are local. This locality leads to advantages in parallel scalability and ease in implementing boundary conditions. However, when using PIC codes to model physics

problems, including plasma based acceleration [1] in the Lorentz boosted frame, relativistic collisionless shocks [2,3], and fast ignition [4–6] particles or plasmas stream across the grid with speeds approaching the speed of light. In these scenarios, the second order FDTD Maxwell solvers support light waves with phase velocities less than the speed of light. This property of the FDTD solver leads to numerical Cerenkov radiation from a single particle that is moving near the speed of light. In addition, when beams or plasmas are moving near the speed of light across the grid a violent numerical instability known as the numerical Cerenkov instability (NCI) arises due to the unphysical coupling of electromagnetic modes and the Langmuir modes (main and higher order aliased beam resonance). The beam resonances are at  $\omega + 2\pi\mu/\Delta t = (k_1 + 2\pi\nu_1/\Delta x_1)v_0$ , where  $\mu$  and  $\nu_1$  refer to the time and space

\* Corresponding author.

E-mail address: [tpc02@ucla.edu](mailto:tpc02@ucla.edu) (P. Yu).

<http://dx.doi.org/10.1016/j.cpc.2015.08.026>

0010-4655/© 2015 Elsevier B.V. All rights reserved.

aliases,  $\Delta t$  and  $\Delta x_1$  are the time step and grid size, and the plasma is drifting relativistically at a speed  $v_0$  in the  $\hat{1}$ -direction.

The NCI was first studied more than 40 years ago [7]. However, it has received much renewed attention [8–14] since the identification [15,16] of this numerical instability as the limiting factor for carrying out relativistic collisionless shock simulations [2,3], and Lorentz boosted frame simulations [17–20] of laser wakefield acceleration (LWFA) [1].

This early and recent work on the NCI [7–11,16,21] have shown that the NCI inevitably arises in EM-PIC simulations when a plasma (neutral or non-neutral) drifts across a simulation grid with a speed near the speed of light. Analysis shows that it is due to the unphysical coupling of electromagnetic (EM) modes and Langmuir modes (including those due to aliasing). As a result, significant recent effort has been devoted to the investigation and elimination of the NCI so that high fidelity relativistic plasma drift simulations can be routinely performed [10–13,19,20].

In previous work Refs. [9,10], we examined the NCI properties for the second order Yee solver [22], as well as a spectral solver [23,24] (in which Maxwell's equation are solved in multi-dimensional  $\vec{k}$  space). We note that what we refer to as simply a spectral solver, others [25] refer to as a pseudo-spectral time domain (PSTD) solver. The NCI theory developed in [9,10] were general and it could be applied to any Maxwell solver. It was found that in the simulation parameter space of interest the fastest growing NCI modes of these two solvers are the  $(\mu, \nu_1) = (0, \pm 1)$  modes, where  $\mu$  and  $\nu_1$  defined above are the temporal aliasing, and spatial aliasing in the drifting direction of the plasma. The  $(\mu, \nu_1) = (0, \pm 1)$  modes for both solvers reside near the edge of the fundamental Brillouin zone (for square or cubic cells), and can be eliminated by applying a low-pass filter. However, due to the subluminal EM dispersion along the direction of the drifting plasma in the Yee solver, the main NCI mode  $(\mu, \nu_1) = (0, 0)$  of the Yee solver has a growth rate that is of the same order as its  $(\mu, \nu_1) = (0, \pm 1)$  counterpart, and these modes reside close to the modes of physical interest. However, the  $(\mu, \nu_1) = (0, 0)$  NCI mode in the spectral solver has a growth rate one order of magnitude smaller than the  $(\mu, \nu_1) = (0, \pm 1)$  modes due to the superluminal dispersion of spectral (FFT based) solver. Furthermore, as shown in [10] these  $(\mu, \nu_1) = (0, 0)$  modes can be moved farther away from the physics modes and their harmonics by reducing the time step in the spectral solver, and can be fully eliminated by slightly modifying the EM dispersion in the spectral solver. Using these methods, it was demonstrated in [10] that a spectral EM-PIC can perform high fidelity simulations of relativistically drifting plasmas where the LWFA physics is highly nonlinear with no evidence of the NCI.

A multi-dimensional spectral Maxwell solver has a superluminal dispersion relation in all the propagation directions. This is due to the fact that the first order spatial derivatives in the Maxwell's equation are greater than  $N$ th order accurate (where  $N$  is the number of grids) since we are solving the Maxwell's equation in  $k$  space. This superluminal dispersion relation leads to highly localized  $(\mu, \nu_1) = (0, 0)$  NCI modes and the reduction of their growth rates (compared with their Yee solver counterpart). In this paper, we propose to use a hybrid Yee-FFT solver, in which the FFT is performed in only one direction, namely the drifting direction of the plasma, while keeping the finite difference form of the Yee solver in the directions transverse to the drifting direction. In other words, EM waves moving in the  $\hat{1}$  direction will have a superluminal dispersion (due to the  $N$ th order accurate spatial derivatives) while those moving in the  $\hat{2}$  (and  $\hat{3}$  in 3D) directions will have a subluminal dispersion due to the second-order-accurate spatial derivatives. The advantages of this approach over a fully spectral solver is that the field solver is local in the transverse directions so that better parallel scalability than a fully FFT based solver can be achieved

(assuming the same parallel FFT routines are used). In addition, it is easier to include a single FFT into the structure of mature codes such as OSIRIS [26]. Furthermore, this idea works well with a quasi-3D algorithm that is PIC in  $r - z$  and gridless in  $\phi$  [27,28], where the FFTs cannot be applied in the  $\hat{r}$  direction. We note that recently a method for achieving improved scalability for FFT based solvers was proposed [25] in which FFTs are used within each local domain, but it introduces as yet unquantified errors in the longitudinal fields. The relative advantages and tradeoffs between the variety of approaches being proposed will be better understood as they begin to be used on real physics problems.

We use the theoretical framework for the NCI developed in Refs. [9,10] to study the NCI of the hybrid solver. As we show below, the fastest growing NCI modes for the proposed hybrid solver behave similarly to those for the spectral solver. In  $\vec{k}$  space they reside at the edge of the fundamental Brillouin zone for square or cubic cells. More importantly, the  $(\mu, \nu_1) = (0, 0)$  NCI mode for the hybrid solver has almost the same properties (pattern, growth rates) as that of a spectral solver. The NCI can therefore be efficiently eliminated in the hybrid solver by applying the same strategy as in the spectral solver. Moreover, simulations have shown that the NCI properties of the quasi-3D  $r - z$  PIC and gridless in  $\phi$  algorithm [27,28] are similar to that of 2D Cartesian geometry [29]. Therefore, the idea of a hybrid Yee-FFT solver can be readily applied to quasi-3D geometry. We also note that the use of local FFTs in domains along  $z$  [25] could also be used within the hybrid approach described here.

In this paper, we first discuss the algorithm for the hybrid Yee-FFT Maxwell solver in Section 2. In Section 3, we apply the theoretical framework in Refs. [9,10] to study the NCI properties of the hybrid solver analytically and in PIC simulations. We compare OSIRIS [26] results with the hybrid solver against UPIC-EMMA [11] results with a fully spectral (FFT based) solver. In Section 4, it is shown that the strategies used to eliminate the NCI for purely spectral solvers are also valid for the hybrid solver. In Section 5, we extend the hybrid solver idea to the quasi-3D algorithm in OSIRIS and present simulation studies of the NCI properties in this geometry. We then present 2D OSIRIS simulations of LWFA in a Lorentz boosted frame using the new hybrid solver. Very good agreement is found when comparing simulation results using the hybrid solver in OSIRIS against results from 2D lab frame OSIRIS using Yee solver and 2D Lorentz boosted frame UPIC-EMMA [11] simulations using spectral solver. Last, in Section 7 we summarize the results and mention directions for future work.

## 2. Hybrid Yee-FFT solver

The basic idea of the hybrid Yee-FFT solver is that the theoretical framework developed in [9,10] indicates that the NCI is easier to eliminate when EM waves are superluminal along the direction of the plasma drift. This can be accomplished with higher order solvers or with an FFT based solver in the drifting direction of the plasma (denoted as  $\hat{1}$ -direction). We note that it is more difficult to satisfy strict charge conservation (Gauss's law) for higher order finite difference solvers by modifying the charge conserving current deposition in real space. Here we replace the finite difference operator of the first spatial derivative  $\partial/\partial x_1$  in the Maxwell's equation in Yee solver with its FFT counterpart that has an accuracy greater than order  $N$ . We then correct for this change in the current deposit to maintain strict charge conservation. Without loss of generality, in the following we will briefly describe the algorithm of the Yee-FFT solver in two-dimensional (2D) Cartesian coordinate. The straightforward extension to the 3D Cartesian case is also discussed.

## 2.1. Algorithm

We start from the standard algorithm for a 2D Yee solver, in which the electromagnetic fields  $\vec{E}$  and  $\vec{B}$  are advanced by solving Faraday's Law and Ampere's Law:

$$B_{1,i1,i2+\frac{1}{2}}^{n+\frac{1}{2}} = B_{1,i1,i2+\frac{1}{2}}^{n-\frac{1}{2}} - c\Delta t \times \frac{E_{3,i1,i2+1}^n - E_{3,i1,i2}^n}{\Delta x_2} \quad (1)$$

$$B_{2,i1+\frac{1}{2},i2}^{n+\frac{1}{2}} = B_{2,i1+\frac{1}{2},i2}^{n-\frac{1}{2}} + c\Delta t \times \frac{E_{3,i1+1,i2}^n - E_{3,i1,i2}^n}{\Delta x_1} \quad (2)$$

$$B_{3,i1+\frac{1}{2},i2+\frac{1}{2}}^{n+\frac{1}{2}} = B_{3,i1+\frac{1}{2},i2+\frac{1}{2}}^{n-\frac{1}{2}} - c\Delta t \times \frac{E_{2,i1+1,i2+\frac{1}{2}}^n - E_{2,i1,i2+\frac{1}{2}}^n}{\Delta x_1} + c\Delta t \times \frac{E_{1,i1+\frac{1}{2},i2+1}^n - E_{1,i1+\frac{1}{2},i2}^n}{\Delta x_2} \quad (3)$$

$$E_{1,i1+\frac{1}{2},i2}^{n+1} = E_{1,i1+\frac{1}{2},i2}^n - 4\pi\Delta t \times J_{1,i1+\frac{1}{2},i2}^{n+\frac{1}{2}} + c\Delta t \times \frac{B_{3,i1+\frac{1}{2},i2+\frac{1}{2}}^{n+\frac{1}{2}} - B_{3,i1+\frac{1}{2},i2-\frac{1}{2}}^{n+\frac{1}{2}}}{\Delta x_2} \quad (4)$$

$$E_{2,i1,i2+\frac{1}{2}}^{n+1} = E_{2,i1,i2+\frac{1}{2}}^n - 4\pi\Delta t \times J_{2,i1,i2+\frac{1}{2}}^{n+\frac{1}{2}} - c\Delta t \times \frac{B_{3,i1+\frac{1}{2},i2+\frac{1}{2}}^{n+\frac{1}{2}} - B_{3,i1-\frac{1}{2},i2+\frac{1}{2}}^{n+\frac{1}{2}}}{\Delta x_1} \quad (5)$$

$$E_{3,i1,i2}^{n+1} = E_{3,i1,i2}^n - 4\pi\Delta t \times J_{3,i1,i2}^{n+\frac{1}{2}} + c\Delta t \times \frac{B_{2,i1+\frac{1}{2},i2}^{n+\frac{1}{2}} - B_{2,i1-\frac{1}{2},i2}^{n+\frac{1}{2}}}{\Delta x_1} - c\Delta t \times \frac{B_{1,i1,i2+\frac{1}{2}}^{n+\frac{1}{2}} - B_{1,i1,i2-\frac{1}{2}}^{n+\frac{1}{2}}}{\Delta x_2} \quad (6)$$

where the EM field  $\vec{E}$  and  $\vec{B}$ , and current  $\vec{j}$  are defined with the proper half-grid offsets according to the Yee mesh [22]. If we perform a Fourier transform of Eqs. (1)–(6) in both  $x_1$  and  $x_2$ , and in time, Maxwell's equations reduce to

$$[\omega]\vec{B} = -[\vec{k}] \times \vec{E} \quad (7)$$

$$[\omega]\vec{E} = [\vec{k}] \times \vec{B} + 4\pi\vec{j} \quad (8)$$

where

$$[\vec{k}] = \left( \frac{\sin(k_1\Delta x_1/2)}{\Delta x_1/2}, \frac{\sin(k_2\Delta x_2/2)}{\Delta x_2/2}, 0 \right) \quad (9)$$

$$[\omega] = \frac{\sin(\omega\Delta t/2)}{\Delta t/2}.$$

In vacuum where  $\vec{j} = 0$ , the corresponding numerical dispersion relation for the EM waves is

$$[\omega]^2 = c^2([k]_1^2 + [k]_2^2). \quad (10)$$

The idea of a hybrid Yee-FFT solver is to keep the finite difference operator  $[k]_2 = \sin(k_2\Delta x_2/2)/(\Delta x_2/2)$  in the directions transverse to the drifting direction, while replacing the finite difference operator  $[k]_1$  in the drifting direction with its spectral counterpart  $[k]_1 = k_1$ . To achieve this, in the hybrid solver we will solve Maxwell's equations in  $k_1$  space. The current is deposited locally using a rigorous charge conserving scheme that is equivalent to [30]. For the EM field and current, we first perform an FFT along  $x_1$  so that all fields are defined in  $(k_1, x_2)$  space. After that we apply

a correction to the current in the drifting direction

$$\tilde{j}_1^{n+\frac{1}{2}} = \frac{\sin k_1\Delta x_1/2}{k_1\Delta x_1/2} j_1^{n+\frac{1}{2}} \quad (11)$$

where  $\tilde{j}_1$  is the corrected current. In [25], the current is also corrected where they combine a pure FFT solver with a charge conserving current deposit. This correction ensures that Gauss's Law is satisfied throughout the duration of the simulation if it is satisfied initially, as will be discussed in more detail in Section 2.3. After the current correction we advance the EM field as

$$B_{1,\kappa1,i2+\frac{1}{2}}^{n+\frac{1}{2}} = B_{1,\kappa1,i2+\frac{1}{2}}^{n-\frac{1}{2}} - c\Delta t \times \frac{E_{3,\kappa1,i2+1}^n - E_{3,\kappa1,i2}^n}{\Delta x_2} \quad (12)$$

$$B_{2,\kappa1,i2}^{n+\frac{1}{2}} = B_{2,\kappa1,i2}^{n-\frac{1}{2}} - i\xi^+ k_1 c\Delta t E_{3,\kappa1,i2}^n \quad (13)$$

$$B_{3,\kappa1,i2+\frac{1}{2}}^{n+\frac{1}{2}} = B_{3,\kappa1,i2+\frac{1}{2}}^{n-\frac{1}{2}} + i\xi^+ k_1 c\Delta t E_{2,\kappa1,i2+\frac{1}{2}}^n + c\Delta t \times \frac{E_{1,\kappa1,i2+1}^n - E_{1,\kappa1,i2}^n}{\Delta x_2} \quad (14)$$

$$E_{1,\kappa1,i2}^{n+1} = E_{1,\kappa1,i2}^n - 4\pi\Delta t \times J_{1,\kappa1,i2}^{n+\frac{1}{2}} + c\Delta t \times \frac{B_{3,\kappa1,i2+\frac{1}{2}}^{n+\frac{1}{2}} - B_{3,\kappa1,i2-\frac{1}{2}}^{n+\frac{1}{2}}}{\Delta x_2} \quad (15)$$

$$E_{2,\kappa1,i2+\frac{1}{2}}^{n+1} = E_{2,\kappa1,i2+\frac{1}{2}}^n - 4\pi\Delta t \times J_{2,\kappa1,i2+\frac{1}{2}}^{n+\frac{1}{2}} + i\xi^- k_1 c\Delta t B_{3,\kappa1,i2+\frac{1}{2}}^{n+\frac{1}{2}} \quad (16)$$

$$E_{3,\kappa1,i2}^{n+1} = E_{3,\kappa1,i2}^n - 4\pi\Delta t \times J_{3,\kappa1,i2}^{n+\frac{1}{2}} - i\xi^- k_1 c\Delta t B_{2,\kappa1,i2}^{n+\frac{1}{2}} - c\Delta t \times \frac{B_{1,\kappa1,i2+\frac{1}{2}}^{n+\frac{1}{2}} - B_{1,\kappa1,i2-\frac{1}{2}}^{n+\frac{1}{2}}}{\Delta x_2} \quad (17)$$

where  $k_1 = 2\pi\kappa_1/N$  and  $N$  is the number of grids in  $x_1$  direction, and  $\kappa_1 = 0, 1, \dots, N/2 - 1$  is the mode number. Note in the hybrid solver, the EM fields  $\vec{E}$ ,  $\vec{B}$ , and current  $\vec{j}$  have the same temporal and spatial centering as in the Yee solver, and

$$\xi^\pm = \exp\left(\pm \frac{k_1\Delta x_1}{2} i\right) \quad (18)$$

is the phase shifting due to the half grid offsets of the  $E_1$ ,  $B_{2,3}$ , and  $j_1$  in the  $\hat{1}$ -direction. Compared with the standard Yee solver algorithm, it is evident that if we replace  $-ik_1$  with the corresponding finite difference form we can recover the standard 2D Yee algorithm. We note for this method one can use a different  $[k]_1$ , e.g. the  $[k]_1$  proposed in [31], to allow error-free vacuum EM dispersion in  $\hat{1}$ -direction.

## 2.2. Courant condition

The Courant condition of the hybrid solver can be easily derived from the corresponding numerical EM dispersion Eq. (10). Substituting into Eq. (10) the finite difference operator in time  $[\omega]$

$$[\omega] = \frac{\sin(\omega\Delta t/2)}{\Delta t/2} \quad (19)$$

and the finite difference operators in space

$$[k]_1 = k_1 \quad [k]_2 = \frac{\sin(k_2\Delta x_2/2)}{\Delta x_2/2} \quad (20)$$

we can obtain the corresponding constraint on the time step

$$\frac{\Delta t}{2} \sqrt{k_1^2 + \left(\frac{\sin(k_2\Delta x_2/2)}{\Delta x_2/2}\right)^2} \leq 1. \quad (21)$$

Note the  $\vec{k}$  range of the fundamental Brillouin zone is  $|k_1| \leq \pi/\Delta x_1$ ,  $|k_2| \leq \pi/\Delta x_2$ , we can obtain the Courant limit on the hybrid solver

$$\Delta t \leq \frac{2}{\sqrt{\frac{\pi^2}{\Delta x_1^2} + \frac{4}{\Delta x_2^2}}}. \quad (22)$$

For square cells with  $\Delta x_1 = \Delta x_2$ , this reduces to  $\Delta t \leq 0.537 \Delta x_1$ .

### 2.3. Charge conservation

In the hybrid Yee-FFT solver, we rely on the Faraday's Law and Ampere's Law to advance the EM field. On the other hand, the local charge conserving current deposition [30] ensures the second-order-accurate finite difference representation of the continuity equation,

$$\frac{\partial}{\partial t} \rho_{1,i2}^n + \frac{j_{1,i1+\frac{1}{2},i2}^{n+\frac{1}{2}} - j_{1,i1-\frac{1}{2},i2}^{n+\frac{1}{2}}}{\Delta x_1} + \frac{j_{2,i1,i2+\frac{1}{2}}^{n+\frac{1}{2}} - j_{2,i1,i2-\frac{1}{2}}^{n+\frac{1}{2}}}{\Delta x_2} = 0 \quad (23)$$

is satisfied, where

$$\frac{\partial}{\partial t} G^n = \frac{G^{n+1} - G^n}{\Delta t} \quad (24)$$

where  $G^n$  is an arbitrary scalar quantity. Therefore, when combining this scheme with the second order accurate Yee solver, Gauss's Law is rigorously satisfied at every time step if it is satisfied at  $t = 0$ . However, when the hybrid solver is used together with the charge conserving current deposition scheme, we need to apply a correction to the current, as shown in Eq. (11), in order that the Gauss's Law is satisfied at every time step. This can be seen by first performing Fourier transform in the  $x_1$  direction for Eq. (23),

$$\frac{\partial}{\partial t} \rho_{\kappa 1,i2}^n - i \frac{\sin(k_1 \Delta x_1 / 2)}{\Delta x_1 / 2} j_{\kappa 1,i2}^{n+\frac{1}{2}} + \frac{j_{2,\kappa 1,i2+\frac{1}{2}}^{n+\frac{1}{2}} - j_{2,\kappa 1,i2-\frac{1}{2}}^{n+\frac{1}{2}}}{\Delta x_2} = 0 \quad (25)$$

then applying the divergence operator of the hybrid solver to the left and right hand side of the Ampere's Law, Eqs. (15)–(17). Using Eq. (25), we obtain

$$\frac{\partial}{\partial t} \left( -4\pi \rho_{\kappa 1,i2}^n - ik_1 E_{1,\kappa 1,i2}^n + \frac{E_{2,\kappa 1,i2+\frac{1}{2}}^n - E_{2,\kappa 1,i2-\frac{1}{2}}^n}{\Delta x_2} \right) = 0 \quad (26)$$

which shows that if Gauss's Law for the 2D hybrid solver given by

$$-ik_1 E_{1,\kappa 1,i2}^n + \frac{E_{2,\kappa 1,i2+\frac{1}{2}}^n - E_{2,\kappa 1,i2-\frac{1}{2}}^n}{\Delta x_2} = 4\pi \rho_{\kappa 1,i2}^n \quad (27)$$

is satisfied at  $t = 0$ , it is satisfied at each time step.

### 2.4. 3D Cartesian geometry

It is straightforward to extend the hybrid solver to 3D Cartesian geometry. In 3D Cartesian coordinates, we solve Maxwell's equation in  $(k_1, x_2, x_3)$  space where we use the same second order accurate finite difference form of the Yee solver in the  $\hat{2}$  and  $\hat{3}$  directions. As in the 2D Cartesian case, the current correction is applied to  $j_1$  to ensure the Gauss's Law is satisfied. We have implemented the hybrid solver in 2D and 3D with current correction in our finite-difference-time-domain (FDTD) code OSIRIS [26].

## 3. Numerical Cerenkov instability

To investigate the NCI properties of the hybrid solver, we first consider its corresponding numerical dispersion relation. Employing the general theoretical framework established in

**Table 1**

Crucial simulation parameters for the 2D relativistic plasma drift simulation.  $n_p$  is the reference plasma density, and  $\omega_p^2 = 4\pi q^2 n_p / m_e$ ,  $k_p = \omega_p / c$  ( $c$  is normalized to 1).

Parameters	Values
grid size ( $k_p \Delta x_1, k_p \Delta x_2$ )	(0.2, 0.2)
time step $\omega_p \Delta t$	$0.4 \Delta x_1$
boundary condition	Periodic
simulation box size ( $k_p L_1, k_p L_2$ )	$51.2 \times 51.2$
plasma drifting Lorentz factor	$\gamma = 50.0$
plasma density	$n/n_p = 100.0$

Refs. [9,10], we can calculate in detail the NCI modes for any Maxwell solver. The roots of the numerical dispersion relation that lead to the NCI can be found numerically by solving Eq. (17) in [9], or by the analytical expression in Eq. (19) of [10]. For convenience we present the corresponding numerical dispersion and analytical expressions of Eq. (17) of [9] in Appendix. For the Yee solver the  $k$  space representation of the finite difference operator is

$$[k]_i = \frac{\sin(k_i \Delta x_i / 2)}{\Delta x_i / 2} \quad (28)$$

where  $i = 1, 2$  in 2D. Meanwhile, in the hybrid solver the  $\vec{k}$  space operator in the drifting direction is replaced with that of the spectral solver  $[k]_1 \rightarrow k_1$ . By substituting the respective operators for each direction into Eq. (19) of Ref. [10] [or Eq. (A.4) in Appendix], we can rapidly find the set of NCI modes for the hybrid solver. In Fig. 1(a)–(d), we plot the  $(\mu, \nu_1) = (0, 0)$  and  $(\mu, \nu_1) = (0, \pm 1)$  modes for the hybrid and spectral solvers by scanning over the  $(k_1, k_2)$  space in the fundamental Brillouin zone and solve for the growth rates of the corresponding unstable modes. The parameters used to generate this plot are listed in Table 1.

We can see from Fig. 1(a) and (b) that the  $(\mu, \nu_1) = (0, \pm 1)$  NCI modes of the two solvers reside near the edge of the fundamental Brillouin zone, although the patterns are slightly different due to their different finite difference operators in the  $\hat{2}$ -direction, which leads to the slightly different EM dispersion curves. In Fig. 1(e) and (f) we show how different EM dispersion curves leads to different  $(\mu, \nu_1) = (0, \pm 1)$  NCI modes for the two solvers. These modes are distinct, and far removed from the modes of physical interest, and are relatively easy to eliminate.

More importantly, we see from Fig. 1(c) and (d) that the hybrid solver leads to  $(\mu, \nu_1) = (0, 0)$  NCI modes that are very similar to their spectral solver counterpart. The pattern of the  $(\mu, \nu_1) = (0, 0)$  modes for these two solvers are both four dots (in 2D) and highly localized in the fundamental Brillouin zone. We also use the theory to perform parameter scan to study the dependence of growth rates (of the fastest growing mode) and the locations in  $k$  space of the  $(\mu, \nu_1) = (0, 0)$  modes on  $\Delta t / \Delta x_1$  for the hybrid solver, and compare this result against that of the fully spectral solver, as shown in Fig. 2(a) and (b). We likewise carried out OSIRIS simulations using the hybrid solver and UPIC-EMMA [11,32] using the spectral solver, to compare against theoretical results. Very good agreement is found between theory and simulations. Fig. 2(a) and (b) shows that both the  $k_1$  location, and growth rates of the  $(\mu, \nu_1) = (0, 0)$  modes are almost identical for the two solvers. This indicates that, just like the spectral solver, the growth rate of the  $(\mu, \nu_1) = (0, 0)$  modes of the hybrid solver is reduced, while their location in  $k_1$  increases when the time step is reduced.

In Fig. 2(c) and (e) we show the locations of the unstable  $(\mu, \nu_1) = (0, \pm 1)$ , and  $(\mu, \nu_1) = (0, 0)$  NCI modes for the hybrid solver in OSIRIS for 2D Cartesian geometry. The agreement between Figs. 2(c) and 1(b), and between Figs. 2(e) and 1(d) are excellent.

The main advantage of the purely spectral solver regarding its NCI properties in comparison to a purely FDTD solver is that the



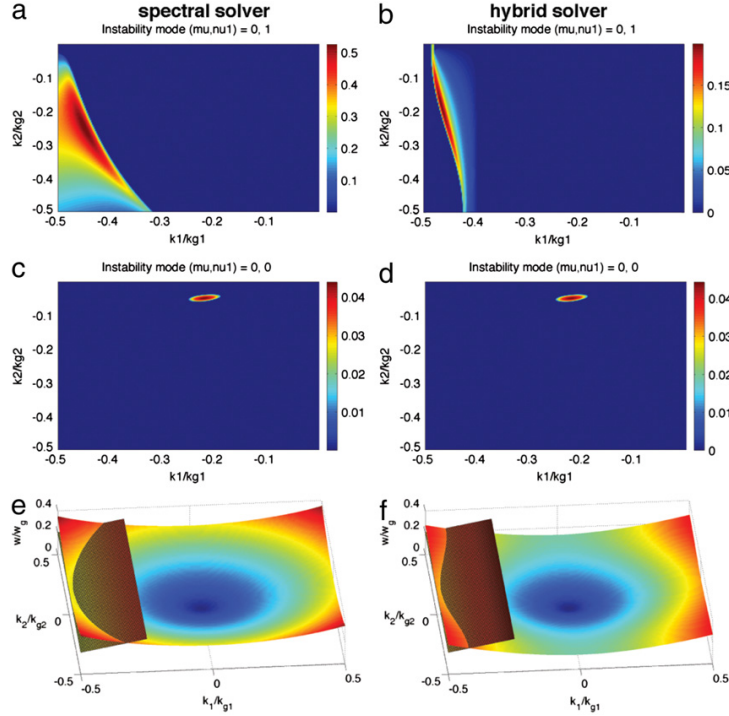


**Fig. 1.** The pattern of the  $(\mu, \nu_1) = (0, \pm 1)$  modes for the two solvers are shown in (a) and (b). The pattern of the  $(\mu, \nu_1) = (0, 0)$  modes for two solvers are shown in (c) and (d). The intersection between the EM dispersion relations with the first spatial aliasing beam modes for the full spectral solver and the hybrid solver are shown in (e) and (f). When generating these plots we use  $\Delta x_1 = \Delta x_2 = 0.2k_0^{-1}$ , and  $\Delta t = 0.08\omega_0^{-1}$ . Other parameters are listed in Table 1.

superluminal dispersion relation makes it much easier to eliminate the NCI modes at  $(\mu, \nu_1) = (0, 0)$ : the modes have a growth rate that is one order of magnitude smaller than that for the  $(\mu, \nu_1) = (0, \pm 1)$  modes, their locations are highly localized in  $\vec{k}$  space, and they can be moved away from the modes of physical interest by reducing the time step. We showed above that similar NCI properties can be achieved by using a hybrid FDTD-spectral solver, where the Maxwell's equation are solved in Fourier space only in the direction of the plasma drift. Comparing with an EM-PIC code using a multi-dimensional spectral solver which solves Maxwell's equation in  $\vec{k}$  space, there are advantages when solving it in  $(k_1, x_2)$  space in 2D [and  $(k_1, x_2, x_3)$  space in 3D]. Firstly, the hybrid solver saves the FFT in the other directions; secondly, since the solver is FDTD in the directions transverse to the drifting direction, it is easier to integrate the algorithm into existing FDTD codes such as OSIRIS where the parallelizations and boundary conditions in the transverse direction can remain untouched. Last but perhaps most important, the idea that one can obtain preferable NCI properties by solving Maxwell's equation in  $k_1$  space in the drifting direction can be readily extended to the quasi-3D algorithm [27], as we can solve the Maxwell's equation in  $(k_1, \rho, \psi)$  space.

#### 4. Elimination of the NCI modes

In Ref. [10], we proposed strategies to eliminate the NCI in the spectral solver. These strategies can be readily applied to the hybrid solver. For square (or cubic) cell, the pattern of the fastest growing modes resides in a narrow range of  $k_1$  near the edge of the fundamental Brillouin zone. Therefore we can apply a low-pass filter in  $k_1$  to the current to eliminate the fastest growing modes. Since the fields are already in  $k_1$  space when solving the Maxwell's

equations, the filtering can be done efficiently by applying a form factor to the current only in  $k_1$ .

As for the  $(\mu, \nu_1) = (0, 0)$  mode, if they are near the main or higher order harmonics of the physical modes, we can move them away and reduce their growth rates by simply reducing the time step. To further mitigate the  $(\mu, \nu_1) = (0, 0)$  NCI modes when they are far away from the physical modes, one can modify the EM dispersion relation, according to the procedure described in Ref. [10], to completely eliminate them. In Fig. 3 we plot how the modification is accomplished in the hybrid solver. As shown in Fig. 3(a) except for the bump region for most  $k_1$  is  $[k]_1$  for a particular  $k_1$  is  $k_1$  itself; near the bump, the  $[k]_1$  for  $k_1$  is  $k_1 + \Delta k_{mod}$ , where  $\Delta k_{mod}$  is a function of  $k_1$  with

$$\Delta k_{mod} = \Delta k_{mod, \max} \cos\left(\frac{k_1 - k_{1m} \pi}{k_{1l} - k_{1m} \frac{\pi}{2}}\right)^2 \quad (29)$$

where  $k_{1l}, k_{1u}$  are the lower and upper  $k_1$  to be modified,  $k_{1m} = (k_{1l} + k_{1u})/2$ , and  $\Delta k_{mod, \max}$  is the maximum value of  $\Delta k_{mod}$ . The values of  $k_{1l}, k_{1u}$  and  $\Delta k_{mod, \max}$  are determined by the position of the  $(\mu, \nu_1) = (0, 0)$  modes and their growth rates. According to the NCI theory, for the parameters in Table 1, when the  $[k]_1$  is as defined in Fig. 3(a) (with  $k_{1l}/k_{g1} = 0.15$ ,  $k_{1u}/k_{g1} = 0.26$ , and  $\Delta k_{mod, \max}/k_{g1} = 0.01$ ), there is no unstable  $(\mu, \nu_1) = (0, 0)$  NCI modes, i.e., the  $(\mu, \nu_1) = (0, 0)$  mode has a theoretical growth rate of zero. To verify the theoretical results in the hybrid solver, in Fig. 3(b) we plot the  $E_2$  energy growth with and without the modification. In these simulations we used the parameters in Table 1. The blue curve in Fig. 3(b) represents the case without the modification, while the red and black curves are those with the modification to  $k_1$ . The cases with blue and red curves used quadratic particle shapes, while the case for the black curve used cubic particle shapes. We have likewise plotted the  $E_2$  spectra at the time point

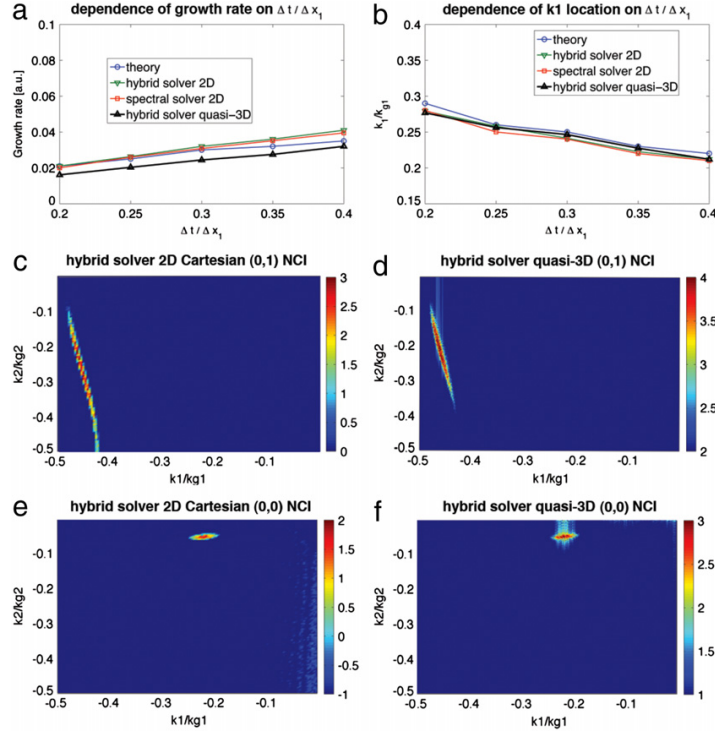


**Fig. 2.** In (a) and (b) the dependence of the growth rate and  $k_1$  for the fastest growing  $(\mu, \nu_1) = (0, 0)$  mode on the time step is shown. The four lines correspond to the theoretical prediction for the hybrid solver in 2D, results from OSIRIS and UPIC-EMMA simulations for the spectral and hybrid solvers in 2D Cartesian geometry, and results for the hybrid solver in the quasi-3D geometry (where the  $k_2$  is obtained from a Hankel transform). In (c)–(f) the spectrum of  $E_2$  ( $E_\rho$ ) is plotted for OSIRIS simulations with the hybrid solver in 2D Cartesian or the quasi-3D geometry. In (c) and (d) results from runs where no filter in  $k_1$  is used to eliminate the  $(\mu, \nu_1) = (0, \pm 1)$  modes. In (e) and (f) a filter in  $k_1$  was used to eliminate the  $(\mu, \nu_1) = (0, \pm 1)$  modes and now the  $(\mu, \nu_1) = (0, 0)$  modes are seen. These results show that the 2D Cartesian and quasi-3D geometries have very similar properties and that the strategies used to eliminate the NCI in 2D Cartesian can be applied to the quasi-3D case.

$t = 3200\omega_0^{-1}$  indicated in Fig. 3(c) and (d) for the two cases with the modifications (red and black curves in 3(b)). We can see from Fig. 3(b) and (c) that after the modification, the growth rate of the  $(\mu, \nu_1) = (0, 0)$  NCI modes reduces to zero. Meanwhile, the red curve rises later in time due to the  $(\mu, \nu_1) = (\pm 1, \pm 2)$  NCI modes. As we showed in Ref. [10] the growth rate of these higher order modes can be reduced by using higher order particle shape. Therefore when cubic particle shapes are used, as is the case for the black curve, the  $(\mu, \nu_1) = (\pm 1, \pm 2)$  NCI modes do not grow exponentially and are therefore much less observable in the corresponding spectrum at  $t = 3200\omega_0^{-1}$  in Fig. 3(d) as compared to 3(c).

## 5. hybrid solver in quasi-3D algorithm

As mentioned in Section 1, the idea of the hybrid solver can be easily incorporated into the quasi-3D algorithm [27,28] in which the fields and current are expanded into azimuthal Fourier modes. We can obtain the hybrid Yee-FFT solver for the quasi-3D algorithm by using FFTs in the  $z$  ( $x_1$ ) direction and finite difference operators in  $r$  ( $x_2$ ) direction in the equations for each azimuthal mode. Note in quasi-3D OSIRIS we use a charge conserving current deposition scheme for the Yee solver (as described in [28]), therefore for the hybrid solver adapted for the quasi-3D algorithm we can apply the same current correction for the use of FFTs to  $j_1$  in order that the Gauss's Law is satisfied throughout the duration of the simulation.

The NCI properties of the hybrid solver for the quasi-3D algorithm are similar to that of the 2D Cartesian geometry [29]. While a rigorous NCI theory for the quasi-3D algorithm is still under development, we can empirically investigate the NCI for this geometry through simulation. In Fig. 2(d) and (f) we plot the  $E_r$  data at a

time during the exponential growth of the EM fields due to the NCI, which shows the  $(\mu, \nu_1) = (0, \pm 1)$  and  $(\mu, \nu_1) = (0, 0)$  modes for the hybrid solver in quasi-3D geometry. For the  $E_r$  data, we conduct an FFT in  $x_1$  and a Hankel transform in  $x_2$ . Similarly to the 2D Cartesian case, we isolate the  $(\mu, \nu_1) = (0, 0)$  modes by applying a low-pass filter in the current in  $k_1$  space to eliminate the fastest growing  $(\mu, \nu_1) = (0, \pm 1)$  NCI modes. The parameters used in the simulations are listed in Table 1, and a conducting boundary is used for the upper  $r$  boundary. We kept azimuthal modes of  $m = -1, 0, 1$  in the simulations.

By comparing Fig. 2(c)–(f) it can be seen that the pattern of the NCI modes are similar for the  $(x_2, x_1)$  and  $(r, z)$  geometries. We have also plotted the dependence of the growth rate and  $k_1$  position of the  $(\mu, \nu_1) = (0, 0)$  NCI modes for the quasi-3D geometry in Fig. 2(a) and (b). These plots show that when the time step decreases the growth rates of the  $(\mu, \nu_1) = (0, 0)$  NCI modes in the quasi-3D geometry decreases, while the  $k_1$  position increases (and move away from the physical modes), in a nearly similar fashion to 2D Cartesian geometry. This indicates that the same strategies for eliminating NCI in 2D Cartesian geometry can be applied to the quasi-3D geometry. The fastest growing modes residing at the edge of the fundamental Brillouin zone can be eliminated by applying a low-pass filter in the current. The  $(\mu, \nu_1) = (0, 0)$  NCI modes can be mitigated by either reducing the time step to lower the growth rate and move the modes away from the physics in  $k_1$  space, or by modifying the  $[k_1]$  operator as discussed in Section 4 to create a bump in the EM dispersion along the  $k_1$  direction. We have implemented the modification to the  $[k_1]$  operator into the hybrid solver for the quasi-3D OSIRIS code, and have confirmed that this modification completely eliminate the  $(\mu, \nu_1) = (0, 0)$  NCI modes. The

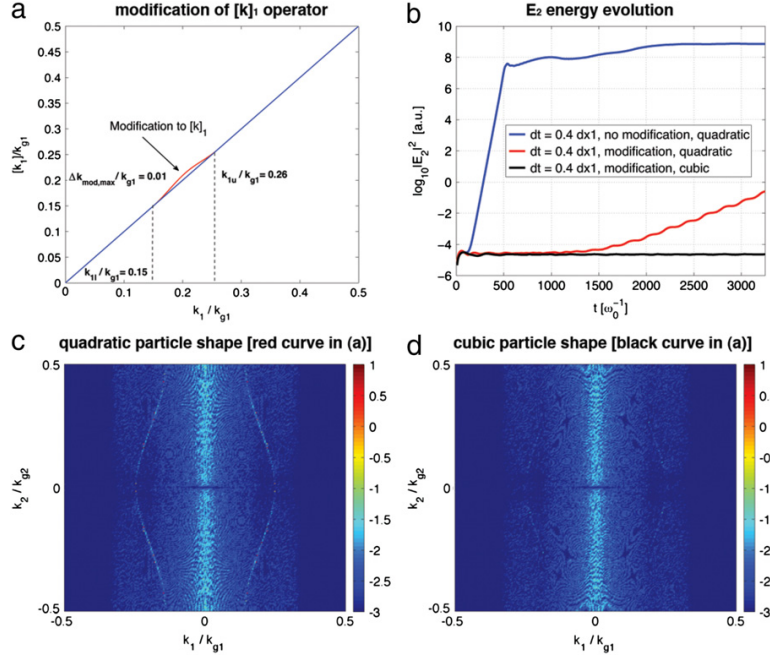


**Fig. 3.** In (a) the perturbation to  $[k]_1$  that is used to eliminate the  $(\mu, \nu_1) = (0, 0)$  NCI modes is shown. In (b) the evolution of the  $\log_{10}|E_2|^2$  for a reference case and for two cases with the EM dispersion modification (one with quadratic and another with cubic particle shapes). In (c) and (d), the spectrum of  $E_2$  at  $t = 3200\omega_0^{-1}$  is shown for the two cases with the EM dispersion modifications. In (c) quadratic particle shapes are used, while in (d) cubic particle shapes are used. (For interpretation of the references to colour in this figure legend, the reader is referred to the web version of this article.)

coefficients used for the modification are the same as those for the 2D Cartesian case discussed in Section 4.

## 6. Sample simulations

In this section, we present preliminary results of Lorentz boosted frame LWFA simulations using the hybrid solver in OSIRIS. For comparison, we performed simulations with the same parameters using UPIC-EMMA which uses a spectral Maxwell solver. Table 2 lists the simulation parameters. We use a moving antenna in both cases to launch lasers into the plasma. The results are summarized in Fig. 4.

In Fig. 4(a)–(b) the  $E_1$  field at  $t' = 3955\omega_0^{-1}$  for simulations with both the hybrid solver and spectral solver in the Lorentz boosted frame are plotted, where  $\omega_0$  is the laser frequency in the lab frame. Both the spectral solver and hybrid solver give similar boosted frame results, and there is no evidence of NCI affecting the physics in either case. We plot the line out of the on-axis wakefield in Fig. 4(c), which shows very good agreement with one another. The very good agreement can also be seen when we transformed the boosted frame data back to the lab frame. In Fig. 4(d)–(h) we plot the on-axis  $E_1$  field for the OSIRIS lab frame data, the transformed data for the OSIRIS boosted frame simulation with the hybrid solver, and the transformed data from the UPIC-EMMA boosted simulation at several values of time in the lab frame. As seen in Fig. 4(d)–(h), the transformed data from the two boosted frame simulations agrees very well with each other.

In this paper, we mainly focus on LWFA simulations in a Lorentz boosted frame. However, it is worth pointing out that the hybrid solver can likewise be used for LWFA lab frame simulations with a moving window. When a self-injected or externally injected electron beam is accelerated by the wakefield, it will also suffer from numerical Cerenkov radiation (NCR), and may even be susceptible to the NCI in some cases. The resulting unphysical

**Table 2**

Parameters for a 2D LWFA simulations in the lab frame and Lorentz boosted frame that were used for in 2D Cartesian geometry with the hybrid solver in OSIRIS and with a fully spectral solver in UPIC-EMMA. The laser frequency  $\omega_0$  and number  $k_0$  in the lab frame are used to normalize simulation parameters. The density is normalized to the critical density in the lab frame,  $n_0 = m_e \omega_0^2 / (4\pi e^2)$ .

Plasma	
density $n_0$	$1.148 \times 10^{-3} n_0 \gamma_b$
length $L$	$7.07 \times 10^4 k_0^{-1} / \gamma_b$
Laser	
pulse length $\tau$	$70.64 k_0^{-1} \gamma_b (1 + \beta_b)$
pulse waist $W$	$117.81 k_0^{-1}$
polarization	$\hat{z}$ -direction
normalized vector potential $a_0$	4.0
Lab frame simulation ( $\gamma_b = 1$ )	
grid size $(\Delta x_1, \Delta x_2)$	$(0.2 k_0^{-1}, 2.75 k_0^{-1})$
time step $\Delta t / \Delta x_1$	0.996
number of grid (moving window)	$4000 \times 512$
particle shape	quadratic
2D boosted frame simulation ( $\gamma_b = 14$ )	
grid size $\Delta x_{1,2}$	$0.0982 k_0^{-1} \gamma_b (1 + \beta_b)$
time step $\Delta t / \Delta x_1$	0.125
number of grid	$8192 \times 512$
particle shape	quadratic

EM fields can lead to unphysical emittance growth. Applying the hybrid solver in lab frame simulations will greatly reduce the NCR, which may lead to more accurate emittance values. As a result, although not shown in this paper, we likewise benchmarked the hybrid solver with Yee solver in LWFA lab frame simulation by comparing the wakefields and laser evolution in the two cases, and very good agreement was obtained.

## 7. Summary

We proposed to use a hybrid Yee-FFT and a rigorous charge conserving current deposit for solving Maxwell's equations in order

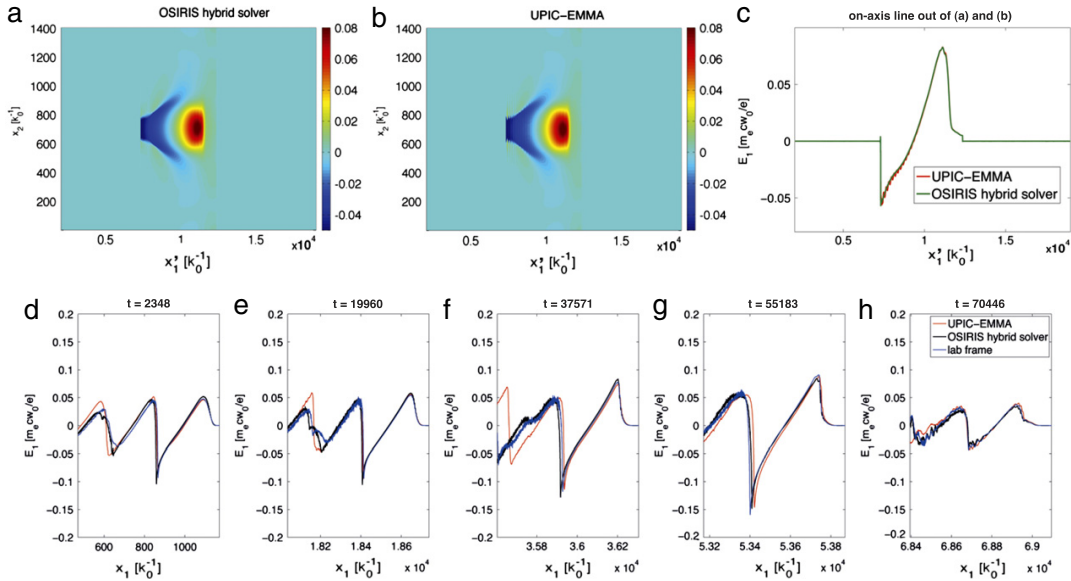


**Fig. 4.** Comparison between OSIRIS lab frame, OSIRIS with the hybrid solver in the boosted frame and UPIC-EMMA in the boosted frame. In (a) and (b), 2D plots of  $E_1$  for OSIRIS with the hybrid solver and UPIC-EMMA at  $t' = 3955\omega_0^{-1}$  are shown in the boosted frame, where  $\omega_0$  is the laser frequency in the lab frame. In (c), lineouts along the laser propagation direction of the same data are shown. In (d)–(h), lineouts of the  $E_1$  data transformed back to the lab frame are shown. The colored lines correspond to an OSIRIS lab frame simulation, an OSIRIS hybrid solver simulation in the Lorentz boosted frame, and UPIC-EMMA simulation in the Lorentz boosted frame. (For interpretation of the references to colour in this figure legend, the reader is referred to the web version of this article.)

to eliminate the numerical Cerenkov instability in PIC codes when modeling plasmas or beams that drift with relativistic speeds in a particular direction. In this solver we solve the Maxwell's equation in  $k_1$  space along the drifting direction ( $\hat{x}_1$  direction), and use second order finite difference representation for the derivatives in the other directions. This provides greater than  $N$ th order accuracy for the spatial derivatives in the  $\hat{x}_1$  direction, while keeping the locality of the field solve and current deposit in the directions transverse to  $\hat{1}$ . For the current deposit, we start from the charge conserving deposit in OSIRIS and then correct it so that it still satisfies the continuity equation for the hybrid solver. Thus, Gauss's law remains rigorously satisfied at every time step if it is satisfied initially.

It is found from the NCI theory that such a hybrid solver has similar NCI properties in comparison to a full spectral solver that solves Maxwell equation in multi-dimensional  $k$  space. As a result, the  $(\mu, \nu_1) = (0, 0)$  NCI modes have a growth rate one order of magnitude smaller than the fastest growing  $(\mu, \nu_1) = (0, \pm 1)$  NCI modes, and are highly localized. In addition, the growth rates of the  $(\mu, \nu_1) = (0, 0)$  modes decrease as one reduces the simulation time step, and their locations in Fourier space also move farther away from the physics.

Compared with the spectral solver, the hybrid solver performs an FFT only along the drifting direction of the plasma. As a result, it saves the computation of FFT in the other directions if this ultimately becomes an issue for parallel scalability. In addition, it can be readily adapted into fully operational FDTD codes without the need to modify various boundary conditions in the transverse directions. Very importantly, this idea can be readily applied to the quasi-3D algorithm in which the quantities are decomposed into azimuthal harmonics. In this algorithm FFTs cannot be used in the  $\hat{r}$  direction. We demonstrate the feasibility of the hybrid Yee-FFT solver in 2D/3D Cartesian geometry, as well as in the quasi-3D geometry. Although we have not conducted a rigorous theoretical analysis for the NCI in the  $r$ - $z$  or quasi-3D geometries, we find in

simulations that the hybrid solver in quasi-3D geometry has very similar NCI properties to that in the 2D Cartesian geometry.

We show that the strategy to eliminate NCI in the hybrid solver for 2D/3D Cartesian geometry, as well as quasi-3D geometry, is similar to that for the spectral solver. The fastest growing NCI modes can be eliminated by applying a low-pass filter in the current. The  $(\mu, \nu_1) = (0, 0)$  NCI modes can be eliminated by reducing the time step which both reduces their growth rates and moves them away from the physical modes in Fourier space. These NCI modes can also be fully eliminated by slightly modifying the EM dispersion relation along  $k_1$  direction at the location in Fourier space where the  $(\mu, \nu_1) = (0, 0)$  modes reside. This approach is demonstrated in both Cartesian and quasi-3D geometry.

We showed that the new hybrid solver in OSIRIS can be used to conduct 2D LWFA simulations in a Lorentz boosted frame. With the low-pass filter applied to current and using reduced time step, we observe no evidence of NCI affecting the physics in the simulation. Very good agreement is found between the results from OSIRIS with the hybrid solver, UPIC-EMMA simulations, as well as OSIRIS lab frame simulations with the standard Yee solver. This demonstrates the feasibility of using the hybrid solver to perform high fidelity relativistic plasma drift simulation.

### Acknowledgments

This work was supported by US DOE under grants DE-SC0008491, DE-SC0008316, DE-FG02-92ER40727, and by the US National Science Foundation under the grant ACI 1339893, OCI 1036224, and by NSFC 11425521, 11535006, 11175102, 11375006, and Tsinghua University Initiative Scientific Research Program, and by the European Research Council (ERC-2010-AdG Grant 267841), and by LLNL's Lawrence Fellowship. Simulations were carried out on the UCLA Hoffman2 and Dawson2 Clusters, and on Hopper Cluster of the National Energy Research Scientific Computing Center, and on Blue Waters cluster at National Center for Supercomputing Applications at UIUC.

### Appendix. Numerical dispersion for relativistically drifting plasma and NCI analytical expression in hybrid solver

According to Refs. [9,10], the numerical dispersion for the hybrid solver can be expressed as

$$\begin{aligned} & \left( (\omega' - k'_1 v_0)^2 - \frac{\omega_p^2}{\gamma^3} (-1)^\mu \frac{S_{j1} S_{E1} \omega'}{[\omega]} \right) \\ & \times \left( [\omega]^2 - [k]_{E1} [k]_{B1} - [k]_{E2} [k]_{B2} \right. \\ & \left. - \frac{\omega_p^2}{\gamma} (-1)^\mu \frac{S_{j2} (S_{E2} [\omega] - S_{B3} [k]_{E1} v_0)}{\omega' - k'_1 v_0} \right) + \mathcal{C} = 0 \end{aligned} \quad (\text{A.1})$$

where  $\mathcal{C}$  is a coupling term in the dispersion relation

$$\begin{aligned} \mathcal{C} = & \frac{\omega_p^2}{\gamma} \frac{(-1)^\mu}{[\omega]} \left\{ S_{j1} S_{E1} \omega' [k]_{E2} [k]_{B2} (v_0^2 - 1) \right. \\ & + S_{j2} S_{E2} [k]_{E2} [k]_{B2} (\omega' - k'_1 v_0) \\ & \left. + S_{j1} [k]_{E2} (S_{E2} [k]_{B1} k_2 v_0 - S_{B3} k_2 v_0^2 [\omega]) \right\} \end{aligned} \quad (\text{A.2})$$

and for the hybrid solver

$$[k]_{E1} = [k]_{B1} = k_1 \quad [k]_{E2} = [k]_{B2} = \frac{\sin(k_2 \Delta x_2 / 2)}{\Delta x_2 / 2}. \quad (\text{A.3})$$

We can expand  $\omega'$  around the beam resonance  $\omega' = k'_1 v_0$  in Eq. (A.1), and write  $\omega' = k'_1 v_0 + \delta\omega'$ , where  $\delta\omega'$  is a small term. This leads to a cubic equation for  $\delta\omega'$  (see [10] for the detailed derivation),

$$A_2 \delta\omega'^3 + B_2 \delta\omega'^2 + C_2 \delta\omega' + D_2 = 0 \quad (\text{A.4})$$

where

$$\begin{aligned} A_2 &= 2\xi_0^3 \xi_1 \\ B_2 &= \xi_0^2 \left\{ \xi_0^2 - [k]_{E1} [k]_{B1} - [k]_{E2} [k]_{B2} \right. \\ & \quad \left. - \frac{\omega_p^2}{\gamma} (-1)^\mu S_{j2} (S_{E2} \xi_1 - \zeta_1 S'_{B3} [k]_{E1}) \right\} \\ C_2 &= \frac{\omega_p^2}{\gamma} (-1)^\mu \left\{ \xi_0^2 S_{j2} (\zeta_0 S'_{B3} [k]_{E1} - S_{E2} \xi_0) - \xi_1 S_{j1} [k]_{E2} k_2 S_{E2} [k]_{B1} \right. \\ & \quad \left. + \xi_0 [k]_{E2} (S_{j2} S_{E2} [k]_{B2} - S_{j1} k_2 \zeta_1 S'_{B3} \xi_0) \right\} \\ D_2 &= \frac{\omega_p^2}{\gamma} (-1)^\mu \xi_0 [k]_{E2} k_2 S_{j1} \left( S_{E2} [k]_{B1} - \zeta_0 S'_{B3} \xi_0 \right) \end{aligned} \quad (\text{A.5})$$

where

$$\begin{aligned} \xi_0 &= \frac{\sin(\tilde{k}_1 \Delta t / 2)}{\Delta t / 2} & \xi_1 &= \cos(\tilde{k}_1 \Delta t / 2) \\ \zeta_0 &= \cos(\tilde{k}_1 \Delta t / 2) & \zeta_1 &= -\sin(\tilde{k}_1 \Delta t / 2) \Delta t / 2 \\ \tilde{k}_1 &= k_1 + v_1 k_{g1} - \mu \omega_g. \end{aligned} \quad (\text{A.6})$$

We use

$$s_{l,i} = \left( \frac{\sin(k_i \Delta x_i / 2)}{\Delta x_i / 2} \right)^{l+1} \quad (\text{A.7})$$

as well as use the corresponding interpolation functions for the EM fields used to push the particles

$$\begin{aligned} S_{E1} &= s_{l,1} s_{l,2} s_{l,3} (-1)^{v_1} & S_{E2} &= s_{l,1} s_{l,2} s_{l,3} & S_{E1} &= s_{l,1} s_{l,2} s_{l,3} \\ S_{B1} &= s_{l,1} s_{l,2} s_{l,3} & S_{B2} &= s_{l,1} s_{l,2} s_{l,3} (-1)^{v_1} \\ S_{B3} &= s_{l,1} s_{l,2} s_{l,3} (-1)^{v_1} \end{aligned} \quad (\text{A.8})$$

when using the momentum conserving field interpolation, and use

$$\begin{aligned} S_{E1} &= s_{l,-1,1} s_{l,2} s_{l,3} (-1)^{v_1} & S_{E2} &= s_{l,1} s_{l,-1,2} s_{l,3} \\ S_{E1} &= s_{l,1} s_{l,2} s_{l,-1,3} \\ S_{B1} &= s_{l,1} s_{l,-1,2} s_{l,-1,3} & S_{B2} &= s_{l,-1,1} s_{l,2} s_{l,-1,3} (-1)^{v_1} \\ S_{B3} &= s_{l,-1,1} s_{l,-1,2} s_{l,3} (-1)^{v_1} \end{aligned} \quad (\text{A.9})$$

when using the energy conserving field interpolation. The  $(-1)^{v_1}$  term is due to the half-grid offsets of these quantities in the  $\hat{1}$  direction. With respect to the current interpolation,

$$\begin{aligned} S_{j1} &= s_{l,-1,1} s_{l,2} s_{l,3} (-1)^{v_1} & S_{j2} &= s_{l,1} s_{l,-1,2} s_{l,3} \\ S_{j3} &= s_{l,1} s_{l,2} s_{l,-1,3}. \end{aligned} \quad (\text{A.10})$$

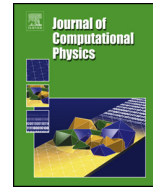
We note that we use expressions for charge conserving current deposition scheme that are strictly true in the limit of vanishing time step  $\Delta t \rightarrow 0$ . The coefficients  $A_2$  to  $D_2$  are real, and completely determined by  $k_1$  and  $k_2$ . By solving Eq. (A.4) one can rapidly scan the NCI modes for a particular set of  $(\mu, v_1)$ .

### References

- [1] T. Tajima, J.M. Dawson, Phys. Rev. Lett. 43 (1979) 267.
- [2] S.F. Martins, R.A. Fonseca, W.B. Mori, L.O. Silva, Astrophys. J. Lett. 695 (2009) L189–L193.
- [3] F. Fiuza, R.A. Fonseca, J. Tonge, W.B. Mori, L.O. Silva, Phys. Rev. Lett. 108 (2012) 235004.
- [4] S.C. Wilks, W.L. Krueer, M. Tabak, A.B. Langdon, Phys. Rev. Lett. 69 (1992) 1383.
- [5] J. Tonge, et al., Phys. Plasmas 16 (2009) 056311.
- [6] J. May, et al., Phys. Rev. E 84 (2011) 025401(R); J. May, et al., Phys. Plasmas 21 (2014) 052703.
- [7] B.B. Godfrey, J. Comput. Phys. 15 (1974) 504.
- [8] B.B. Godfrey, J.-L. Vay, J. Comput. Phys. 248 (2013) 33–46.
- [9] X. Xu, et al., Comput. Phys. Comm. 184 (2013) 2503–2514.
- [10] P. Yu, et al., Comput. Phys. Comm. 192 (2015) 32–47.
- [11] P. Yu, et al., J. Comput. Phys. 266 (2014) 124.
- [12] B.B. Godfrey, J.-L. Vay, I. Haber, J. Comput. Phys. 258 (2014) 689.
- [13] B.B. Godfrey, J.-L. Vay, J. Comput. Phys. 267 (2014) 1.
- [14] B.B. Godfrey, J.-L. Vay, I. Haber, IEEE Trans. Plasma Sci. 42 (2014) 1339.
- [15] K. Nagata, (Ph.D. thesis), Osaka University, 2008.
- [16] P. Yu, et al., Proc. 15th Advanced Accelerator Concepts Workshop, Austin, TX, 2012, in: AIP Conf. Proc. 1507, 416 (2012).
- [17] J.-L. Vay, Phys. Rev. Lett. 98 (2007) 130405.
- [18] S.F. Martins, R.A. Fonseca, W. Lu, W.B. Mori, L.O. Silva, Nat. Phys. 6 (2010) 311.
- [19] J.-L. Vay, C.G.R. Geddes, E. Cormier-Michel, D.P. Grote, J. Comput. Phys. 230 (2011) 5908.
- [20] S.F. Martins, R.A. Fonseca, L.O. Silva, W. Lu, W.B. Mori, Comput. Phys. Comm. 181 (2010) 869.
- [21] B.B. Godfrey, J. Comput. Phys. 19 (1975) 58.
- [22] K. Yee, IEEE Trans. Antennas and Propagation 14 (1966) 302.
- [23] J.M. Dawson, Rev. Modern Phys. 55 (2) (1983) 403.
- [24] A.T. Lin, J.M. Dawson, H. Okuda, Phys. Fluids 17 (1974) 1995.
- [25] J.-L. Vay, I. Haber, B.B. Godfrey, J. Comput. Phys. 243 (2013) 260.
- [26] R.A. Fonseca, et al., in: P.M.A. Sloat, et al. (Eds.), ICCS, in: Lect. Notes Comput. Sci., vol. 2331, 2002, pp. 342–351.
- [27] A. Lifschitz, et al., J. Comput. Phys. 228 (2009) 1803.
- [28] A. Davidson, et al., J. Comput. Phys. 281 (2015) 1063.
- [29] P. Yu, et al., Proc. 16th Advanced Accelerator Concepts Workshop, San Jose, California, 2014.
- [30] T. Esirkepov, Comput. Phys. Comm. 135 (2001) 144.
- [31] I. Haber, et al. in: Proc. Sixth Conf. on Num. Sim. Plasmas, Berkeley, CA, 1973, pp. 46–48.
- [32] V.K. Decyk, Comput. Phys. Comm. 177 (2007) 95.

Contents lists available at [ScienceDirect](http://ScienceDirect)

## Journal of Computational Physics

[www.elsevier.com/locate/jcp](http://www.elsevier.com/locate/jcp)

## Enabling Lorentz boosted frame particle-in-cell simulations of laser wakefield acceleration in quasi-3D geometry



Peicheng Yu <sup>a,\*</sup>, Xinlu Xu <sup>a,b</sup>, Asher Davidson <sup>b</sup>, Adam Tableman <sup>b</sup>,  
 Thamine Dalichaouch <sup>b</sup>, Fei Li <sup>c</sup>, Michael D. Meyers <sup>b</sup>, Weiming An <sup>a,b</sup>,  
 Frank S. Tsung <sup>b</sup>, Viktor K. Decyk <sup>b</sup>, Frederico Fiuza <sup>d</sup>, Jorge Vieira <sup>e</sup>,  
 Ricardo A. Fonseca <sup>e,f</sup>, Wei Lu <sup>c</sup>, Luis O. Silva <sup>e</sup>, Warren B. Mori <sup>a,b</sup>

<sup>a</sup> Department of Electrical Engineering, University of California Los Angeles, Los Angeles, CA 90095, USA

<sup>b</sup> Department of Physics and Astronomy, University of California Los Angeles, Los Angeles, CA 90095, USA

<sup>c</sup> Department of Engineering Physics, Tsinghua University, Beijing 100084, China

<sup>d</sup> SLAC National Accelerator Laboratory, Menlo Park, CA 94025, USA

<sup>e</sup> GOLP/Instituto de Plasma e Fusão Nuclear, Instituto Superior Técnico, Universidade de Lisboa, 1049-001, Lisbon, Portugal

<sup>f</sup> ISCTE – Instituto Universitário de Lisboa, 1649-026, Lisbon, Portugal

## ARTICLE INFO

## Article history:

Received 24 October 2015

Received in revised form 6 April 2016

Accepted 6 April 2016

Available online 12 April 2016

## Keywords:

PIC simulation

Hybrid Maxwell solver

Relativistic plasma drift

Numerical Cerenkov Instability

Quasi-3D algorithm

Lorentz boosted frame

Moving window

## ABSTRACT

When modeling laser wakefield acceleration (LWFA) using the particle-in-cell (PIC) algorithm in a Lorentz boosted frame, the plasma is drifting relativistically at  $\beta_b c$  towards the laser, which can lead to a computational speedup of  $\sim \gamma_b^2 = (1 - \beta_b^2)^{-1}$ . Meanwhile, when LWFA is modeled in the quasi-3D geometry in which the electromagnetic fields and current are decomposed into a limited number of azimuthal harmonics, speedups are achieved by modeling three dimensional (3D) problems with the computational loads on the order of two dimensional  $r - z$  simulations. Here, we describe a method to combine the speedups from the Lorentz boosted frame and quasi-3D algorithms. The key to the combination is the use of a hybrid Yee-FFT solver in the quasi-3D geometry that significantly mitigates the Numerical Cerenkov Instability (NCI) which inevitably arises in a Lorentz boosted frame due to the unphysical coupling of Langmuir modes and EM modes of the relativistically drifting plasma in these simulations. In addition, based on the space-time distribution of the LWFA data in the lab and boosted frame, we propose to use a moving window to follow the drifting plasma, instead of following the laser driver as is done in the LWFA lab frame simulations, in order to further reduce the computational loads. We describe the details of how the NCI is mitigated for the quasi-3D geometry, the setups for simulations which combine the Lorentz boosted frame, quasi-3D geometry, and the use of a moving window, and compare the results from these simulations against their corresponding lab frame cases. Good agreement is obtained among these sample simulations, particularly when there is no self-trapping, which demonstrates it is possible to combine the Lorentz boosted frame and the quasi-3D algorithms when modeling LWFA. We also discuss the preliminary speedups achieved in these sample simulations.

© 2016 Elsevier Inc. All rights reserved.

\* Corresponding author.

E-mail address: [tpc02@ucla.edu](mailto:tpc02@ucla.edu) (P. Yu).

<http://dx.doi.org/10.1016/j.jcp.2016.04.014>

0021-9991/© 2016 Elsevier Inc. All rights reserved.

## 1. Introduction

Laser wakefield acceleration (LWFA) [1] offers the potential to construct compact accelerators that have numerous potential applications, including the building blocks for a next generation linear collider and the electron beam source for ultra-compact XFELs. It has thus attracted extensive interest, and the last decade has seen an explosion of experimental results. Fully nonlinear particle-in-cell (PIC) simulations have been instrumental in this progress as an aid in designing new experiments, in interpreting experimental results, and in testing new ideas. Furthermore, developing predictive theoretical models is challenging due to the strong nonlinear effects that are present in the blowout and bubble regimes of LWFA [2]; therefore numerical simulations are also critical in exploring the physics of LWFA. Particle-in-cell simulations have been extensively applied in LWFA research because the PIC algorithm follows the self-consistent interactions of particles through the electromagnetic (EM) fields directly calculated from the full set of Maxwell equations. When modeling LWFA using the PIC algorithm the laser wavelength needs to be resolved which is usually on the scale of 1  $\mu\text{m}$ ; meanwhile, the length of the plasma column that the laser propagates through can be on the scale of  $10^4$  to  $10^6$   $\mu\text{m}$ . As a result of this disparity in cell size and propagation distance, full three-dimensional (3D) PIC simulations of LWFA can be very CPU-time consuming. To capture the key physics while reducing the computation time, reduced models are continually being proposed. These include models that combine the ponderomotive guiding center with full PIC for the wake [3] or with the quasi-static approach [4,5]. However, these models cannot as yet model full pump depletion lengths, and the quasi-static approach cannot model self-injection.

Recently, two methods have been proposed that can speed up the LWFA simulation without losing key physics in the modeling of LWFA. One method is the Lorentz boosted frame technique [6]. In this method the LWFA simulations are performed in an optimized Lorentz boosted frame with velocity  $v_b$ , in which the length of the plasma column is Lorentz contracted, while the laser wavelength is Lorentz expanded. Assuming the reflection of the laser light is not important in the lab frame, then in a properly chosen Lorentz transformed frame the time and space scales to be resolved in a numerical simulation are minimized, and savings of factors that scale as  $\gamma_b^2 = (1 - v_b^2/c^2)^{-1}$  can be achieved.

Another speedup method that has been recently proposed is to decompose the EM fields and current density into a Fourier series in the azimuthal angle  $\phi$ ,

$$\begin{aligned}\vec{F}(r, z, \phi) &= \text{Re} \left\{ \sum_{m=0} \vec{F}^m(r, z) e^{im\phi} \right\} \\ &= \vec{F}^0(r, z) + \text{Re}\{\vec{F}^1\} \cos \phi - \text{Im}\{\vec{F}^1\} \sin \phi \\ &\quad + \text{Re}\{\vec{F}^2\} \cos(2\phi) - \text{Im}\{\vec{F}^2\} \sin(2\phi) \\ &\quad + \dots\end{aligned}$$

and truncate the expansion at a low  $m$  value [7]. This expansion is substituted into Maxwell's equations to generate a series of equations for the complex amplitudes for each harmonic. The harmonics are then summed to get the total fields. The particles are pushed in 3D Cartesian geometry and are then used to obtain the complex amplitudes for each harmonic of the current. This method can reduce the computational costs of modeling 3D problems with low azimuthal asymmetry to that on the order of 2D  $r - z$  simulations. This algorithm, together with a charge conserving current deposition scheme in quasi-3D geometry has been implemented in OSIRIS [8].

It was pointed out in Refs. [9,10] that it would be intriguing to combine these two methods in order to combine the speedups provided by each. Similar to full PIC simulations in the Cartesian geometry, it was found that in the quasi-3D geometry one of the main obstacles to performing Lorentz boosted frame simulations is the multi-dimensional Numerical Cerenkov Instability (NCI) [11–14] that inevitably arises due to the unphysical coupling between Langmuir modes (main and aliasing) and EM modes of the relativistic drifting plasma in the simulations. The coupling arises in the Lorentz boosted frame between modes which are purely longitudinal (Langmuir modes) and purely transverse (EM modes) in the lab frame. The coupling occurs at specific resonances  $(\omega - 2\pi\mu/\Delta t) = (k_z - 2\pi\nu_z/\Delta z)v_b$  where  $\mu$  and  $\nu_z$  are the time and space aliases and  $\Delta t$  and  $\Delta z$  are the time step and grid size respectively, and  $\omega$  and  $k_z$  are the frequency and wave number in  $\hat{z}$  direction.

While the multi-dimensional NCI theory in Cartesian coordinates has been well studied (see e.g. [12–18]), there are currently no analytical expressions for the numerical dispersion relation of a relativistic plasma drift in the quasi-3D geometry. However, OSIRIS [22] simulations have shown that its behavior in the quasi-3D  $r - z$  geometry is very similar to that in the Cartesian geometry. It was therefore recently proposed and demonstrated that a hybrid Yee-FFT solver could be used to suppress the NCI in the Cartesian and quasi-3D geometries [18]. In the regular Yee (a finite difference) solver in a quasi-3D geometry [7,21], Maxwell equations are solved in  $(r, z)$  space for each azimuthal mode  $m$ . In the hybrid Yee-FFT solver, we perform a (discrete) Fourier transform in the drifting direction of the plasma (denote as  $\hat{z}$  direction), and solve Maxwell equations in  $k_z$  space for each azimuthal mode  $m$ ; meanwhile, in the  $\hat{r}$  direction the derivatives are represented as second order finite difference operators on a Yee grid. The current is corrected to maintain the satisfaction of Gauss' Law. When Maxwell's equations are solved in this way, the corresponding NCI modes can be systematically eliminated by applying similar strategies used for a multi-dimensional spectral Maxwell solver [14,17]. The fastest growing modes of the NCI at  $(\mu, \nu_1) = (0, \pm 1)$  can be conveniently suppressed by applying a low-pass filter in the current, the highly localized

$(\mu, \nu_z) = (0, 0)$  NCI modes can be moved away from physical modes by reducing the time step, and can be subsequently eliminated by modifying the EM dispersion at the  $k_z$  range where the  $(\mu, \nu_z) = (0, 0)$  NCI modes are located. Furthermore, higher order spatial aliasing NCI modes can be mitigated by applying higher order particle shapes. In this paper, we present OSIRIS simulation results which show that Lorentz boosted simulations of LWFA can be performed in this geometry with no evidence of NCI. It is worth noting that recently a PIC algorithm based on a fully spectral solver in quasi-3D geometry has been proposed by Lehe et al. [23] and was demonstrated with a single-node algorithm.

In addition, according to how the lab frame information is located in the  $(z', t')$  space, we show that the computational loads can be further reduced by applying a moving window in the boosted frame simulation. In the boosted frame the window follows the plasma as opposed to the laser, which is the case when using a moving window in the lab frame.

The remainder of this paper is organized as follows: in section 2 we briefly discuss the hybrid Yee–FFT solver in quasi-3D geometry, and the corresponding NCI mitigation strategies. In section 3, we discuss the simulation setups for modeling LWFA in the Lorentz boosted frame. We discuss the distribution of the data needed for the reconstruction of lab frame information with an emphasis on showing that using a moving window in the direction of the plasma drift can further reduce the computational load. We then show sample quasi-3D simulations of LWFA in the Lorentz boosted frame in section 4, and compare the results with the corresponding 3D boosted frame and lab frame data. In particular, we concentrate on the study of the laser driver evolution as it propagates through the plasma. Good agreement is obtained when comparing the driver evolution in lab frame against that obtained from the boosted frame simulation. This demonstrates the feasibility of combining Lorentz boosted frame technique, quasi-3D algorithm, and a moving window. We also discuss the preliminary speedups achieved in these sample simulations. The results are summarized in section 5.

## 2. NCI elimination scheme in quasi-3D geometry

### 2.1. Quasi-3D hybrid Yee–FFT solver

A key issue that needs to be addressed when performing LWFA simulations in a Lorentz boosted frame is the existence of a violent numerical instability, called the Numerical Cerenkov Instability (NCI). The NCI arises when a plasma drifts relativistically on the grid. There has been much recent progress in identifying the NCI as the source of the instability, in deriving the numerical dispersion relations and determining growth rates, and in identifying mitigation strategies [11–18]. In Ref. [18] a hybrid Yee–FFT solver was proposed for the elimination of the NCI in the Cartesian geometry. In this solver, Maxwell equations are Fourier transformed in the drifting direction of the plasma (denoted as the  $\hat{z}$  direction). The fields are solved in the corresponding  $(k_z, x, y)$  space, where conventional second order finite difference operators on a Yee mesh are used in  $(x, y)$ . When Maxwell equations are solved in this way, the corresponding EM dispersion of the solver leads to NCI patterns that are very similar to those from a fully spectral Maxwell solver in which Maxwell equations are solved in multi-dimensional  $k$ -space. Therefore one can systematically eliminate the main and first spatial aliasing NCI using approximately the same strategies developed for a fully spectral solver. More importantly, the hybrid Yee–FFT solver works for both Cartesian geometry  $(z, x, y)$ , and quasi-3D geometry  $(z, r, \phi)$ . Although at present there is no rigorous theory on the NCI in the quasi-3D geometry, it has been found through OSIRIS simulations that the NCI patterns and growth rates are very similar to its counterpart in Cartesian 2D geometry [9]. Therefore, the idea of hybrid Yee–FFT solver can be readily applied to the quasi-3D geometry.

When the Maxwell solver is modified from a standard Yee solver to a hybrid Yee–FFT solver, essentially the spatial finite difference operator in the  $\hat{z}$  direction is modified from second-order accuracy (derived from its finite difference form) into a greater than  $N$ -th order accuracy. However, in OSIRIS (and most of the modern PIC codes) the  $\vec{E}$  and  $\vec{B}$  fields are advanced using Faraday's Law and Ampere's Law, while Gauss's Law is satisfied by applying a charge conserving current deposition scheme [8,24,25]. This scheme begins by calculating the current using the charge conserving current deposit scheme of [24,25] for a purely  $r - z$  code. It then uses this as a common factor in the amplitude for each azimuthal harmonic of  $J_z$  and  $J_r$  together with a factor that depends on the particle position in  $\phi$  at the half time step; and it uses this together with the particle motion in  $\phi$  to get  $J_\phi$  for each harmonic (see section 3.2 of Ref. [8] for more details). If the continuity equation is rigorously satisfied at each time step then by taking the finite difference version of the divergence of Ampere's law, Gauss' Law is seen to be satisfied if it is satisfied at  $t = 0$ .

However, the rigorous charge conserving current deposit is known only for second order finite difference operators in the  $\hat{z}$  direction. Therefore, when we use a FFT for the differential operator along  $\hat{z}$  direction in Faraday's and Ampere's Law, we need to modify the current appropriately so the continuity equation is still true for the modified differential operator. To accomplish this, for each azimuthal mode of current  $\tilde{J}^m(z, r)$  obtained from the charge conserving current deposition scheme described in [8], we Fourier transform it along  $\hat{z}$ -direction, and then apply a correction with the form,

$$\tilde{J}_z^m(k_z, r) = \frac{[k]_z}{k_z} J_z^m(k_z, r) \quad (1)$$

where

$$[k]_z = \frac{\sin(k_z \Delta z / 2)}{\Delta z / 2} \quad (2)$$



is the second order first spatial finite difference operator. This correction ensures the satisfaction of Gauss' Law throughout the simulation, as will be discussed shortly afterwards.

Each azimuthal mode of the EM fields is initially stored in the memory in  $(z, r)$  space, and is advanced in  $(k_z, r)$  space. We Fourier transform  $\vec{E}$  and  $\vec{B}$  along  $\hat{z}$ -direction, and solve Faraday's Law and Ampere's Law for each azimuthal mode  $m$ , and each Fourier mode  $k_z$ , using the corrected current as the source term,

$$\partial_t B_r^m = -\frac{im}{r} E_z^m - ik_z E_\phi^m \quad (3)$$

$$\partial_t B_\phi^m = ik_z E_r^m + \partial_r E_z^m \quad (4)$$

$$\partial_t B_z^m = -\frac{1}{r} \partial_r (r E_\phi^m) + \frac{im}{r} E_r^m \quad (5)$$

$$\partial_t E_r^m = \frac{im}{r} B_z^m + ik_z B_\phi^m - J_r^m \quad (6)$$

$$\partial_t E_\phi^m = -ik_z B_r^m - \partial_r B_z^m - J_\phi^m \quad (7)$$

$$\partial_t E_z^m = -\frac{1}{r} \partial_r (r B_\phi^m) - \frac{im}{r} B_r^m - \tilde{J}_z^m \quad (8)$$

Here  $\vec{E}^m$ ,  $\vec{B}^m$ , and  $\vec{J}^m$  are all in  $(k_z, r)$  space. Note that  $\partial_t$  and  $\partial_r$  adopt the conventional finite difference form as in the Yee solver. The code is gridless in  $\phi$  so  $\partial_\phi$  is replaced with  $im$ . The fields are then transformed back to  $(z, r)$  space, summed over  $m$  modes, and gathered for the particle pushing.

The reasoning behind the current correction Eq. (1) is that the charge conserving current deposition scheme described in [8] ensures that

$$\partial_t \rho^m(k_z, r) + i[k]_z J_z^m(k_z, r) + \nabla_r J_r^m(k_z, r) + \frac{im}{r} J_\phi^m(k_z, r) = 0 \quad (9)$$

where  $[k]_z$  is given in Eq. (2) for this expression, and  $\nabla_r(\cdot)$  is the second order accurate finite difference operator in  $\hat{r}$ . Therefore this correction ensures that Gauss's Law in the hybrid solver

$$ik_z E_z^m(k_z, r) + \nabla_r E_r^m(k_z, r) + \frac{im}{r} E_\phi^m(k_z, r) = 4\pi \rho^m(k_z, r) \quad (10)$$

is satisfied throughout the simulation if it is satisfied at  $t = 0$  (see section 2.3 of Ref. [18] for more details).

## 2.2. Elimination of Numerical Cerenkov Instability

We have found previously that the NCI pattern for the quasi-3D hybrid Yee-FFT solver is similar to its counterpart in the Cartesian 3D geometry [9,18]. As a result, we can apply approximately the same mitigation strategies used for the fully spectral solver in Cartesian geometry to systematically eliminate the NCI modes for this solver [14,17].

We first eliminate the fastest growing  $(\mu, \nu_z) = (0, \pm 1)$  modes ( $\nu_z$  is the spatial aliasing in  $\hat{z}$  direction) by applying a low-pass filter in the current. The filter covers the entire  $k_z$  range in which the  $(\mu, \nu_z) = (0, \pm 1)$  NCI modes reside to prevent an unphysical exponential energy growth in these  $k_z$  modes. This can be efficiently accomplished since the current density is already in  $k_z$  space after the Fourier transform. For instance, in the sample simulation in section 4 we are using a low pass filter that has the following expression:

$$F(k_z) = \begin{cases} 1, & |k_z| < f_l k_{gz} \\ \sin^2\left(\frac{k_z - f_u k_{gz}}{f_l k_{gz} - f_u k_{gz}} \frac{\pi}{2}\right), & f_l k_{gz} \leq |k_z| \leq f_u k_{gz} \\ 0, & f_u k_{gz} < |k_z| \end{cases} \quad (11)$$

where  $k_{gz} = 2\pi/\Delta z$ . This filter cuts off all the  $k_z$  modes larger than  $f_u k_{gz}$ , while allowing modes smaller than  $f_l k_{gz}$  to go through the filter. A sine square function connects the two regions to ensure a smooth filtering function. The filter parameters  $f_l$  and  $f_u$  are listed in Table 1 and 2.

The second fastest growing NCI modes  $(\mu, \nu_z) = (0, 0)$  can be eliminated by reducing the time step, and then slightly modifying the  $k_z$  operator to create a small bump in the dispersion relation to precisely avoid intersections between the main EM modes and main Langmuir modes that are highly localized in  $k_z$  [17]. When determining the simulation time step, we first choose a time step such that the  $(\mu, \nu_z) = (0, 0)$  NCI modes are significantly far away from the physical modes. After that, we apply the  $[k]_z$  modification in the highly localized  $|k_z|$  range. This modification makes the growth rate of the  $(\mu, \nu_z) = (0, 0)$  NCI modes to be zero in theory. The  $[k]_z$  modification is straightforward in a hybrid Yee-FFT solver since we are essentially solving the Maxwell equation in  $k_z$  space. In the sample simulation presented in section 4 we applied the following correction to the  $[k]_z$  operator

**Table 1**

Parameters for the 3D and quasi-3D LWFA simulations in the Lorentz boosted frame (discussed in section 4.1). The laser frequency  $\omega_0$  and number  $k_0$  in the lab frame are used to normalize simulation parameters. The density is normalized to the critical density in the lab frame,  $n_0 = m_e \omega_0^2 / (4\pi e^2)$ . The normalized vector potential  $a_0$  for the laser corresponds to linear polarization.

Plasma	
density $n_p$	$8.62 \times 10^{-4} n_0 \gamma_b$
length $L$	$8.0 \times 10^4 k_0^{-1} / \gamma_b$
Laser	
pulse length $\tau$	$86.9 k_0^{-1} \gamma_b (1 + \beta_b)$
pulse waist $W$	$153.0 k_0^{-1}$
polarization	circular
normalized vector potential $a_0$	4.0
Quasi-3D boosted frame simulation ( $\gamma_b = 15.0$ )	
grid size $\Delta z = \Delta r$	$0.1 k_0^{-1} \gamma_b (1 + \beta_b)$
time step $\Delta t / \Delta x_z$	0.125
number of grid (moving window)	$2048 \times 256$
particle shape	quadratic
particle per cell ( $\hat{z}, \hat{r}, \hat{\phi}$ )	(2, 2, 16)
$[k]_z$ modification ( $( k _{zl}, k_{zm}, \Delta k_{\max}) / k_{gz}$ )	(0.141, 0.240, 0.007)
low pass filter ( $f_l, f_u$ )	(0.3, 0.35)
Full 3D boosted frame simulation ( $\gamma_b = 15.0$ )	
grid size $\Delta z = \Delta r = \Delta y$	$0.1 k_0^{-1} \gamma_b (1 + \beta_b)$
time step $\Delta t / \Delta z$	0.125
number of grid (moving window)	$2048 \times 512 \times 512$
particle shape	quadratic
particle per cell ( $\hat{z}, \hat{x}, \hat{y}$ )	(2, 2, 2)
$[k]_z$ modification ( $( k _{zl}, k_{zm}, \Delta k_{\max}) / k_{gz}$ )	(0.141, 0.240, 0.007)
low pass filter ( $f_l, f_u$ )	(0.3, 0.35)

**Table 2**

Parameters for the quasi-3D LWFA simulations in the lab frame and Lorentz boosted frame (discussed in section 4.2). The laser frequency  $\omega_0$  and number  $k_0$  in the lab frame are used to normalize simulation parameters. The density is normalized to the critical density in the lab frame,  $n_0 = m_e \omega_0^2 / (4\pi e^2)$ . The normalized vector potential  $a_0$  for the laser corresponds to linear polarization.

Plasma	
density $n_p$	$1.433 \times 10^{-4} n_0 \gamma_b$
length $L$	$1.63 \times 10^6 k_0^{-1} / \gamma_b$
Laser	
pulse length $\tau$	$296.4 k_0^{-1} \gamma_b (1 + \beta_b)$
pulse waist $W$	$351.9 k_0^{-1}$
polarization	circular
normalized vector potential $a_0$	4.44
Lab frame simulation ( $\gamma_b = 1$ )	
grid size in ( $\hat{z}, \hat{r}$ )	$(0.2 k_0^{-1}, 4.74 k_0^{-1})$
time step $\Delta t / \Delta x_z$	0.9974
number of grid (moving window)	$7920 \times 1248$
particle shape	quadratic
particle per cell ( $\hat{z}, \hat{r}, \hat{\phi}$ )	(2, 1, 8)
Boosted frame simulation ( $\gamma_b = 26.88$ )	
grid size (square cell)	$0.2 k_0^{-1} \gamma_b (1 + \beta_b)$
time step $\Delta t / \Delta x_z$	0.25
number of grid (moving window)	$8192 \times 792$
particle shape	quadratic
particle per cell ( $\hat{z}, \hat{r}, \hat{\phi}$ )	(2, 2, 16)
$[k]_z$ modification ( $( k _{zl}, k_{zm}, \Delta k_{\max}) / k_{gz}$ )	(0.135, 0.231, 0.005)
low pass filter ( $f_l, f_u$ )	(0.3, 0.35)

$$[k]_z = \begin{cases} k_z + \Delta k_{\max} \cos^2\left(\frac{kz - k_{zm}}{k_{zl} - k_{zm}} \frac{\pi}{2}\right), & k_{zl} < |k_z| < k_{zu} \\ k_z, & \text{otherwise} \end{cases} \quad (12)$$

where  $k_{zu} = 2k_{zm} - k_{zl}$ , and  $k_{zm}, k_{zl}, \Delta k_{\max}$  are listed in Table 1 and 2.

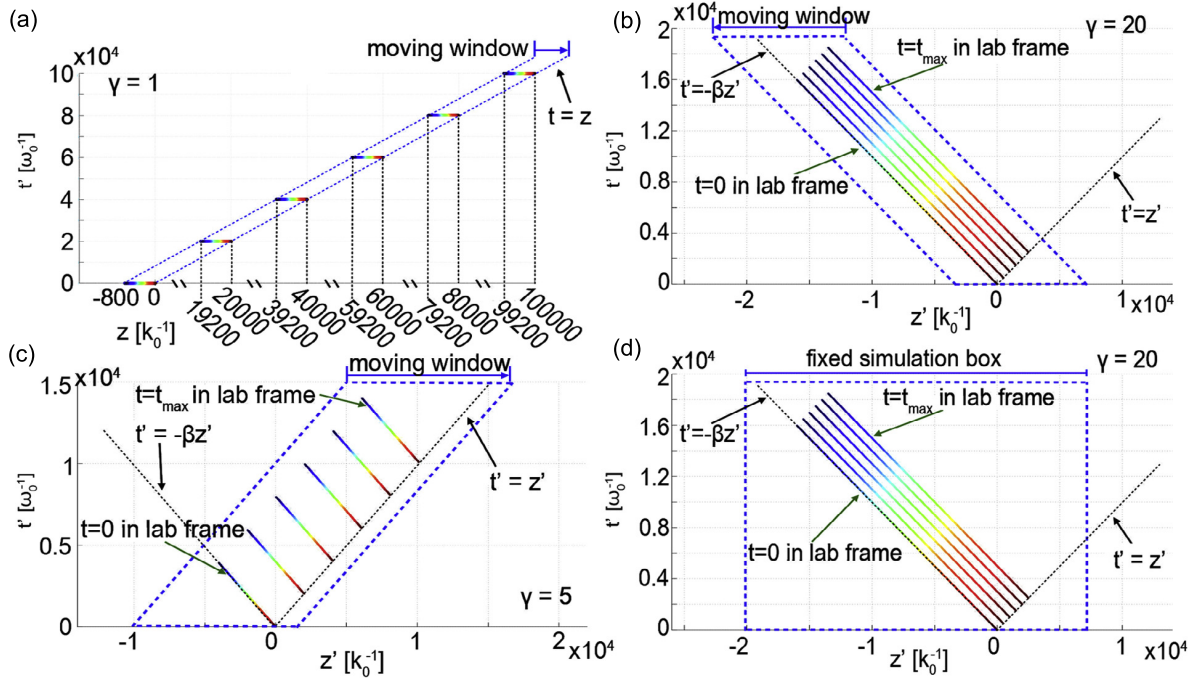


**Fig. 1.** Range of important data in lab and boosted frame simulations. (a) Range of data in lab frame (stationary plasma) simulation with a moving window, (b) range of data in a boosted frame simulation at  $\gamma_b = 20$  with a moving window following the drifting plasma, (c) range of data in a boosted frame simulation at  $\gamma_b = 5$  with a moving window following the laser driver, and (d) range of data in a boosted frame simulation at  $\gamma_b = 20$  without a moving window. (For interpretation of the references to color in this figure, the reader is referred to the web version of this article.)

As for higher order NCI modes, their growth rates can be reduced if needed by applying higher order particle shapes. However, for the parameter space explored in this paper, the higher order NCI modes have growth rates several orders of magnitude smaller than the fastest growing modes, and are not seen in the simulations even when the modes with higher growth rates are suppressed. Therefore, for the simulations presented here we used the quadratic particle shapes.

Applying the strategies described above, we can systematically mitigate the NCI modes in the quasi-3D geometry. Note the Fourier transform of the current into  $k_z$  space is not only important for the efficient filtering of the NCI modes, but also required to accurately correct (compensate) the current in  $k_z$  space to exactly match the modified Maxwell solver. It is worth noting that it is now a common practice to modify either the Maxwell solver or the field interpolation to change the EM dispersion relation in order to obtain a more desirable dispersion relation [12–19]. Within these schemes, Gauss' Law is satisfied by either directly solving it (as is the case in UPIC [26–28]), or by using a current that satisfies the continuity equation through a correction (compensation) to match the current deposition scheme with the Maxwell solver (as is the case here and in [18]).

### 3. Simulation setups in the boosted frame

The setup of a quasi-3D LWFA simulation in a Lorentz boosted frame is almost identical to its counterpart in Cartesian 2D/3D geometry. In a boosted frame with a Lorentz factor  $\gamma_b$  that moves in the propagation direction of the laser, the laser pulse is colliding with a counter-propagating relativistically drifting plasma [29–31]. Due to the Lorentz transform, the plasma density increases by  $\gamma_b$  while the total plasma column length contracts by  $\gamma_b$ . The laser wavelength and pulse length stretch by  $\gamma_b(1 + \beta_b)$ , while its Rayleigh length contracts by  $\gamma_b$ . To avoid initializing a laser with very wide transverse size due to the contracted Rayleigh length and stretched pulse length, a moving antenna is placed at the edge of the plasma boundary to inject a laser pulse into the plasma [32,33].

#### 3.1. Relationship between lab and boosted frame data

In LWFA simulations in the lab frame (i.e., a stationary plasma) the use of a moving window [34], which only follows the physical domain near the laser, significantly reduces the computational load. The moving window essentially drops plasma sufficiently far behind the laser and adds fresh plasma in front of the laser. This is illustrated in Fig. 1 (a) where we plot the range of space time data from a lab frame simulation. The solid box shows the total space time area while the dashed box shows the reduced area through the use of a moving window. The moving window has a length 800  $k_0^{-1}$ , and the

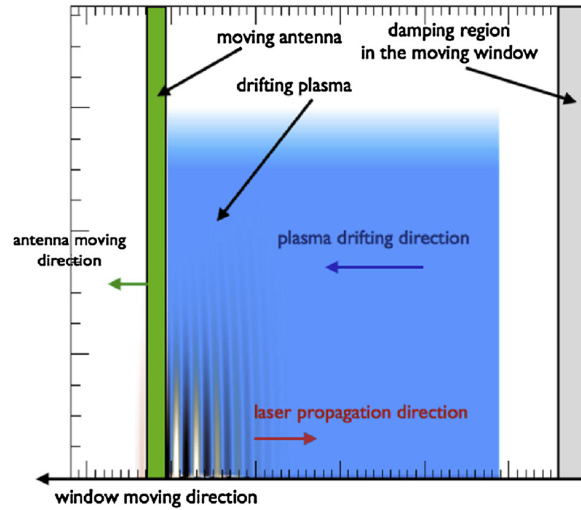


**Fig. 2.** Simulation setup for a typical LWFA simulation in the boosted frame. The moving window follows the drifting plasma moving from right to left. A moving antenna injects laser pulse that propagates from left to right, and a damping region is located at the rear end of the moving window.

simulation duration is  $t_{\max} = 100000 [\omega_0^{-1}]$  (where  $\omega_0$  and  $k_0$  are the frequency and wave number of the laser in the lab frame). We also show the simulation data that is dumped as colored lines. The data is dumped every  $20000 [\omega_0^{-1}]$ . The red ends of the data lines indicate the starting end of the moving window, while the blue ends indicate the rear end. Connecting the red ends of the data lines, we obtain the  $z - t$  relation for the head of the moving windows,  $t = z$  (the speed of light  $c$  is normalized to 1). The data obtained in the lab frame (assuming the code dumps data at a constant time interval) rotates in space–time in the boosted frame since the Lorentz transform is essentially a hyperbolic rotation of coordinates in Minkowski space [31,35]. Therefore lines of data in  $\hat{z}$  taken at fixed time from a Lorentz boosted frame are rotated by the Lorentz transform, i.e.,  $t' = t/\gamma_b - \beta_b z'$ . The slope of each data line now becomes  $-\beta_b$ , where  $\beta_b = (1 - \gamma_b^{-2})^{-1/2}$  and each data line in the lab frame which belongs to the same point in time in lab frame is now spread over a range of  $t'$  and  $z'$ . Interestingly, when we connect the red end of each data line in the boosted frame it still has a slope of  $c$ , i.e.  $t' = z'$ . The range of data in the boosted frame is shown in Figs. 1 (b), (c) and (d). The data in Figs. 1 (b), (d) corresponds to  $\gamma_b = 20$  while that in Fig. 1 (c) corresponds to  $\gamma_b = 5$ . In Figs. 1 (b) and (c) we also show the smallest area (domain enclosed by dashed lines) in  $t', z'$  space that includes the area needed to reconstruct the lab frame data for the two different values of  $\gamma_b$ . This illustrates that the space–time area in the boosted frame can be minimized by using a moving window in this frame. In Fig. 1 (b) it is seen that this window moves to the left (backwards); while in Fig. 1 (c) the window moves to the right (forwards). In the LWFA Lorentz boosted frame simulations presented in section 4 we use the moving windows to follow the drifting plasmas, as indicated by Fig. 1 (b). Currently, in UPIC-EMMA boosted frame simulations in Cartesian 2D/3D geometry a stationary window is used [see Fig. 1 (d)] [20].

From Fig. 1 it is evident that in lab frame simulations we usually dump data sparsely in time (large time intervals between time outputs), but the data at each grid is dumped at each time output. On the other hand, in order to recover the equivalent lab frame data in a boosted frame simulation, we need to sample boosted frame data at a much higher rate in time, but only need a small number of spatial locations. This can be seen by plotting a line across  $z'$  for a fixed  $t'$  in Fig. 1 (b). This line only intersects the equivalent lab frame data at the same number of spatial locations as the number of time outputs. We typically dump the boosted frame data in a standard form (all grid points at small number of time steps) as well as the data needed to transform the results back to the lab frame (a small number of interpolated grid points at a large number of time steps). We then post-process the later data by performing the inverse rotation back into lab frame for comparison with the lab frame data. When running in the lab frame we also plot the necessary data needed to reconstruct the data into a boosted frame. This inverse construction method is useful during the development of a boosted frame code, as one can transform the lab frame data that has been extensively cross checked with theory, to the boosted frame, and compare the results against the results obtained by the boosted frame code.

### 3.2. Basic setup

In Fig. 2, we present a typical setup for a boosted frame simulation. The moving window moves from right to left following the drifting plasma. The moving antenna is also moving from right to left and injects the laser pulse from the left plasma boundary into the plasma. We place a damping section at the rear (right) end of the moving window (there is a gap between the plasma and the damping region) to damp the EM field to zero in this region. This is done because periodic boundary conditions are applied in the  $\hat{z}$  direction when using the hybrid Yee–FFT solver, which requires that the EM fields

need to be zero at the rear end of the simulation window to match the fields at the opposite side; otherwise the EM field at the rear end will reappear at the starting end. We note that there will be a low level of EM reflection from the damping section. In the hybrid Yee–FFT solver, the group velocity of light propagating in  $\hat{z}$  direction in vacuum is slightly greater than the speed of light, however, the drifting plasma is drifting ultra-relativistically in the same direction, the reflected wave does not have enough time to catch up with the drifting plasma for the cases of interest. Hence the physics inside the plasma will not be affected by the reflecting EM waves. We have compared cases with the moving window plus the damping regions against cases without the moving window to confirm that the moving window plus damping region works [10]. We also note that for high  $\gamma_b$  boosted frame simulations, we find that the modified pusher described in Ref. [36] is required in order to get the evolution of the bubble correct. As pointed out in Ref. [36] the usual leap frog staggering [37] leads to issues for the Lorentz force when there is near cancellation of the electric and magnetic forces for relativistically moving particles. Determining at what  $\gamma_b$  the modified pusher in [36] is needed is an area of future work.

#### 4. Sample simulations

In this section, we present two sets of sample simulations. In section 4.1, we compare results from two boosted frame simulations where in one case we use full 3D OSIRIS and in the second case we use quasi-3D OSIRIS, in order to justify the truncation of higher azimuthal modes  $m$  in the quasi-3D boosted frame simulations. In both cases hybrid Yee–FFT solvers and the corresponding NCI mitigation schemes are used. The parameters match those in Ref. [2] whereby a 200 TW laser is focused to a spot size of 19.5  $\mu\text{m}$  at the entrance of a  $1.5 \times 10^{18} \text{ cm}^{-3}$  density plasma. The FWHM pulse length of the laser was 35 fs and the normalized vector was  $a_0 = 4.0$  for a linearly polarized laser or  $a_0 = 4.0/\sqrt{2}$  for a circularly polarized laser. This corresponds to a 1.3 GeV output electron energy according to the scaling laws in Ref. [2]. The numerical parameters are shown in Table 1. We then compare the output in the boosted frame for various azimuthal mode numbers. This comparison requires the use of a post-processing algorithm which decomposes the full 3D data into azimuthal modes [38].

In section 4.2 we compare the data of a LWFA boosted frame simulation in quasi-3D lab with the corresponding quasi-3D boosted frame simulation. For these simulations we explore parameters for which a full 3D lab frame simulation is not feasible due to the large CPU hours required. The parameters correspond to a 1.8 PW laser focused to a spot size of 45  $\mu\text{m}$  at the entrance of a  $2.5 \times 10^{17} \text{ cm}^{-3}$  density plasma. The FWHM pulse length of the laser was 130 fs and the normalized vector potential was  $a_0 = 4.44$  for a linearly polarized laser or  $a_0 = 4.44/\sqrt{2}$  for a circularly polarized laser. This corresponds to a 10.4 GeV output electron energy according to the scaling laws in Ref. [2]. The numerical parameters are shown in Table 2. The data from the boosted frame simulation is transformed back to the lab frame and it is compared against the data from the lab frame simulation.

##### 4.1. Comparison of 3D vs quasi-3D boosted frame data with a 1.3 GeV case

When modeling LWFA in quasi-3D geometry, whether it is in the lab frame or boosted frame, the accelerating ( $E_z$ ) and focusing fields ( $E_r$  and  $B_\phi$ ) in the bubble are mainly in the  $m = 0$  modes of the EM fields. On the other hand, the fields associated with the laser are associated with the  $|m| = 1$  mode of the fields. Therefore, by keeping at least the  $|m| \leq 1$  modes the self-consistent evolution of the laser and wake fields can be examined when there is nearly azimuthal symmetry. For this comparison we truncate the azimuthal harmonics keeping only the  $|m| \leq 1$  modes [7,8]. More modes can be kept in principle to study laser hosing and asymmetric spot size effects as well as to test the convergence of the results. In addition, the results and the needed truncation can be verified by comparing LWFA boosted frame simulation results from the full 3D and quasi-3D geometries. To verify the azimuthal mode truncation, we decompose the data from the full 3D boosted frame OSIRIS simulation into azimuthal harmonics and compare it against the corresponding quasi-3D simulation using the parameters listed in Table 1. In Fig. 3, we plot the azimuthal decomposition of the 3D data for  $E_z$  and  $E_r$  at  $t' = 4494.99 [\omega_0^{-1}]$ , and compare it against the corresponding quasi-3D boosted frame data at the same time. For the  $|m| \leq 1$  modes, very good agreement is observed. In addition, we plot the higher order  $m = 2, 3$  modes from the 3D data in Fig. 4. We can see that the higher order modes are at least one order of magnitude smaller than those of the  $m = 0, 1$  modes, which verifies the truncation of azimuthal harmonics at  $|m| \leq 1$  in the quasi-3D simulations when the laser is nearly symmetric.

The main purpose of this subsection is to justify the truncation of higher azimuthal modes in quasi-3D boosted frame simulations. Nonetheless, in Appendix A we show comparison of the final self-injected electron spectra in the lab frame transformed from the two boosted frame simulations, as well as from a 3D lab frame simulation [2]. Reasonable agreement is obtained but this is an area for future work.

##### 4.2. Comparison of quasi-3D lab frame vs boosted frame data with a 10.4 GeV case

Next, we compare data from a quasi-3D LWFA simulation in the lab frame against data Lorentz transformed back to the lab frame from a quasi-3D simulation. A laser with normalized vector potential of  $a_0 = 4.44$  (converted to linear polarization) with pulse length of 130 fs, and spot size of 45  $\mu\text{m}$  propagates into a plasma column 20.8 cm long (in the lab frame).

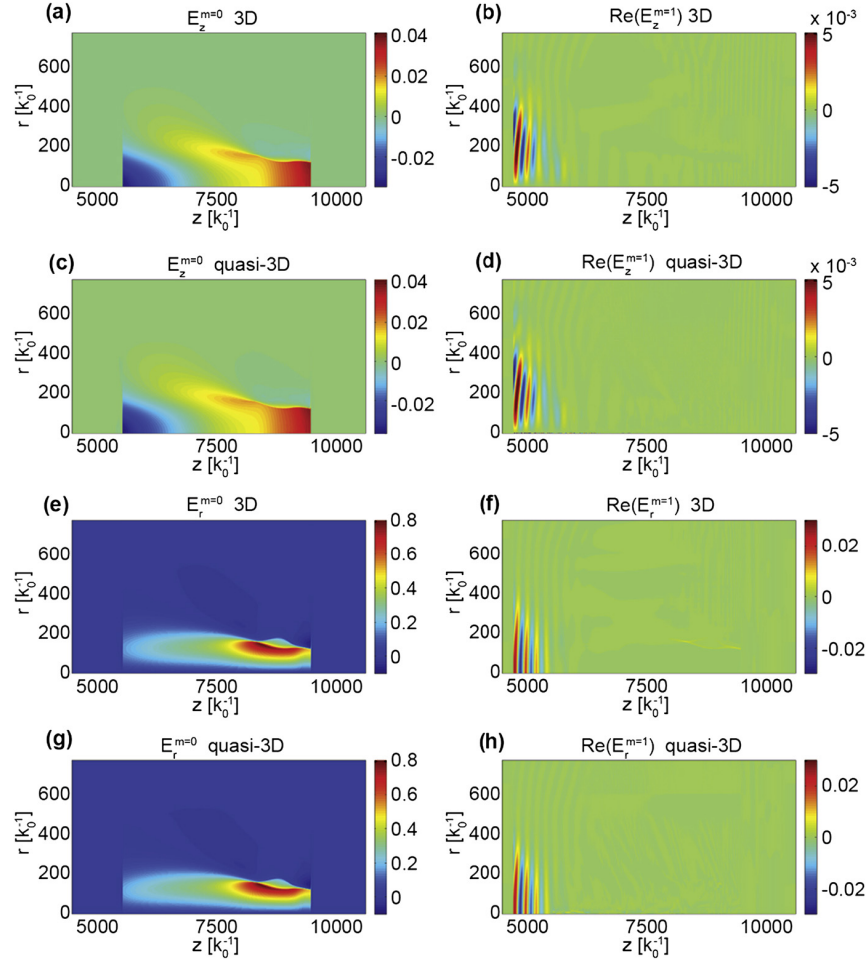


**Fig. 3.** Comparison of simulation results in 3D and quasi-3D geometries for the  $a_0 = 4.0$  (converted to linear polarization) 1.3 GeV LWFA stage run (as discussed in section 4.1). All results are from boosted frame simulations. On the left are the  $m = 0$  modes of  $E_z$  and  $E_r$ . On the right are the real part of  $E_z^{m=1}$  and  $E_r^{m=1}$ . Results from a full 3D boosted frame case are compared against a quasi-3D OSIRIS case where only  $|m| \leq 1$  modes were kept. Simulation parameters are listed in Table 1.

We use a boosted frame with  $\gamma_b = 26.88$ , and use a moving window as described earlier that follows the relativistically drifting plasma. A moving antenna injects the laser pulse into the plasma, and a damping region absorbs the EM field at the rear end of the moving window. In the upper  $\hat{r}$  boundary of the simulation box we applied the Perfectly-Matched-Layer boundary condition (see Ref. [10] for more details). The plasma density is uniform along the  $\hat{z}$  direction. It is uniform in  $\hat{r}$  direction from  $0 \leq r \leq 7000 [k_0^{-1}]$  (where  $k_0$  is the wave number of the laser in the lab frame), and then the density linearly ramps to zero at  $r = 8000 [k_0^{-1}]$  near the  $\hat{r}$  upper boundary (an additional gap of  $500 [k_0^{-1}]$  is left between the  $\hat{r}$  upper plasma boundary and simulation box boundary). The linear plasma density ramp is used to prevent reflection when the laser crosses the upper  $\hat{r}$  plasma boundary into vacuum. Detailed simulation parameters are listed in Table 2.

As mentioned in section 3, in the boosted frame each azimuthal mode of the EM field is dumped frequently in time, and sparsely in space. The results can be transformed back to the lab frame for post-processing. In Fig. 5 (a) we present 2D envelope plots of the real part of  $E_r^{m=1}$  fields. The upper plot in Fig. 5 (a) is the boosted frame simulation results (transferred back to lab frame), while the lower plot is the lab frame data. The 2D envelope of  $E_z^{m=0}$  fields for the two simulations is presented in Fig. 5 (b). In Figs. 5 (c)–(h) we present the corresponding line outs from the two simulations. As we can see from Fig. 5 the data from the two simulations agree well with each other, except for the area around the rear of the first bubble, which indicates that the two simulations give different self-injection results. On the other hand, the laser profiles from the two cases agree extremely well [Figs. 5 (e)–(h)]. In Fig. 5 (c) and (d) line outs of  $E_z^{m=0}$  at various time steps are plotted, and they show that in the transformed boosted frame data there is stronger beam loading, which indicates that more charge is self-injected into the bubble. This may be due to the difference in statistics between the lab frame simulation and boosted frame simulation. In the boosted frame a macro-particle represents  $\sim 2\gamma_b^2$  more charge than

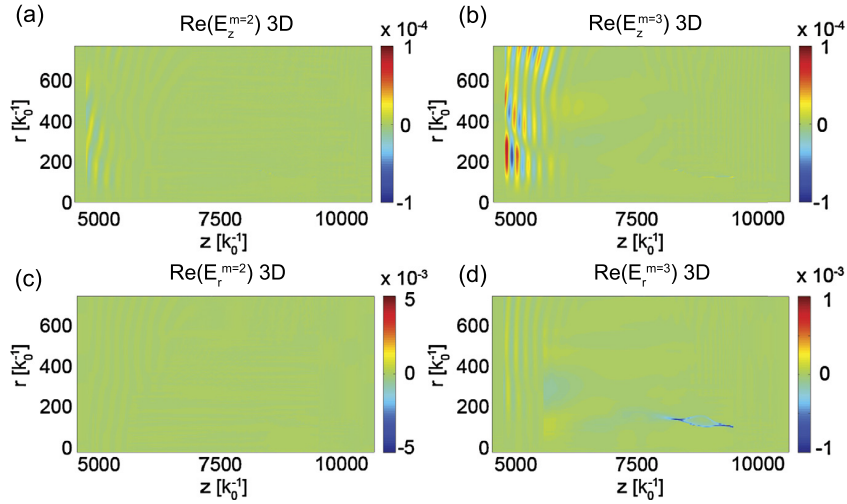


**Fig. 4.** Higher order  $m$  modes of  $\text{Re}(E_z)$  and  $\text{Re}(E_r)$  obtained from a full 3D LWFA boosted frame data (as discussed in section 4.1). On the left are  $\text{Re}(E_z)$  and  $\text{Re}(E_r)$  for mode  $m = 2$ , while on the right are  $\text{Re}(E_z)$  and  $\text{Re}(E_r)$  for mode  $m = 3$ . The simulation parameters used are listed in Table 1.

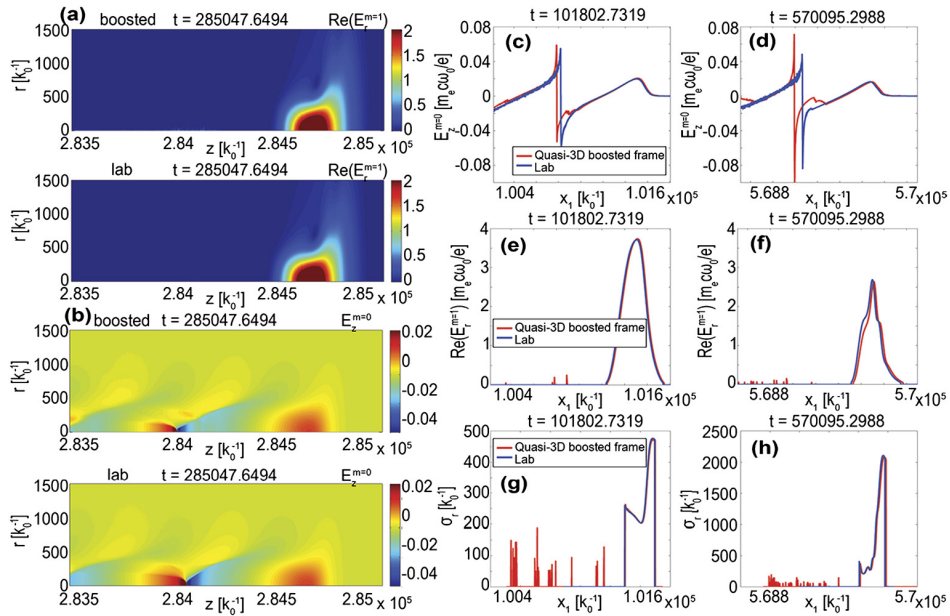


**Fig. 5.** Simulation results for a  $a_0 = 4.44$  (converted to linear polarization) 10.4 GeV LWFA stage run (as discussed in section 4.2). (a) shows the comparison of 2D envelope of  $\text{Re}(E_r^{m=1})$  field, which shows the evolution of laser driver as it propagates through the plasma; (b) shows the corresponding comparison of the amplitude of  $E_z^{m=0}$ , which shows how the wakefield of the bubble varies in the two frames due to the different self-injection results; (c), (e), and (g) are comparisons of the  $E_z^{m=0}$  lineout, laser envelope  $\text{Re}(E_r^{m=1})$  lineout, and laser spot size respectively at lab frame time  $t = 101802.7 \omega_0^{-1}$ , while (d), (f), (h) are the corresponding plots at  $t = 570095.3 \omega_0^{-1}$ . The simulation parameters used are listed in Table 2.

in the lab frame, while particles in the boosted frame are  $\sim 2\gamma_b$  times “fatter” since the grid size in the boosted frame is  $\sim 2\gamma_b$  times larger, and this could affect the self-injection process.

To confirm the differences in wakefield are related to the self-injection process, we repeated the lab frame and boosted frame simulations in regimes with no self-injection, at  $a_0 = 3.0$  (converted to linear polarization), while keeping the other parameters as listed in Table 2. In Figs. 6 (a) and (b) we show the line out of the wakefield  $E_z^{m=0}$  at two different times in the lab frame, and in Figs. 6 (c) and (d) we show the corresponding line outs of the envelope of  $\text{Re}(E_r^{m=1})$ . We see from Fig. 6 that for this case where there is no self-injection in the lab frame simulation, the wake field results from the lab frame and boosted frame simulations agree very well. It still appears to be challenging to accurately modeling the

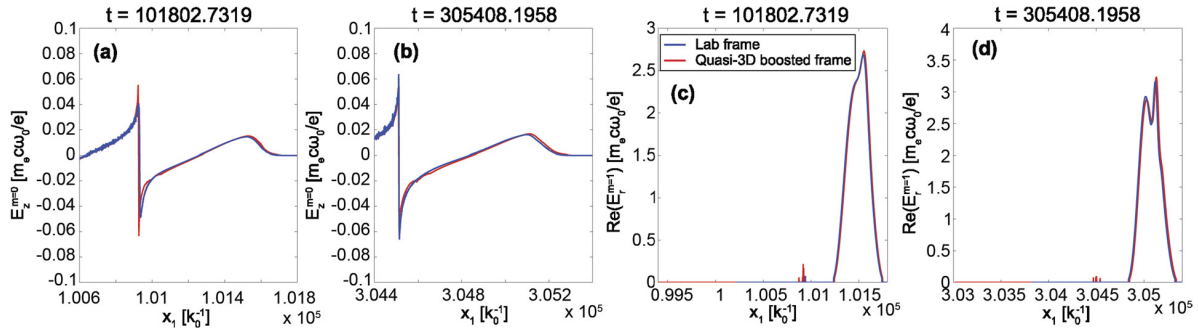


**Fig. 6.** Line outs of wakefield  $E_z^{m=0}$  and line outs laser field envelope of  $\text{Re}(E_r^{m=1})$  at various lab frame time for a  $a_0 = 3.0$  case (as discussed in section 4.2). Since there are no self-injection in the lab frame for this case, much better agreements are obtained for the wakefield part. The simulation parameters used are listed in Table 2.

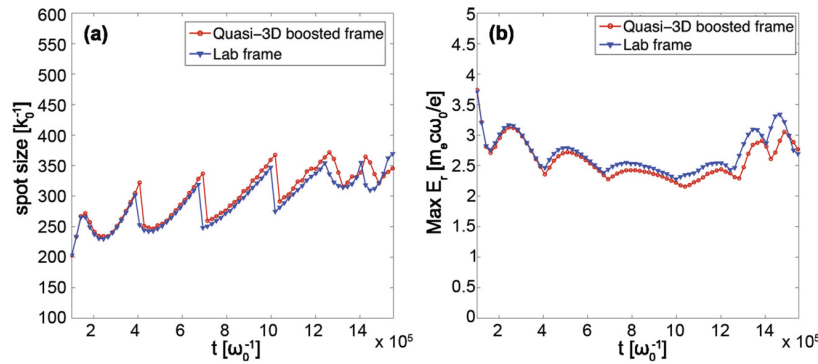


**Fig. 7.** Evolution of the laser spot size and peak amplitude (discussed in section 4.2). (a) shows the comparison of laser spot size evolution as the laser propagates into the plasma for the two frames. The laser spot size is defined at the location where the laser has the maximum amplitude. The corresponding maximum laser amplitude evolution is shown in (b). The simulation parameters used are listed in Table 2.

self-injection process in the LWFA blowout regime. Determining the best practices for using the boosted frame technique to study self-injection at high  $\gamma_b$  is an area for future work.

We plot the laser envelope and spot size obtained from the two cases in Figs. 5 (e)–(h). Excellent agreement can be seen for the two time points presented in Fig. 5. Excellent agreement is also seen for the evolution of the spot size, and laser amplitude of the laser driver as it propagates through the plasma column. In Fig. 7 we show a detailed time history of the laser spot size and amplitude at the position of the laser where its amplitude is largest. Fig. 7 clearly supports the conclusion that very accurate results can be obtained when using Lorentz boosted frame technique in quasi-3D geometry to study the evolution of laser driver in the plasma.

We have not yet attempted to optimize choices of parameters or the algorithm itself. However, it is still useful to compare the total CPU hours for the limited set of lab and boosted frame simulations presented in the paper. The quasi-3D lab frame simulations presented in section 4.2 used around 1.6 million CPU hours. Load balancing significantly reduced the performance, and a corresponding full 3D simulation (using 8 particles per cell) would take around 300 million CPU hours in theory. Meanwhile the corresponding quasi-3D boosted frame simulation takes 2000 CPU hours. The speedup from the quasi-3D lab frame is around 800. Note when calculating the speedup we take into account the fact that the transverse resolution, and particle per cell are different in the two simulations. Correspondingly the speedup achieved from the full 3D lab frame simulation to quasi-3D boosted frame is on the order of 100,000. Note if the full 3D simulation was run on large number of processors then load balancing issues can sometimes increase the CPU hours by a factor of between 5 and 10. We note the theoretical speedup for boosted frame simulations is actually not straightforward to calculate as it depends on  $\gamma_b$ , the plasma length, and the laser pulse length. In addition, load imbalance is another factor that would greatly affect the speedup.

### 5. Summary

In this paper, we described how it is possible to perform LWFA simulations in Lorentz boosted frames using the quasi-3D algorithm. In order to carry out high fidelity Lorentz boosted frame simulations in this geometry, we use a hybrid Yee–FFT solver that solves the Maxwell equation in  $k_z$  space in the direction that the plasma drifts, while keeping the second order



finite-difference operators in the transverse directions as in a conventional Yee solver. Using this Maxwell solver we can then use the same strategies for eliminating main and first spatial NCI in Cartesian geometry to significantly mitigate them in the quasi-3D geometry. For the parameters that we have simulated this appears to have practically eliminated the NCI. A current correction is applied to ensure the code rigorously conserves charge. In addition, we analyzed the space–time area of the lab and boosted frame simulation data. We showed how using a moving window which follows the drifting plasma in the boosted frame further reduces the computational load. We were able to combine Lorentz boosted frame technique with quasi-3D algorithm, together with moving window technique, leading to significant speedup and potential unprecedented speedup for the modeling of LWFA. In the future we will optimize the algorithm for performance both on a single core, and in parallel computers.

We presented comparisons of lab frame against boosted frame simulation results for a 10.4 GeV LWFA example that operates in the blowout regime. It was shown that the evolution of the laser driver in the plasma can be very well reproduced by the boosted frame simulation. We also found that the self-injection process is different in the boosted frame. This is probably due to the difference in statistics between the simulations in the two frames since in the boosted frame each macro-particle represents many more real particles than in the corresponding lab frame simulation. We found excellent agreement between the lab and boosted frame results for the wake fields when  $a_0$  was reduced to avoid self-injection. An area of future work is to systematically explore methods to accurately model self-injection process in the Lorentz boosted frame simulation. Another area is the integration of this algorithm into our GPU and Intel-Phi enabled version of OSIRIS.

### Acknowledgements

This work was supported by US DOE under grants DE-SC0014260, DE-SC0008316, DE-SC0010064, and by the US National Science Foundation under grants ACI 1339893, OCI 1036224, 1500630, and by NSFC 11425521, 11535006, 11175102, 11375006, and Tsinghua University Initiative Scientific Research Program, and by the European Research Council (ERC-2010-AdG Grant 267841). Simulations were carried out on the UCLA Hoffman2 and Dawson2 Clusters, and on Hopper Cluster of the National Energy Research Scientific Computing Center, and on Blue Waters cluster at National Center for Supercomputing Applications at UIUC.

### Appendix A. Comparison of final spectrum of injected particles of 1.3 GeV case

In this Appendix, we present the comparison of the final spectrum in the lab frame of the injected particles for the 1.3 GeV simulation in the 3D lab frame, 3D boosted frame, and quasi-3D boosted frame that are previously discussed in section 4.1. The parameters for the 3D/quasi-3D boosted frame simulations are listed in Table 1, and the corresponding lab frame simulation parameters are listed in Table A.3 below.

We can see from Fig. A.8 that the final particle energy spectrum for the three cases agree reasonably well. The two boosted frame simulations almost overlap each other, while the lab frame data is shifted to higher energy with a similar shape. We note that determining how the Lorentz boosted frame factor  $\gamma_b$ , cell sizes, time step, particle per cell, and other simulation parameters affect the modeling of LWFA in the Lorentz boosted frame remains an open question, and will be part of our future work.

**Table A.3**

Parameters for the 3D lab frame LWFA simulation (discussed in section 4.1 and Appendix A). The laser frequency  $\omega_0$  and number  $k_0$  in the lab frame are used to normalize simulation parameters. The density is normalized to the critical density in the lab frame,  $n_0 = m_e \omega_0^2 / (4\pi e^2)$ . The normalized vector potential  $a_0$  for the laser corresponds to linear polarization.

Plasma	
density $n_p$	$8.62 \times 10^{-4} n_0$
length $L$	$8.0 \times 10^4 k_0^{-1}$
Laser	
pulse length $\tau$	$86.9 k_0^{-1}$
pulse waist $W$	$153.0 k_0^{-1}$
polarization	circular
normalized vector potential $a_0$	4.0
Simulation parameters	
grid size $(\Delta x_1, \Delta x_{2,3})$	$(0.2 k_0^{-1}, 3.4 k_0^{-1})$
time step $\Delta t / \Delta x_1$	0.995
number of grid (moving window)	$4000 \times 512 \times 512$
particle shape	quadratic

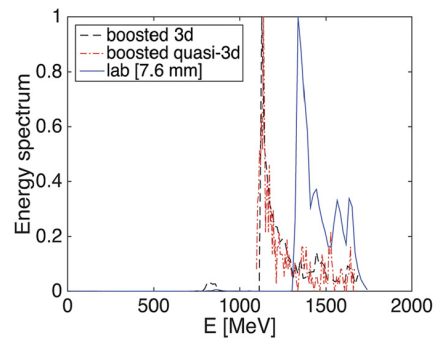


**Fig. A.8.** Comparison of the final spectrum of the injected particles for the 1.3 GeV simulation in the 3D lab frame, 3D boosted frame, and quasi-3D boosted frame for the  $a_0 = 4.0$  (converted to linear polarization) 1.3 GeV LWFA stage run (as discussed in section 4.1 and Appendix A). The simulation parameters used are listed in Table 1 and A.3.

## References

- [1] T. Tajima, J.M. Dawson, *Phys. Rev. Lett.* 43 (1979) 267.
- [2] W. Lu, et al., *Phys. Rev. Spec. Top., Accel. Beams* 10 (2007) 061301; A. Pukhov, J. Meyer-ter-vehn, *Appl. Phys. B* 74 (2002) 355.
- [3] D.F. Gordon, W.B. Mori, T.M. Antonsen, *IEEE Trans. Plasma Sci.* 28 (2000) 1135.
- [4] P. Mora, T.M. Antonsen, *Phys. Plasmas* 4 (1997) 217.
- [5] C. Huang, et al., *J. Comput. Phys.* 217 (2006) 658.
- [6] J.-L. Vay, *Phys. Rev. Lett.* 98 (2007) 130405.
- [7] A.F. Lifschitz, et al., *J. Comput. Phys.* 228 (2009) 1803.
- [8] A. Davidson, et al., *J. Comput. Phys.* 281 (2015) 1063.
- [9] P. Yu, et al., in: *Proc. Advanced Accelerator Concept Workshop, San Jose, CA, USA, 2014.*
- [10] P. Yu, et al., in: *Proc. International Particle Accelerator Conference, Richmond, VA, USA, 2015.*
- [11] B.B. Godfrey, *J. Comput. Phys.* 15 (1974) 504.
- [12] P. Yu, et al., in: *Proc. 15th Advanced Accelerator Concepts Workshop, Austin, TX, 2012*, in: *AIP Conf. Proc.*, vol. 1507, 2012, p. 416.
- [13] B.B. Godfrey, J.-L. Vay, *J. Comput. Phys.* 248 (2013) 33–46.
- [14] X. Xu, et al., *Comput. Phys. Commun.* 184 (2013) 2503–2514.
- [15] B.B. Godfrey, J.-L. Vay, I. Haber, *J. Comput. Phys.* 258 (2014) 689.
- [16] B.B. Godfrey, J.-L. Vay, I. Haber, *J. Comput. Phys.* 267 (2014) 1.
- [17] P. Yu, et al., *Comput. Phys. Commun.* 192 (2015) 32.
- [18] P. Yu, et al., *Comput. Phys. Commun.* 197 (2015) 144.
- [19] R. Lehe, et al., *Phys. Rev. Spec. Top., Accel. Beams* 16 (2013) 021301.
- [20] P. Yu, et al., *J. Comput. Phys.* 266 (2014) 124.
- [21] K. Yee, *IEEE Trans. Antennas Propag.* 14 (1966) 302.
- [22] R.A. Fonseca, et al., in: P.M.A. Sloot, et al. (Eds.), *ICCS*, in: *Lect. Notes Comput. Sci.*, vol. 2331, 2002, pp. 34–351; R. Hemker, PhD thesis, UCLA, 2000, arXiv:1503.00276.
- [23] R. Lehe, et al., arXiv:1507.04790, 2015.
- [24] J. Villasenor, O. Buneman, *Comput. Phys. Commun.* 69 (1992) 306.
- [25] T. Esirkepov, *Comput. Phys. Commun.* 135 (2001) 144.
- [26] J.M. Dawson, *Rev. Mod. Phys.* 55 (2) (1983) 403.
- [27] A.T. Lin, J.M. Dawson, H. Okuda, *Phys. Fluids* 17 (1974) 1995.
- [28] V.K. Decyk, *Comput. Phys. Commun.* 177 (2007) 95.
- [29] S.F. Martins, R.A. Fonseca, W. Lu, W.B. Mori, L.O. Silva, *Nat. Phys.* 6 (2010) 311.
- [30] J.-L. Vay, C.G.R. Geddes, E. Cormier-Michel, D.P. Grote, *J. Comput. Phys.* 230 (2011) 5908.
- [31] S.F. Martins, R.A. Fonseca, L.O. Silva, W. Lu, W.B. Mori, *Comput. Phys. Commun.* 181 (2010) 869.
- [32] J.-L. Vay, C.G.R. Geddes, E. Esarey, C.B. Schroeder, W.P. Leemans, *Phys. Plasmas* 18 (2011) 123103.
- [33] J.-L. Vay, et al., in: *Proc. 14th Advanced Accelerator Concepts Workshop, Annapolis, MD*, in: *AIP Conf. Proc.*, 2010, pp. 244–249.
- [34] C.D. Decker, W.B. Mori, *Phys. Rev. Lett.* 72 (1994) 490.
- [35] J.-L. Vay, C.G.R. Geddes, E. Cormier-Michel, *Phys. Plasmas* 18 (2011) 030701.
- [36] J.-L. Vay, *Phys. Plasmas* 15 (2008) 056701.
- [37] J.P. Boris, in: *Proc. 4th Conference on Numerical Simulation Plasmas, Naval Research Laboratory, Washington, DC, 1970*, pp. 3–67.
- [38] T. Dalichaouch, et al., *Bull. Am. Phys. Soc.* 60 (2015).

# Modeling of Laser Wakefield Acceleration In Lorentz Boosted Frame Using a Quasi-3D OSIRIS Algorithm

P. Yu<sup>\*</sup>, A. Davidson<sup>†</sup>, X. Xu<sup>\*\*</sup>, A. Tableman<sup>†</sup>, V. K. Decyk<sup>†</sup>, F. S. Tsung<sup>†</sup>, J. Vieira<sup>‡</sup>,  
R. A. Fonseca<sup>‡,§</sup>, W. Lu<sup>\*\*</sup>, L. O. Silva<sup>‡</sup> and W. B. Mori<sup>\*,†</sup>

<sup>\*</sup>*Department of Electrical Engineering, University of California Los Angeles, Los Angeles, CA 90095, USA*

<sup>†</sup>*Department of Physics and Astronomy, University of California Los Angeles, Los Angeles, CA 90095, USA*

<sup>\*\*</sup>*Department of Engineering Physics, Tsinghua University, Beijing 100084, China*

<sup>‡</sup>*Instituto Superior Técnico, 1049-001, Lisbon, Portugal*

<sup>§</sup>*ISCTE - Instituto Universitário de Lisboa, 1649-026, Lisbon, Portugal*

**Abstract.** Recently it was proposed in [A. F. Lifschitz, et. al., J. Comp. Phys. 228, 1803 (2009)] that laser wakefield acceleration could be modeled efficiently using a particle-in-cell code in cylindrical coordinates if the fields and currents were expanded into Fourier modes in the azimuthal angle,  $\phi$ . We have implemented this algorithm into OSIRIS, including a new rigorous charge conserving deposition routine applicable for it [A. Davidson, et. al., J. Comp. Phys. 281, 1063 (2014)]. This algorithm can be interpreted as a PIC description in  $r-z$  and a gridless description in  $\phi$  in which the expansion into  $\phi$  modes is truncated at a desired level. This new quasi-3D algorithm greatly reduces the computational load by describing important three-dimensional (3D) geometrical effects with nearly two-dimensional calculations. In this paper, we propose to combine this algorithm with the Lorentz boosted frame method for simulations of Laser wakefield acceleration (LWFA). We show preliminary results, including an investigation of the unstable numerical Cherenkov instability modes for this geometry, and discuss directions for future work. These preliminary results indicate that combining the quasi-3D method and the Lorentz boosted frame method together may provide unprecedented speed ups for LWFA simulations.

**Keywords:** Particle-in-cell, laser wakefield acceleration, numerical Cherenkov instability, quasi-3D algorithm, Lorentz boosted frame

## 1. INTRODUCTION

Laser wakefield acceleration (LWFA) [1] has attracted extensive interest due to its potential for developing ultra-compact, high-gradient accelerators that have numerous potential applications, including the building blocks for next generation linear colliders and being the driver for compact light sources. Due to relativistic and nonlinear effects, numerical simulations that follow the trajectories of individual electrons are critical for studying the physics of LWFA. In particular, particle-in-cell (PIC) simulations include the necessary physics and have therefore played an integral role in the development of LWFA. In the nonlinear blowout regime [2, 3, 4], it is important to include 3D geometrical effects in order to accurately model laser propagation, wakefield excitation, and beam loading [5]. Therefore, 3D rather than 2D slab ( $x-y$ ) simulations are required for quantitative rather than qualitative predictions. Although 2D  $r-z$  PIC simulations have proven useful and accurate for modeling beam driven wakefield acceleration (PWFA), they are not amenable to LWFA modeling because the laser fields are not purely azimuthally symmetric (they are radially polarized). Unfortunately, simulating LWFA using a standard PIC code in 3D can be very CPU demanding. For example, 3D PIC simulations of  $\sim 10$  GeV stages for the nonlinear blowout regime are already reaching the limits of the CPU resources currently available. This makes it difficult to carry out parameter scans in full three dimensions. Therefore, reduced models of LWFA such as the ponderomotive guiding center [6, 7, 8] and the quasi-static approximation have been proposed to find the balance between accuracy of the models and the computational load [8, 9]. In addition, the Lorentz boosted frame has been proposed to significantly reduce the needed CPU time. However, this method is still being tested in the nonlinear blowout regime where self-trapping of electrons is occurring.

Recently, Lifschitz et. al. [10] proposed a method to use  $r-z$  2D PIC simulations to model LWFA. The idea was to expand the electromagnetic fields and the currents into azimuthal modes,  $e^{im\phi}$ , and to truncate the expansion. This is effective because a linearly polarized laser is represented by only the  $m = 1$  mode. Therefore, LWFA for nearly azimuthally symmetric cases can be simulated by truncating the expansion after  $m = 1$ . This can reduce modeling a 3D problem with low azimuthal asymmetry into a similar computational cost as using a 2D  $r-z$  code. This algorithm was implemented into OSIRIS, which required development of a new rigorous charge conserving scheme valid for the

azimuthal mode expansion [11]. The new charge conserving scheme makes clear that this algorithm is a hybrid scheme between a PIC description in  $r-z$  and a gridless description in  $\phi$ . It should be noted that the use of such a hybrid scheme was considered many years earlier to study particle beam plasma interactions [12].

As noted earlier, it has been proposed and demonstrated that by performing the simulation in an optimal Lorentz boosted frame with normalized velocity  $\beta$ , the time and space scales to be resolved in a numerical simulation may be minimized [13]. The basic idea is that in the boosted frame the plasma length is Lorentz contracted while the plasma wake wavelength and laser pulse length are Lorentz expanded. The number of laser cycles is an invariant, so the necessary number of cells needed to resolve the laser is also an invariant while the cell size and hence time step are Lorentz expanded. The increase in time step and cell size, and decrease in the plasma length lead to savings of factors of  $\gamma^2 = (1 - \beta^2)^{-1}$  as compared to a lab frame simulation using the so-called moving window [14]. Although straightforward in principle, this idea is challenging because the physics on a grid is actually not Lorentz invariant. This is seen by the fact that in a frame where the plasma drifts there is a violent numerical instability, called the Numerical Cerenkov Instability (NCI) [15]. The potential of the Lorentz boosted frame technique has led to a detailed reexamination of the NCI and to techniques to mitigate (effectively eliminate) it [16, 17, 18, 19, 20, 21].

In this paper, we propose to combine together the Lorentz boosted frame technique and the quasi-3D algorithm to achieve unprecedented speed-ups in LWFA simulations. If successful, this will provide the ability to perform rapid parameter scans and real-time steering of experiments. Based on these parameter scans, full 3D (including boosted frame) simulations can be performed for quantitative prediction. We have implemented the quasi-3D algorithm into our finite-difference-time-domain (FDTD) EM-PIC code OSIRIS [22], and have recently begun to explore using it to carry out LWFA simulations in a Lorentz boosted frame.

The rest of the paper is organized as follows. In section 2 we discuss the NCI and explore the unstable modes in the  $r-z$  geometry of the quasi-3D code. We show that the optimal time step derived for cartesian geometry [17, 18] still works for the  $r-z$  geometry. In section 3, we present preliminary simulation results. We compare simulation results from quasi-3D OSIRIS against UPIC-EMMA (which uses a spectral Maxwell solver) [23, 24] simulations. Good agreement is seen in some cases, illustrating the potential speed-ups that can be possible by combining these two methods. The results are summarized in section 4.

## 2. NUMERICAL CERENKOV INSTABILITY

When modeling LWFA in the Lorentz boosted frame, the plasma is drifting relativistically towards the laser. This inevitably leads to a numerical instability called the Numerical Cerenkov Instability (NCI) that is due to the unphysical coupling between the plasma Langmuir modes and EM modes [17, 18, 21]. This numerical artifact interferes with the physics being studied in the simulation, and therefore it is crucial to reduce the NCI growth rate to enable accurate modeling of physics problem involving relativistically drifting plasmas.

To study behavior of the NCI in the  $r-z$  geometry, we performed simulations using the quasi-3D OSIRIS with only a cold relativistic plasma drift, i.e., no laser. Conducting boundary conditions were used in the  $r$  direction, while periodic boundary conditions are used in the  $z$  direction. The plasma has a drift velocity corresponding to  $\gamma = 50$  in the  $z$  direction. It has a very small but finite temperature in order to seed the instability. The Yee solver [25] is used in this simulation. For comparison, we likewise performed a 2D Cartesian OSIRIS simulation with the same simulation setups and parameters.

In Fig. 1 (b) and (c) we present snapshots of the NCI spectrum observed in the simulations, for both the quasi-3D and 2D Cartesian algorithms. For the quasi-3D case we use the  $m = 0$  fields. In Fig. 1 (a) the corresponding growth rates are plotted for various time steps. When calculating the spectra of the NCI, we performed a Fourier transform to  $E_2$  in both  $x_1$  and  $x_2$  directions (where  $x_1$  is the drifting direction) for the 2D cartesian case, and performed a Fourier transform in the  $z$  direction and a Hankel transform in the  $r$  direction for the quasi-3D case. Interestingly, the two geometries show very similar patterns when the same simulation parameters are used. In addition, the growth rates are also close to each other. More importantly, as is well known for the NCI in Cartesian coordinates, when the momentum conservation field interpolation scheme (others refer to this as the uniform field interpolation) is used (as is the case in this paper), we find an optimal time step [17, 18, 26] at which the maximum NCI growth rate is minimized. It is interesting to see that this same optimal time step is the same value for both the 2D and quasi-3D geometries, and we used this optimal time step in the quasi-3D OSIRIS LWFA simulations in a Lorentz boosted frame. We are currently working on the theory of the NCI for the quasi-3D algorithm in order to explain what we observe in Fig. 1 (a).

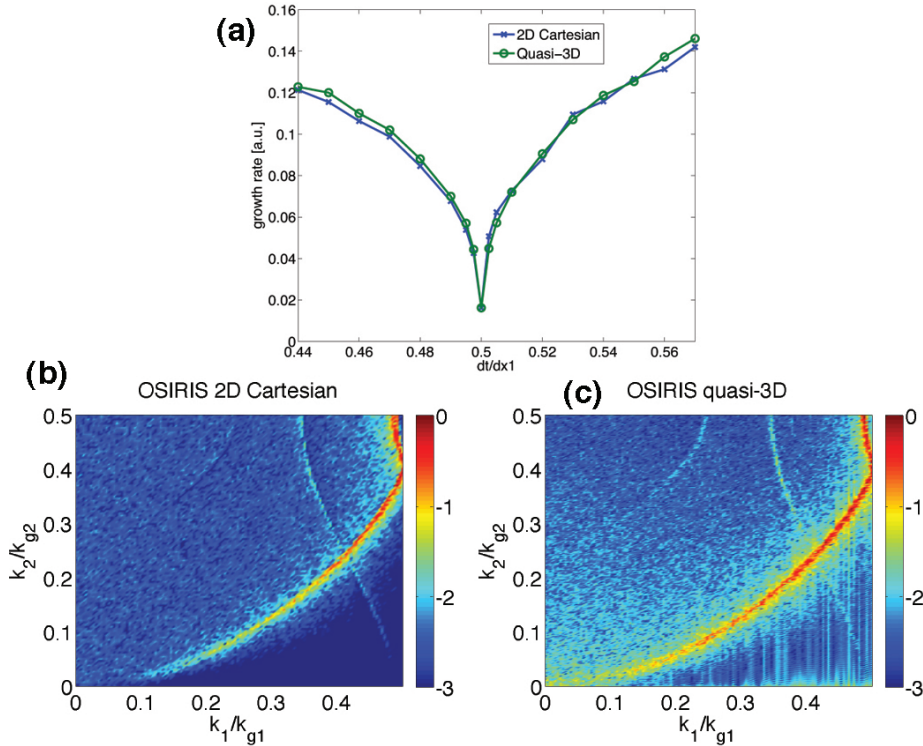


**FIGURE 1.** (a) The dependence of the maximum NCI growth rate on the time step used in the 2D Cartesian and quasi-3D simulations. In both cases an optimal time step at  $c\Delta t = \Delta x/2$  can be found, where  $\Delta x$  is the grid size along the drift direction. (b) Snapshot of the FFT of  $E_2$  field of a 2D Cartesian OSIRIS simulation. (c) Snapshot of the FFT of  $E_\phi$  field for the corresponding quasi-3D OSIRIS simulation. In (b) and (c) only the first quadrants are shown due to the symmetry of the pattern.

### 3. PRELIMINARY LWFA SIMULATIONS

The simulation setup used for performing LWFA in the boosted frame using quasi-3D OSIRIS is very similar to that for Cartesian 2D and 3D OSIRIS simulations. The plasma is drifting relativistically in  $z$  direction at  $\beta_z = -\beta$ , where  $\gamma = (1 - \beta^2)^{-1/2}$  is the Lorentz factor of the boosted frame. The length of the plasma column contracts by  $\gamma$ , while its density increases by  $\gamma$ . Due to the Lorentz transform, the laser wavelength and pulse length stretch by  $\gamma(1 + \beta)$ , and its Rayleigh length contracts by  $\gamma$ . Meanwhile the spot size at the focal point (which is always at the moving plasma edge) does not change. As a result, when  $\gamma$  is sufficiently large one needs to use a moving antenna [27] to launch the laser pulse in order to avoid using a simulation box that is too wide in the  $r$  direction. In the quasi-3D OSIRIS, each azimuthal mode is independently launched by the moving antenna. We are currently using conducting boundary conditions in the  $r$  direction and a moving window in the  $z$  direction, and are implementing the perfectly-matched-layers in the  $r$  direction in the quasi-3D OSIRIS code.

To investigate the feasibility of combining the quasi-3D OSIRIS and the LWFA boosted frame technique, we conducted 5.8 GeV stage runs [4] using both quasi-3D OSIRIS and UPIC-EMMA. The parameters of the 5.8 GeV stage run in the lab frame is listed in Table 1. We performed quasi-3D OSIRIS simulations at  $\gamma = 4$  and  $\gamma = 8$ , and UPIC-EMMA simulation at  $\gamma = 30$ . Moving windows are used for the quasi-3D OSIRIS run, and we chose the optimal time step in order to minimize the NCI growth rate. As for the UPIC-EMMA run, we used a low-pass filter to eliminate the fastest growing modes of NCI [18, 21, 24].

In Fig. 2 (a) we present a snapshot of the plasma density in the boosted frame for a  $\gamma = 4$  quasi-3D OSIRIS run. As seen in Fig. 2 (a), the NCI is present at the left edge of the simulation box (these are short wavelength perturbations). However, we are mostly interested in the physics of the first bubble where there is much less evidence of the NCI. We likewise compared the corresponding wakefield in the first bubble in the lab frame by transforming the data from the  $\gamma = 4, 8$  quasi-3D OSIRIS, and the  $\gamma = 30$  UPIC-EMMA simulations back to the lab frame. This is shown in Fig. 2 (b). Good agreement is found within the first bubble. There is significantly more noise in the quasi-3D OSIRIS simulations

at the rear of the first bubble. This noise is due to the unphysical numerical Cerenkov radiation from the self-trapped electrons. As noted in [24] there can be differences in the amount of self-trapped particles (and the associated beam loading) in boosted frame simulations with different  $\gamma$ . This is expected since the macro-particles in each simulation have different charges. For fixed number of particles per cell, the charge represented by a simulation particles increases in proportion to  $\sim \gamma^2$  due to length contraction of the plasma and the increase in the cell size. Therefore, the statistics and the resolution of the details of the physics is different in the various frames. A full exploration of how the simulation codes, setups, and parameters influence the modeling of self-injection process in the Lorentz boosted frame are areas of future work.

**TABLE 1.** Parameters of LWFA 5.8 GeV stage simulations using quasi-3D OSIRIS and UPIC-EMMA.  $k_0$  is the wavenumber of the driving laser.

Parameters	Values
Plasma	
Density $n$ [ $\text{cm}^{-3}$ ]	$5 \times 10^{17}$
Length $L$ [m]	0.08
Laser	
Wavelength $\lambda$ [nm]	800
Pulse length $\tau$ [fs]	80
Waist width $W_0$ [ $\mu\text{m}$ ]	35
Normalized vector potential $a_0$	5.1
Quasi-3D OSIRIS simulation parameters	
Boosted frame Lorentz factor	$\gamma = 4, 8$
Grid size $(\Delta x_z, \Delta x_\phi)$ [ $k_0^{-1}$ ]	$(0.2\gamma(1 + \beta), 5.0)$
Time step $c\Delta t$	$0.5\Delta x_z$
Particle shape	quadratic
UPIC-EMMA simulation parameters	
Boosted frame Lorentz factor	$\gamma = 30$
Grid size $(\Delta x_1 = \Delta x_2 = \Delta x_3)$ [ $k_0^{-1}$ ]	$0.196\gamma(1 + \beta)$
Time step $c\Delta t$	$0.184\Delta x_1$
Particle shape	quadratic

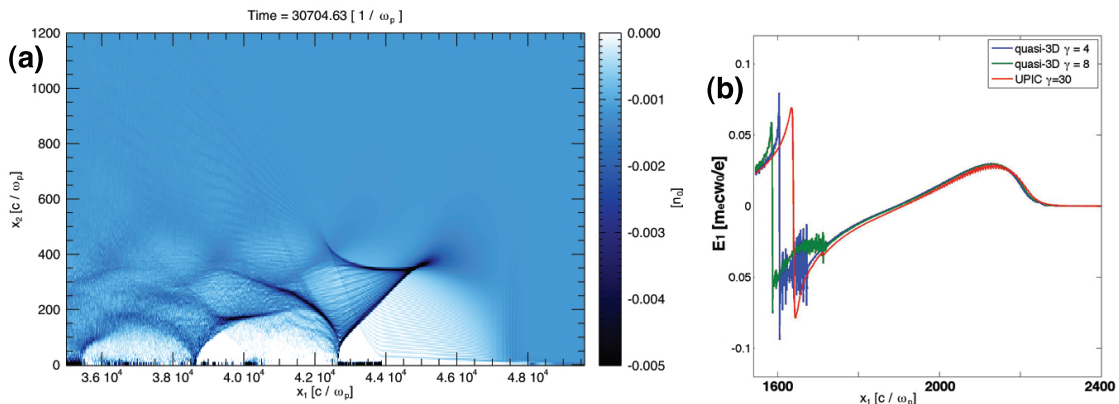


**FIGURE 2.** (a) shows the snapshots of plasma density for a quasi-3D OSIRIS simulation in the Lorentz boosted frame with  $\gamma = 4$ . (b) shows the on-axis wakefield line outs for the quasi-3D simulations at  $\gamma = 4, 8$  and UPIC-EMMA simulations at  $\gamma = 30$ .

#### 4. SUMMARY AND FUTURE WORK

In this paper, we propose combining a new quasi-3D (a hybrid PIC in  $r - z$  and gridless in  $\phi$ ) algorithm [10] together with the Lorentz boosted frame technique to obtain unprecedented speed-ups for LWFA simulations. We recently incorporated the quasi-3D algorithm into OSIRIS, including a new rigorous charge conserving scheme [11]. We present preliminary results of performing Lorentz boosted frame LWFA simulations using the quasi-3D algorithm within OSIRIS. We first investigated the NCI in the quasi-3D algorithm and found that both the pattern in  $k$  space and

growth rates of the NCI are similar to its counterpart in 2D Cartesian coordinates. In particular, the same optimal time step which minimizes the NCI growth rate in cartesian coordinates is found for the quasi-3D algorithm. We present sample LWFA simulations of a 5.8 GeV stage in the nonlinear self-guided regime using both the quasi-3D boosted frame simulations at  $\gamma = 4$  and  $\gamma = 8$ , as well as UPIC-EMMA simulations at  $\gamma = 30$ . We compared the corresponding on-axis wakefield line outs by transforming them back to the lab frame. Good agreement was found between the three simulations, especially in the  $z$  range where the front half of the first bubble and the laser are located. The disagreement appears to be due to numerical Cerenkov radiation as well as due to the different statistics of self-trapped electrons. These results demonstrate the potential of conducting Lorentz boosted frame simulation using the quasi-3D OSIRIS.

In the future, we plan on experimenting with smoothers, and alternative field solvers, to eliminate both the NCI and the numerical Cerenkov radiation of the trapped electrons, which would allow for modeling LWFA in higher  $\gamma$  frames. We will also work to incorporate the quasi-3D algorithm onto our GPU and Intel Phi [28] enabled versions of OSIRIS for even greater speed ups. The quasi-3D code runs at the same speed as a 2D simulation. If we take 5.8 GeV case as an example, the combination of using the quasi-3D algorithm, the Lorentz boosted frame, and GPUs or Intel Phis could lead to a speed up of  $\sim 500000$ .

## ACKNOWLEDGMENTS

This work was supported by the U.S. Department of Energy under grants DE-SC0008491, DE-SC0008316, DE-FG02-92ER40727, by the US National Science Foundation under the grant ACI 1339893, and by NSFC Grant 11175102, the thousand young talents program, and by FCT (Portugal), grant EXPL/FIS-PLA/0834/1012, and by the European Research Council (ERC-2010-AdG Grant 267841). Simulations were carried out on the UCLA Hoffman2 and Dawson2 Clusters, and on Hopper at the National Energy Research Scientific Computing Center.

## REFERENCES

1. T. Tajima, J. M. Dawson, *Phys. Rev. Lett.* 43 (1979) 267.
2. J. B. Rosenzweig, B. Breizman, T. Katsouleas, J. J. Su, *Phys. Rev. A*, 44, R6189 (1991).
3. W. Lu, C. Huang, M. Zhou, W.B. Mori and T. Katsouleas, *Phys. Rev. Lett.* 96, 165002 (2006).
4. W. Lu, et. al., *Phys. Rev. Spec. Top., Accel. Beams* 10 (2007) 061301.
5. M. Tzoufras, et. al., *Phys. Rev. Lett.* 101, 145002 (2008).
6. D. F. Gordon, W. B. Mori, T. M. Antonsen, *IEEE Trans. Plasma Sci.* 28 (2000) 1135.
7. P. Mora, T. M. Antonsen, *Phys. Plasmas* 4 (1997) 217.
8. C. Benedetti, et. al., in Proc. ICAP 2012, Rostock-Warnemünd, Germany (2012)
9. C. Huang, et. al., *J. Comp. Phys.* 217 (2006) 658.
10. A. F. Lifschitz, et. al., *J. Comp. Phys.* 228 (2009) 1803.
11. A. Davidson, et. al., *J. Comp. Phys.* 281, 1063 (2014).
12. B. B. Godfrey, Mission Research Corp Albuquerque NM., The IPROP Three-Dimensional Beam Propagation Code, Defense Technical Information Center, 1985.
13. J. -L. Vay, *Phys. Rev. Lett.* 98, 130405 (2007)
14. C. D. Decker, W. B. Mori, *Phys. Rev. Lett.* 72 (1994) 490.
15. B. B. Godfrey, *J. Comp. Phys.* 15, 504 (1974)
16. P. Yu, et. al., in: Proc. 15th Advanced Accelerator Concepts Workshop, Austin, TX, in: AIP Conf. Proc. 1507, 416 (2012);
17. B. B. Godfrey, J. -L. Vay, *J. Comp. Phys.* 248 (2013), 33–46.
18. X. Xu, et. al., *Comp. Phys. Comm.* 184 (2013) 2503–2514.
19. B. B. Godfrey, J.-L. Vay, I. Haber, *J. Comp. Phys.* 258, 689 (2014)
20. B. B. Godfrey, J. -L. Vay, *J. Comp. Phys.* 267, 1 (2014)
21. P. Yu, et. al., [arXiv:1407.0272](https://arxiv.org/abs/1407.0272)
22. R. A. Fonseca, et. al., in: P.M.A. Sliot, et al. (Eds.), ICCS, in: LNCS, Vol. 2331, 2002, pp. 342–351.
23. V. K. Decyk, *Comp. Phys. Comm.* 177, 95 (2007).
24. P. Yu, et. al., *J. Comp. Phys.* 266, 124 (2014).
25. K. Yee, *IEEE Transactions on Antennas and Propagation*, Vol. 14, 302 (1966)
26. J. -L. Vay, et. al., *J. Comp. Phys.* 230, 5908 (2011).
27. J. -L. Vay, et. al., in: Proc. 14th Advanced Accelerator Concepts Workshop, Annapolis, MD, in: AIP Conf. Proc., 1299, 244 (2010).
28. V. K. Decyk and T. V. Singh, *Comp. Phys. Comm.*, 182, 641 (2011); V. K. Decyk and T. V. Singh, *Comp. Phys. Comm.* 185, 708 (2014); A. Tableman, et. al., in preparation; R. Fonseca et. al., in preparation.



Contents lists available at ScienceDirect

## Computer Physics Communications

journal homepage: [www.elsevier.com/locate/cpc](http://www.elsevier.com/locate/cpc)

## Controlling the numerical Cerenkov instability in PIC simulations using a customized finite difference Maxwell solver and a local FFT based current correction



Fei Li<sup>a</sup>, Peicheng Yu<sup>b,\*</sup>, Xinlu Xu<sup>b,c</sup>, Frederico Fiuza<sup>d</sup>, Viktor K. Decyk<sup>c</sup>,  
Thamine Dalichaouch<sup>c</sup>, Asher Davidson<sup>c</sup>, Adam Tableman<sup>c</sup>, Weiming An<sup>b,c</sup>,  
Frank S. Tsung<sup>c</sup>, Ricardo A. Fonseca<sup>e,f</sup>, Wei Lu<sup>a</sup>, Warren B. Mori<sup>b,c</sup>

<sup>a</sup> Department of Engineering Physics, Tsinghua University, Beijing 100084, China

<sup>b</sup> Department of Electrical Engineering, University of California Los Angeles, Los Angeles, CA 90095, USA

<sup>c</sup> Department of Physics and Astronomy, University of California Los Angeles, Los Angeles, CA 90095, USA

<sup>d</sup> SLAC National Accelerator Laboratory, Menlo Park, CA 94025, USA

<sup>e</sup> GOLP/Instituto de Plasma e Fusão Nuclear, Instituto Superior Técnico, Universidade de Lisboa, Lisbon, Portugal

<sup>f</sup> ISCTE - Instituto Universitário de Lisboa, 1649-026, Lisbon, Portugal

## ARTICLE INFO

## Article history:

Received 12 May 2016

Received in revised form

2 November 2016

Accepted 4 January 2017

Available online 12 January 2017

## Keywords:

PIC simulation

Hybrid Maxwell solver

Relativistic plasma drift

Numerical Cerenkov instability

Lorentz boosted frame

## ABSTRACT

In this paper we present a customized finite-difference-time-domain (FDTD) Maxwell solver for the particle-in-cell (PIC) algorithm. The solver is customized to effectively eliminate the numerical Cerenkov instability (NCI) which arises when a plasma (neutral or non-neutral) relativistically drifts on a grid when using the PIC algorithm. We control the EM dispersion curve in the direction of the plasma drift of a FDTD Maxwell solver by using a customized higher order finite difference operator for the spatial derivative along the direction of the drift ( $\hat{1}$  direction). We show that this eliminates the main NCI modes with moderate  $|k_{\perp}|$ , while keeps additional main NCI modes well outside the range of physical interest with higher  $|k_{\perp}|$ . These main NCI modes can be easily filtered out along with first spatial aliasing NCI modes which are also at the edge of the fundamental Brillouin zone. The customized solver has the possible advantage of improved parallel scalability because it can be easily partitioned along  $\hat{1}$  which typically has many more cells than other directions for the problems of interest. We show that FFTs can be performed locally to current on each partition to filter out the main and first spatial aliasing NCI modes, and to correct the current so that it satisfies the continuity equation for the customized spatial derivative. This ensures that Gauss' Law is satisfied. We present simulation examples of one relativistically drifting plasma, of two colliding relativistically drifting plasmas, and of nonlinear laser wakefield acceleration (LWFA) in a Lorentz boosted frame that show no evidence of the NCI can be observed when using this customized Maxwell solver together with its NCI elimination scheme.

© 2017 Elsevier B.V. All rights reserved.

## 1. Introduction

When modeling physics problems involving relativistically drifting plasmas or particle beams using the electromagnetic (EM) particle-in-cell (PIC) algorithm, a violent numerical instability, called the numerical Cerenkov instability (NCI) [1–5], arises due to the unphysical coupling of the electromagnetic (EM) modes and

Langmuir modes (both main and aliasing) of the drifting plasma in the numerical system [6]. Such scenarios arise in laser wakefield acceleration [7] simulations in the Lorentz boosted frame [8,9] in which a laser pulse is colliding head-on with a relativistically drifting plasma (henceforth moving in the  $\hat{1}$  direction), and in relativistic collisionless shock simulations in which two counter-propagating relativistically drifting plasmas collide head-on with each other [10–13]. The NCI creates unphysical energy exchange between the kinetic energy of the drifting plasma, and EM field fluctuations. The growth of the fastest growing modes drives fluctuations that can quickly dwarf the physical processes being

\* Corresponding author.

E-mail address: [tpc02@ucla.edu](mailto:tpc02@ucla.edu) (P. Yu).

<http://dx.doi.org/10.1016/j.cpc.2017.01.001>

0010-4655/© 2017 Elsevier B.V. All rights reserved.



studied, while slower growing modes can affect the physics in subtle ways. Thus, it is essential to eliminate all NCI modes for the accurate modeling of physics problems.

Recently, several studies have focused on the understanding and elimination of this instability [3–6,14–17]. This includes the use of a multi-dimensional spectral solver [6,18–20], or a hybrid Yee-FFT solver that uses a FFT in the direction of the drifting plasma [16]. Applying these solvers together with current correction and filtering strategies, one can systematically eliminate the NCI modes. The key idea is that by changing the EM dispersion relation of the solver it is possible to eliminate NCI modes at moderate  $|\vec{k}|$  leaving all the remaining NCI modes of interest at high  $|\vec{k}|$  in the fundamental Brillouin zone. These high  $|\vec{k}|$  modes can be filtered without altering the physics of interest. However, each of these solvers is FFT-based, either in all directions for the pure spectral solver, or only in the drifting direction of the plasma. The use of FFTs in the Maxwell solver can limit the parallel scalability of the algorithm when there are many more cells along a given direction. Typically, in parallel PIC codes based on FFT solvers, one uses a domain decomposition one order lower than the physical dimension because there are currently no effective parallel 1D FFTs. In the hybrid Yee-FFT solver, there is only a 1D FFT, so the problem can only be decomposed in the two transverse directions.

In this paper, we take advantage of the previous progress described in [6,16], and develop a method to design a finite-difference-time-domain (FDTD) solver that has similar (yet different) NCI properties to the FFT-based solver described in [6,16]. Although it was based on the use of FFTs, when examined more carefully the previous progress showed that the key to essentially eliminate the NCI is to first isolate the range of unstable  $\vec{k}$ 's for which we refer to as the main NCI mode. This is accomplished by using a solver that has sufficiently small numerical errors in the spatial derivatives (and thus small dispersion errors for light waves) for moderate  $|k_1|$ . Even with perfect dispersion for light waves in vacuum, there will always be an intersection from the first spatial aliased beam modes at high  $|k_1|$  that needs to be filtered out, and coupling between the EM mode and the main Langmuir mode at moderate  $|k_1|$ . We note that for this reason the use of the PSATD solver described in Ref. [14] does not appear to have advantages with respect to eliminating the NCI. As we have recently shown [6], when the main mode is isolated to a small range of  $\vec{k}$ s then a small modification to the dispersion for the range of unstable modes can remove the coupling between the EM (purely transverse in the lab frame) modes and Langmuir (purely longitudinal in the lab frame) modes.

Recognizing how the NCI is being controlled and eliminated by the use of an FFT along the plasma drifting direction ( $\hat{1}$  direction) leads us to consider the possibility to design a customized and higher order finite difference operator for the spatial derivatives that provides sufficiently accurate dispersion for moderate  $|\vec{k}|$ . This finite difference operator for the spatial derivative can be implemented into a FDTD solver which is purely local and should thus scale well on massively parallel computers using domain decomposition. This new solver can eliminate the unstable main (0, 0) modes which exist at a moderate  $|\vec{k}|$  by introducing a localized modification to the numerical dispersion relation only near the unstable modes. However, such a solver will not conserve charge, i.e., Gauss's law will not be satisfied. The current can be corrected by performing local FFTs such that the continuity equation is now satisfied for the higher order solver and this does not use any global communication. In addition, a low pass filter can be applied to the local current to eliminate the modes at high  $|\vec{k}|$  near the edge of the first Brillouin zone.

Similar to the hybrid Yee-FFT solver, to ensure the Gauss' Law is satisfied for the customized solver, we correct the component of

the current in the  $\hat{1}$  direction in  $k_1$  space. This is done locally on each parallel partition along  $\hat{1}$  and because the current is already in  $k_1$  space, we can also use a low pass filter and eliminate the unstable high  $k_1$  NCI modes. This filter can also be included into the current correction. We will show that overall this method is effective at eliminating the NCI while allowing good parallel scalability when domain decomposition is required along  $\hat{1}$ .

We note that in Ref. [21] a PIC algorithm based on using a "local" FFT Maxwell solver was proposed. Their work was motivated for maintaining high parallel efficiency and was not focused on eliminating the NCI. They did show results from LWFA simulations in a boosted frame, however, no analysis for the NCI for FFT based algorithms was presented. We note that there are distinct differences between their approaches and ours. In our case, FFTs are performed only on current. This is done to ensure that the continuity equation is satisfied, and also to filter the current for NCI elimination. Because the current from a single particle is not global this can lead to a current that satisfies the continuity equation at every location and it can eliminate the NCI. The EM fields remain in real space and are advanced using Faraday's and Ampere's law. So long as the solution for the current satisfies the continuity equation locally for the finite difference operators used in Ampere's Law, then Gauss's law will be maintained. If the longitudinal components of the fields are also solved using local FFTs in each partition (as is proposed in Ref. [21]), there will be errors in the longitudinal components of  $\vec{E}$  and  $\vec{B}$  due to the enforcement of periodicity.

The remainder of this paper is organized as follows. In Section 2 we first present a method to construct a customized FDTD Maxwell solver that has preferable NCI properties. The corresponding current correction and filtering strategies are discussed in Section 3. We show that the use of local FFTs can provide a current that satisfies the continuity equation for a customized solver. We then present sample simulations in Section 4 showing that good accuracy and scalability can be obtained. Finally, in Section 5 a summary is given.

## 2. Customized Maxwell solver

The Numerical Cerenkov Instability (NCI) occurs when a plasma drifts relativistically on a grid in a PIC code due to the unphysical coupling between the Langmuir modes (both main and aliasing) and electromagnetic (EM) modes [6]. Categorizing the NCI modes with their temporal aliasing mode number  $\mu$ , and spatial aliasing mode number  $\nu_1$ , it is found that usually the most violently growing NCI modes are those at  $(\mu, \nu_1) = (0, \pm 1)$  (we call them first spatial aliasing NCI modes), and  $(\mu, \nu_1) = (0, 0)$  (main NCI modes) [6]. The first spatial NCI modes usually reside near the edges of the fundamental Brillouin zone, making them relatively easy to eliminate with a sharp low-pass filter to the current. On the other hand, the main NCI modes are usually located within the inner half of the  $\vec{k}$  modes, where modes of physical interest are located. It was shown for typical FDTD solvers that these modes were contained in a broad spectrum such that they cannot be eliminated through a low pass or mask filter. On the other hand, as shown in [6,16], for FFT-based solvers (and cell sizes  $\Delta x_1 \leq \Delta x_2$ ), the main NCI modes are very localized in  $\vec{k}$  space and they move to large  $|\vec{k}|$  as the time step is reduced.

Therefore, as discussed in [6,16], to eliminate the NCI modes in FFT-based solvers, the first step is to find a reduced time step which moves the main NCI modes away from the physical modes. After these modes are far enough from the physical modes, one can then apply a highly localized modulation to the EM dispersion relation in  $k$  space where the  $(\mu, \nu_1) = (0, 0)$  modes reside in order to completely eliminate them. For a multi-dimensional spectral

solver, the modification of the EM dispersion is accomplished by directly modifying the finite difference operator  $[\vec{k}]$  in that localized area in  $\vec{k}$  space [6]. For the hybrid Yee-FFT solver, only the operator  $[k_1]$  is modified in the  $k_1$  range where the main NCI modes are located [16]. The modification of the operator usually creates a bump in the dispersion curve in the range where the main NCI modes are located, which removes the coupling between the EM modes and the Langmuir modes in that area, thereby eliminating the main NCI modes in that range completely.

When solving the Maxwell's equation using the FFT-based solvers, the differential operators in  $\vec{k}$  space are explicitly used in the equations, therefore it is straightforward to modify the operators in  $\vec{k}$  space. However, as mentioned in introduction, the use of a 1D FFT when there are many cells along that direction affects the scalability of the solver (or a multi-dimensional FFT solver when there are "many" more cells along one direction). Therefore, a question that naturally follows is whether it is possible to design an FDTD solver to imitate the characteristics of the EM dispersion curves of a FFT-based solver that make it possible to effectively eliminate the NCI. In the following sections, we describe a "recipe" for designing a finite difference derivative that when written in  $\vec{k}$  space leads to the proper characteristics for the EM dispersion.

In [16] it is found that by replacing the finite difference spatial derivative in the direction of the plasma drift from a stencil that is second order accurate in cell size with a spectral solver (which is greater than  $N$ th order accurate), one can restrict the  $(\mu, \nu_1) = (0, 0)$  NCI modes to a highly localized area in the fundamental Brillouin zone [16]. Meanwhile, the spatial derivatives in the other direction(s) can be kept as second order accurate. Therefore, when we design an FDTD solver for the purpose of NCI elimination, it is natural to start with a "hybrid" FDTD solver that resembles the hybrid Yee-FFT solver. We use a higher order FDTD finite difference stencil [22,23] in the direction of the drift while keeping them second order accurate in the other direction(s). Examination of the NCI growth rate where  $[k_1]$  is replaced with the expression for a higher order stencil reveals that indeed the NCI is localized. In addition, we find that new  $(\mu, \nu_1) = (0, 0)$  modes arise at large  $k_1$  where the EM dispersion curve rolls over, i.e., the phase velocity drops. We then show how to modify the expression  $[k_1]$  for the higher order finite difference operator such that the EM dispersion curve has a slight bump at moderate  $|k_1|$  in order to precisely avoid the coupling between the EM modes and main Langmuir modes for the main,  $(\mu, \nu_1) = (0, 0)$ , NCI modes of moderate  $|k_1|$ . To accomplish that, we expand the number of terms in the stencil [see Eq. (3)] to add extra degrees of freedom which can create the bump in the  $k_1$  range where the main NCI modes reside, as we will explain in the following sections. In addition the new  $(\mu, \nu_1) = (0, 0)$  modes at high  $k_1$  can be filtered out since they are outside the range of physically relevant modes.

### 2.1. NCI for high order finite difference solvers

Without loss of generality, we describe the method outlined above in the 2D Cartesian geometry. In a Maxwell solver, the electromagnetic fields  $\vec{E}$  and  $\vec{B}$  are advanced by solving Faraday's law and Ampere's law,

$$\vec{B}^{n+\frac{1}{2}} = \vec{B}^{n-\frac{1}{2}} - c \Delta t \nabla_p^+ \times \vec{E}^n \quad (1)$$

$$\vec{E}^{n+1} = \vec{E}^n + c \Delta t \nabla_p^- \times \vec{B}^{n+\frac{1}{2}} - 4\pi \Delta t \vec{j}^{n+\frac{1}{2}} \quad (2)$$

where the EM fields  $\vec{E}$  and  $\vec{B}$ , and current  $\vec{j}$  are defined on the staggered Yee grid [24], and  $\nabla_p^\pm = (\partial_{p,x_1}^\pm, \partial_{2,x_2}^\pm)$  is the discrete finite difference operator for the staggered scheme. We now

show that an FDTD solver can be designed such that for small to moderate (to be defined later)  $|k_1|$  the corresponding  $[k_1] = k_1$  plus a bump near the unstable  $(0, 0)$  main NCI modes. We apply a  $p$ th order operator in the  $\hat{1}$  direction and a standard second order Yee solver in the  $\hat{2}$  direction. The  $p$ th order operator is defined as

$$\begin{aligned} \partial_{p,x_1}^+ f_{i_1,i_2} &= \frac{1}{\Delta x_1} \sum_{l=1}^{p/2} C_l^p (f_{i_1+l,i_2} - f_{i_1-l,i_2}) \\ \partial_{p,x_1}^- f_{i_1,i_2} &= \frac{1}{\Delta x_1} \sum_{l=1}^{p/2} C_l^p (f_{i_1+l-1,i_2} - f_{i_1-l,i_2}) \end{aligned} \quad (3)$$

where  $f$  is an arbitrary quantity and the coefficients of the finite difference operator  $C_l^p$  can be expressed as [22,23]:

$$C_l^p = \frac{(-1)^{l+1} 16^{1-\frac{p}{2}} (p-1)!^2}{(2l-1)^2 (\frac{p}{2}+l-1)! (\frac{p}{2}-l)! (\frac{p}{2}-1)!^2}. \quad (4)$$

If we perform a Fourier transform to Eqs. (1) and (2) in both time and space, Maxwell's equations become

$$[\omega] \vec{B} = -[\vec{k}] \times \vec{E} \quad (5)$$

$$[\omega] \vec{E} = [\vec{k}] \times \vec{B} + 4\pi \vec{j} \quad (6)$$

where the operators in frequency and wavenumber space are

$$\begin{aligned} [\omega] &= \frac{\sin(\omega \Delta t / 2)}{\Delta t / 2} \\ [\vec{k}] &= \left( \sum_{l=1}^{p/2} C_l^p \frac{\sin[(2l-1)k_1 \Delta x_1 / 2]}{\Delta x_1 / 2}, \frac{\sin(k_2 \Delta x_2 / 2)}{\Delta x_2 / 2} \right) \end{aligned} \quad (7)$$

where  $\omega$  and  $k_{1,2}$  are the frequency and wave numbers, and  $\Delta t$  and  $\Delta x_{1,2}$  are the time step and grid sizes of the PIC system, respectively. Note that when the current vanishes,  $\vec{j} = \vec{0}$ , in Eq. (6), we obtain the numerical dispersion relation for EM waves in vacuum, i.e.,

$$[\omega]^2 = c^2 ([k_1]_p^2 + [k_2]_2^2) \quad (8)$$

where  $[k_1]_p$  and  $[k_2]_2$  are the components of  $[\vec{k}]$ , and the order of accuracy is denoted by the subscripts outside the square brackets.

We plot the numerical dispersion relation  $\omega$  v.s.  $k_1$  (assuming  $k_2 = 0$ ) in Fig. 1. We can see from Fig. 1 that, when the order  $p$  of  $[k_1]$  increases, the dispersion curve is converging to (but never approaches) that of the spectral solver (black solid line). To quantify the locations and growth rates of the NCI modes for high order solvers, in Fig. 2, we plot the patterns of the  $(\mu, \nu_1) = (0, 0)$  and  $(0, 1)$  NCI modes over the  $(k_1, k_2)$  space in the fundamental Brillouin zone. The plot is generated by applying the  $p$ th order finite difference operator in  $k_1$  and second order finite difference operator in  $x_2$  into the theoretical framework developed in Refs. [5,6]. For completeness we write out the dispersion relation in the Appendix. From Fig. 2(a) we can see that the main NCI modes of a high order solver split into two parts: a highly localized part, i.e., a "dot", near  $k_1/k_{g1} = 0.2$  (that has a lower growth rate), and another "strip" component that is very close to the edge of the fundamental Brillouin zone (that has a higher growth rate). To make both visible on the same scale we multiply the growth rate of the "dot" modes by ten. It is interesting to note that the highly localized "dot" part of the main NCI modes is located at almost the same place as for the hybrid Yee-FFT solver [shown in Fig. 2(c)]. Meanwhile, the "strip" component has a growth rate on the same order of magnitude as the main NCI modes of the Yee solver, which are comparable to the  $(\mu, \nu_1) = (0, 1)$  modes for either FFT or finite difference solvers [see Fig. 2(b) and (d)]. This can be explained by the fact that in the low  $k_1$  range the dispersion curve of the higher order solver almost overlaps that of the hybrid solver, while

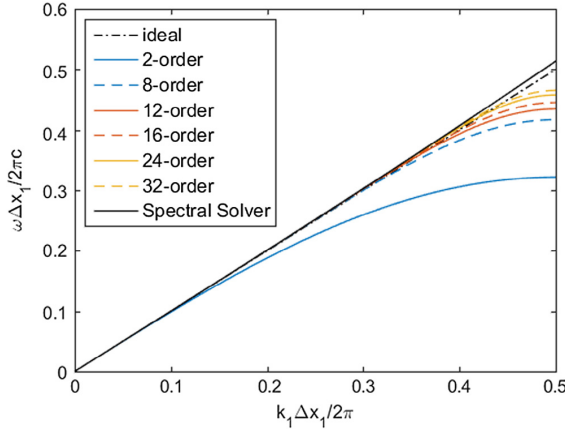


**Fig. 1.** 1D numerical dispersion relations of different finite difference solver and spectral solver.  $\Delta x_1 = 0.2k_0^{-1}$  and  $\Delta t = 0.05\omega_0^{-1}$  are used to generate this plot.

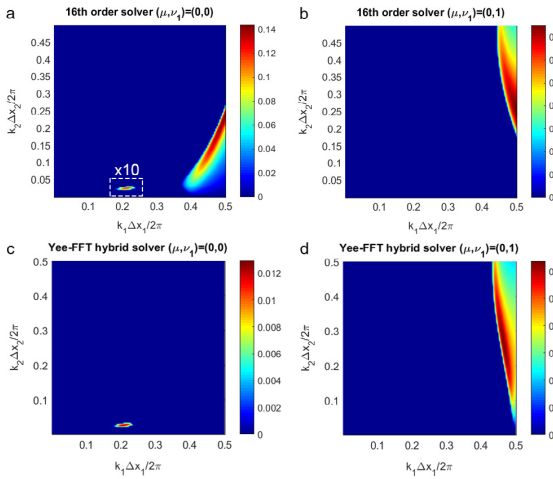


**Fig. 2.** The NCI patterns of 16th order solver and hybrid Yee-FFT solver. (a) and (b) show the  $(\mu, \nu_1) = (0, 0)$  and  $(\mu, \nu_1) = (0, 1)$  NCI mode of the high order (16th order) solver. The values in the dashed line box in (a) are multiplied by 10 for better visualization. (c) and (d) show the  $(\mu, \nu_1) = (0, 0)$  and  $(\mu, \nu_1) = (0, 1)$  NCI mode of the hybrid solver.  $\Delta x_{1,2} = 0.2k_0^{-1}$ ,  $\Delta t = 0.05\omega_0^{-1}$  and  $n_p = 30n_0$  are used to generate the plots, where  $n_0$  is the reference density used in the simulation and  $\omega_0^2 = 4\pi e^2 n_0 / m_e$ ,  $k_0 = \omega_0 / c$ .

for the high  $k_1$  range the curve bends down, resulting in a similar NCI pattern to that of the Yee solver (which rolled over for lower  $k_1$  values). In the meantime, the  $(\mu, \nu_1) = (0, \pm 1)$  modes of the higher order solver reside very close to the edge of the fundamental Brillouin zone [shown in Fig. 2(b)], which is similar to the case of the hybrid Yee-FFT solver [Fig. 2(d)]. This enables us to readily eliminate these modes by applying a low-pass filter to the current in  $k_1$ -space.

Just as was the case for the hybrid Yee-FFT solver, the location of the “dot” part of the main NCI modes also changes for the higher order solver as one reduces the time step. In Fig. 3, we scan the location of the “dot” part of the main NCI modes with different time steps for various solvers. We can see that the main NCI modes at moderate  $|\vec{k}|$  move towards higher  $|\vec{k}|$  for both the hybrid Yee-FFT solver, 16th order solver, and 24th order solver. Therefore, it is possible to apply the strategies used for the hybrid Yee-FFT solver to effectively eliminate the NCI for the hybrid higher-order-Yee solver. In addition, as  $\Delta t / \Delta x_1$  decreases, so do the growth rates for the “dot” part of the main NCI modes.

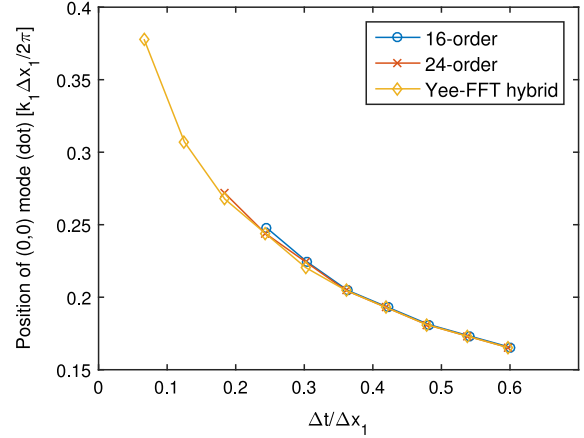


**Fig. 3.** The position of the split “dot” in  $(\mu, \nu_1) = (0, 0)$  NCI mode at different time step for 16th order, 24th order solver and Yee-FFT hybrid solver. We scan the position using  $\Delta x_{1,2} = k_0^{-1}$  and  $n_p = n_0$ , from  $\Delta t = 0.1\Delta t_{\text{CFL}}$  to  $\Delta t = 0.9\Delta t_{\text{CFL}}$ .

For given simulation parameters, we first calculate the locations of the main NCI modes for the 16th order solver (16th order in  $\hat{1}$  direction, and 2nd order in other directions). If they are too close to the physical modes, we reduce the time step to move them away from the center towards the edge of the fundamental Brillouin zone. In the next section, we describe how to modify the higher order stencil such that its  $k_1$  v.s.  $[k_1]_p$  curve has a bump to eliminate the “dot” part of the main NCI modes.

## 2.2. Customization of $[k_1]$

In this subsection, we explain how we customize a higher order finite difference first derivative that also has a slight modification near the location of the NCI modes in wave number space. For the FFT-based solvers described in [6,16] this modification to the EM dispersion relation in the  $k_1$  range where the main NCI modes are located can be easily implemented. Specifically, this is accomplished by changing the definition of  $k_1$  inside the field solver to  $[k_1](k_1)$  in the range  $k_1 \in [k_{1l}, k_{1u}]$ , where the  $(\mu, \nu_1) = (0, 0)$  NCI modes reside close to  $[k_1] = k_1 + \Delta k_{\text{mod}}(k_1)$  where  $\Delta k_{\text{mod}}(k_1)$  is a small localized perturbation (see Fig. 3(a) in [16]). It usually takes the form of

$$\Delta k_{\text{mod}}(k_1) = \begin{cases} \Delta k_{\text{mod,max}} \sin\left(\pi \frac{k_1 - k_{1l}}{k_{1u} - k_{1l}}\right)^2, & k_{1l} \leq k_1 \leq k_{1u} \\ 0, & \text{otherwise} \end{cases} \quad (9)$$

where  $k_{1l}$ ,  $k_{1u}$  are the lower and upper bounds of the region that is modified, and  $\Delta k_{\text{mod,max}}$  is the maximum of  $\Delta k_{\text{mod}}$ . In an FFT-based solver this modification is straightforward to implement, while in a high order FDTD solver, one has to find a stencil that has both higher order accuracy for the derivative over a wide range of wave number space as well as a modification in a local region of wave number space. For a regular  $p$ th order solver (where  $p$  is an even number), there are  $p/2$  coefficients,  $C_l^p$ , for the stencil and the numerical dispersion relation is uniquely determined. It naturally follows that if we want to customize the dispersion relation based on the high order solver, we will need to add more degrees of freedom, i.e., more coefficients, into the operator. This means the stencil will be broader. The coefficients will still need to be constrained so that the operator has higher-order accuracy, while at the same time it has the desired modification in a local region of  $k_1$  space.

We denote the high order solver as  $\nabla_{p^*}^\pm = (\partial_{p^*,x_1}^\pm, \partial_{2,x_2}^\pm)$ . The first component has the form

$$\partial_{p^*,x_1}^+ f_{i_1,i_2} = \frac{1}{\Delta x_1} \sum_{l=1}^M \tilde{C}_l^p (f_{i_1+l,i_2} - f_{i_1-l+1,i_2}) \quad (10)$$

$$\partial_{p^*,x_1}^- f_{i_1,i_2} = \frac{1}{\Delta x_1} \sum_{l=1}^M \tilde{C}_l^p (f_{i_1+l-1,i_2} - f_{i_1-l,i_2}) \quad (11)$$

while the second component is still the standard second order accurate operator. The modified solver has  $M$  coefficients,  $\tilde{C}_l^p$ , where  $M > p/2$ . The corresponding finite difference operator in  $k$ -space becomes

$$[k_1]_{p^*} = \sum_{l=1}^M \tilde{C}_l^p \frac{\sin[(2l-1)k_1 \Delta x_1/2]}{\Delta x_1/2}. \quad (12)$$

In order to construct the ‘‘bump’’ in the dispersion curve for the proposed solver, we need to find an ‘‘optimized’’ set of  $\tilde{C}_l^p$  such that  $[k_1]_{p^*}$  will best approximate the modified  $[k_1] = [k_1]_p + \Delta k$  described in Eq. (9). For the purpose of simplifying the notation, in the following we normalize  $[k_1]_{p^*}$ ,  $[k_1]_p$ ,  $\Delta k_{\text{mod}}$ ,  $k_{1l}$ ,  $k_{1u}$  and  $k_1$ , with  $k_{g1} = 2\pi/\Delta x_1$ . In the spirit of the least square approximation, we construct a function  $F_1$

$$F_1 = \int_0^{1/2} ([k_1]_{p^*} - [k_1]_p - \Delta k_{\text{mod}})^2 dk_1 \quad (13)$$

which we will minimize to find an optimum set of  $\tilde{C}_l^p$ . We note that a weight function  $w(k_1)$  can be employed and this is an area for future work. In addition, the high order solver should also meet the requirement of  $p$ th order accuracy and satisfy the condition  $\partial_{p^*,x_1}^\pm \rightarrow \partial_{x_1}$  as  $\Delta x_1 \rightarrow 0$ . Therefore, the coefficients should be subject to the linear equations below

$$\mathcal{M}\tilde{C}^p = \hat{e}_1 \quad (14)$$

where  $\tilde{C}^p = (\tilde{C}_1^p, \dots, \tilde{C}_M^p)^T$ ,  $\hat{e}_1 = (1, 0, \dots, 0)^T$  and the elements of the matrix  $\mathcal{M}$  are  $\mathcal{M}_{ij} = (2j-1)^{2i-1}/(2i-1)!$  ( $i = 1, \dots, p/2$ ) and ( $j = 1, \dots, M$ ). This is a constrained least-square minimization problem so we can use the Lagrange multipliers to solve it.

The Lagrangian is defined by  $\mathcal{L} = F_1 + F_2$  where  $F_2 = \bar{\lambda}^T (\mathcal{M}\tilde{C}^p - \hat{e}_1)$  and  $\bar{\lambda} = (\lambda_1, \dots, \lambda_{p/2})^T$ . Solving the constrained least-square minimization problem is equivalent to solving,

$$\begin{aligned} \partial \mathcal{L} / \partial \tilde{C}_j^p &= 0 \quad (j = 1, \dots, M) \text{ and} \\ \partial \mathcal{L} / \partial \lambda_i &= 0 \quad (i = 1, \dots, p/2). \end{aligned} \quad (15)$$

It can be straightforward to show that this results in the following set of equations,

$$\frac{\partial F_1}{\partial \tilde{C}_j^p} = \begin{cases} \frac{1}{2\pi^2} (\tilde{C}_j^p - C_j^p - A_j), & 1 \leq j \leq \frac{p}{2} \\ \frac{1}{2\pi^2} (\tilde{C}_j^p - A_j), & \frac{p}{2} + 1 \leq j \leq M \end{cases} \quad (16)$$

$$\frac{\partial F_2}{\partial \tilde{C}_j^p} = \sum_i \lambda_i \mathcal{M}_{ij} \quad (17)$$

$$\frac{\partial F_2}{\partial \lambda_j} = \sum_i \mathcal{M}_{ji} A_i - e_j \quad (18)$$

where

$$A_j = \frac{8\Delta k_{\text{mod,max}} [\cos[(2j-1)\pi k_{1u}] - \cos[(2j-1)\pi k_{1l}]]}{(2j-1)[(2j-1)^2(k_{1u} - k_{1l})^2 - 4]}. \quad (19)$$

Combining Eqs. (16)–(18), we can reformat Eq. (15) into a matrix equation

$$\begin{pmatrix} \frac{1}{2\pi^2} \bar{I} & \mathcal{M}^T \\ \mathcal{M} & \bar{0} \end{pmatrix} \begin{pmatrix} \tilde{C}^p \\ \bar{\lambda} \end{pmatrix} = \begin{pmatrix} \frac{1}{2\pi^2} (\bar{A} + \tilde{C}^p) \\ \hat{e}_1 \end{pmatrix} \quad (20)$$

where  $\bar{I}$  is the  $M \times M$  unit matrix and  $\tilde{C}^p = (C_1^p, \dots, C_{p/2}^p, 0, \dots, 0)^T$ . For given ‘‘bump’’ parameters  $\Delta k_{\text{mod,max}}$ ,  $k_{1l}$  and  $k_{1u}$ , Eq. (20) can be solved numerically. Henceforth, in this paper we use  $M = p$ .

In Fig. 4 we show the comparison of the  $[k_1]$  operator and the NCI mode patterns between the regular and customized high order solver. We use a 16th order solver as an example. In Fig. 4(a), we show that a perturbation (red line) can be introduced to the  $[k_1]_{16}$  operator within the bump region, while the operators  $[k_1]_{16}$  and  $[k_1]_{16^*}$  are almost overlapped outside the region. Fig. 4(b)(c) show the NCI mode patterns for the regular 16th order solver. We can see the dot of  $(\mu, \nu_1) = (0, 0)$  modes presented in the middle of the fundamental Brillouin zone, for which we aim to eliminate through the use of the modified solver. In Fig. 4(d), the dot has been eliminated and  $(\mu, \nu_1) = (0, 1)$  modes and the remaining of  $(\mu, \nu_1) = (0, 0)$  modes are almost identical to what was seen for the regular high order solver.

### 2.3. Courant condition

The derivation of the Courant condition for the proposed high order solver is straightforward. From the numerical dispersion relation

$$[\omega]^2 = c^2 ([k_1]_{p^*}^2 + [k_2]^2), \quad (21)$$

it can be shown that to keep  $\omega$  a real number, the corresponding constraint on the time step must be satisfied, *i.e.*

$$\begin{aligned} \frac{\Delta t}{2} \sqrt{\left( \sum_{l=1}^M \tilde{C}_l^p \frac{\sin[(2l-1)k_1 \Delta x_1/2]}{\Delta x_1/2} \right)^2 + \left( \frac{\sin(k_2 \Delta x_2/2)}{\Delta x_2/2} \right)^2} \\ \leq 1. \end{aligned} \quad (22)$$

Note that  $|k_1| \leq \pi/\Delta x_1$  and  $|k_2| \leq \pi/\Delta x_2$ , we obtain the Courant condition of the proposed high order solver

$$\Delta t \leq 1 / \sqrt{\frac{\left( \sum_{l=1}^M \tilde{C}_l^p \right)^2}{\Delta x_1^2} + \frac{1}{\Delta x_2^2}}. \quad (23)$$

For the standard high order solver, given the cell sizes, the Courant limit only depends on cell sizes and the order solver's accuracy. For instance, the Courant limit of a 16th order solver (16th order in  $x_1$ , while second order in  $x_2$ ) is  $\Delta t_{\text{CL}} = 0.6575\Delta x_1$  with  $\Delta x_1 = \Delta x_2$ . As for the customized solver, although the specified solver coefficients  $\tilde{C}_l^p$  depend on the modification of numerical dispersion we introduce, the Courant limit on the time step varies little as we alter the ‘‘bumps’’ in the numerical dispersion curve. Taking the 16th order customized solver with 16 coefficients and  $\Delta x_1 = \Delta x_2$  for example, the Courant condition reduces to  $\Delta t_{\text{CL}} = 0.6550\Delta x_1$  for  $k_l = 0.1$ ,  $k_u = 0.3$ ,  $\Delta k_{\text{mod}} = 0.01$ , and  $\Delta t_{\text{CL}} = 0.6562\Delta x_1$  for  $k_l = 0.15$ ,  $k_u = 0.3$ ,  $\Delta k_{\text{mod}} = 0.005$ . As we can see, the Courant condition changes little when switching from the standard high order solver to the customized solver.

### 2.4. Cartesian 3D and quasi-3D scenarios

As can be seen from previous sections, this FDTD solver only modifies the finite difference operator in the plasma drifting direction. As a result, although not presented in this paper, the method described above can be extended to Cartesian 3D and quasi-3D geometry [25,26] in a straightforward way.

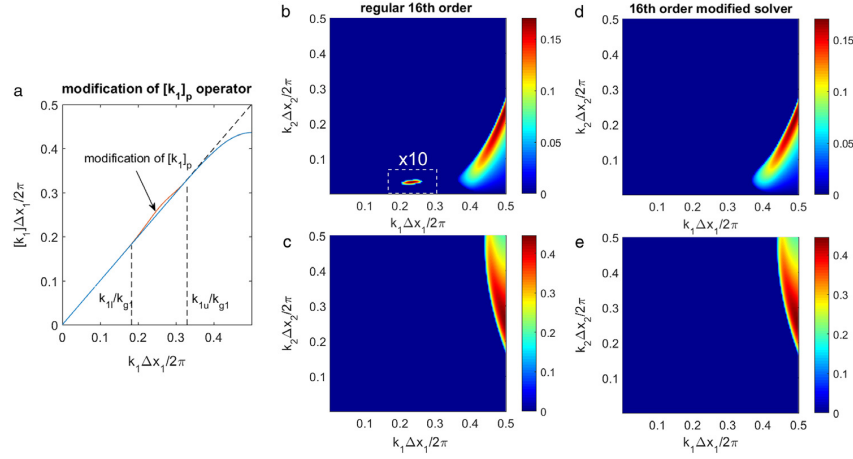


**Fig. 4.** In (a) the perturbation (red line) introduced by the modified 16th order solver is shown. The blue line denotes the  $[k_1]$ - $k_1$  relation of the regular 16th order solver. The lower and upper limits of perturbation are  $k_{l1}/k_{g1} = 0.18$  and  $k_{u1}/k_{g1} = 0.33$ . The perturbation magnitude  $\Delta k_{\text{mod,max}} = 0.01$ . (b) and (c) are  $(\mu, \nu_1) = (0, 0)$  and  $(\mu, \nu_1) = (0, 1)$  NCI mode patterns of the regular 16th order solver respectively. The values in the dashed line box in (b) are multiplied by 10 for better visualization. (d) and (e) are the patterns of the modified 16th order solver. When generating these plots we use  $\Delta x_{1,2} = 0.2k_0^{-1}$ ,  $\Delta t = 0.05\omega_0^{-1}$  and  $n_p = 50n_0$ . (For interpretation of the references to color in this figure legend, the reader is referred to the web version of this article.)

### 3. Charge conservation and parallelization of the solver

Similar to the case in hybrid Yee-FFT solver, when the  $[k_1]$  of the solver is different from the second order accurate  $[k_1]_2$ , one needs to apply a correction to the current in order to satisfy Gauss' Law. This is due to the fact that in a typical FDTD EM-PIC code, the EM fields are advanced by the Faraday's law and Ampere's law, while the Gauss' Law is satisfied by applying a charge conserving current deposit [27]. The charge conserving current deposition is second order accurate in all directions, which matches exactly the standard Yee solver. As a result, when the finite difference operator for the derivative along a particular direction changes in a solver, Gauss' Law is no longer satisfied if the current is not corrected correspondingly.

More specifically, the charge conserving current deposition ensures the second-order-accurate finite difference representation of the continuity equation,

$$\frac{\partial}{\partial t} \rho^n + \nabla_2^- \cdot \vec{J}^{n+\frac{1}{2}} = 0 \quad (24)$$

where  $\frac{\partial}{\partial t} G^n = \frac{G^{n+1} - G^n}{\Delta t}$  for an arbitrary scalar quantity  $G^n$ . For the Yee solver, Gauss's law is rigorously satisfied every time step if it is satisfied at the beginning. However, when combining the high order solver and the second-order-accurate current deposition scheme, we need to apply a correction to the current in the drifting direction in order that Gauss's law remains satisfied throughout the whole simulation. After the current has been calculated locally, we then "correct" them by performing an FFT along the  $x_1$  direction,

$$\vec{J}_1^{n+\frac{1}{2}} = \frac{[k_1]_2}{[k_1]_{p*}} \vec{J}_1^{n+\frac{1}{2}} \quad (25)$$

where  $\vec{J}_1$  is the corrected current, in a similar manner to what was employed for the hybrid Yee-FFT solver. Performing Fourier transform in the  $x_1$  direction and applying the correction scheme in Eq. (25), we guarantee

$$\frac{\partial}{\partial t} \rho^n(k_1, x_2) + i[k_1]_{p*} \vec{J}_1^{n+\frac{1}{2}}(k_1, x_2) + \partial_{2,x_2}^- \vec{J}_2^{n+\frac{1}{2}}(k_1, x_2) = 0. \quad (26)$$

Combining Eq. (26) with Ampere's law, Eq. (2), (replacing  $\nabla_p^-$  with  $\nabla_{p*}^-$  to be consistent with the modified high order solver), we obtain

$$\frac{\partial}{\partial t} \left( -4\pi \rho^n + i[k_1]_{p*} E_1^n + \partial_{2,x_2}^- E_2^n \right) = 0. \quad (27)$$

We carry out inverse Fourier transform to retrieve the equation in real space,

$$\frac{\partial}{\partial t} \left( -4\pi \rho^n + \nabla_{p*}^- \vec{E}^n \right) = 0 \quad (28)$$

which indicates that Gauss's law is satisfied if it is satisfied initially.

It is important to note that one effect that arises from the current correction is that the current from one particle extends to more cells. Therefore, an originally localized current distribution would be spread out over more cells after we correct the current in the  $k$ -space and transform back to real space. This results from the use of a "less" local operator for the derivative. Nevertheless, the current still rigorously satisfies the continuity equation for the desired particle shape.

To quantify the broadening of the current from a single particle (which is needed when determining how many guard cells are needed each parallel domain), we assume that the current is only located at a single point (grid) in the real space, located at the grid index  $i_1 = 0$ , i.e.  $J_{1,i_1} = \delta(i_1)$ . After performing the discrete Fourier transform, the current in the  $k$ -space becomes unity for all  $k_1$ , i.e.  $J_{1,\kappa_1} = 1$ , where  $\kappa_1 = -N/2, \dots, N/2-1$  is the mode number, and  $k_1 = 2\pi\kappa_1/N\Delta x_1$  with  $N$  the number of cells in  $x_1$  direction. The corrected current  $\vec{J}_{1,\kappa_1}$  in Fourier space is therefore the correction factor

$$\left( \frac{[k_1]_2}{[k_1]_{p*}} \right)_{\kappa_1} = \frac{\sin\left(\frac{\pi}{N}\kappa_1\right)}{\sum_l \tilde{C}_l^p \sin\left[\frac{(2l-1)\pi}{N}\kappa_1\right]}. \quad (29)$$

When the corrected current is transformed back to real space by applying an inverse discrete Fourier transform (IDFT), the retrieved current is seen to extend to all grids outside of the original grid. However, as we show next the values of the corrected current for an initial delta function (at the origin) fall off rapidly for grids away from the origin. In fact, the values fall below double precision

accuracy quickly making the corrected current effectively only non-zero in finite region. We illustrate this through 1D numerical calculations. We initialize the current as a Dirac-delta distribution in the center of the grid, *i.e.*  $J_1 = \delta(x_0)$ . Then we perform a 1D FFT to the current, use the correction according to Eq. (25) for solvers with different orders in the  $k$ -space, and finally perform an IFFT to transform the current back into real space. Fig. 5 shows the spatial distribution of the corrected current. It can be seen that the extent of the current is widened by the correction process and the width increases as the order of the solver is increased. Nonetheless, the expansion remains in a localized region in real space and beyond this region the amplitude is on the order of  $10^{-16}$ , which corresponds to double precision roundoff. The fact that the current is localized indicates that the current correction can be done on a local domain so long as a sufficient number of guard cells are used. This permits using domain decomposition along the  $\hat{1}$  direction and the use of a local FFT on each subdomain. For example, we have decreased the size of the subdomain from 256 gridpoints in Fig. 5(a) to 128 gridpoints in Fig. 5(b). The current distribution, the width expansion, and noise level are almost the same. Therefore, we can see that the size of a parallel partition makes little impact on the simulation results. Although the width of the current from each particle is now greatly expanded as mentioned before, the precision of the numerical algorithm essentially limits the width to a finite number of grids so it is in a sense localized. When a sufficient number of guard cells for each simulation partition is used, this current correction scheme will be nearly free of any error brought by the current expansion. Here, we take the 16th order 16-coefficient customized FDTD solver as an example. Typically, the number of guard cells (on each boundary of a subdomain) is two times that of the EM field solver coefficients. As shown in Fig. 5, the current of a single particle after a 16th order correction expands to around 20 gridpoints (half width) (see Fig. 5) whereas the number of guard cells used is 32, so that there are enough guard cells to contain the expanded current.

In addition, because of the assumption of periodicity, when using local FFTs on each subdomain to correct the current so that Gauss's law remains satisfied and to filter the current to eliminate the  $(0, 1)$  NCI modes, we also include additional data from the neighboring subdomains. The total number of guard cells each side is  $N + D$  where for the cells of thickness  $D$  we multiply the data by a function that smoothly goes to zero. This eliminates any spurious signal that arises because we are using FFTs on a subdomain and the function over the entire domain is not periodic over the subdomains. The value of  $N$  is set from the arguments from above to be twice the order of the solver. The value of  $D$  is obtained through empirical experimentation. For the 16th order customized solver we use  $N = 32$  and  $D = 12$ .

#### 4. Sample simulations

In this section we present sample simulations using the customized solver and its corresponding NCI elimination schemes. In these simulations, we used the low-pass filtering for current in the form of

$$F(k_1) = \begin{cases} 1, & |k_1| < f_l k_{g1} \\ \sin^2\left(\frac{k_1 - f_u k_{g1}}{f_l k_{g1} - f_u k_{g1}} \frac{\pi}{2}\right), & f_l k_{g1} \leq k_1 \leq f_u k_{g1} \\ 0, & |k_1| > f_u k_{g1}. \end{cases} \quad (30)$$

The filter retains the  $k_1$  modes smaller than  $f_l k_{g1}$  and cuts off the modes larger than  $f_u k_{g1}$ . A  $\sin^2$  function is used between  $f_l k_{g1}$  and  $f_u k_{g1}$  for smooth connection between unity and zero.

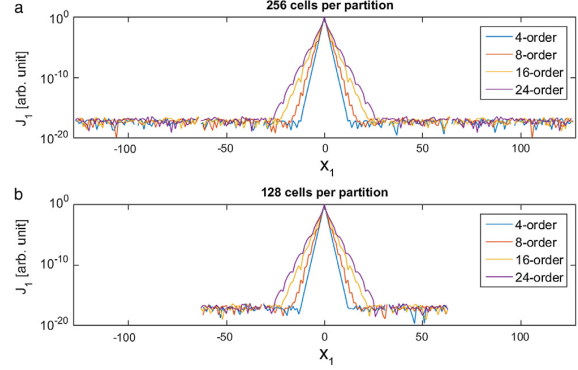


**Fig. 5.** Effect of the current expansion tested by point current. Numerical calculations are carried out on 256 gridpoints (a) and 128 gridpoints (b), to model the cases using different partition sizes. Current with Dirac-delta distribution is initialized and the current corrections of different orders of solver are applied in the  $k$ -space. (a) and (b) show the current distributions in real space with different correction schemes. We set  $\Delta x_1 = 1$  for the calculations.

**Table 1**

Simulation parameters for the 2D drifting plasma simulation. The parameters are normalized to the plasma density  $n_p$  with  $\omega_p^2 = 4\pi q^2 n_p / m_e$ ,  $k_p = \omega_p / c$ .

Parameters	Values
grid size ( $\Delta x_1, \Delta x_2$ )	$(k_p^{-1} / \sqrt{2}, k_p^{-1} / \sqrt{2})$
time step $\Delta t$	$0.25 \Delta x_1$
number of grids	$512 \times 512$
particle shape	quadratic, cubic
$[k_1]$ modification ( $k_{1l}, k_{1u}, \Delta k_{\text{mod,max}}$ )	
customized FDTD solver <sup>a</sup>	(0.1, 0.3, 0.005)
hybrid Yee-FFT solver <sup>b</sup>	(0.1, 0.3, 0.01)
lowpass filter ( $f_l, f_u$ )	
customized FDTD solver	(0.325, 0.35)
hybrid Yee-FFT solver	(0.325, 0.35)
electron drifting momentum $p_{10}$	$19.975 m_e c$
plasma density	$n_p$

<sup>a</sup> It corresponds to the blue and green lines in Fig. 6.

<sup>b</sup> It corresponds to the dashed line in Fig. 6.

#### 4.1. Drifting plasma

In this subsection we demonstrate the NCI elimination capability of the customized FDTD Maxwell solver with a 2D Cartesian OSIRIS simulation of drifting plasma. We fill the simulation box with a plasma drifting relativistically at  $\gamma = 20$  along  $\hat{1}$  direction. The plasma has a very small but finite temperature to seed the NCI. Periodic boundary conditions are used for both the  $\hat{1}$  and  $\hat{2}$  directions. We performed simulations using both the 16th order solver, the customized solver, and the hybrid Yee-FFT solver, with and without the low-pass filters. Other simulation parameters are presented in Table 1, and the corresponding coefficients for the customized solver are listed in Table 2.

We can see from Fig. 6 that, by comparing the red line (16th order solver without any filters) and the orange line (16th order solver plus low-pass filter), that applying the low-pass filter to a 16th order solver significantly reduces the growth of the  $E_2$  energy. This is because the fastest growing  $(\mu, \nu_1) = (0, \pm 1)$  NCI modes are eliminated by the low-pass filter. Besides using the low-pass filter, when we add the bump to the 16th order solver (thus making it a customized solver), the growth rate is further reduced since the main NCI modes are completely eliminated (see the blue line). Even higher order NCI modes [6] are attributed to the slight growth in energy for this case (blue line in Fig. 6), and when the cubic particle shape is applied, the corresponding energy growth is effectively suppressed (green line in Fig. 6). We can see that when the low-pass filter, bump, and higher order particles are applied to the cases

**Table 2**

Coefficients  $\tilde{C}_i^{16}$  in Eq. (12) for the customized solver based on the 16th order solver, for the single plasma drift simulation discussed in Section 4.1.

Coefficients	Values	Coefficients	Values
$\tilde{C}_1^{16}$	1.237042976225048	$\tilde{C}_2^{16}$	-0.102548201854464
$\tilde{C}_3^{16}$	0.022015354460742	$\tilde{C}_4^{16}$	-0.009258452621442
$\tilde{C}_5^{16}$	0.000410036656959	$\tilde{C}_6^{16}$	0.002572239519500
$\tilde{C}_7^{16}$	0.001482836071727	$\tilde{C}_8^{16}$	-0.001392055950412
$\tilde{C}_9^{16}$	-0.001472515326959	$\tilde{C}_{10}^{16}$	0.000478783514362
$\tilde{C}_{11}^{16}$	0.001200462462019	$\tilde{C}_{12}^{16}$	-0.000187062256742
$\tilde{C}_{13}^{16}$	-0.001059471474041	$\tilde{C}_{14}^{16}$	0.000873314953435
$\tilde{C}_{15}^{16}$	-0.000281855449164	$\tilde{C}_{16}^{16}$	0.000034281167855

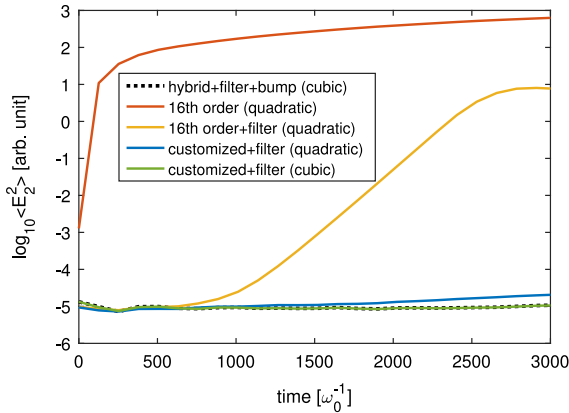


**Fig. 6.** Evolutions of the  $E_2$  energies in the numerical systems for various setups in drifting plasma 2D Cartesian PIC simulations, as discussed in Section 4.1. (For interpretation of the references to color in this figure legend, the reader is referred to the web version of this article.)

of both customized solver (green line) and hybrid Yee-FFT solver (black dotted line), both the hybrid Yee-FFT solver and customized solver schemes effectively eliminate the NCI.

#### 4.2. Relativistic shock

We next present an example where two plasmas collide against each other which is relevant for relativistic shock simulations. The two plasmas drift towards each other with a Lorentz factor of  $\gamma = 20.0$ . The simulation has a box size of  $131\,072 \times 2048$  cells, for which the number of cells in the  $\hat{1}$  direction is much larger than that in the  $\hat{2}$  direction. For a 2D code with FFTs one typically uses a 1D decomposition and the number of cores is limited by the number of cells in the direction with the least number of cells ( $\hat{2}$  in this case). When using the hybrid FFT/FD solver to remove the NCI the FFT is done in the drifting direction ( $\hat{1}$  in this case) for which there are many more cells. At the moment we are not aware of an efficient 1D parallel FFT so the problem can only be decomposed in the  $\hat{2}$  direction as well. We are currently exploring using OpenMP/MPI hybrid parallelization approaches including 1D parallel FFTs to see if the parallel scaling of the aforementioned approaches can be improved. However, with the customized solver and corresponding NCI elimination scheme, we are able to also partition in the  $\hat{1}$  direction in a straightforward manner. For this example, we used a 2D domain decomposition with  $256 \times 16$  partitions along the  $\hat{1}$  and  $\hat{2}$  directions respectively. For each subdomain, there are  $512 \times 128$  cells (guard cells not included) in total. When correcting the current, along the 1 direction, we

**Table 3**

Parameters for 2D relativistic collisionless plasma simulations in lab frame using the modified high order solver and Yee solver. The plasma density  $n_0$  and corresponding wave number  $k_0$  are used to normalize the simulation parameters. The parameters of  $[k_1]$  modification are normalized to  $k_{g1} \equiv 2\pi/\Delta x_1$ .

Parameters	Values
<b>Plasma</b>	
density $n_{pe}, n_{pi}$	$n_0$
initial Lorentz factor $\gamma_0$	20.0
initial thermal velocity $v_{th,e,i}$	$8.7 \times 10^{-5} c$
mass ratio $m_i/m_e$	32
<b>Simulation using customized high order solver</b>	
cell size $\Delta x_{1,2}$	$0.5k_0^{-1}$
time step $\Delta t/\Delta x_1$	0.2
number of cells	$2^{17} \times 2^{11}$
particle shape	quadratic
particle per cell	(1, 2)
$[k_1]$ modification ( $k_{1l}, k_{1u}, \Delta k_{mod,max}$ )	(0.1, 0.35, 0.01)
lowpass filter ( $f_l, f_u$ )	(0.275, 0.3)
<b>Simulation using standard Yee solver</b>	
cell size $\Delta x_{1,2}$	$0.5k_0^{-1}$
time step $\Delta t/\Delta x_1$	0.5
number of cells	$2^{17} \times 2^{11}$
particle shape	quadratic
particle per cell	(1, 2)

used 44 additional cells ( $N = 32$  and  $D = 12$ ) on each side of the subdomain. When advancing the fields we need 32 guard cells. Other simulation parameters are listed in Table 3, and the corresponding coefficients for the customized solver are listed in Table 4.

In Fig. 7 we plot the 2D color isosurface plots of the ion density, and line outs of the  $x_2$  averaged ion density for the Yee solver and customized solver. For the Yee solver case, we used both a time step that is close to the Courant limit and one that is equal to the optimal time step of  $\Delta t = 0.5\Delta x_1$  for which the NCI is minimized. We also use a 5-pass smoothing and compensation for the current which is done to limit self-heating from aliasing. These results show clearly that the NCI is occurring in the upstream region (the area enclosed by the dashed box in Fig. 7(a)–(c)) for both Yee cases. The evidence of the NCI is very noticeable when using a time step near Courant limit, where the presence of the NCI prevents filaments from occurring at all at the shock front. For the case with the customized solver, we used the same NCI elimination scheme as is used for the single drifting plasma case, but with slightly different coefficients because we used different time steps and plasma densities (the location of the unstable modes depends on the density and time step). We can see from Fig. 7(c) that there are noticeable differences between this simulation and the Yee cases. The filaments are narrower and much cleaner in the upstream region than when compared to Yee solver case with the optimized  $\Delta t$ . On the other hand, the differences in the transversely averaged ion density are much less pronounced. The averaged ion density profile of the customized solver and the Yee with optimized  $\Delta t$

is very similar except for the evidence of noise in the upstream region for the Yee case. This noise arises from the NCI (see Fig. 7(e)). However, as shown above the density filaments are narrower in the shock for the customized solver. Additional differences can be seen in the particle phase space plots. In Fig. 8, it is clearly shown that the plasma in the upstream region is heating up due to the NCI for the two Yee cases. This also affects how the reflected ions penetrate into the upstream region. For the Yee case with  $\Delta t$  near Courant limit, the heating is very severe while for Yee with optimized  $\Delta t$  the NCI is significantly suppressed. The presence of the NCI clearly still leads to plasma heating in the upstream region and as noted above it affects the penetration of the reflected ions into the upstream region. For customized solver, no heating (no evidence of the NCI) is shown and  $p_1$  vs.  $x_1$  always is narrow along  $p_1$  in the upstream region.

From our NCI theory we know that the Yee solver with the optimized time step does not eliminate the main  $(\mu, \nu_1) = (0, 0)$  modes. The growth rate for these modes is reduced, but they are not localized in space; instead they reside within the range of physics. It is not obvious when, and how these modes are altering the physics. On the other hand, the customized solver together with our filters completely removes the  $(\mu, \nu_1) = (0, \pm 1)$  and  $(\mu, \nu_1) = (0, 0)$  modes; and the use of the higher order particle shapes reduces the growth rate for the next highest growing modes. These preliminary results show that the NCI (even the slowly growing  $(\mu, \nu_1) = (0, 0)$  modes) can seed to noise that affects the plasma in the shock and downstream regions. Understanding the details of the physics and studying shock formation and particle acceleration in relativistic shocks will be left for future work.

#### 4.3. LWFA boosted frame simulation

In this subsection, we present 3D Cartesian LWFA boosted frame PIC simulations using the customized FDTD Maxwell solver in OSIRIS. For comparison, we carried out simulations using the hybrid Yee-FFT solver and customized FDTD Maxwell solver respectively. The corresponding lab frame simulation is the 1.3 GeV case discussed in [28], and we have also listed the parameters in Table 5. Note that although the simulation parameters in this scenario are different from those of the relativistic shock simulations discussed in Section 4.2, the locations of the main NCI modes for a 16th order solver under these two sets of parameters are very close to each other. Therefore we used the same coefficients for the customized solver as in Section 4.2, as listed in Table 4.

In Fig. 9(a) and (b) we plot the  $E_1$  field at  $t' = 3746 \omega_0^{-1}$  for simulations with either a modified high order solver or a hybrid Yee-FFT solver. Both solvers give nearly identical results and no evident numerical Cerenkov radiation is observed in either cases. In Fig. 9(c) and (d) 2D plots of the electron density in the two cases are given. We also plot the line out of the on-axis  $E_1$  fields for different time points in the boosted frame, as shown in Fig. 9(e)–(h). As we can see from the comparisons, very good agreement between the results with these two solvers is obtained.

We note that there are differences for the bump parameters listed in Table 5 between those for the customized high order solver and for the Yee-FFT hybrid solver. Although the position of the unstable  $(0, 0)$  mode is essentially the same for both solvers, the customized solver cannot accurately replicate the bump in  $[k_1]$  that is used for the hybrid solver. Since the construction of the bump in  $[k_1]$  of the customized solver is based on approximating a specified function using only a limited number of  $\tilde{C}_p^l$ , the bump obtained from the resulting coefficients may not be ideal. The error gets smaller as the order of the customized solver gets higher or the number of  $\tilde{C}_p^l$  increases. We then modify the target function slightly

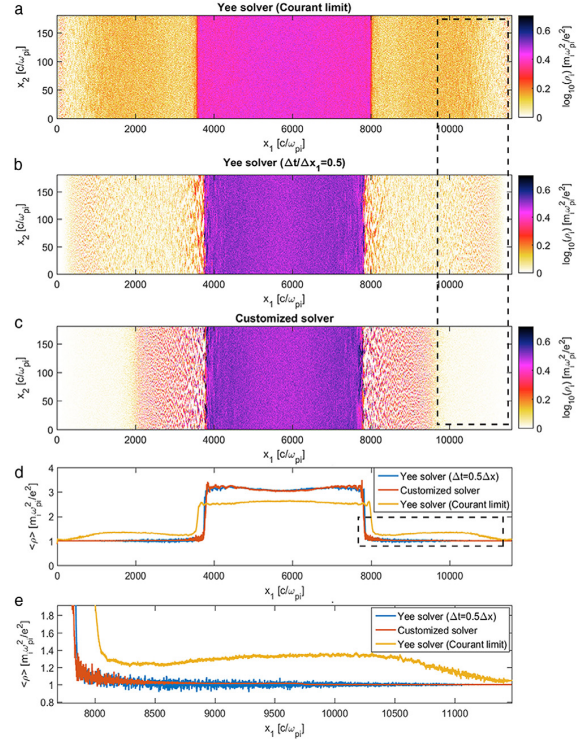


Fig. 7. The 2D plots of ion densities for (a) Yee solver with  $\Delta t$  approaching Courant limit, (b) Yee solver with  $\Delta t = 0.5\Delta x_1$  and (c) customized solver, and (d) their average along  $x_2$  for a relativistic shock simulation. The corresponding simulation parameters are listed in Table 3. (e) The zoom-in details of the dashed box in (d). These plots are generated at  $t = 4525\omega_{pi}^{-1}$ .

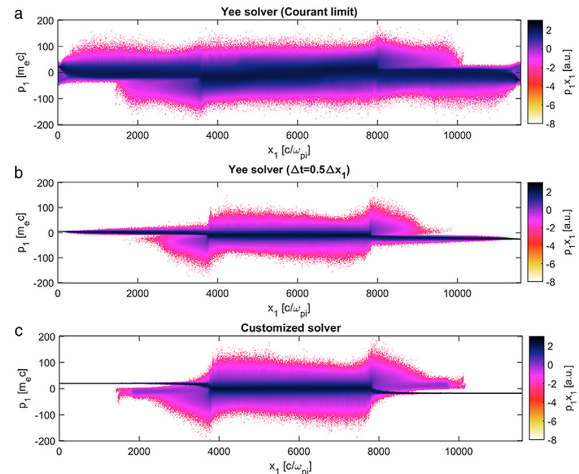


Fig. 8. The 2D plots of  $x_1$ - $p_1$  phase space for (a) Yee solver with  $\Delta t$  approaching Courant limit, (b) Yee solver with  $\Delta t = 0.5\Delta x_1$  and (c) customized solver. These plots are generated at  $t = 4525\omega_{pi}^{-1}$ . The colormap is shown in logarithmic scale. (For interpretation of the references to color in this figure legend, the reader is referred to the web version of this article.)

to see if the resulting approximate function actually more closely resembles the original target function. This iterative process is carried out one or two times. Optimizing this process is an area for future work.



**Table 4**

Coefficients  $\tilde{C}_i^{16}$  in Eq. (12) for the customized solver based on the 16th order solver, for the relativistic shock simulations, and LWFA simulations in the Lorentz boosted frame, as discussed in Sections 4.2 and 4.3.

Coefficients	Values	Coefficients	Values
$\tilde{C}_1^{16}$	1.243205632406442	$\tilde{C}_2^{16}$	-0.096527073844747
$\tilde{C}_3^{16}$	0.017018941335700	$\tilde{C}_4^{16}$	-0.013839950216042
$\tilde{C}_5^{16}$	0.003588768352855	$\tilde{C}_6^{16}$	0.005153133591937
$\tilde{C}_7^{16}$	0.000007068893273	$\tilde{C}_8^{16}$	-0.002317133408538
$\tilde{C}_9^{16}$	-0.001166192174494	$\tilde{C}_{10}^{16}$	0.000552266782136
$\tilde{C}_{11}^{16}$	0.001508596910066	$\tilde{C}_{12}^{16}$	-0.000134050410326
$\tilde{C}_{13}^{16}$	-0.001599956501178	$\tilde{C}_{14}^{16}$	0.001305552125425
$\tilde{C}_{15}^{16}$	-0.000423469804615	$\tilde{C}_{16}^{16}$	0.000051829248350

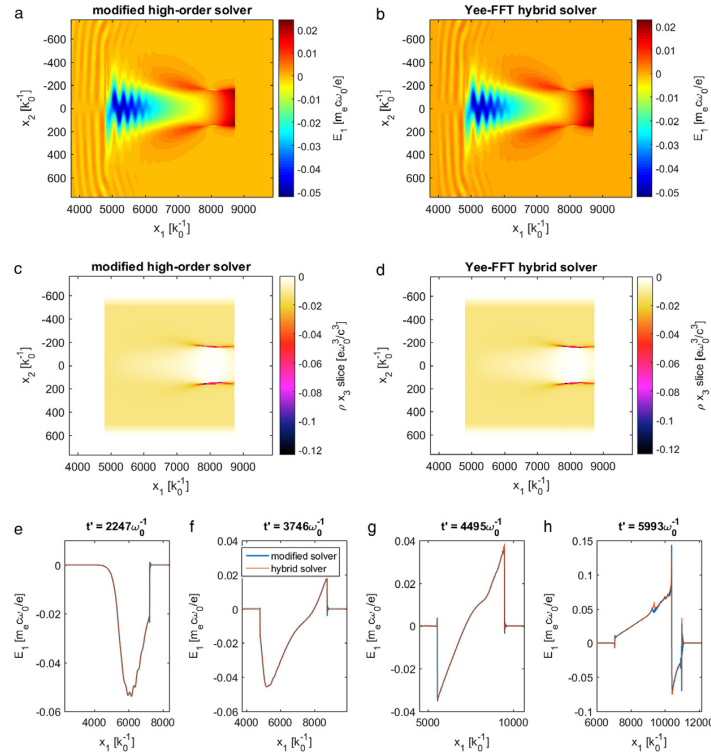


**Fig. 9.** Comparison of simulations in the boosted frame between the customized high order solver and Yee-FFT hybrid solver. 2D plots of  $E_1$  field at  $t' = 3746 \omega_0^{-1}$  for both solvers are shown in (a) and (b). The electron density profiles are shown in (c) and (d). (e)–(h) Plot the on-axis lineouts of  $E_1$  fields at different times.

### 5. Summary

In this paper, we have presented a new customized high-order FDTD solver combined with a current correction (such that Gauss’s law remains satisfied) that effectively eliminates the NCI. The current is corrected and filtered by using a local FFT on each parallel partition when using domain decomposition. The customized higher order solver, and the corresponding current correction/filtering that is done locally on each partition permit the systematic elimination of the Numerical Cerenkov Instability (NCI), while also permitting high parallel scalability in particle-in-cell codes. Using the theoretical framework we developed previously [5,6] and through the results from illustrative PIC simulations, it is found that a high-order FDTD solver has similar NCI properties to that of a fully spectral solver or a hybrid Yee-FFT solver. By reducing the time step, the fastest growing  $(\mu, \nu_1) = (0, \pm 1)$  NCI

modes and  $(\mu, \nu_1) = (0, 0)$  NCI modes can reside very close to the edge of the fundamental Brillouin zone. This enables the use of a lowpass filter on the current to effectively eliminate the NCI. For regular high-order FDTD solvers, highly localized NCI modes [which are part of the  $(\mu, \nu_1) = (0, 0)$  modes] are seen in analogy to those observed in a spectral or hybrid Yee-FFT solver. These modes reside close to the physical modes in  $k$ -space. Elimination of these modes can be achieved by a combination of applying reduced time step and creating a bump in the EM dispersion relation in  $k_1$  space. This solver can be readily implemented in 2D/3D Cartesian and quasi-3D geometries contained within the existing framework of OSIRIS without the need to modify the boundary conditions in the transverse directions. We note that the boundary conditions in the  $\hat{1}$  direction do not need to be changed since we can gradually reduce the order of the solver from 16th to 2nd order in the last 16 cells to match the second order accurate boundary condition.

**Table 5**

Parameters for a 3D LWFA simulations in the Lorentz boosted frame using the customized high order solver and hybrid Yee-FFT solver. The laser frequency  $\omega_0$ , wave number  $k_0$  and the critical density  $n_0 = m_e \omega_0^2 / (4\pi e^2)$  in the lab frame are used to normalize the simulation parameters. The parameters of  $[k_1]$  modification are normalized to  $k_{g1} \equiv 2\pi / \Delta x_1$ .

Parameters	Values
Plasma	
density $n_p$	$8.62 \times 10^{-4} n_0 \gamma_b$
length $L$	$8.0 \times 10^4 k_0^{-1} / \gamma_b$
Laser	
normalized vector potential $a_0$	4.0
focal waist $w_0$	$153.0 k_0^{-1}$
pulse length $\tau$	$86.9 k_0^{-1} \gamma_b (1 + \beta_b)$
polarization	circular
Simulation setups	
cell size $\Delta x_{1,2,3}$	$0.1 k_0^{-1} \gamma_b (1 + \beta_b)$
time step $\Delta t / \Delta x_1$	0.125
number of cells	$2048 \times 512 \times 512$
particle shape	quadratic
particle per cell	(2, 2, 2)
NCl elimination parameters	
Customized solver	
$[k_1]$ modification ( $k_{1l}, k_{1u}, \Delta k_{\text{mod,max}}$ )	(0.1, 0.35, 0.01)
lowpass filter ( $f_l, f_u$ )	(0.3, 0.325)
Hybrid Yee-FFT solver	
$[k_1]$ modification ( $k_{1l}, k_{1u}, \Delta k_{\text{mod,max}}$ )	(0.141, 0.24, 0.007)
lowpass filter ( $f_l, f_u$ )	(0.3, 0.325)

When the finite difference operators are modified, then the charge conserving current deposit must also be appropriately modified. We first deposit the current using the second order accurate charge conserving current deposit [27] in OSIRIS. The current is then Fourier transformed on each local partition, and then corrected, and filtered; it is then transformed back to real space for use in the field solver. The use of a current deposit that satisfies the continuity equation for the higher order divergence operator is necessary such that Gauss' Law remains satisfied at each time step. We show that making such correction to the current will expand the range of cells over which the current for a particle is increased. Although a point current would extend very widely after the correction, it falls below the double precision roundoff within a finite number of cells. Therefore, the current from a single particle is effectively localized. This permits using FFTs and the current correction and filtering for only the data on each parallel partition if the number of guard cells is properly chosen.

We have shown how the customized solver, together with its NCl elimination scheme, can systematically eliminate the NCl in a single drifting plasma. We have also shown that this scheme eliminates the NCl when it is applied to colliding plasma simulations that are used to study relativistic shocks without sacrificing the parallel scalability of an FDTD EM-PIC code for problems with disproportionate number of cells in one direction. We have also shown the usefulness of the proposed high-order solver combined with local FFTs by conducting full 3D LWFA simulations in a Lorentz boosted frame.

### Acknowledgments

This work was supported by NSFC 11425521, 11535006 and 11375006, by the US National Science Foundation under grants ACI 1339893, 1500630, and 1614949, and by the US Department of Energy under DE-SC0014260, DE-SC0010064, and DE-SC0008316. Simulations were carried out on the UCLA Hoffman2 and Dawson2 Clusters, and on Edison Cluster of the National Energy Research Scientific Computing Center, and on Blue Waters cluster at National Center for Supercomputing Applications at UIUC.

### Appendix. 2D Numerical dispersion for relativistically drifting plasma and NCl analytical expression in customized solver

According to Ref. [5,6], the numerical dispersion for the hybrid solver can be expressed as

$$\left( (\omega' - k'_1 v_0)^2 - \frac{\omega_p^2}{\gamma^3} (-1)^\mu \frac{S_{j1} S_{E1} \omega'}{[\omega]} \right) \times \left( [\omega]^2 - [k]_{E1} [k]_{B1} - [k]_{E2} [k]_{B2} \right) - \frac{\omega_p^2}{\gamma} (-1)^\mu \frac{S_{j2} (S_{E2} [\omega] - S_{B3} [k]_{E1} v_0)}{\omega' - k'_1 v_0} + \mathcal{C} = 0 \quad (\text{A.1})$$

where  $\mathcal{C}$  is a coupling term in the dispersion relation

$$\mathcal{C} = \frac{\omega_p^2}{\gamma} (-1)^\mu \left\{ S_{j1} S_{E1} \omega' [k]_{E2} [k]_{B2} (v_0^2 - 1) + S_{j2} S_{E2} [k]_{E2} [k]_{B2} (\omega' - k'_1 v_0) + S_{j1} [k]_{E2} (S_{E2} [k]_{B1} k_2 v_0 - S_{B3} k_2 v_0^2) \right\} \quad (\text{A.2})$$

and for the customized solver discussed in this paper,  $[k]_{E1} = [k]_{B1} = [k_1]_{p*}$ , where  $[k_1]_{p*}$  is defined in Eq. (12), and

$$[k]_{E2} = [k]_{B2} = \frac{\sin(k_2 \Delta x_2 / 2)}{\Delta x_2 / 2}. \quad (\text{A.3})$$

We can expand  $\omega'$  around the beam resonance  $\omega' = k'_1 v_0$  in Eq. (A.1), and write  $\omega' = k'_1 v_0 + \delta\omega'$ , where  $\delta\omega'$  is a small term. This leads to a cubic equation for  $\delta\omega'$  (see [6] for the detailed derivation),

$$A_2 \delta\omega'^3 + B_2 \delta\omega'^2 + C_2 \delta\omega' + D_2 = 0 \quad (\text{A.4})$$

where

$$\begin{aligned} A_2 &= 2\xi_0^3 \xi_1 \\ B_2 &= \xi_0^2 \left\{ \xi_0^2 - [k]_{E1} [k]_{B1} - [k]_{E2} [k]_{B2} - \frac{\omega_p^2}{\gamma} (-1)^\mu S_{j2} (S_{E2} \xi_1 - \zeta_1 S'_{B3} [k]_{E1}) \right\} \\ C_2 &= \frac{\omega_p^2}{\gamma} (-1)^\mu \left\{ \xi_0^2 S_{j2} (\zeta_0 S'_{B3} [k]_{E1} - S_{E2} \xi_0) - \xi_1 S_{j1} [k]_{E2} k_2 S_{E2} [k]_{B1} + \xi_0 [k]_{E2} (S_{j2} S_{E2} [k]_{B2} - S_{j1} k_2 \zeta_1 S'_{B3} \xi_0) \right\} \\ D_2 &= \frac{\omega_p^2}{\gamma} (-1)^\mu \xi_0 [k]_{E2} k_2 S_{j1} \left( S_{E2} [k]_{B1} - \zeta_0 S'_{B3} \xi_0 \right) \end{aligned} \quad (\text{A.5})$$

where

$$\begin{aligned} \xi_0 &= \frac{\sin(\tilde{k}_1 \Delta t / 2)}{\Delta t / 2} & \xi_1 &= \cos(\tilde{k}_1 \Delta t / 2) \\ \zeta_0 &= \cos(\tilde{k}_1 \Delta t / 2) & \zeta_1 &= -\sin(\tilde{k}_1 \Delta t / 2) \Delta t / 2 \\ \tilde{k}_1 &= k_1 + v_1 k_{g1} - \mu \omega_g. \end{aligned} \quad (\text{A.6})$$

We use

$$s_{l,i} = \left( \frac{\sin(k_i \Delta x_i / 2)}{\Delta x_i / 2} \right)^{l+1} \quad (\text{A.7})$$

as well as use the corresponding interpolation functions for the EM fields used to push the particles

$$\begin{aligned} S_{E1} &= s_{l,1}s_{l,2}s_{l,3}(-1)^{\nu_1} & S_{E2} &= s_{l,1}s_{l,2}s_{l,3} & S_{E3} &= s_{l,1}s_{l,2}s_{l,3} \\ S_{B1} &= s_{l,1}s_{l,2}s_{l,3} & S_{B2} &= s_{l,1}s_{l,2}s_{l,3}(-1)^{\nu_1} & S_{B3} &= s_{l,1}s_{l,2}s_{l,3}(-1)^{\nu_1} \end{aligned} \quad (\text{A.8})$$

when using the momentum conserving field interpolation. The  $(-1)^{\nu_1}$  term is due to the half-grid offsets of these quantities in the  $\hat{1}$  direction. With respect to the current interpolation,

$$\begin{aligned} S_{j1} &= s_{l-1,1}s_{l,2}s_{l,3}(-1)^{\nu_1} & S_{j2} &= s_{l,1}s_{l-1,2}s_{l,3} \\ S_{j3} &= s_{l,1}s_{l,2}s_{l-1,3}. \end{aligned} \quad (\text{A.9})$$

We note that we use expressions for charge conserving current deposition scheme that are strictly true in the limit of vanishing time step  $\Delta t \rightarrow 0$ . The coefficients  $A_2$  to  $D_2$  are real, and completely determined by  $k_1$  and  $k_2$ . By solving Eq. (A.4) one can rapidly scan the NCI modes for a particular set of  $(\mu, \nu_1)$  for the customized solver.

## References

- [1] B.B. Godfrey, J. Comput. Phys. 15 (1974) 504.
- [2] B.B. Godfrey, J. Comput. Phys. 19 (1975) 58.
- [3] P. Yu, et al., Proc. 15th Advanced Accelerator Concepts Workshop, Austin, TX, 2012; AIP Conf. Proc. 1507 (2012) 416.
- [4] B.B. Godfrey, J.-L. Vay, J. Comput. Phys. 248 (2013) 33.
- [5] X. Xu, et al., Comput. Phys. Comm. 184 (2013) 2503–2514.
- [6] P. Yu, et al., Comput. Phys. Comm. 192 (2015) 32.
- [7] T. Tajima, J.M. Dawson, Phys. Rev. Lett. 43 (1979) 267.
- [8] W.B. Mori, V.K. Decyk, T.C. Katsouleas, D.W. Forslund, R.D. Ferraro, E. Horowitz, Full-Scale Numerical Experiment to Test a Future Plasma-Based Accelerator, Submitted to NSF as part of the US High Performance Computing and Communications Program, 1992.
- [9] J.-L. Vay, Phys. Rev. Lett. 98 (2007) 130405.
- [10] S.F. Martins, R.A. Fonseca, W.B. Mori, L.O. Silva, Astrophys. J. Lett. 695 (2009) L189–L193.
- [11] F. Fiuzza, R.A. Fonseca, J. Tonge, W.B. Mori, L.O. Silva, Phys. Rev. Lett. 108 (2012) 235004.
- [12] A. Spitkovsky, Astrophys. J. Lett. 682 (2008) L5.
- [13] L. Sironi, A. Spitkovsky, J. Arons, Astrophys. J. 771 (2013) 54.
- [14] B.B. Godfrey, J.-L. Vay, I. Haber, J. Comput. Phys. 258 (2014) 689.
- [15] B.B. Godfrey, J.-L. Vay, J. Comput. Phys. 267 (2014) 1.
- [16] P. Yu, et al., Comput. Phys. Comm. 197 (2015) 144.
- [17] B.B. Godfrey, J.-L. Vay, Comput. Phys. Comm. 196 (2015) 221.
- [18] P. Yu, et al., J. Comput. Phys. 266 (2014) 124.
- [19] A.T. Lin, J.M. Dawson, H. Okuda, Phys. Fluids 17 (1974) 1995.
- [20] J.M. Dawson, Rev. Modern Phys. 55 (2) (1983) 403.
- [21] J.-L. Vay, I. Haber, B.B. Godfrey, J. Comput. Phys. 243 (2013) 260.
- [22] I.R. Khan, R. Ohba, J. Comput. Appl. Math. 107 (1999) 179.
- [23] I.R. Khan, R. Ohba, N. Hozumi, J. Comput. Appl. Math. 150 (2003) 303.
- [24] K. Yee, IEEE Trans. Antennas and Propagation 14 (1966) 302.
- [25] A. Lifschitz, et al., J. Comput. Phys. 228 (2009) 1803.
- [26] A. Davidson, et al., J. Comput. Phys. 281 (2015) 1063.
- [27] T. Esirkepov, Comput. Phys. Comm. 135 (2001) 144.
- [28] W. Lu, et al., Phys. Rev. ST - Accel. Beams 10 (2007) 061301.

## Interactions of Laser Speckles Due to Kinetic Stimulated Raman Scattering

B. J. Winjum,<sup>1,2</sup> A. Tableman,<sup>2,3</sup> F. S. Tsung,<sup>2,3</sup> and W. B. Mori<sup>1,2,3,4</sup>

<sup>1</sup>*Institute for Digital Research and Education, University of California Los Angeles, Los Angeles, CA 90095*

<sup>2</sup>*Particle-in-Cell and Kinetic Simulation Software Center,*

*University of California Los Angeles, Los Angeles, CA 90095*

<sup>3</sup>*Department of Physics and Astronomy, University of California Los Angeles, Los Angeles, CA 90095*

<sup>4</sup>*Department of Electrical Engineering, University of California Los Angeles, Los Angeles, CA 90095*

We examine the possible interactions of two laser speckles due to the exchange of particles and waves generated by stimulated Raman scattering (SRS) using two-dimensional particle-in-cell simulations. By controlling the relative polarization, spatial placement, and timing of two laser speckles, one above-threshold and one below-threshold for SRS, we isolate and characterize SRS growth stimulated in below-threshold speckles due to inter-speckle interactions via energetic electrons, scattered light waves, and scattered plasma waves. We show that scattered light alone or electrons alone can be an intermediary trigger for SRS. Possible theory statement to put in two-speckle paper.

PACS numbers: 52.38.Bv, 52.35.Mw, 52.35.Fp, 52.65.-y

Under proper conditions, a light wave traveling through a plasma can decay into a scattered light wave and an electron plasma wave (EPW), a process known as stimulated Raman scattering (SRS). The growth of this parametric instability depends on the wave amplitudes, damping rates, frequencies, and wavenumbers. If a primary light wave enters a region of plasma in which there exists a non-zero amplitude scattered light wave, or in which the local electron distribution is such that the Landau damping rate of EPWs is modified, then the level of SRS activity for that light wave may not match the theoretically predicted growth of SRS for an equivalent light wave traveling through a quiescent plasma. This potential scenario can arise for any laser beam with a non-uniform intensity profile. Regions of the laser beam which are most intense and have the highest SRS growth rate can, via SRS, generate a spectrum of light waves, EPWs, and accelerated electrons that travel from unstable regions into neighboring regions which in isolation would be stable against SRS. As a result, the entire laser beam can generate more SRS than one might initially predict.

SRS is of particular interest to laser-driven inertial fusion energy devices such as the National Ignition Facility (NIF), where SRS can decrease the driving laser energy and threaten to preheat the fuel by generating energetic particles. The laser beams at NIF consist of a distribution of hot spots, or speckles, due to their smoothing by phase plates. These speckles are on the order of  $5f^2\lambda_0$  long by  $f\lambda_0$  wide [12], where  $f$  is the laser f-number and  $\lambda_0$  is the laser wavelength. While the theoretical growth rate for the average laser beam intensity may be relatively low in the given volume of plasma, a percentage of the speckles may have a relatively large growth rate and undergo significant SRS. Instability growth in one speckle will produce scattered waves and particles that travel into neighboring speckles. An important question is how the

influx of these waves and particles into speckles that otherwise would not undergo significant SRS in isolation will result in different SRS behavior for the laser beam as a whole. A collective increase in SRS activity for speckled laser beams due to interspeckle interactions has been shown by Yin *et al.* [2–4]. However, Yin *et al.* claim that neither electrons nor scattered waves alone can alter the SRS threshold in below-threshold speckles. Rousseaux *et al.* [5] and Glize *et al.* [6] demonstrated experimentally and numerically that a strong laser speckle could trigger SRS in a weak speckle, though their work was for plasmas in which  $k\lambda_D < 0.2$  ( $k$  is the EPW wavenumber and  $\lambda_D$  the electron Debye length) and hot electrons enhanced the fluctuation levels underlying SRS growth rather than modified the collisionless Landau damping.

Here we show the mechanisms by which SRS in a below-threshold laser beam can be triggered in the kinetic regime solely by electrons or scattered light resulting from SRS in a neighboring laser beam. “Above-” and “below-” threshold are here defined in the context of a threshold between strongly damped convective growth and kinetically inflated growth. Most SRS at NIF is in the strongly damped convective regime (in contrast to the regime studied in Refs. [5, 6]), but for convective growth of SRS, an EPW may grow to an amplitude at which it can trap particles for more than a bounce period. The EPW’s damping rate will then drop and SRS can transition into the weakly damped or even absolute regime. Kinetic inflation of SRS has been demonstrated in seeded SRS simulations [11], but the present results are also a direct demonstration of kinetically inflated SRS due solely to a modification of the electron distribution function. Through two-dimensional (2D) particle-in-cell (PIC) simulations of two neighboring laser beams (speckles), one below-threshold for SRS and one above-threshold, we isolate the intermediary interactions by varying the speckles’ relative polarization, spatial position, and timing and

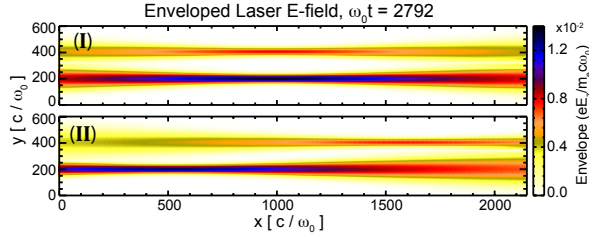


FIG. 1: Transverse electric field showing the relative speckle positions in (I) side-by-side scenario and (II) staggered scenario with the below-threshold speckle placed ahead of the above-threshold speckle.

by utilizing an external magnetic field.

In this article, we simulate the scattering processes in 2D using the electromagnetic PIC code OSIRIS [1]. The electrons have a temperature  $T_e = 2.5$  keV and density  $n_e = 0.13n_{cr}$  ( $k\lambda_D \approx 0.27$  for backward SRS); ions are fixed to focus solely on SRS interactions. We emulate  $f/8$  speckles with Gaussian laser beams of wavelength  $\lambda_0 = 0.351\mu\text{m}$  and focal width  $w_s = f\lambda_0 = 2.8\mu\text{m}$  (intensity full-width half-max) launched from an antenna at the boundary. We study one above-threshold laser of focal intensity  $2 \times 10^{15}$  W/cm<sup>2</sup> ( $eE/mc\omega_0 = 0.0134$ ) interacting with neighboring laser speckles with intensity ranging between  $5$  and  $8 \times 10^{14}$  W/cm<sup>2</sup> ( $eE/mc\omega_0 = 0.0067$  and  $0.0078$ ). The lasers propagate along  $\hat{x}$  and the above-threshold laser is polarized out of the 2D plane in  $\hat{z}$ . The simulations have absorbing boundaries for the fields and thermal-bath boundaries for the particles. We used 256 particles per cell with quadratic interpolation and  $10740 \times 2004$  cells to simulate plasma of size  $120 \times 33.6 \mu\text{m}^2$ .

We show two scenarios in this article for spatial placement: one scenario is for side-by-side placement (Figure 1-I), and a second is for staggered placement in  $\hat{x}$  (Figure 1-II). We will use “ $S_b$ ” (“ $S_a$ ”) to refer to the below-threshold (above-threshold) speckle.  $S_a$  is always focused below  $S_b$  in  $\hat{y}$ , and in the staggered scenario,  $S_b$  is focused ahead of  $S_a$  in  $\hat{x}$ , with “ahead of” referring to the laser propagation direction ( $+\hat{x}$ ). The simulation length corresponds to the central portion of an  $f/8$  speckle of length  $5f^2\lambda_0 = 120\mu\text{m}$  and the width is such that  $4w_s$  separate the speckle centers from each other transversely and separate each speckle from the boundary. The lasers have a rise time of  $300\omega_0^{-1}$  but are otherwise always on during the duration of the simulation ( $35000\omega_0^{-1}$ , or approximately 6.6 ps).

To begin, we tested our notion of above- and below-threshold by simulating single laser beams. For these plasma parameters, there was an abrupt onset of SRS at  $9 \times 10^{14}$  W/cm<sup>2</sup>. Again, we emphasize that this is a threshold for kinetically inflated growth. Previous authors have commented on the abrupt onset of SRS due to kinetic inflation [10, 11, 17], and we have previously

noted that the onset of kinetically inflated growth in simulations occurs when the number of gain lengths is approximately equal to the system length [18, 19]. We can calculate the approximate number of gain lengths in the system using the convective gain length  $L_c = \gamma_p v_- / \gamma_0^2$ , where  $\gamma_p$  is the EPW damping rate,  $v_-$  is the scattered light’s group velocity,  $\gamma_0 = (kv_{osc}/4)(\omega_p/\sqrt{\omega(\omega_0 - \omega)})$  is the homogenous undamped temporal growth rate [20],  $v_{osc}$  is the electron quiver velocity, and  $\omega$  and  $k$  are the EPW frequency and wavenumber, respectively, for which we initially solve by using both the frequency and wavenumber matching conditions for SRS and the kinetic dispersion relation,  $1 - (1/2(k\lambda_D)^2)Z'(\omega/\sqrt{2}v_{the}k) = 0$ , with  $Z'$  the derivative of the plasma dispersion function. For a light wave with  $I_0 = 9 \times 10^{14}$  W/cm<sup>2</sup>,  $L/L_c \approx 2$ , matching our notion that kinetic inflation can be seen for lengths on the order of a gain length. This scaling will be explored more fully in a subsequent article. Here we note that for  $I = 2 \times 10^{15}$  W/cm<sup>2</sup> there was significant SRS with time-averaged reflectivity of 22%, while for  $I = 5 - 8 \times 10^{14}$  W/cm<sup>2</sup> there was no SRS over 6.6ps.

Next, we place  $S_a$  and  $S_b$  side-by-side (Figure 1-I) and set  $S_b$  with  $I_b = 7 \times 10^{14}$  W/cm<sup>2</sup>. For relative polarizations that are parallel, SRS is triggered in  $S_b$ , while if they are perpendicular, SRS in  $S_b$  is not triggered. This is illustrated in Figure 2, where we plot the time evolution of the EPW activity due to SRS via  $\bar{E}^2(y, t) = L_x^{-1} \int_0^{L_x} dx |E_x(x, y, t)|^2$  and plot the reflected light at the incident edge as the deviation of the Poynting flux from its initial value. For both relative polarizations, strong bursts of reflected light and EPW activity can be seen in the region of  $S_a$ , while weaker or no bursting activity is seen in the region of  $S_b$ . The bursts from  $S_a$  are similar to single-speckle simulation results.

There is clearly speckle interaction when the polarizations are parallel (Fig. 2A). Scattered light from  $S_a$  can be convectively amplified as it passes through  $S_b$ , and secondly, it can resonantly trigger further SRS growth in  $S_b$  even though  $S_b$  is below-threshold by itself. The reflected light diagnostic has streaks between  $S_a$  and  $S_b$  which are indicative of scattered light traveling at an angle within the box and getting to the domain edge at later times for larger angles and/or for positions deeper into the domain. This initially triggers low levels of EPW activity at  $\omega_0 t \approx 10000$ . At  $\omega_0 t \approx 17000$ , these EPWs grow to larger amplitude, and several bursts of reflected light occur in the region of  $S_b$ . They are small in amplitude relative to the burst of reflected light from  $S_a$ , but one must keep in mind that the intensity of  $S_b$  is approximately three times smaller than that of  $S_a$ . Even a burst of 100% reflectivity from  $S_b$  would only be about half the amplitude of the initial reflectivity burst of  $S_a$ . The total time-averaged reflectivity over the entire domain is approximately 21% and does not deviate significantly from the reflectivity of  $S_a$  alone. This again is due to the rel-

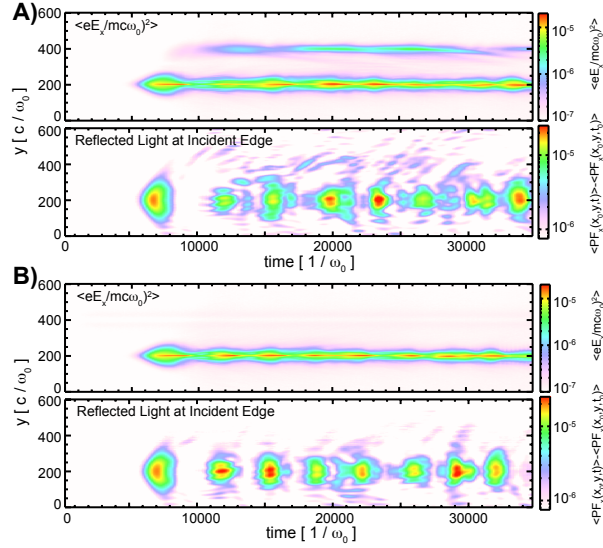


FIG. 2: EPW activity and reflected light at the incident edge for side-by-side speckles with (A) parallel and (B) perpendicular relative polarizations.

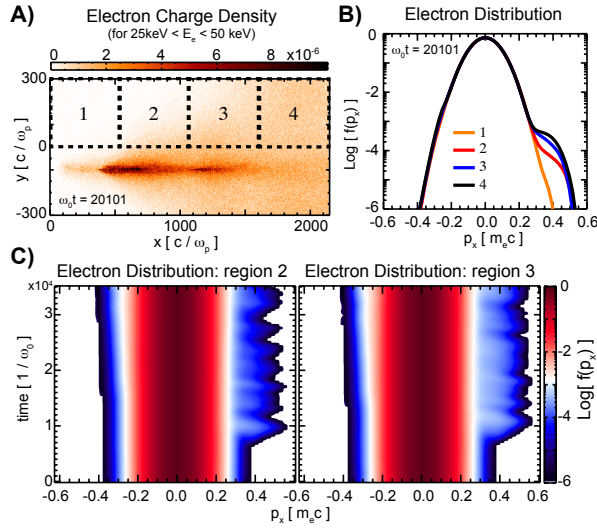


FIG. 3: Electron phasespace showing trapped particles during SRS of an above-threshold speckle. A) charge density in space for electrons between 25 and 50 keV ( $E_e$  typical of electrons accelerated by SRS), B) electron distribution averaged over  $p_y$  and  $[x, y]$  regions labeled in top-left plot; C) time history of the electron distribution functions averaged over  $p_y$  and  $[x, y]$  regions labeled 2 and 3 in top-left plot.

atively small amplitude of  $S_b$  relative to  $S_a$ , even if it is contributing to the SRS activity.

There is no speckle interaction when the polarizations are perpendicular (Fig. 2B). The absence of SRS activity for  $S_b$  is due to the fact that (i)  $S_b$  does not un-

dergo SRS when beating with the perpendicularly polarized scattered light streaming into it from  $S_a$  and (ii)  $S_b$ 's interaction with the particles coming from  $S_a$  is too weak to trigger it to undergo SRS. Figure 3A shows, at one time during an SRS burst of  $S_a$  in Fig. 2B, the charge density of electrons with kinetic energies between 25 and 50 keV, that is, electrons that have been accelerated above the phase velocity of the daughter EPW during SRS. The region of largest charge density is that region where SRS is occurring in  $S_a$ . Particles resonant with the SRS EPW are those traveling in the  $+\hat{x}$  direction with velocity range  $[v_\phi - v_{tr}, v_\phi + v_{tr}]$ , where  $v_\phi$  is the EPW phase velocity and  $v_{tr}$  is the trapping velocity. The resonant electrons also have a spread of transverse momenta characteristic of the background thermal distribution; the EPW traps and accelerates electrons only in  $\hat{x}$ . Since there is therefore an angular dependence to the charge density of resonant electrons that exit an unstable region of SRS, the modification to local electron distribution functions that neighbor SRS activity depend on their location relative to the unstable region. For example, the electron distributions spatially averaged over the labeled sub-regions of Fig. 3A are plotted in Fig. 3B, where averaging has also been carried out over transverse momentum. The distribution functions first flatten at  $p_x \approx 0.30$ , corresponding to  $v_\phi$  of the SRS EPW. However, the degree of flattening is quite different depending on whether one considers region 1 versus region 4. The speckles are focused to the boundary of regions 2 and 3, and the daughter EPWs that grow due to SRS spray trapped particles most strongly toward regions 3 and 4, that is, those regions ahead of the speckles' foci and into which any daughter SRS EPWs travel. It follows that a neighboring speckle will encounter a more strongly modified electron distribution, and therefore be more impacted by influxing electrons, if it is focused ahead of the unstable speckle.

We tested a scenario in which the intensities of  $S_a$  and  $S_b$  are the same as in Figure 2 but in which  $S_b$  is focused ahead of  $S_a$ , that is, the relative speckle placements are staggered as shown in Figure 1-II. With these placements, the energetic electrons generated by SRS bursts of  $S_a$  now have a higher flux into  $S_b$ . Figure 4 shows that indeed  $S_b$  is triggered in this case. Triggering by hot electrons alone is possible, provided the distribution function is sufficiently modified. Simply altering the relative spatial placement of  $S_b$  can influence speckle interactivity. We note that Yin *et al.* [3] focused a below-threshold speckle behind an above-threshold speckle, likely influencing their conclusion that electrons alone could not trigger a below-threshold speckle.

In addition to altering the speckle's placement, one could simply increase the intensity of  $S_b$  while still keeping it below threshold. We repeated the side-by-side scenario of Fig. 2B and increased  $I_b$  to  $8 \times 10^{14}$  W/cm<sup>2</sup>. Though we do not show results here, this scenario in-

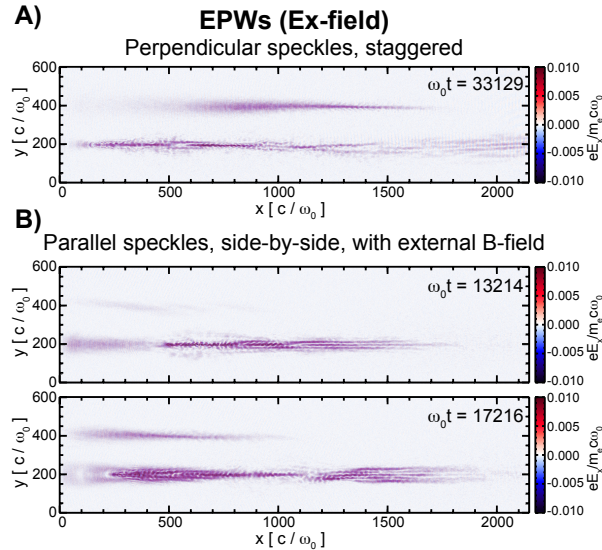


FIG. 4: EPW activity in (A) staggered speckles with perpendicular relative polarization and (B) side-by-side speckles with parallel relative polarization and an applied external B-field show that SRS can be triggered in  $S_b$  due to electrons alone (in A) and scattered light alone (in B).

deed resulted in  $S_b$  undergoing SRS. Despite having the lower influx of trapped particles when being side-by-side with  $S_a$ , the slightly higher  $I_b$  brings  $S_b$  closer to threshold, and it therefore requires less modification of the local distribution for  $S_b$  to transition into a kinetically inflated state.

To investigate another claim of Ref. [3] that scattered light alone could not trigger a below-threshold speckle either, we applied an external 42 T magnetic field aligned along  $\hat{x}$ , the laser-propagation direction.  $eB_x/mc\omega_0 = 0.00138$  gives a gyroradius of  $2.8 \mu\text{m}$  for an electron with  $v_\perp = v_{th}$ , i.e., a gyroradius equal to the speckle width. Using the same set-up as for Fig. 2A, the magnetic field has essentially no effect on the amount of SRS triggered in  $S_b$ . EPW activity is shown in Figure 4B at two times. In this case, we conclude that scattered light is solely responsible for the speckle interaction, and in contrast with Ref. [3], conclude that scattered light alone can trigger a below-threshold speckle. Nevertheless, despite the reduction in trapped particle motion between  $S_a$  and  $S_b$  due to the B-field, there can arise a modified electron distribution in the region of  $S_b$  due to SRS stimulated by the scattered light interaction. In Figure 4B, the EPWs at  $y\omega_0/c \approx 400$  and  $\omega_0 t = 11632$  have a negative slope, due to their being stimulated by the scattered light coming from  $S_a$ . At the later time,  $\omega_0 t = 22334$ , the EPWs stretch horizontally and have a shape similar to a burst of SRS in a single speckle. Between the two times shown, the EPWs produced in the region of  $S_b$  during the initial scattered light interaction

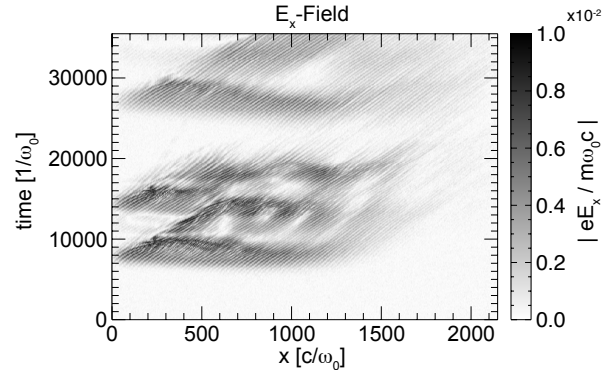


FIG. 5: EPW activity along the speckle axes.

have accelerated electrons and modified the electron distribution function local to the region of  $S_b$ , which itself contributes to the later bursts of SRS.

The effect of B fields is in fact more complex. B fields that constrain electrons to stay within a speckle alter the nonlinear damping and may act to make any SRS more 1D-like. This could result in lower thresholds along the speckle axis or different damping rates across a speckle transversely, affecting for example transverse localization. These effects should be considered more carefully before claiming that B fields limit SRS activity, and is left for future work.

Finally, we have investigated the action of electron plasma waves as a trigger for below-threshold speckles. To do so, we focused both speckles at the same point in  $\hat{y}$  and  $\hat{x}$  but altered their timing.  $S_a$  was on between  $\omega_0 t = 0 - 17000$  and  $S_b$  was turned on afterwards from  $\omega_0 t = 20000 - 35000$ . The time between  $\omega_0 = 17000 - 20000$  was left for the most energetic electrons to exit the region of SRS activity. The EPW activity along the central axis is shown in Figure 5. SRS activity that grows during  $S_a$ 's presence creates plasma waves. These EPWs that are left behind serve as the background for the below-threshold speckle and its resulting SRS. This interaction is sensitive to the damping rate of the plasma waves, which is in turn sensitive to the remaining energetic electrons. It is quite difficult to separate the action of EPWs from the energetic electrons, but we conclude that remnant EPWs left behind by bursts of SRS activity can act as a stimulus for subsequent speckles.

In conclusion, by controlling the relative placement, polarization, and timing of two laser speckles, as well as by using an external B-field, we have shown that plasma waves, scattered light waves, and energetic electrons stimulate SRS in below-threshold speckles. The spray of energetic electrons creates a background distribution that lowers the threshold for SRS, scattered light is the most efficient intermediary, and plasma waves,

while tied together with hot electrons, may nevertheless affect a changing speckle pattern. In addition to incident laser and plasma parameters, total SRS levels will be determined by the evolving state of scattered waves and particles. Even though reflectivity from SRS stimulated in below-threshold speckles may be smaller than that from above-threshold speckles due to their lower intensity, the intensity distribution of speckled laser beams is likely to include many such speckles, and collective effects can dominate over the activity of any one speckle.

The authors gratefully acknowledge support from DOE under Grant No. DE-NA0001833 and from NSF under Grant No. NSF-Phy-0904039. Simulations were performed on UCLA's Dawson2 Cluster, NERSC's Hopper and Edison, and NSF's BlueWaters.

- 
- [1] R. G. Hemker. Ph.D. thesis, University of California, Los Angeles, 2000; R.A. Fonseca *et al.*, Lecture Notes in Computer Science **2331**, 342 (2002); R.A. Fonseca *et al.*, Plasma Physics and Controlled Fusion **50**, 124034 (2008).
- [2] L. Yin, B. J. Albright, H. A. Rose, K. J. Bowers, B. Bergen, R. K. Kirkwood, D. E. Hinkel, A. B. Langdon, P. Michel, D. S. Montgomery, and J. L. Kline, Phys. Plasmas **19**, 056304 (2012).
- [3] L. Yin, B. J. Albright, H. A. Rose, D. S. Montgomery, J. L. Kline, R. K. Kirkwood, P. Michel, K. J. Bowers, and B. Bergen, Phys. Plasmas **20**, 012702 (2013).
- [4] L. Yin, B. J. Albright, H. A. Rose, D. S. Montgomery, J. L. Kline, R. K. Kirkwood, J. Milovich, S. M. Finnegan, B. Bergen, and K. J. Bowers, Phys. Plasmas **21**, 092707 (2014).
- [5] C. Rousseaux, K. Glize, S. D. Baton, L. Lancia, D. Bénisti, and L. Gremillet, Phys. Rev. Lett. **117**, 015002 (2016).
- [6] K. Glize, C. Rousseaux, D. Bénisti, V. Dervieux, L. Gremillet, S. D. Baton, and L. Lancia, Phys. Plasmas **24**, 032708 (2017).
- [7] B. J. Albright, W. Daughton, L. Yin, K. J. Bowers, J. L. Kline, D. S. Montgomery, and J.C. Fernández, J. Phys. IV France **133**, 253 (2006).
- [8] H. X. Vu, D. F. DuBois, and B. Bezzerides, Phys. Rev. Lett. **86**, 4306 (2001); Phys. Plasmas **9**, 1745 (2002).
- [9] H. X. Vu, D. F. DuBois, and B. Bezzerides, Phys. Plasmas **14**, 012702 (2007).
- [10] D. J. Strozzi, E. A. Williams, A. B. Langdon, and A. Bers, Phys. Plasmas **14**, 013104 (2007).
- [11] I. N. Ellis, D. J. Strozzi, B. J. Winjum, F. S. Tsung, T. Grismayer, W. B. Mori, J. E. Fahlen, and E. A. Williams, Phys. Plasmas **19**, 112704 (2012).
- [12] J. Garnier and L. Videau, Phys. Plasmas **8**, 4914 (2001).
- [13] J. E. Fahlen, B. J. Winjum, T. Grismayer, and W. B. Mori, Phys. Rev. E **83**, 045401(R) (2011).
- [14] J. Banks, R. L. Berger, S. Brunner, B. I. Cohen, and J. A. F. Hittinger, Phys. Plasmas **18**, 052102 (2011).
- [15] L. Yin, B. J. Albright, K. J. Bowers, W. Daughton, and H. A. Rose, Phys. Plasmas **15**, 013109 (2008).
- [16] H. A. Rose and L. Yin, Phys. Plasmas **15**, 042311 (2008).
- [17] L. Yin, W. Daughton, B. J. Albright, B. Bezzerides, D. F. DuBois, J. M. Kindel, and H. X. Vu, Phys. Rev. E **73**, 025401(R) (2006).
- [18] B. J. Winjum, "Particle-in-cell simulations of stimulated Raman scattering for parameters relevant to inertial fusion energy," Ph.D. dissertation, University of California, Los Angeles (2010).
- [19] B. J. Winjum, J. E. Fahlen, F. S. Tsung, and W. B. Mori, Phys. Rev. E **81**, 045401(R) (2010).
- [20] D. W. Forslund, J. M. Kindel, and E. L. Lindman. Phys. Fluids **18**, 1002 (1975).



# CHAPTER 12

## Conclusion

This dissertation detailed the production and use of two kinetic plasma simulation software packages. Examined first was OSHUN - a VFP code capable of modeling large systems by fully exploiting modern (i.e. massively parallel) computing resources. Then the addition of 3 modules to the PIC code OSIRIS were detailed:

- Quasi-3D: a novel coordinate system that allows 3D simulations at costs approaching those of 2d (speed up of  $\approx 100$  )
- Lorentz Boost Frame: simulating systems in a relativistic frame (speedup of  $\approx \gamma^2$  — typically 100 to 100,000 in LWFA systems).
- Graphics Processing Units (GPUs): Adding support for cutting-edge massive-parallelism (speed up of  $\approx 100$  )

If used simultaneously, these modules can give an amazing factor  $\approx 1e^6$  or more speed increase for 3D laser-plasma simulations. The full scale unification of these three modules required to enable such immense speed increases is challenging. The dissertation described efforts to reach this goal including the creation of OSIRIS Version 4.0 which provides the infrastructure to enable complex software integration. Initial results coupling Quasi-3D to the Lorentz Boosted Frame were shown. This work is an ongoing and rich area for future researchers.

## BIBLIOGRAPHY

- [1] M. Tzoufras, A. R. Bell, P. A. Norreys, and F. Tsung, “A vlasov-fokker-planck code for high energy density physics,” *J. Comput. Physics*, vol. 230, pp. 6475–6494, 07 2011.
- [2] R. A. Fonseca, L. O. Silva, F. S. Tsung, V. K. Decyk, W. Lu, C. Ren, W. B. Mori, S. Deng, S. Lee, T. Katsouleas, and J. C. Adam, “Osiris: A three-dimensional, fully relativistic particle in cell code for modeling plasma based accelerators,” in *Computational Science — ICCS 2002* (P. M. A. Sloot, A. G. Hoekstra, C. J. K. Tan, and J. J. Dongarra, eds.), (Berlin, Heidelberg), pp. 342–351, Springer Berlin Heidelberg, 2002.
- [3] R. G. Hemker, F. S. Tsung, V. K. Decyk, W. B. Mori, S. Lee, and T. Katsouleas, “Development of a parallel code for modeling plasma based accelerators,” in *Proceedings of the 1999 Particle Accelerator Conference (Cat. No.99CH36366)*, vol. 5, pp. 3672–3674 vol.5, March 1999.
- [4] Hines, Jonathan (8 June 2018), “Genomics code exceeds exaops on summit supercomputer,” 2017. <https://www.olcf.ornl.gov/2018/06/08/genomics-code-exceeds-exaops-on-summit-supercomputer>. Oak Ridge Leadership Computing Facility. Retrieved 21 September 2018.
- [5] M. Tzoufras, A. Tableman, F. S. Tsung, W. B. Mori, and A. R. Bell, “A multi-dimensional Vlasov-Fokker-Planck code for arbitrarily anisotropic high-energy-density plasmas,” *Phys. Plasmas*, vol. 20, no. 5, p. 056303, 2013.
- [6] W. Rozmus, T. Chapman, A. Brantov, B. J. Winjum, R. L. Berger, S. Brunner, V. Y. Bychenkov, A. Tableman, M. Tzoufras, and S. Glenzer, “Resonance between heat-carrying electrons and Langmuir waves in inertial confinement fusion plasmas,” *Phys. Plasmas*, vol. 23, no. 1, p. 012707, 2016.
- [7] A. S. Joglekar, B. J. Winjum, A. Tableman, H. Wen, M. Tzoufras, and W. B. Mori, “Validation of OSHUN against collisionless and collisional plasma physics,” *Plasma Phys. Controlled Fusion*, vol. 60, no. 6, p. 064010, 2018.
- [8] A. Davidson, A. Tableman, W. An, F. S. Tsung, W. Lu, J. Vieira, R. A. Fonseca, L. O. Silva, and W. B. Mori, “Implementation of a hybrid particle code with a PIC description in r-z and a gridless description in phi into osiris,” *J. Computational Phys.*, vol. 281, pp. 1063–1077, 2015.
- [9] A. Davidson, A. Tableman, P. C. Yu, W. M. An, F. Tsung, W. Lu, R. A. Fonseca, and W. B. Mori, “An Examination of the Scaling Laws for LWFA in the Self-Guided Nonlinear Blowout regime,” *Adv. Accelerator Concepts*, vol. 1812, pp. UNSP 040014–1, 2017.
- [10] P. C. Yu, X. L. Xu, A. Tableman, V. K. Decyk, F. S. Tsung, F. Fiuza, A. Davidson, J. Vieira, R. A. Fonseca, W. Lu, L. O. Silva, and W. B. Mori, “Mitigation of numerical Cerenkov radiation and instability using a hybrid finite difference-FFT Maxwell

- solver and a local charge conserving current deposit,” *Computer Phys. Comm.*, vol. 197, pp. 144–152, 2015.
- [11] P. C. Yu, X. L. Xu, A. Davidson, A. Tableman, T. Dalichaouch, F. Li, M. D. Meyers, W. M. An, F. S. Tsung, V. K. Decyk, F. Fiuza, J. Vieira, R. A. Fonseca, W. Lu, L. O. Silva, and W. B. Mori, “Enabling Lorentz boosted frame particle-in-cell simulations of laser wakefield acceleration in quasi-3D geometry,” *J. Computational Phys.*, vol. 316, pp. 747–759, 2016.
- [12] P. Yu, A. Davidson, X. Xu, A. Tableman, V. K. Decyk, F. S. Tsung, J. Vieira, R. A. Fonseca, W. Lu, L. O. Silva, and W. B. Mori, “Modeling of Laser Wakefield Acceleration In Lorentz Boosted Frame Using a Quasi-3D OSIRIS algorithm,” *Adv. Accelerator Concepts*, (*aac 2014*), vol. 1777, p. UNSP 040020, 2016.
- [13] F. Li, P. C. Yu, X. L. Xu, F. Fiuza, V. K. Decyk, T. Dalichaouch, A. Davidson, A. Tableman, W. M. An, F. S. Tsung, R. A. Fonseca, W. Lu, and W. B. Mori, “Controlling the numerical Cerenkov instability in PIC simulations using a customized finite difference Maxwell solver and a local FFT based current correction,” *Computer Phys. Comm.*, vol. 214, pp. 6–17, 2017.